Evaluation of 3D printing technologies for the development of wide-band directive antennas for millimeter wave backhaul links in E and V frequency bands

Nour Nachabe

UNIVERSITÉ CÔTE D'AZUR

ÉCOLE DOCTORALE
SCIENCES ET TECHNOLOGIES DE L'INFORMATION ET DE LA COMMUNICATION

THÈSE DE DOCTORAT

Evaluation des technologies d'impression 3D pour le développement d'antennes directives à large bande passante pour les liaisons backhaul en bandes millimétriques V et E

Nour NACHABE

Laboratoire Polytech'lab

Présentée en vue de l'obtention du grade de docteur en électronique
d'Université Côte d'Azur
Dirigée par : Cyril Luxey
Co-encadrée par : Frédéric Gianesello
Soutenue le : 6 Décembre 2018

Devant le jury, composé de :
Hervé Aubert, Professeur, ENSEEIHT, Rapporteur
Ana Arboleya, Professeur, URJC
Jorge Rodriguez Da Costa, Professeur, ISCTE-IUL
Frédéric Gianesello, Ingénieur de recherche, STMicroelectronics
Raphaël Gillard, Professeur, INSA Rennes, Rapporteur
Cyril Luxey, Professeur, Polytech'lab
Alain Sibille, Professeur, Télécom ParisTech
Diane Titz, Professeur, Polytech'lab

POLYTECH NICE-SOPHIA POLYTECH'LAB
life.augmented
CONCEPTION CIM PACA

Evaluation des technologies d'impression 3D pour le développement d'antennes directives à large bande passante pour les liaisons « backhaul » en bandes millimétriques V et E.

Résumé : Face à la demande croissante de débits de données de plus en plus élevées, l'une des principales solutions proposées par la 5G est de densifier le réseau en y intégrant notamment de nouvelles « Small cells ». La réorganisation de l'architecture du réseau mobile pour s'adapter à l'intégration poussée de ces Small cells, fait naître la problématique de la connexion backhaul entre les stations de bases desservant les Small cells et le cœur de réseau. Ainsi, des liaisons backhaul de plusieurs Gb/s de données sont nécessaires pour pouvoir assurer un débit de données d'au moins 100Mb/s à l'utilisateur qui est l'un des objectifs fixés pour la 5G. Les solutions de connexion backhaul sans fils ont un avantage indiscutable face aux coûts de déploiements de fibres optiques qui sont très élevés. Pour augmenter la capacité spectrale des liaisons sans fils, l'utilisation des fréquences millimétriques au-delà de 6 GHz caractérisées par des larges bandes passantes sera prochainement discutée pour la 5G durant le World Radiocommunication Conference 2019. Parmi ces fréquences, les bandes V (57-66GHz) et E (71-76 GHz et 81-86 GHz) ont un intérêt indéniable grâce aux larges bandes passantes disponibles ainsi qu'aux conditions de licenciement peu exigeantes. Les travaux développés dans cette thèse consistent à concevoir des antennes directives à large bande passante permettant d'établir les liens backhaul point-à-point sans fils (LoS). En exploitant les technologies de fabrications à faibles coût telles que l'impression 3D et Printed Circuit Board (PCB) sur des substrats FR4, la conception de deux types d'antenne directives a été étudiée à savoir des antennes lentilles et des antennes réseaux.

Mots clés : 5G, backhaul, bandes de fréquences millimétriques, antenne réseau, antenne lentille, PCB FR4, impression 3D.

Evaluation of 3D printing technologies for the development of wide-band directive antennas for millimeter wave backhaul links in E and V frequency bands.

Abstract: In order to address the ever-increasing demand of higher data rates, adding small cells to the existing macro-cells infrastructure is one of the most important milestones of the 5G roadmap. With the integration of small cells and the re-organization of the network topology, backhaul bottleneck is the main challenge to address in the near future. Facing the costs of deployments of fiber optic connections, point-to-point wireless backhaul links using millimeter wave (mmW) frequencies are gaining prominence. 5G future frequencies, to be discussed under the World Radiocommunication Conference 2019 (WRC-19) open-up the way towards mmW frequency band where large bandwidths are naturally available. The high bandwidths available at these frequencies enable several Gbps data rate backhaul links, which is un utmost necessity to respect the 100 Mbps user-experienced data rate promised by the 5G standard. Millimeter-wave frequencies in V and E-bands unlicensed/light licensed spectrum are considered as primary candidates for backhaul links. In addition to the light license regime, the high free space path loss experienced at these frequencies is rather beneficial to limit the interference between small cells links. Moreover, the high available bandwidths at V and E-bands enable to achieve multi Gb/s links without using complex modulation schemes. In this thesis, we focused our research study on developing high gain wide-band antennas usable in point-to-point backhaul links in a Line of Sight (LoS) context. Leveraging cost-efficient technologies like 3D printing and Printed Circuit Board (PCB) on FR4 substrates, we studied two high-gain antenna types: lens antennas and flat array antennas.

Keywords: 5G, backhaul, millimeter wave frequency bands, antenna array, lens antenna, PCB FR4, 3D printing.

Acknowledgements

Firstly, I would like to sincerely thank my supervisors, Pr. Cyril Luxey and Dr. Frederic Gianesello, for their valuable guidance, patience and motivation. Surely their highly-appreciated advices and help brought this work to a higher level. I also like to thank all those who have participated in this work and helped me to overcome many obstacles, especially Pr. Diane Titz, Dr. Aimeric Bisognin and Pr. Ana Arboleya. Special thanks to Frederic Devillers for all the mechanical conception tips and help in realizing the prototypes. I also thank all the members of Polytech'lab for all their favors.

Besides the mentioned above, I would like to thank all the committee members, Pr. Raphael Gillard, Pr. Hervé Aubert, Pr. Alain Sibille and Pr. Jorge Costa for accepting to report on this work and recognizing its value.

Special gratitude for all the research teams we have cooperated with for their help to accomplish this work, ISCTE-IUL, Public University of Navarra, Cimpaca conception and Orangle labs Cremant.

Sincere thanks to all my labmates with whom I shared my moments of success and failure. Thank you for your encouragement and your friendship.

I thank from the deep of my heart all my family members. Especially my mother, father and husband thank you for your sacrifice, patience and for believing in me, I remain grateful for you. I finally give a big thanks to my daughter Rim thank you for your smiles, for your love.

Table of contents

Table of Acronyms

Acronym	Meaning
3GPP	Third Generation Partnership Project
AM	Additive Manufacturing
AuT	Antenna under Test
BBU	BaseBand Unit
BtB	Back to Back
CAD	Computer Aided Design
CAGR	Compound Annual Growth Rate
CPRI	Common Public Radio Interface
C-RAN	Cloud-Radio Access Network
DAM	Digital Additive Manufacturing
DMLS	Direct Metal Laser Sintering
eMBB	Enhanced Mobile Broadband
eWLB	embedded Wafer Level Ball Grid Array
ETSI	European Telecommunication Standards Institute
ESA	European Space Agency
FDM	Fused Deposition Modeling
FDMA	Frequency-Division Multiple Access
FF	Far Field
FSS	Frequency Selective Surface
GSG	Ground Signal Ground
HBW	Half-Beamwidth
HDI	High Density Interconnect
HetNet	Heterogeneous Network
HTCC	High Temperature Co-fired Ceramic
IC	Integrated Circuit
IMT-2020	International Mobile Telecommunication 2020
IMT-Advanced	International Mobile Telecommunications Advanced
IPA	IsoPropyl Alcohol
ITU-R	International Telecommunications Union – Radio sector
LoS	Line of Sight
LTCC	Low Temperature Co-fired Ceramic
LTE	Long-Term Evolution
M2M	Machine-to-Machine
MIMO	Multiple Input, Multiple Output

mmW	Millimeter Wave
MS-to-WG	Microstrip-to-Waveguide
NF	Near Field
NFV	Network Function Virtualization
NR	New Radio
NS	Not Specified
OOK	On/Off Keying
P2MP	Point-to-multipoint
P2P	Point to Point
PCB	Printed Circuit Board
RAN	Radio Access Network
RF	Radio Frequency
RFIC	Radio Frequency Integrated Circuit
RPE	Radiation Pattern Envelope
SCP	Slot Coupled Patch
SIW	Substrate Integrated Waveguide
SLA	Stereo Lithography Apparatus
UHD	Ultra-High Definition
URLLC	Ultra-Reliable Low Latency Communication
WLAN	Wireless Local Area Network
WRC	World Radiocommunication Conference
XPD	Cross-Polarization Discrimination level

Introduction

Today, the number of connected devices has reached the number of the world human population (8 billion). By 2021, it is expected to surpass the population of the world projected at that time reaching 11.6 billion of mobile connected devices. On the other hand, data hungry applications are further growing with the emergence of virtual reality and augmented reality applications putting more burden on the communicating networks. The evolution of the actual 4G network to 5G is hence inevitable to keep pace with the demands of connectivity. 5G key goals consist on increasing the user experienced data rate and peak data rate up to 100 Mb/s and 1 Gb/s respectively along with increasing connection density, spectrum efficiency and area traffic capacity. To achieve those targets, small cells will play an ever-more-important role in boosting the mobile network capacity with the support of several access technologies (Wireless Local Area Network (WLAN) and mobile). With the integration of small cells, the infrastructure of the mobile network is moving toward a split between the control plane and data plane to enable an easy deployment and organization of the network. This new network topology gives rise to the challenge of backhaul bottleneck, which links the small cells radio heads to the core of the network. Facing the high costs of fiber optics deployment especially for high density areas, wireless links are an undisputed preference for the establishment of these links due to their lower cost and ease-of-deployment. More precisely, millimeter-wave (mmW) frequencies (above 3 GHz) wireless links are gaining prominence because of the high bandwidth resources naturally available at these frequencies. In a first step towards 5G, C-band (3.7-4.2 GHz) will play an important role, however the full establishment of the 5G concept will not be feasible without frequencies beyond 6 GHz. Among these frequencies, V (57-66 GHz) and E-bands (71-76 GHz and 81-86 GHz) are gaining popularity for backhaul applications. Due to their license exempt/light license regime, those bands are widely available for use at affordable costs and enable multi-Gb/s links thanks to the large chunk of spectrum they naturally offer. Moreover, the high free space loss experienced at these frequencies, especially in V-band due to the high oxygen absorption is rather considered as an advantage to enable low interference with surrounding links in a dense context. Today's integrated circuits technology is sufficiently mature for the development of highly integrated systems at E and V-bands. Several transceivers using silicon CMOS and BiCMOS technologies have been commercialized and together with highly directive antennas, radio systems have enabled data rates up to 10 Gbps over a distance ranging from 200 m to several kilometers. To develop a cost-effective radio system, designing low-cost compact antennas easily integrable with the Radio Frequency Integrated Circuit (RFIC) is the main challenge targeted in this PhD. Hence, we focused our research work on evaluating low-cost technologies like 3D printing and Printed Circuit Board (PCB) for the design of low-cost wide-band directive antennas for backhaul links in V and E-bands. Avoiding reflector antennas for their cumbersome size, we targeted two main types of high-gain antennas, namely lenses and antenna arrays fed by waveguide.

We introduce the context of this PhD in **Chapter I** by first specifying 5G targets and use cases which led to the backhaul bottleneck challenge. Then we concisely discuss the main advantages of millimeter-wave frequencies, especially V and E bands frequencies which make them the best

candidates for multi-Gb/s wireless backhaul links. With the maturity of silicon technologies which enabled low-cost transceivers in V and E band and the evolving performances of today's 3D printing technologies, we emphasize the opportunity of developing cost-efficient high-gain compact antennas for millimeter wave backhaul links.

In **Chapter II**, we focus on designing high-gain plastic lens antennas. In order to present a low-cost system, we study the viability of PCB technology with FR4 substrate to design a lens-source. The source consists of a slot-coupled patch antenna and a via ring structure which is optimized to enable an efficient re-use of the power lost in surface waves modes. We also consider the possibility of integrating a microstrip-to-waveguide (MS-to-WG) transition into the antenna PCB to enable a low-loss connection with the Radio Frequency (RF) PCB. Furthermore, Fused Deposition Modeling (FDM) 3D printing technique using low-cost ABS-M30 plastic filament is evaluated for the fabrication of the lens.

Chapter III features wide-band flat antenna array designs. The unit-cell composing the array consists on a slot-coupled patch fed by a dielectric-filled waveguide demonstrating a high total efficiency on a wide bandwidth. The main challenge addressed in this chapter is to design a wide impedance-bandwidth and low-loss feeding network to maintain the performances of the unit-cells in the array configuration. To fulfill this target, we study several topologies of waveguide feeding networks using waveguide T-junction dividers and twists. 3D printing technologies are discussed for the fabrication of the designed arrays.

In **Chapter IV** we study the use of a double-ridge waveguide as an alternative for dielectric-filled waveguide to enable a one-time fabrication process avoiding assembly and air gaps problems. Our aim is to design a 2×2 subset array of open double-ridged waveguide radiating elements featuring the same wide bandwidth performance than the one of the proposed antenna from chapter 3. For prototyping, a new high-precision 3D printing technique, namely micro Direct Metal Laser Sintering (DMLS), is evaluated for the validation of the proposed design.

We finally conclude our work in **Chapter V** and project our antenna solutions toward broadband satellite applications in Ku and Ka bands employed by massive satellite constellation networks.

I. STATE-OF-THE-ART OF MILLIMETER WAVE BACKHAUL LINKS RADIO SYSTEMS

As data-hungry applications gain popularity, it is unlikely to sustain the ongoing traffic explosion in the long run with the existing 4G technologies. Evolving today's networks to 5G is key to keeping pace with the demands for connectivity. 5G key goals aim to achieve multi Gb/s links for Enhanced Mobile Broadband (eMBB) along with Ultra-Reliable and Low Latency Communication (uRLLC) services. To reach those targets, a manifold increase in the network capacity is needed, leading to the deployment of ultra-dense high capacity small cells networks. However, densifying the network pushes to rethink the network architecture and radio technology to enable multi Gb/s backhaul links between the small cells and the core network. In this context, mmW frequencies from 3 to 300 GHz emerge as the driving force behind high-capacity backhaul links due to the large bandwidth available at these frequencies. In this chapter, we briefly describe the evolution toward 5G and highlight the role of mmW wireless technologies in addressing the backhaul bottleneck challenge. Then, we discuss the rising need for designing cost-effective radio components especially with the maturity of integrated circuits silicon technologies.

I.1 DATA TRAFFIC EXPONENTIAL GROWTH AND SATURATION OF THE EXISTING NETWORK

I.1.1. Data traffic growth rate

Facing the ever-increasing number of wireless devices that are accessing the mobile networks worldwide, the global mobile traffic is expected to grow exponentially. In 2016, more than 400 million (429 million) mobile devices and connections were added to the mobile network [I.1], leading to increase the global mobile connections from 7.6 billion in 2015 to 8 billion. Mobile data traffic has grown 18-fold over the past 5 years and 63% in 2016, as shown in Figure I.1 (a). Most of that growth originates from smartphones, followed by Machine-to-Machine (M2M) modules. Mobile data traffic continues to grow featuring a strong increase in data traffic and voice traffic per year. The main contributors for the growth in data traffic are the increased smartphone subscriptions along with the increase in average data volume per

subscription, mainly due to more viewing of video content, as illustrated in Figure I.1 (b) [I.2]. Mobile video traffic was the main consuming application as it accounted for 60% of total mobile data traffic in 2016. To keep up with the increasing data consumption, mobile network connection speeds grew more than 3-fold in 2016. Globally, the average mobile network downstream speed increased from 2 Mb/s in 2015 to 6.8 Mb/s in 2016. However, these data rates are still insufficient as highly data-consuming emerging applications like Augmented Reality, Virtual Reality and Ultra-High Definition (UHD) videos (4K, 8K) put an enormous burden on the network in terms of bandwidth and latency requirements [I.2]. 4K and 8K UHD videos, for example, require data rates up to 15 to 25 Mb/s and 80 to 100 Mb/s respectively [I.3].

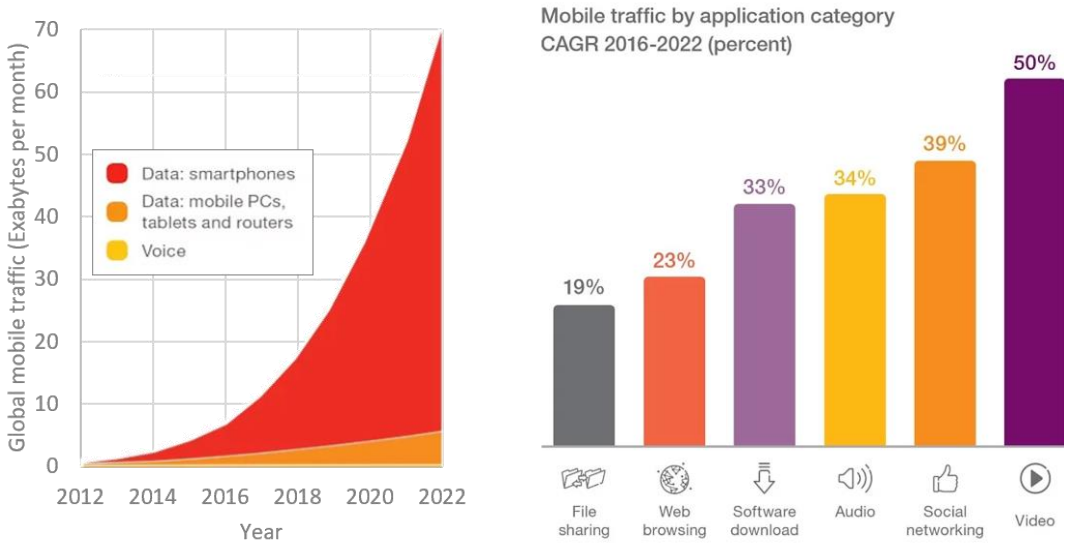

(a) (b)

Figure I.1 (a) Global mobile data traffic exponential growth and (b) Compound Annual Growth Rate (CAGR) 2016-2022 of mobile traffic by application category from [I.2].

Following this trend of high data consumption, Cisco reports that mobile data traffic will reach 49 exabytes per month by 2021, increasing sevenfold between 2016 and 2021 and growing at a compound annual growth rate (CAGR) of 47% from 2016 to 2021 [I.2]. This is certainly accompanied with the increase of the number of mobile connected devices, which by 2021, will exceed the projected population at that time: 11.6 billion of mobile-connected devices versus a population of 7.8 billion. To cope with the demand of higher data rates, mobile network connection speeds will need to increase threefold by 2021, reaching 20.4 Mb/s by 2021.

On the hand, to boost the cellular network capacity Wi-Fi and wireless local area networks (WLAN) could play a further important role to reduce the burden on mobile networks. This was illustrated by the fact that, in 2016, 63% of all traffic from mobile-connected devices (almost 84 exabytes) were offloaded to the fixed network by means of Wi-Fi devices and femtocells each month. Of all IP traffic (fixed and mobile) in 2021, 50% will be Wi-Fi, 30%

will be wired, and 20% will be mobile [I.1]. Therefore, developing the current 4G network to accompany the transition toward 5G is an utmost necessity.

I.1.2. Legacy network limitations

4G standards requirements were specified by The International Telecommunications Union-Radio communications sector (ITU-R) under a specification set named the International Mobile Telecommunications Advanced (IMT-Advanced). The latter set the peak speed requirement for 4G service at 100 Mbit/s for high mobility communications and 1 Gbit/s for low mobility communications. Using an All-IP packet switched network, Orthogonal Frequency-Division Multiple Access (OFDMA) and spatial multiplexing to increase the spectrum efficiency, it was expected that those goals would be reached in 2013.

However, latest statistics show that measured speeds in the first quarter of 2017 are ten times less than the promised rates according to Akamai reports [I.4]. Global average connection speed was found to be 7.2 Mbps (an increase of 15% year-over-year) reaching a global average peak connection of 44.6 Mbps.

Hence, developing today's networks to 5G is key to keeping pace with the demands for a faster connection. The roadmap towards 5G was discussed under the International Mobile Telecommunication 2020 (IMT-2020) set by the ITU-R. The detailed investigation of the key elements of IMT-2020 is ongoing with trials of 5G technologies starting the initial implementations in 2018 [I.5]. According to Ericsson mobility report [I.2], by 2021, 5G will begin to take its place with 0.2% of connections (25 million) generating 1.5 percent of the total traffic (cf. Figure I.2).

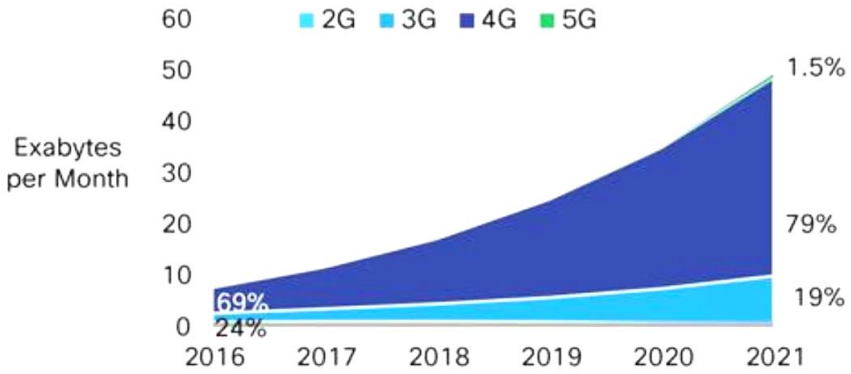

Figure I.2 Global mobile traffic by connection standard from [I.2].

I.2 TOWARDS 5G MMW BACKHAUL

I.2.1. 5G requirements and use cases

5G key requirements are described under the IMT-2020 standards reported in ITU-R M.2410 report. The report fixes the minimum technical performance of candidate radio interface technologies for 5G [I.6]. An overall view of those requirements and comparison to 4G requirements are depicted in Figure I.3. 5G is expected to increase downlink peak data rate and downlink user-experience data rate up to tenfold, reaching 20 Gb/s and 100 Mb/s respectively. Latency is also largely reduced down to 4 ms for eMBB and 1 ms for uRLLC. Most of all, the principle requirement for 5G is to increase the network capacity significantly to support a connection density of 1 million devices per km^2 (ten times more than 4G). Supporting this capacity along with the promised data rates will require an extreme enhancement in area traffic capacity reaching 10 Mbit/s/m^2 compared to 0.1 Mb/s/m^2 that was required for 4G [I.6]. The latter fixed targets are indispensable for 5G use cases, listed in Figure I.4, like Gbps links, 3D video, UHD screens and augmented reality.

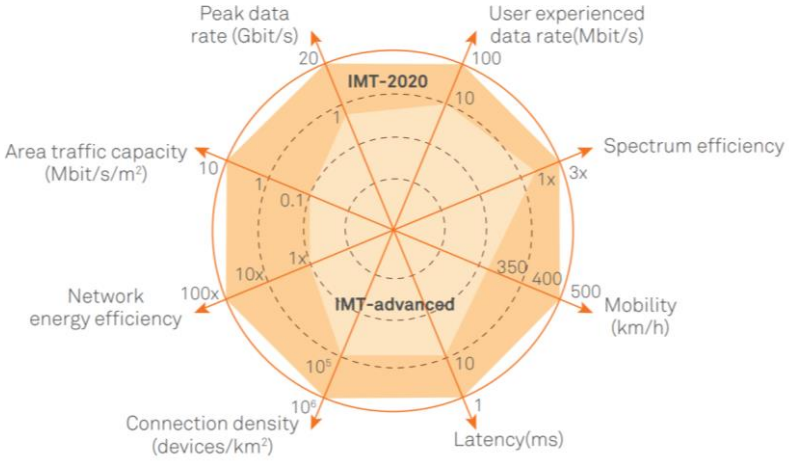

Figure I.3 IMT-2020 key requirements from [I.7].

The development toward 5G will not be abrupt but will take place in several phases. The first phases consist on the evolution of 4G, aimed at enhanced functionality while securing a backward compatibility with the Long-Term Evolution (LTE) standard employed in 4G. The latter phases are revolutionary phases consisting on deploying a new radio (NR) access technology aimed primarily for spectrum bands that have not been used in LTE [I.8]. The NR concept has been designed to meet all the foreseen 5G system requirements including new use cases as well as a wide range of spectrum bands and deployment options. The Third Generation Partnership Project (3GPP) is currently standardizing 5G in Release 15 and completed the non-standalone version of 5G in March 2018, which implements an architecture supporting LTE and NR access to a LTE core network [I.9].

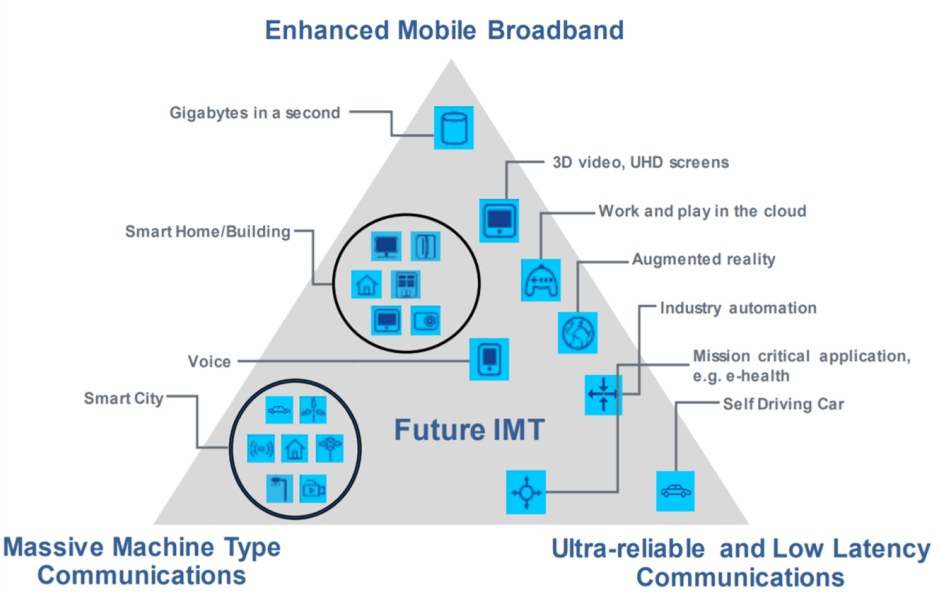

Figure I.4 5G use cases from [I.6].

According to 5G Release 15, the capabilities of NR in 5G will include among others:

- Ability to operate in frequency bands above 3.5 GHz.
- Support of both LTE and 5G NR, including simultaneous connections to LTE and NR.
- A system architecture that enables user services with different access systems, such as WLAN.
- 5 Gb/s peak downlink throughput in initial releases, increasing to 50 Gb/s in subsequent versions.
- Aggregation up to approximately 1 GHz of bandwidth.
- Standards-based Cloud Radio Access Network (C-RAN) support that specifies a split between the control and data layers [I.9].

Release 16, expected in March 2020, specifies the next phase of 5G. It mainly adds spectrum operation above 24 GHz.

I.2.2. 5G spectrum

The wireless network capacity depends on spectral efficiency and bandwidth but is also related to the cell size. To increase capacity, cell sizes are becoming small and physical layer technology is already at the boundary of Shannon capacity. The system bandwidth is the only solution that remains unexplored. Currently, almost all wireless communications use spectrum 300 MHz to 3 GHz band, often termed as “beachfront spectrum” [I.10]. Nonetheless, it is questionable that these frequency bands will accommodate to the exploding mobile traffic and connectivity due to lack of available spectrum. The principal revolution of next generation 5G wireless networks lies in exploring the unused, high frequency mmW bands ranging from 3 to 300 GHz [I.11]. mmW spectrum bands offer large bandwidths enabling the establishment of

high-capacity wireless links on the expense however of a shorter link distance due to increased free space path loss and atmospheric attenuation.

The C-band (3300-4200 and 4400-5000 MHz) is considered as the primary frequency band for the introduction of 5G by 2020 with uplink coverage assistance from frequencies below 2 GHz. It offers at least 100 MHz channel bandwidth, enabling to boost peak, average and cell edge throughput with affordable complexity and is available worldwide as shown in Figure I.5 [I.7]. In fact, a good compromise between free space path loss (coverage) and capacity can be obtained by the 3300-4200 and 4400- 5000 MHz frequency bands [I.12].

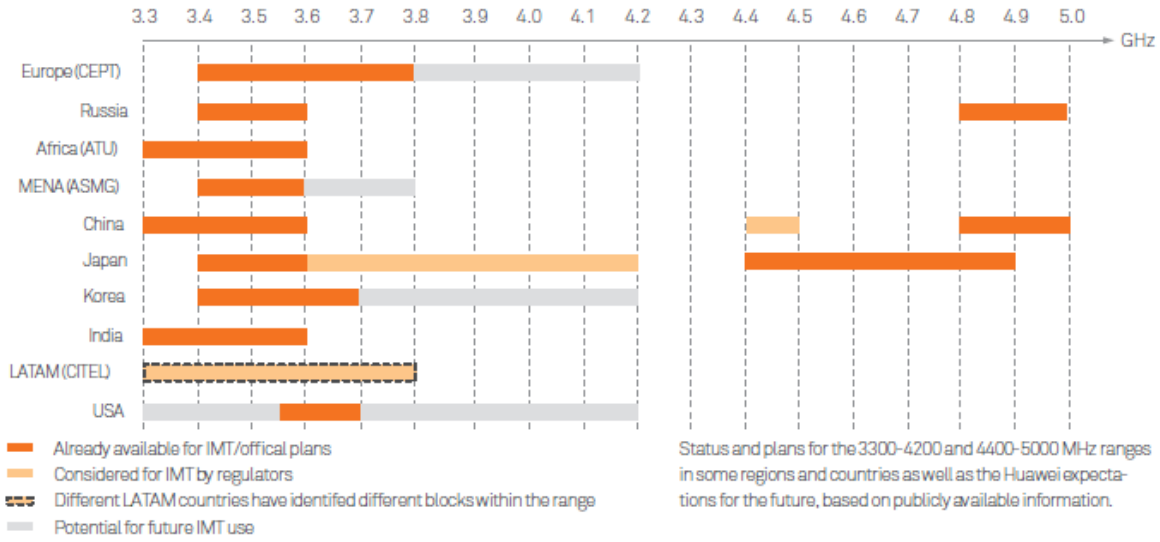

Figure I.5 Global availability and planning of the 3300-4200 MHz and 4400-5000 MHz frequency ranges (C band) for 5G from [I.13].

The next step toward 5G introduces frequencies above 6 GHz. The World Radiocommunication Conference 2015 (WRC-15) identified several higher frequency bands to study for possible identification for IMT under Agenda Item 1.13 of WRC-19. Those frequency bands range from 24 to 86 GHz and are listed in Figure I.6. Other 5G frequency bands not mentioned in the table also include the 60 GHz unlicensed band (57 to 66 GHz) which is allocated to the wireless fixed service on a primary basis in the European Common Allocation table and the ITU-R regulations [I.14]. Even though radio systems at frequencies 24 to 86 GHz are available today, tests are still undergoing and the implementation of those radios didn't reach yet its final state [I.15].

Group 30 (GHz)	Group 40 (GHz)	Group 50 (GHz)	Group 70/80 (GHz)
24.25-27.5 31.8-33.4	37-40.5 40.5-42.5 42.5-43.5	45.5-47 47-47.2 47.2-50.2 50.4-52.6	66-71 71-76 81-86

Figure I.6 Candidate frequency bands of WRC-19 Agenda Item 1.13 from [I.7].

While C-band will be primarily used for the access link between the user and the base stations, the use of frequencies from 24 GHz and above will rather include the backhaul links between the base stations and even fixed wireless access (cf. Figure I.7). Nonetheless, exploiting the wide bandwidth available at mmW frequencies will not be sufficient to meet 5G requirements without a re-organization of the network architecture. A new network architecture is crucial to minimize the complexity and cost of deployment and maintenance, as discussed in the next section.

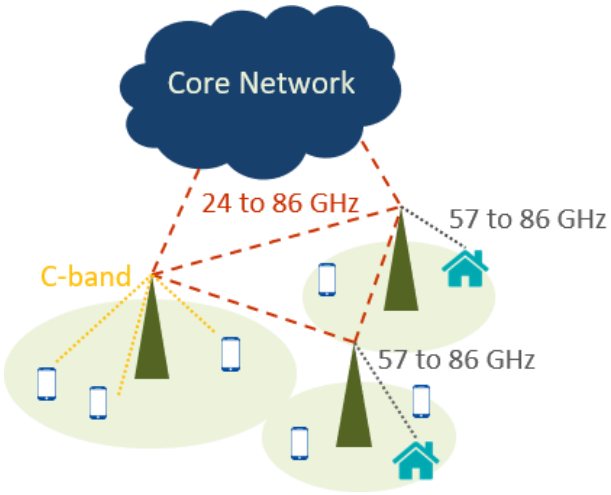

Figure I.7 Possible spectrum use in the mobile network.

I.2.3. C-RAN architecture enabling low-cost small cell deployment

A small cell is basically a base station that breaks up a cell site into much smaller pieces and hence naturally increase the capacity of the system. Small cells can be of different size: picocells, microcells, femtocells and can comprise of indoor/outdoor systems, as shown in Table I.1 [I.16]. In the past decade, small cells deployment was hampered by implementation difficulties such as the cost of optical fiber deployments. Nowadays with the microwave wireless links capacity increase, large scale deployments of small cells are envisaged in the near future leading ultimately to densities as high as four-to-ten small cells for every macro cell [I.17]. Small cells can be of different size depending on the zone of deployment and can use different bandwidth access technologies giving rise to Heterogeneous Networks (HetNets) [I.10].

	Cell Radius (km)	Users	Locations
Femtocell	0.01 to 0.1	1 to 30	Indoor
Picocell	0.1 to 0.2	30 to 100	Indoor/Outdoor
Microcell	0.2 to 2	100 to 2000	Indoor/Outdoor
Macrocell	8 to 30	> 2000	Outdoor

Table I.1 Features of different base stations types from small cells to macro cells [I.16].

To enable the densification of the network, the cellular infrastructure must be flexible and support simplified management of increasingly heterogeneous Radio Access Networks (RANs) to avoid added complexity to the network architecture. Hence, there are many hurdles that need to be overcome in order to establish an efficient small cells network planning such as inter-cell interference and deployment expenses. To address these issues, C-RAN in conjunction with Network Function Virtualization (NFV) offers to improve system architecture, mobility, coverage performance and energy efficiency in a cost-efficient manner [I.17]. By combining virtualization, centralization and coordination techniques, future C-RAN architectures offer a spectral efficient solution while exploiting the available transport infrastructure.

A typical C-RAN architecture combining those functionalities is shown in Figure I.8 deploying a fully centralized baseband approach. The baseband resources are pooled at BaseBand Unit (BBU), situated at remote central office (not at the cell sites). BBUs from many remote sites are centralized at a virtual BBU pool [I.18]. Virtual BBU pools further facilitate scalability, cost reduction, integration of different services and reduction in time consumption for field trials as the execution platform can perform the same tasks with less hardware or capacity. A star connection, named Common Public Radio Interface (CPRI), links the BBUs to the remote radio heads (RRH), handling the analog processing on the channel [I.15]. Transceiver components enabling digital processing, analog-digital conversions, power amplification and filtering are located at the RRH. RRHs do not need any refrigeration or costly on-site construction, therefore, the cost and time of deploying RRHs decreases considerably since the installation footprint is much smaller compared to traditional integrated base stations.

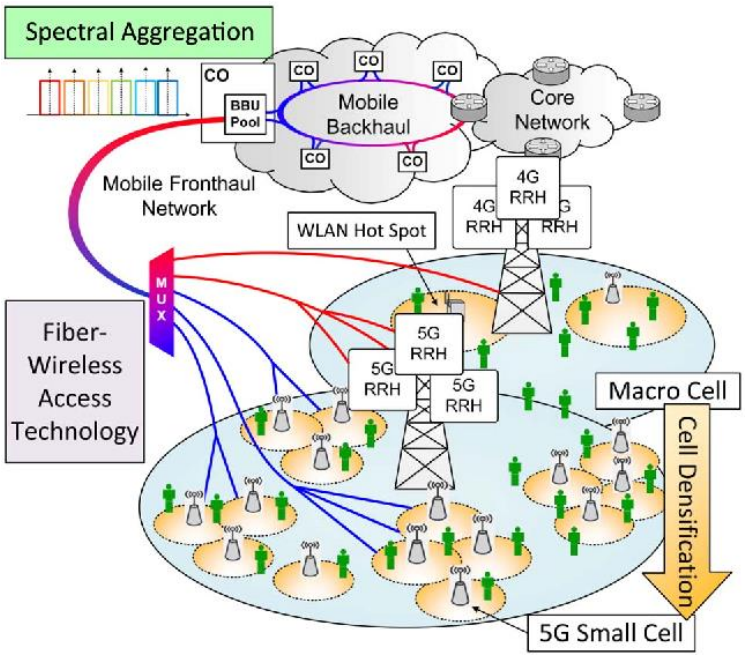

Figure I.8 C-RAN global architecture from [I.19].

Moreover, NFV along with software defined networking was initiated in order to simplify the deployment of new services by separating the physical network resources from the logical network (split plane between higher and lower network layers). It aims to apply standard information technologies to execute RAN functionality on more generic and generally available execution hardware and software platform, together with cloud core applications. The main aim of this architecture is to reduce excessive time to market for the deployment [I.20].

The challenge of C-RAN deployments is that such a functional split plane requires a connection between the RRHs and the BBU pool featuring high-speed (data rates higher than 1 Gb/s), low-latency, and accurately synchronized network, the so-called “fronthaul”. However, the potential gains in hardware pooling may in practice be outweighed by the cost for CPRI, which is the main challenge to be addressed in this context [I.14]. Alternatives to fiber based CPRI, including wireless solutions that enable somewhat relaxed fronthaul requirements are being investigated in the industry (cf. Figure I.9).

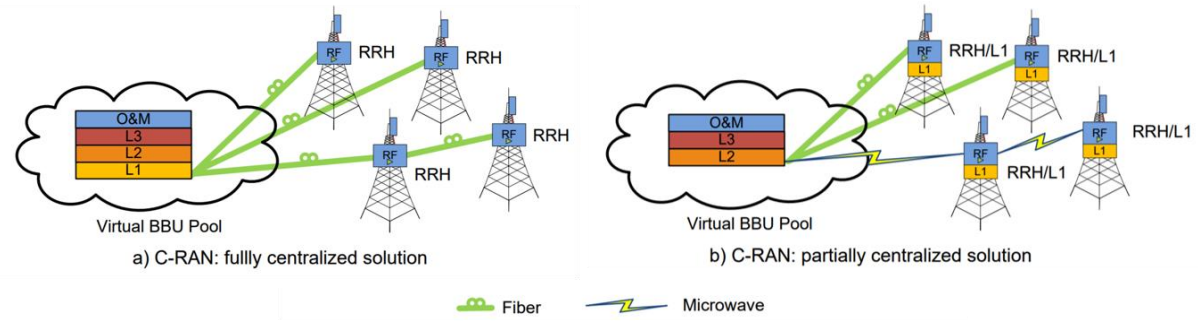

Figure I.9 Exclusive fiber optic links from RRHs to BBU pool versus hybrid microwave and optic fiber links from [I.21].

I.3 V AND E-BAND RADIO SYSTEMS FOR BACKHAUL/FRONTHAUL LINKS

I.3.1. V and E-band unlicensed/Light licensed spectrum

With the introduction of new RAN topologies where access and backhaul platforms should cope with high density small cells networks, the need for a new and revolutionary approach for backhauling uncovers a plethora of new research challenges. The cost of deployment, flexibility and scalability naturally give the advantage for wireless links over optical fibers and copper links for backhaul/fronthaul deployment. In fact, a board member of the Wireless Internet Service Provider Association stated that wireless costs are one fifth to one tenth that of copper cable or optical fiber [I.22]. Furthermore, Figure I.10 shows that the biggest share of mobile backhaul connections was for wireless links between 2011 and 2016 (cf. Figure I.10) illustrating the clear advantage of wireless links over wired links.

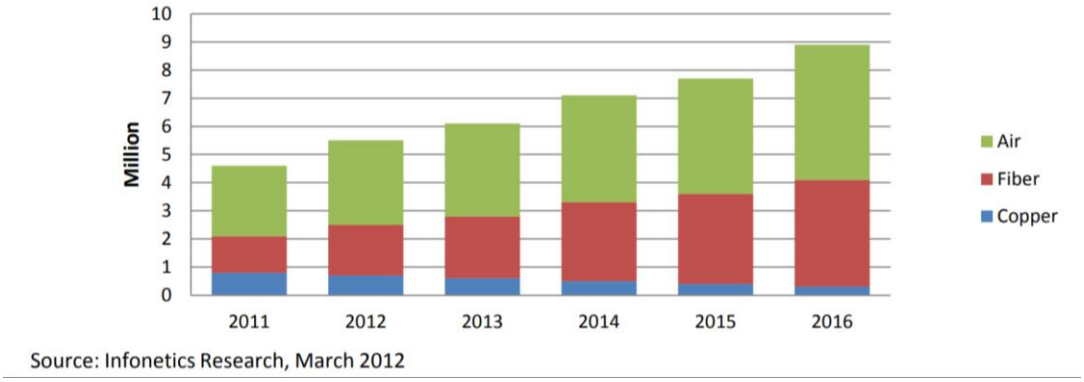

Figure I.10 Mobile backhaul connections by medium from [I.23].

To deliver higher capacity wireless links, lower frequency technologies rely on complex RF techniques (multi-path propagation and channel aggregation below 6 GHz), or spatial multiplexing at higher frequencies up to 42 GHz [I.24]. In contrast, mmW technologies operating beyond 42 GHz rely on the availability of wideband RF-channels to deliver multi-Gbps of throughput, using simple single-channel modulation schemes. This simplicity in design gives these spectrums the advantage of offering the best cost-per-bit for high-capacity backhaul [I.25]. More especially a huge interest in 60 GHz and 70-80 GHz bands, also commonly referred to as V-band and E-band, was demonstrated in the last decade by three European Framework Programme 7 (FP7) research projects:

- E3NETWORK [I.26] addressing mainly a backhaul solution in E-Band.
- MiWaves [I.27] addressing backhaul and access solutions in 60 GHz and 71-86 GHz Bands.
- IPHOBAC-NG [I.28] addressing the integration of mm-wave radio and photonics for backhaul.

The interest in V-band and E-band is especially due to their propagation characteristics featuring high free space path loss, which ideally suits the evolution of backhaul towards high capacity short-range link. This effect is furthermore accentuated in V-band by the oxygen absorption (20 dB/km) to a greater degree than lower frequencies (few tenth of dB/km) [I.14] as illustrated in Figure I.11. This implies an exceptional immunity to interference and enhanced frequency re-use. To compensate for the high atmospheric attenuation at E and V bands, highly directive narrow beamwidth (3°) antennas are employed which also results in lowering the risk of interferences. This enables a maximum practical reach of about 1 km at V-band [I.29] and up to a few kilometers in E-band. Moreover, the short wavelength at V and E-band ranging from 3.8 to 5 mm enables to achieve directive antennas with a small form factor of about 10 cm^2. Small equipment size is one of the key requirements for the small cell environment. V and E-band radios enable an implementation approach where all baseband, RF and antenna are physically integrated. In this implementation the antenna dimensions tend to be the determining factor in the overall physical size of the whole equipment.

The interference resistance criteria means that the system operators can realize networks with minimal frequency coordination and a high degree of frequency reuse [I.30]. This results in the license exempt/ light license options used in these bands. In fact the use of V-band was encouraged by its widely available unlicensed spectrum (cf. Figure I.12) [I.31] [I.32].

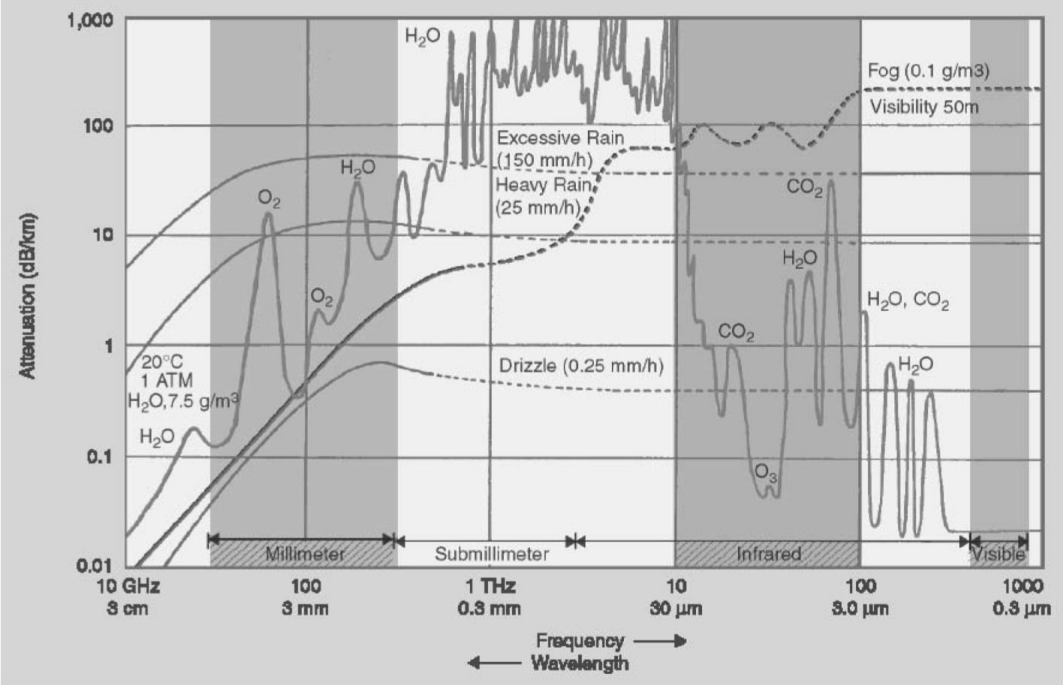

Figure I.11 The propagation attenuation characteristics (dB/km) versus frequency (wavelength) for Earth's atmosphere under various conditions from [I.33].

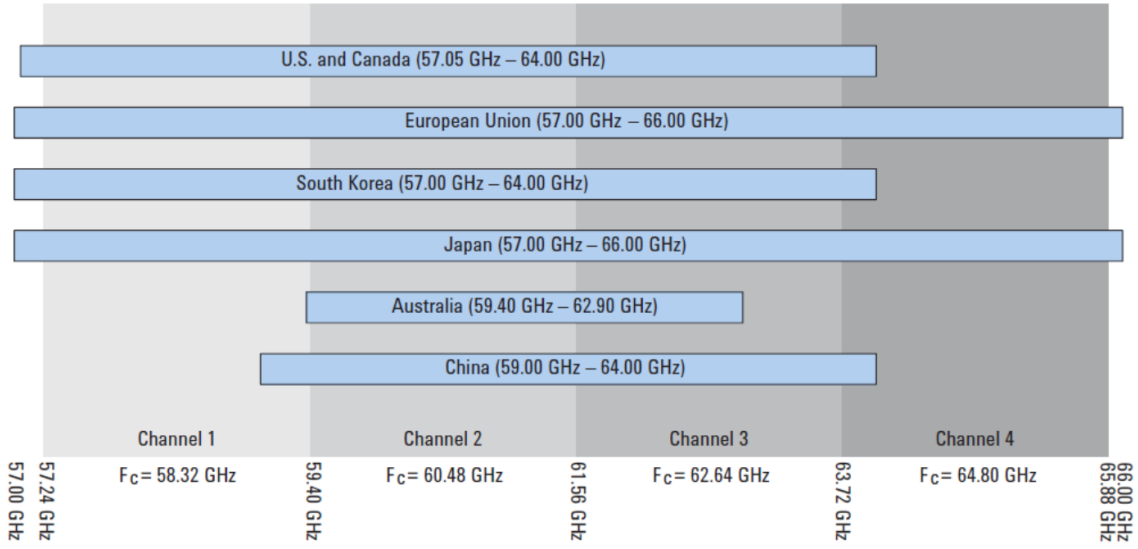

Figure I.12 60 GHz unlicensed band channel plan and frequency allocations by region [I.34].

E-band on the other hand is widely available in a light-license scheme, as illustrated by Figure I.13 and Table I.2 [I.30]. A 'light licensing regime' is a combination of license-exempt use and protection of users of spectrum. Mainly it states that the operator using this spectrum

should notify the regulator with the position and characteristics of the stations. The database of installed stations containing appropriate technical parameters is publicly available allowing to resolve claimed interference issues. The main advantage of either license-exempt or light-licensing approach is a significantly lower cost of spectrum compared to some of the other technology options.

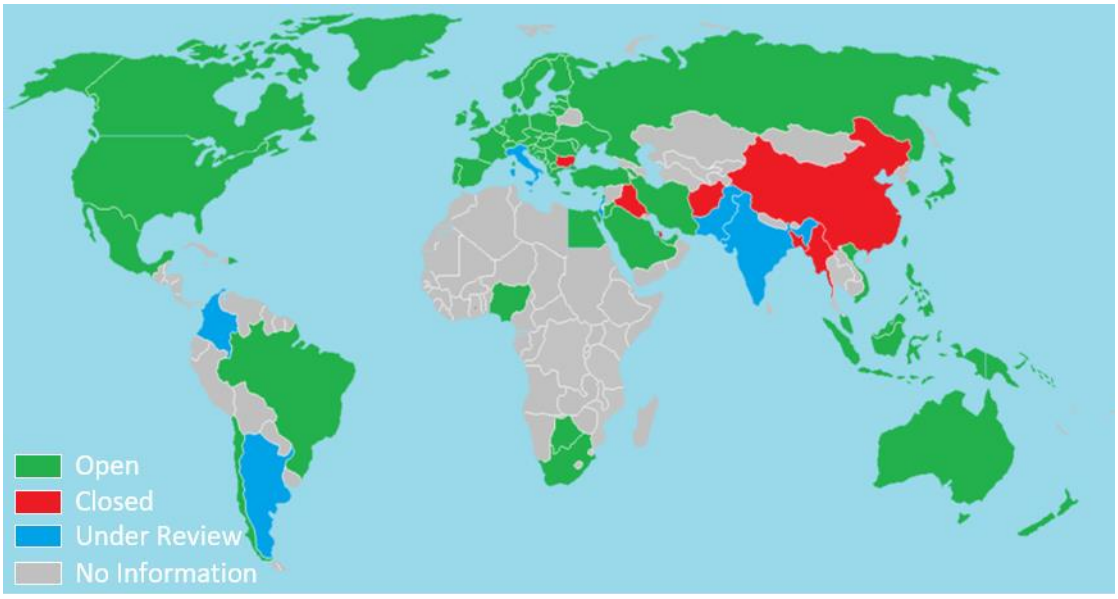

Figure I.13 E-band worldwide situation [I.14].

Country	E-band license structure	Typical E-Band license fee
USA	On-line light license	$75 for 10-year license
UK	Light license	£50 per year (~$100)
Czech Republic	Unlicensed	Free of charge
Russia	Light license	Minimal registration fee
Australia	Light license	AU$187 per year (~$175)

Table I.2 Examples of E-band license schemes and fees in some countries [I.30].

All these characteristics make out of V and E-band ideal spectrums for linking the small cells to the core network in a dense deployment context. However, due to high fading losses caused by obstacles at these frequencies, Line of Sight (LoS) links are an undisputable preference. 60 GHz is shorter in reach and well suited for connectivity to the small cell while E-band can reach further and is a better fit for 'rooftop aggregation' of small cells. Figure I.14 illustrates a use-case example where 60 GHz is employed for street-to-street and street-to-rooftop links and E-band, by contrast, is preferred for roof-to-roof connectivity. To conclude Table I.3 recalls the basic characteristics of the two frequency bands and illustrate the best-fit use case for each.

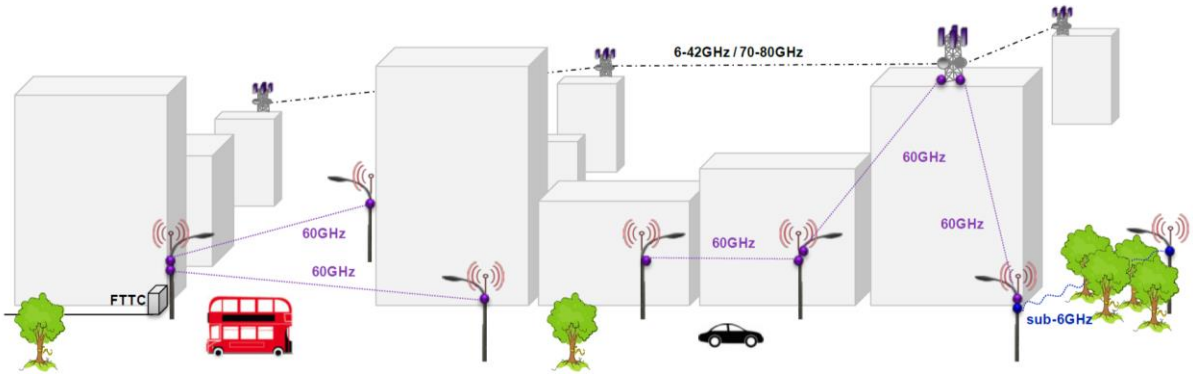

Figure I.14 Use case illustration for 60 GHz and 70-80 GHz technologies from [I.25].

	60GHz 57-66GHz	70-80GHz 71-76GHz and 81-86GHz
Link capacity versus link reach	100Mbps – 1Gbps up to 1km	multi-Gbps up to 3km
Spectrum availability and licensing	~9GHz contiguous mostly unlicensed occasionally light licensed	2 x 5GHz mostly light licensed occasionally fully licensed
Physical size of the equipment	Very compact (all-outdoor) antenna diameter ~7-15cm	Compact (all-outdoor) antenna diameter 20/30/60cm
Relative equipment cost (BoM & manufacture)	Lower	Higher

Table I.3 Comparison of key aspects of 60 GHz and 70-80 GHz technologies from [I.25].

The regulatory emission limitations for the design of radio equipment destined to be deployed for V and E-band backhaul links, are listed in Table I.4. Cited regulations are fixed by the ECC recommendations [I.22] in the CEPT area (European conference of postal and telecommunications administrations) and European Telecommunication Standards Institute (ETSI) technical specifications [I.12]. Amongst these, we highlight the high gain required of 30 dBi in V-band and 38 dBi in E-band which we tried to satisfy in our work.

	V-band (ECC/REC) [I.32]	E-band (ETSI) [I.14]
Maximum transmitter output power	10 dBm	30 dBm
Maximum equivalent isotropically radiated power (EIRP)	55 dBm	85 dBm
Minimum antenna gain	30 dBi	Pout (dBm) +15; or 38 dBi (whichever is the greater)
Maximum antenna gain	Not Specified (NS)	85-Pout(dBm)

Table I.4 Regulatory emissions limitations in V-band and E-band.

Finally, E-band and V-band are considered as strong candidate today thanks to the continuously-evolving integrated circuits silicon technologies that reached maturity at these frequency bands enabling cost-effective transceivers as discussed in the next paragraph.

I.3.2. V and E-band transceivers for backhaul links and link-budget study

The development made in the integration of complete RF components by the evolving silicon technology is considered as the driving force behind the emergence of mmW applications (cf. Figure I.15). Currently, different mmW system implementations based on silicon bipolar or silicon CMOS technologies have been reported [I.35], especially with the WiGig IEEE802.11ad (60 GHz WLAN) standardization. The advancements in SiGe based technologies in the last years have resulted in their increased use for applications in the mmW regime and their successful employment in several existing commercial mmW applications [I.24].

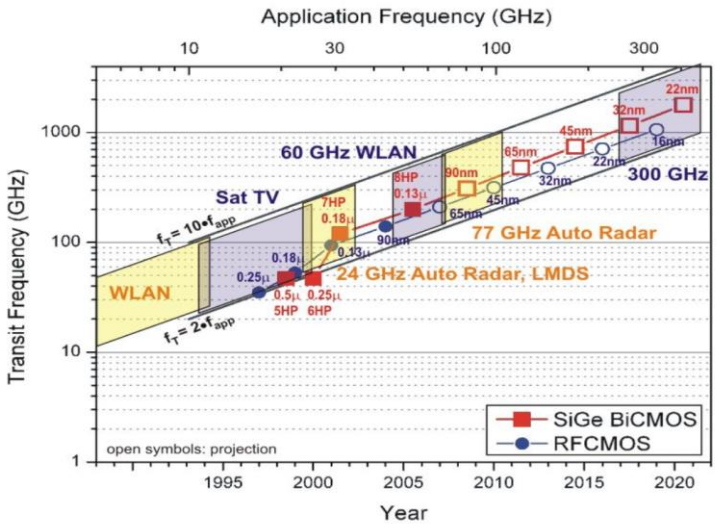

Figure I.15 Projection of the transit frequency of SiGe BiCMOS and RFCMOS technologies versus technology node and year from [I.37].

I.3.2.a Commercial V and E-band transceivers

Among several commercial V and E-band transceivers, we cite the example of Infineon which has developed a complete family of packaged RF Transceivers for mobile backhaul applications – supporting both the V-band and E-band for links up to 1 km [I.38]. The chipsets, BGT60, BGT70 and BGT80 Inegrated Circuits (IC), are housed into a plastic embedded Wafer Level Ball Grid Array (eWLB) package which can be processed in standard surface mount technology flow. The ICs are designed in Silicon Germanium:Carbon (SiGe:C) technology with device transit frequency of 200 GHz, that enables the integration of several mmW building blocks with high performance into a single chip. The output power delivered by the BGTx0 family goes up to 18 dBm along with a low noise figure of 6 dB. These characteristics allow the implementation of high modulation schemes up to QAM32 with a sample rate of 500 Msymbol and QAM64 with 1 Gsymbol at a 10^{-6} Bit Error Rate (BER). Figure I.16 illustrates the BGT60 specific to the 57 GHz to 64 GHz band and housed into the eWLB package.

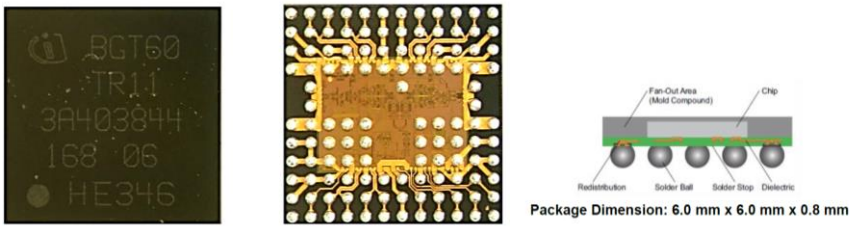

(a) (b) (c)

Figure I.16 (a) Top view, (b) bottom view, (c) and side view of BGT60 in eWLB package from [I.39].

A FR frontend reference design implementing the two E-band transceivers (BGT70 and BGT80) on a compact baseband motherboard are shown in Figure I.17. The RF module is designed on RO3003 PCB and a diplexer is mounted directly on transceiver mechanics to achieve a small form factor of the final assembly along with a standard WR12 waveguide port for direct antenna connection. The main parameters of BGT70 and BGT80 transceivers are listed in Table I.5, indicating a noise figure of 7 dB at the 70 GHz band and a power consumption of 1.5 W and 1.2 W at the transmitter and receiver respectively.

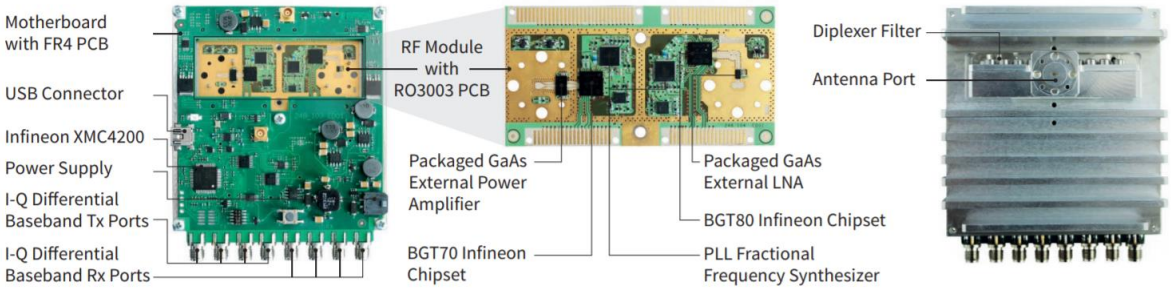

Figure I.17 RF frontend reference design integrating the BGT70 and BGT80 from [I.37].

Supported Channel bandwidth	50 MHz to 1 GHz
Output Saturation power at antenna port	Psat = +21 dBm typical
Transmitter output power at antenna port	PTx = +12 dBm typical @ 64-QAM
Rx noise figure 70 GHz band	7 dB typical at antenna port
Rx noise figure 80 GHz band	8 dB typical at antenna port
Diplexer insertion loss	<0.7 dB
Diplexer return loss at antenna port	>15 dB
Power consumption (BGT Tx/BGT Rx/GaAs PA)	1.5/1.2/4.8 W
Rx Sensitivity	-60 dBm typical @ 64-QAM modulation

Table I.5 Main technical parameters of BGT70 and BGT80 from [I.38].

Another mmW IC system developed by Analog Devices offers a silicon-germanium (SiGe) 60 GHz chipset for small cell backhaul applications [I.40]. The transmitter chip is a complete

analog baseband to millimeter-wave upconverter. An improved frequency synthesizer covers 57 GHz to 66 GHz in 250 MHz steps with low phase noise that can support modulations of up to at least 64 QAM. Complementing this device is a receiver chip which key features include a low 6 dB noise figure at the maximum gain settings; adjustable low-pass baseband filters and high-pass baseband filters. The receiver is designed to detect the simplest modulations such as on/off keying (OOK) up to more complex modulations like 64QAM. Both transmitter and receiver come in a 4 mm × 6 mm BGA-style wafer level package. A demonstration platform was implemented jointly with Xilinx to demonstrate the capabilities of the system and is illustrated in Figure I.18. The demo platform includes a variable RF attenuator to replicate the path loss of a typical millimeter wave link. This platform contains all the hardware and software needed to demonstrate point-to-point backhaul connections of up to 1.1 Gbps in 250 MHz channels for each direction of a frequency division duplex connection.

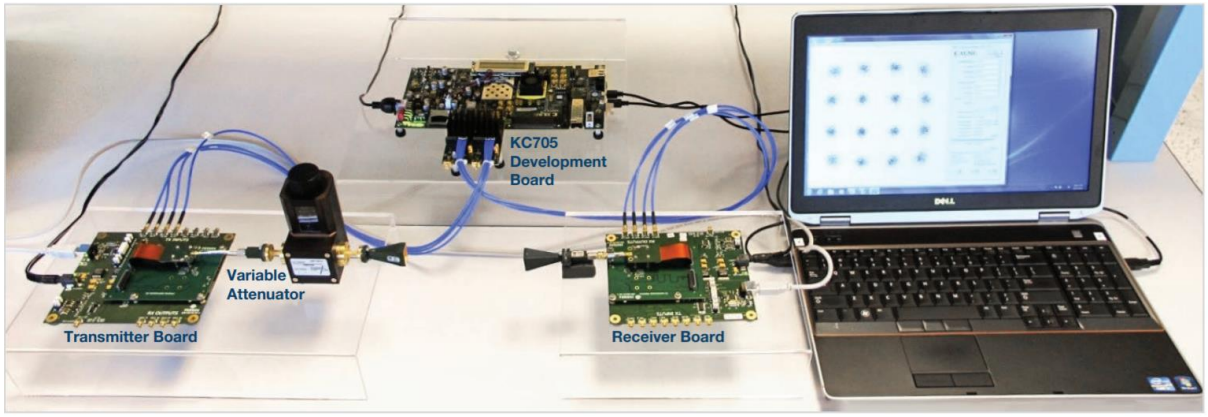

Figure I.18 Demonstration platform of the Analog devices 60 GHz chipset from [I.40].

Several demonstrations were also developed to prove the functionality of mmW backhaul links. At the Mobile World Congress'15, Nokia Bell Labs presented a steerable lens antenna demonstrating tracking of moving users. The lens operated @73 GHz as a bidirectional system with a peak throughput rate of 2.3 Gbps in 1 GHz bandwidth with a one-way latency less than 1 ms [I.41]. It was field-tested with DOCOMO and Verizon in outdoor and indoor environments, both in Japan and the United States. A maximum range of 160–200 meters with peak throughput exceeding 2 Gbps was achieved. At Mobile World Congress'16, Nokia Bell Labs demonstrated the next version, a unidirectional 15 Gbps system incorporating 2-stream MIMO (Multiple Input, Multiple Output) in the 2 GHz bandwidth [I.41].

I.3.2.b Link budget study

For more insight into the antenna gain requirement needed to operate in small cell backhaul links going up to 1 km, we take the example of the parameters of the Infineon BGT 70 to carry out a link budget study. In this study we consider a LoS context in an ideal free space environment regardless of considering the effect of shadowing. Table I.5 indicates a Rx sensitivity of -60 dBm typical @ 64-QAM modulation. Hence, we can compute the needed

antenna gain to obtain a receiver power exceeding the Rx sensitivity. In fact, the received power in dB, P_{Rx}, can be calculated by the following equation derived from the Friis transmission formula,

$$P_{Rx} = P_{Tx} - FSPL + G_R + G_T \quad \text{(I.1)}$$

Where P_{Tx} is the transmitter output power, G_R and G_T are the gain of the receiving and transmitting antennas respectively. FSPL is the free space path loss calculated by the following expression,

$$FSPL = 20 \log \frac{4\pi d}{\lambda_0} \quad \text{(I.2)}$$

where d is the distance of the link and λ_0 is the free space wavelength. Taking d = 1 km, the maximum link distance, and λ_0 at 71 GHz FSPL is evaluated to 129.5 dB. Using the typical transmitter power equal to 12 dBm (cf. Table I.5) and considering that $G_R = G_T = G$, equation I.1 gives

$$P_{Rx} = -117.5 + 2G > -60dBm \quad \text{(I.3)}$$

Hence, the antenna gain at the receiver or transmitter should exceed 28.75 dBi. Therefore, an antenna respecting the gain specifications determined by ETSI of a minimum gain of 38 dBi can be used with this transceiver while leaving a margin for rain losses or other losses in a LoS context.

I.3.3. Millimeter wave Wi-Fi to boost cellular networks

On the other hand, Wi-Fi technologies have gained momentum due to increased offloading from the core network to Wi-Fi connections. The goal of future integrated cellular/Wi-Fi networks is to intelligently load balance between the two and enable simultaneous cellular/Wi-Fi connections [I.42].

The IEEE 802.11 family of technologies has experienced rapid growth, mainly in private deployments. In the mmW frequencies, IEEE has developed 802.11ad standard (WiGig), which operates at 60 GHz offering a maximum rate of 7 Gbit/s (using OFDM/64-QAM modulation). Wi-Gig standard is being considered to contribute into mobile connections not only by offloading but also by employing it for long range links. In fact, Peraso have indeed employed WiGig standards for “long-haul” links [I.43]. The Peraso X710 long range WiGig phased array chipset, shown in Figure I.19, is an 802.11ad compliant chipset targeting fixed wireless broadband applications. The chipset includes the PRS4601 WiGig baseband IC and the PRS1151 60GHz phased array RFIC. Based on Silicon Germanium (SiGe) technology, the RFIC features up to eight transceivers controlling a ceramic substrate-based phased array antenna comprising 32 patch antennas for beamforming at 60GHz (PRA710). Moreover, it is

capable of supporting all the IEEE 02.11ad coding schemes, delivering data rates up to 4.62 Gb/s. The chipset main applications are Point-to-Multipoint Fixed Wireless Broadband, 60 GHz point-to-point links and 60 GHz WiGig Mesh Networks.

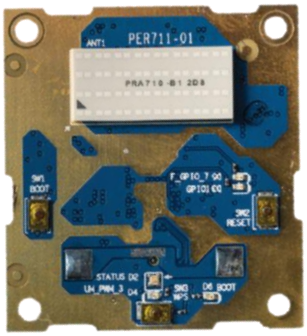

Figure I.19 PERASO X710 long range WiGig array chipset featuring the PRA710 phased array from [I.43].

Moreover, the standards body is currently working on a successor technology, dubbed 802.11ay, to further improve Wi-Fi range and data rates. The goal is to increase the peak data rate to 100 Gbps through supporting multiple independent data streams and higher channel bandwidth, among other advancements, while ensuring backward compatibility and coexistence with IEEE 802.11ad [I.42]. IEEE802.11ay is expected to deliver an average transmission rate of 20 to 30 Gbps over a range of 1 to 3 km with 11ay-to-11ay device setups. This new standard has the potential to be included for fixed point-to-point (P2P) and point-to multipoint (P2MP) transmissions, either indoor or outdoor, to meet the high requirement of tomorrow's connectivity [I.44].

I.4 LOW-COST DIGITAL ADDITIVE MANUFACTURING TECHNOLOGIES FOR ANTENNAS FABRICATION

In the past years, Digital additive manufacturing (DAM), or 3D printing, technologies have been employed massively in the radio-frequency field more especially for antennas development [I.47]. They are gaining popularity due to the emergence of desktop printers [I.45] on one side and high-end industrial printers on the other side [I.47], opening up the way for a variety of applications.

I.4.1. General overview of DAM advantages

Key aspects enabling DAM popularity are the fast, ease of prototyping and cost-efficiency. With DAM, little knowledge is required to fabricate parts as there's no need of additional mechanic expertise in handling machining tools. It also enables the fabrication of new geometrical possibilities in one shot that were not possible with traditional machinery process.

Hence, it permits a design-driven manufacturing process [I.48]. Moreover, the availability of a wide variety of plastic materials and metal alloys suitable for DAM allows for a myriad of applications. Presently, industrial 3D printers suitable for mass production and offering precisions down to few tens of microns are commercially available [I.49]. Therefore, the maturity of this cost-efficient technology opened up the way to an increasing use of DAM in several applications like aerospace and telecommunications.

By definition, DAM consists on building a 3D object, given by a Computer Aided Design (CAD) file, by adding layer-upon-layer of material. DAM Technologies differ by the material used and the process by which each technology bonds the material particles together. We cite here some of the most employed 3D printing technics.

I.4.2. DAM technologies

3D printing first began with the Stereolithography apparatus (SLA) process. SLA process consists on converting a liquid plastic resin to solid objects using photopolymerization, a process by which light causes chains of molecules to link, therefore forming polymers [I.50], [I.51]. Objects made using stereolithography generally have smooth surfaces relatively to other technologies even if the same thickness layer is used. The smooth surface is obtained because the newly printed layer interacts with the previous layer, smoothing out the staircase effect [I.52]. A general schematic of SLA printers is shown in Figure I.20. Today SLA desktop printers can achieve a layer thickness down to 25 µm with a dimensional tolerance of +/- 100 µm [I.53].

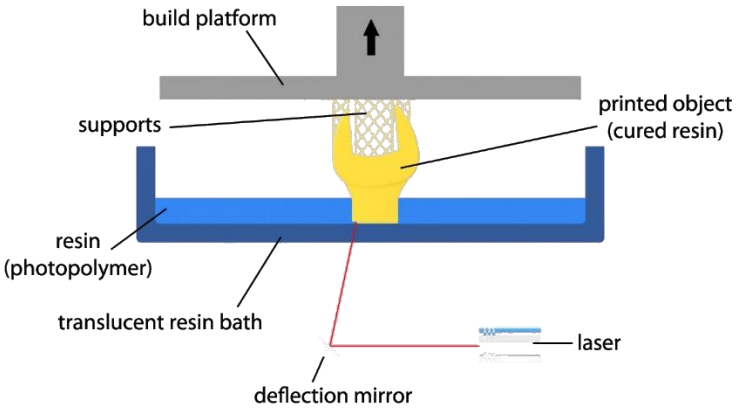

Figure I.20 General schematic of SLA printers from [I.54].

Another more affordable 3D printing technic, which stood out a few years ago, is the Fused Deposition Modeling (FDM), first developed by Stratasys [I.55]. In this process, a plastic material is extruded through a heating nozzle that traces the part's cross-sectional geometry layer by layer [I.51]. The plastic hardens immediately after flowing from the nozzle and bonds

to the layer below. Once a layer is built, the platform lowers, and the extrusion nozzle deposits another layer, the process is illustrated in Figure I.21.

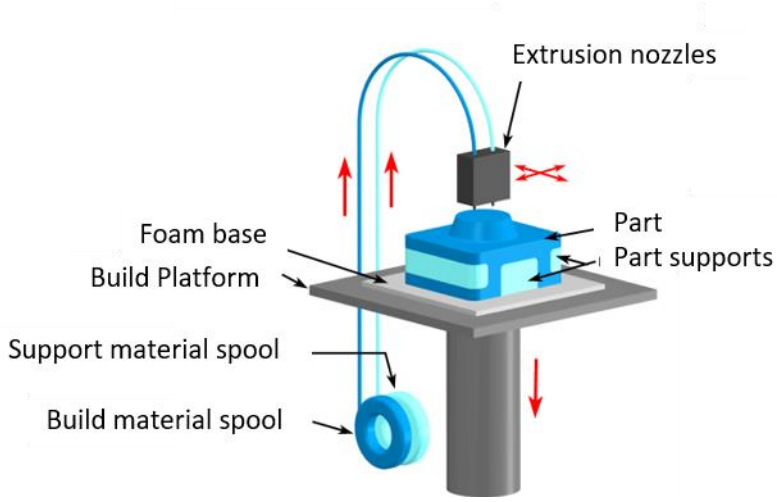

Figure I.21 General schematic of FDM printers from [I.56].

The layer thickness and vertical dimensional accuracy of FDM printers is determined by the extruder die diameter, which ranges from 330 to 227 µm. Industrial FDM printers achieve dimensional accuracy of about +/-200 µm [I.53]. A range of materials are available including ABS (Acrylonitrile Butadiene Styrene), polyamide, polycarbonate and most recently PEEK (Polyether Ether Ketone). Fused filament printing is now the most popular process because it is available in affordable costs for individuals. Other techniques such as photopolymerization and powder sintering may offer better results, however their costs are greatly superior.

Direct Metal Laser Sintering (DMLS) was developed as the first commercial rapid prototyping method to produce metal parts in a single process [I.57]. DMLS employs a laser to selectively sinter (heating the metal up to a temperature before melting) or melt a fine metal powder in either stainless steel or aluminum materials as shown in Figure I.22. An additional benefit of the DMLS process is higher detail resolution due to the use of thinner layers, enabled by a smaller powder diameter (typically 20 µm). DMLS dimensional tolerance can reach +/-100 µm for standard metal powders and a resolution down to 15 µm using special micro laser sintering and micro powders [I.58]. Material options that are currently offered include alloy steel, stainless steel, tool steel, aluminum, bronze, cobalt-chrome and titanium. In addition to functional prototypes, DMLS is often used to produce rapid tooling, medical implants, and aerospace parts for high heat applications [I.59].

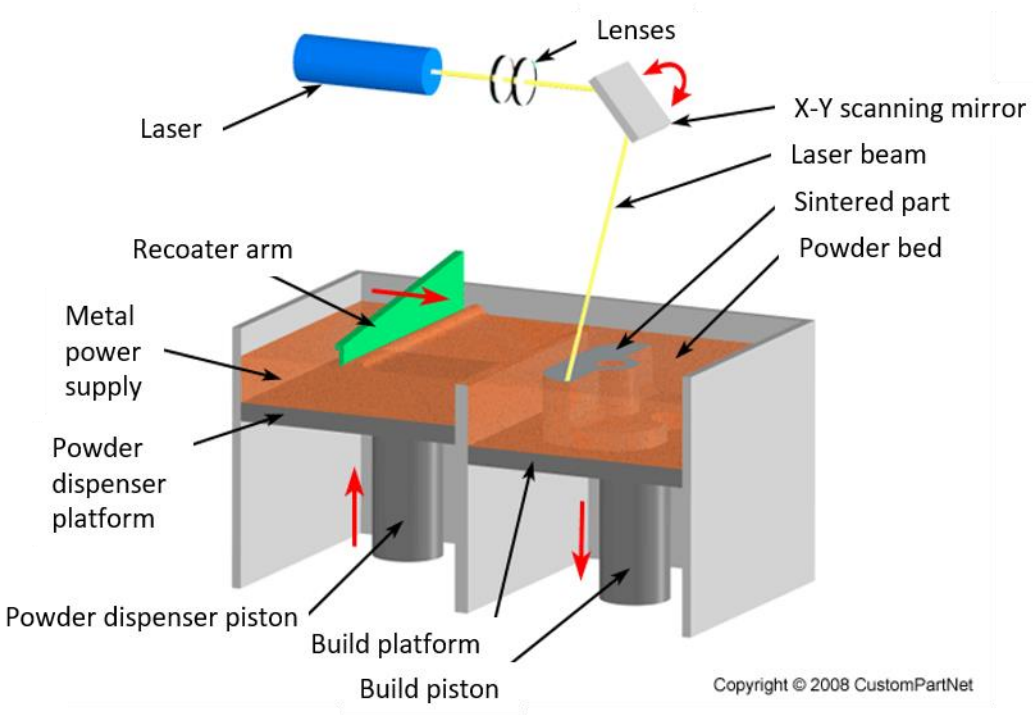

Figure I.22 General schematic of DMLS printers from [I.60].

Table I.6 shows a comparison between 3D printers developed by the leading companies in the DAM field and using different technologies. FDM has the advantage of offering the bigger part size however the quality of the final piece in terms of surface and accuracy is the lowest. SLA and DMLS deliver the best pieces in terms of accuracy, however SLA surface finish is smoother but DMLS is faster. Hence, each technique can be suitable for a certain type of applications.

3D-Printer	Form 2 [I.45]	Stratasys Fortus 450 mc [I.61]	EOS M290 [I.46]
Technology	SLA	FDM	DMLS
Material type	Liquid (photopolymer)	Solid (filaments)	Powder (metal)
Materials	Thermoplastics	Thermoplastics	Metals such as steel alloys, aluminum, bronze, etc…
Max. part size	145×145×175 mm^3	406 × 355 × 406 mm^3	250 × 250 × 325 mm^3
Min. layer thickness	100 to 25 µm	330 to 127 µm	NS
Typical achievable accuracy	+/- 100 µm	+/- 127 µm	+/- 100 µm
Surface finish	Smooth	Rough	Average
Build speed	Average	Slow	Fast

Table I.6 Comparison between the specifications of each DAM techniques.

Following these advances, a dedicated project looking into the application of metal 3D printing to RF equipment was supported through the European Space Agency's (ESA) Basic Technology Research Programme [I.62]. Based on this work, Airbus Defense and Space has

developed prototype 3D-printed RF filters and demonstrated their suitability for space applications. The piece was printed by DMLS using aluminum alloys and was silver-plated by electrolysis, the fabricated piece is shown in Figure I.23. The printed piece exceeded required performance after demonstrating great reduction of time, production cost and reduction of weight (50% cut in mass), leading to the continuous research in this field.

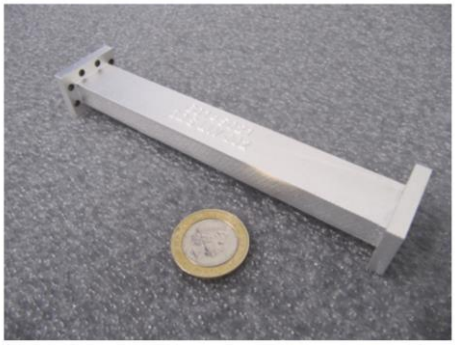

Figure I.23 3D-printed filter developed by Airbus Defense and Space based on ESA's research from [I.62].

This work, among many others, proved the functionality of 3D printing technologies for cost-efficient mmW radio components for backhaul links. Nowadays, the adoption of DAM technics is not limited to research departments but have also started to take its place in the industrial market. In May 2015, Stratasys revealed that it had produced over 1000 parts for the Airbus A350 XWB passenger plane. The main advantages of 3D printing in this industrial context were the low weight and the considerable minimization of wasted material with respect to traditional manufacturing processes. However, the suitability of 3D printing to mass production is still under development but enhancements in this direction have been achieved. Stratasys and Desktop Metal have recently teamed up to develop a stack of multiple 3D printers enabling a chain production. This stack, named the Continuous Build 3D Demonstrator consisted of three scalable, FDM printers, one on top of the other, as illustrated in Figure I.24.

Figure I.24 Stratasys Continuous Build 3D Demonstrator from [I.63].

The Stratasys Demonstrator helps increase print capacity for 3D printers, for example nine machines can produce 1,500 parts per day and production can be increased by simply adding

more stacks. Whereas typically 3D printing is adopted for manufacturing from 300 to 400 parts, with Continuous Build 3D Demonstrator, that number goes way up to around 1,500 to 2,000 parts [I.63]. Hence, it will not be long before 3D printing become conform with mass-production industrial chains.

I.5 CONCLUSION

The evolution towards 5G to respond to future connectivity demands brought by data-hungry applications is inevitable. To increase the capacity of the network the main solution consists in increasing its density by adding small cells of different sizes and employing different access technologies. To cope with the network densification, new architectures are proposed to permit a scalable and easy-to-deploy infrastructure, which gives rise to C-RAN. C-RAN consists on splitting the physical layer (located at the RRHs) from the upper network layers and centralizing the baseband resources in a common BBU pool. To achieve such centralization the main challenge is to achieve high capacity link with low deployments cost to link the RRH to the BBU pool. Generous bandwidth available at mmW frequencies made of this spectrum the best candidate for those backhaul/fronthaul links. International and European regulations allocated the unlicensed/light licensed V and E-band spectrums for millimeter wave backhaul links. Indeed, the atmospheric attenuation characterizing those bands especially at V-band is a valuable characteristic as it highly limits the interference between the cells. Moreover, the adoption of mmW radio components in the cellular network is powered by the maturity of silicon technology. Nowadays, several transceiver chips and complete RF systems have been developed and are commercially available demonstrating data rates higher than 1 Gbps over distances ranging between 100 m and 1 km. The cost-effectiveness of radio systems remains the main quality for pushing forward the adoption of mmW backhaul links in a massive way. Leveraging the high-potential of DAM technologies, fast and cheap manufacturing can be accessed. Therefore, we focused our research study on exploiting 3D printing capabilities to develop low-cost wide-band directive antennas operating at V and E-bands for backhaul links.

I.6 REFERENCES

[I.1] "Cisco Visual Networking Index: Global Mobile Data Traffic Forecast Update, 2016–2021 White Paper," Cisco. [Online]. Available: https://www.cisco.com/c/en/us/solutions/collateral/service-provider/visual-networking-index-vni/mobile-white-paper-c11-520862.html. [Accessed: 04-Aug-2018].

[I.2] "Future mobile data usage and traffic growth – Ericsson," Ericsson.com, 11-Aug-2016. [Online]. Available: https://www.ericsson.com/en/mobility-report/future-mobile-data-usage-and-traffic-growth. [Accessed: 04-Aug-2018].

[I.3] "Worried About Bandwidth for 4K? Here Comes 8K!," Light Reading. [Online]. Available: https://www.lightreading.com/video/4k-8k-video/worried-about-bandwidth-for-4k-here-comes-8k!/d/d-id/737330. [Accessed: 08-Oct-2018].

[I.4] "Global Average Connection Speed Increases 15 Percent Year over Year, According to Akamai's 'First Quarter, 2017 State of the Internet Report' | Akamai." [Online]. Available: https://www.akamai.com/uk/en/about/news/press/2017-press/akamai-releases-first-quarter-2017-state-of-the-internet-connectivity-report.jsp. [Accessed: 06-Aug-2018].

[I.5] "M.2012 : Detailed specifications of the terrestrial radio interfaces of International Mobile Telecommunications Advanced (IMT-Advanced)." [Online]. Available: https://www.itu.int/rec/R-REC-M.2012/en. [Accessed: 05-Aug-2018].

[I.6] "ITU-R FAQ on International Mobile Telecommunications (IMT)," p. 12, 2018.

[I.7] "5G Spectrum - Huawei Corporate Information," huawei. [Online]. Available: https://www.huawei.com/en/about-huawei/public-policy/5g-spectrum. [Accessed: 07-Aug-2018].

[I.8] "3GPP." [Online]. Available: http://www.3gpp.org/. [Accessed: 10-Sep-2018].

[I.9] "Release 15." [Online]. Available: http://www.3gpp.org/release-15. [Accessed: 10-Sep-2018].

[I.10] M. Agiwal, A. Roy, and N. Saxena, "Next Generation 5G Wireless Networks: A Comprehensive Survey," IEEE Commun. Surv. Tutor., vol. 18, no. 3, pp. 1617–1655, 2016.

[I.11] J. G. Andrews et al., "What Will 5G Be?," IEEE J. Sel. Areas Commun., vol. 32, no. 6, pp. 1065–1082, Jun. 2014.

[I.12] "5G spectrum recommendations." 5G Americas, Apr-2017.

[I.13] "The Need for Globally Harmonised 5G Spectrum - About Huawei," huawei. [Online]. Available: https://www.huawei.com/de/about-huawei/public-policy/5g-spectrum/need-for-globally-harmonised-5g-spectrum. [Accessed: 11-Sep-2018].

[I.14] M. G. L. Frecassetti, "ETSI White Paper No. 9: E-Band and V-Band - Survey On Status Of Worldwide Regulation," p. 40.

[I.15] "Verizon tees up prototypes for more tests in 28 GHz band | FierceWireless." [Online]. Available: /wireless/verizon-tees-up-prototypes-for-more-tests-28-ghz-band. [Accessed: 08-Oct-2018].

[I.16] "Small Cell Networks and the Evolution of 5G - Qorvo." [Online]. Available: https://www.qorvo.com/design-hub/blog/small-cell-networks-and-the-evolution-of-5g. [Accessed: 07-Oct-2018].

[I.17] "FixedRadiosystems:Small cell microwave backhauling." [Online]. Available: http://www.etsi.org/deliver/etsi_tr/103200_103299/103230/01.01.01_60/tr_103230v010101p.pdf. [Accessed: 13-Mar-2018].

[I.18] Telefonica and Ericsson, "Cloud RAN Architecture for 5G." .

[I.19] M. Xu et al., “Bidirectional Fiber-Wireless Access Technology for 5G Mobile Spectral Aggregation and Cell Densification,” J. Opt. Commun. Netw., vol. 8, no. 12, p. B104, Dec. 2016.
[I.20] EventHelix, “Cloud RAN and eCPRI fronthaul in 5G networks,” 5G NR, 05-Feb-2018. .
[I.21] A. Checko, “Cloud Radio Access Network architecture,” Technical university of Denmark, 2016.
[I.22] “BroadbandBreakfast.com: Wireless Internet Service Providers Pitch Fixed Wireless Technology in Forthcoming Infrastructure Bill.” [Online]. Available: http://broadbandbreakfast.com/2017/10/wireless-internet-service-providers-pitch-fixed-wireless-technology-in-forthcoming-infrastructure-bill/.
[I.23] A. Checko, “Cloud RAN fronthaul : Options, benefits and challenges.,” [Online]. Available: https://www.slideshare.net/wiless/cloud-ran-fronthaul?from_action=save.
[I.24] “60 GHz Wireless Technology,” LightPointe Wireless Bridges. [Online]. Available: http://lightpointe.com/60-ghz-technology-overview.html. [Accessed: 13-Mar-2018].
[I.25] “Small Cell Forum Releases.” [Online]. Available: https://scf.io/en/documents/049_Backhaul_technologies_for_small_cells.php. [Accessed: 05-Sep-2018].
[I.26] “E3Network FP7 Project.” [Online]. Available: http://www.ict-e3network.eu/. [Accessed: 10-Aug-2018].
[I.27] “MiWaveS.” [Online]. Available: http://www.miwaves.eu/. [Accessed: 10-Aug-2018].
[I.28] “Integrated Photonic Broadband Radio Access Units for Next Generation Optical Access Networks | Projects | FP7-ICT,” CORDIS | European Commission. [Online]. Available: https://cordis.europa.eu/project/rcn/111275_en.html. [Accessed: 10-Aug-2018].
[I.29] Rec. ITU-R P.676-7 “Attenuation by atmospheric gases.” [Online]. Available: https://www.itu.int/rec/R-REC-P.676-7-200702-S/en. [Accessed: 05-Sep-2018].
[I.30] J. Wells, “Licensing and License Fee Considerations for E-band 71-76 GHz and 81-86 GHz Wireless Systems,” E-Band Communications Corp.
[I.31] “ECC Recommendation (05)02 USE OF THE 64-66 GHz FREQUENCY BAND FOR FIXED SERVICE.” CEPT, Feb-2009.
[I.32] “ECC Recommendation (09)01 USE OF THE 64-66 GHz FREQUENCY BAND FOR POINT TO POINT FIXED WIRELESS SYSTEMS.” CEPT, Jan-2009.
[I.33] A. M. Niknejad, S. Emami, B. Heydari, E. Adabi, B. Afshar, and B. A. Floyd, “Amplifiers and Mixers,” in mm-Wave Silicon Technology, Eds. Boston, MA: Springer US, 2008, pp. 109–157.
[I.34] “New Frontiers in Personal Communications (and Investment Opportunities!),” Frank Rayal, 25-Jun-2013. [Online]. https://frankrayal.wordpress.com/2013/06/24/new-frontiers-in-personal-communications-and-investment-opportunities/. [Accessed: 06-Oct-2018].
[I.35] S. Shahramian, Y. Baeyens, N. Kaneda, and Y. Chen, “A 70–100 GHz Direct-Conversion Transmitter and Receiver Phased Array Chipset Demonstrating 10 Gb/s Wireless Link,” IEEE J. Solid-State Circuits, vol. 48, no. 5, pp. 1113–1125, May 2013.
[I.36] J. Lee, Y. Chen, and Y. Huang, “A Low-Power Low-Cost Fully-Integrated 60-GHz Transceiver System With OOK Modulation and On-Board Antenna Assembly,” IEEE J. Solid-State Circuits, vol. 45, no. 2, pp. 264–275, Feb. 2010.
[I.37] “Nanotec | background.” [Online]. Available: http://project-nanotec.com/background.html. [Accessed: 11-Sep-2018].

[I.38] I. T. AG, “mmW Backhaul and Fronthaul - Infineon Technologies.” [Online]. Available: https://www.infineon.com/cms/en/product/rf-wireless-control/mmwave-mmic-transceivers-24-86-ghz/mmw-backhaul-and-fronthaul/. [Accessed: 06-Mar-2018].

[I.39] I. T. AG, “BGT60 - Infineon Technologies.” [Online]. Available: https://www.infineon.com/cms/en/product/rf-wireless-control/mmwave-mmic-transceivers-24-86-ghz/mmw-backhaul-and-fronthaul/bgt60/. [Accessed: 06-Sep-2018].

[I.40] J. Kilpatrick, R. Shergill, and M. Sinha, “60 GHz Line of Sight Backhaul Links Ready to Boost Cellular Capacity,” Analog Devices. Available: http://www.analog.com/media/en/technical-documentation/tech-articles/60-ghz-line-of-sight-backhaul-links-ready-to-boost-cellular-capacity.pdf.

[I.41] “New spectrum for 5G, one step closer with mmWaves.” [Online]. Available: https://www.nokia.com/en_int/blog/new-spectrum-5g-one-step-closer-mmwaves. [Accessed: 06-Sep-2018].

[I.42] B. Brown, “FAQ: What is 802.11ay wireless technology?,” Network World, 28-Mar-2017. [Online]. Available: https://www.networkworld.com/article/3184827/wi-fi/faq-what-is-80211ay-wireless-technology.html. [Accessed: 07-Sep-2018].

[I.43] “‘X’ Series Products – Peraso.” [Online]. Available: https://perasotech.com/x-series-products/ [Accessed: 07-Sep-2018].

[I.44] P. Zhou et al., “IEEE 802.11ay based mmWave WLANs: Design Challenges and Solutions,” IEEE Commun. Surv. Tutor., vol. 20, no. 3, pp. 1654–1681, 2018.

[I.45] “Form 2 | Formlabs.” [Online]. Available: https://formlabs.com/store/eu/form-2/ [Accessed: 10-Sep-2018].

[I.46] “EOS M 290 - industrial 3D printed parts from metal materials.” [Online]. Available: https://www.eos.info/eos-m290. [Accessed: 10-Sep-2018].

[I.47] K. V. Hoel, S. Kristoffersen, J. Moen, G. Holm, and T. S. Lande, “Characterization of a 3D printed wideband waveguide and horn antenna structure embedded in a UAV wing,” EuCAP 2016, pp. 1–4.

[I.48] “EOS Industrial 3D printing - Process, method and benefits.” [Online]. Available: https://www.eos.info/additive_manufacturing/for_technology_interested. [Accessed: 10-Sep-2018].

[I.49] “Stratasys F900 3D Printer | Stratasys.” [Online]. Available: http://www.stratasys.com/3d-printers/stratasys-f900. [Accessed: 11-Sep-2018].

[I.50] C. W. Hull, “Apparatus for production of three-dimensional objects by stereolithography,” US4575330A, 11-Mar-1986.

[I.51] E. Palermo, A. E. | July 16, and 2013 02:39am ET, “What is Stereolithography?,” Live Science. [Online]. Available: https://www.livescience.com/38190-stereolithography.html. [Accessed: 10-Sep-2018].

[I.52] “3D Printing with Desktop SLA | White Paper | Formlabs.” [Online]. Available: https://formlabs.com/introduction-to-stereolithography/ [Accessed: 10-Sep-2018].

[I.53] “Dimensional accuracy of 3D printed parts,” 3D Hubs. [Online]. Available: https://www.3dhubs.com/knowledge-base/dimensional-accuracy-3d-printed-parts. [Accessed: 11-Sep-2018].

[I.54] “SLA - Stereolithography (and DLP, CDLP, CLIP),” Additive Blog, [Online]. Available: https://www.additive.blog/knowledge-base/3d-printers/sla-stereolithography-dlp-cdlp-clip/. [Accessed: 11-Sep-2018].

[I.55] “FDM Technology for 3D Printing | Stratasys.” [Online]. Available: http://www.stratasys.com/fr/fdm-technology. [Accessed: 10-Sep-2018].

[I.56] “Fused Deposition Modeling (FDM).” [Online]. Available: https://www.custompartnet.com/wu/fused-deposition-modeling. [Accessed: 07-Oct-2018].
[I.57] “EOS Electro Optical Systems: Industrial 3D Printing.” [Online]. Available: https://www.eos.info/en. [Accessed: 10-Sep-2018].
[I.58] “DMP60 series - 3D MicroPrint GmbH.” [Online]. Available: http://www.3dmicroprint.com/products/machines/dmp60-series/. [Accessed: 11-Sep-2018].
[I.59] “DMLS Applications.” [Online]. Available: https://dmlstechnology.com/dmls-applications. [Accessed: 10-Sep-2018].
[I.60] “DMLS - Direct Metal Laser Sintering.” [Online]. Available: https://www.custompartnet.com/wu/direct-metal-laser-sintering. [Accessed: 07-Oct-2018].
[I.61] “Imprimantes 3D Fortus 380mc et 450mc | Stratasys.” [Online]. Available: http://www.stratasys.com/fr/3d-printers/fortus-380mc-450mc. [Accessed: 10-Sep-2018].
[I.62] “Metal 3D-printed waveguides proven for telecom satellites,” European Space Agency. [Online]. Available: http://www.esa.int/Our_Activities/Space_Engineering_Technology/Metal_3D-printed_waveguides_proven_for_telecom_satellites. [Accessed: 10-Sep-2018].
[I.63] “3D Printing Dives into Mass Production,” Machine Design, 30-Jun-2017. [Online]. Available: https://www.machinedesign.com/3d-printing/3d-printing-dives-mass-production. [Accessed: 07-Oct-2018].

II. V-BAND LENS ANTENNAS

Following the densification of the network architecture leading to the need of wireless backhaul links massive deployment, designing low-cost and compact radio systems appear as an utmost necessity. In this chapter, we focus on the design of low-cost dielectric lens antennas for backhaul applications in V-band (57 to 66 GHz). FR4 PCB standard technology is leveraged for the fabrication of printed antennas suitable for mass production. Furthermore, 3D printing fabrication techniques are chosen for the fabrication of cost-efficient and easy to manufacture lens antenna systems. We begin this study by defining the specifications of antennas used for millimeter Wave (mmW) backhaul links and we present state-of-the-art V-band lens antennas. In a second part, we discuss the viability of PCB FR4 substrate to design a planar source for the lens. Moreover, to enable an easy integration with the transceiver PCB, we also propose to integrate the PCB with a waveguide connection by means of a microstrip-to-waveguide (MS-to-WG) transition. Finally, different high-gain lenses are presented using commonly employed plastic material and 3D printing techniques.

II.1 ANTENNAS FOR BACKHAUL APPLICATIONS

II.1.1 Backhaul point-to-point link specifications

In order to limit interferences between small cells backhaul, the European Telecommunications Standards Institute (ETSI) fixed the specifications that antennas of those links should meet. We present in this section the required characteristics for antennas used in mmW E and V-bands backhaul P2P fixed links fixed by the ETSI EN 302 217-4 standard [II.1]. In addition to the gain requirements mentioned in Chapter 1, ETSI defines the Radiation Pattern Envelopes (RPE) considered as an “absolute worst case not to be exceeded in 100 % of cases”. Figure II.1 and II.2 show the required RPE in co- and cross-polarizations for a backhaul link antenna from 47 to 66 GHz and from 71 to 86 GHz respectively [II.1]. Many classes of RPE are defined for each frequency band depending on the application (femtocell, picocell or macrocell), class 1 being the least demanding RPE. Concerning the cross-polarization discrimination level (XPD) in the broadside direction, no specific values are given by ETSI for V and E-bands.

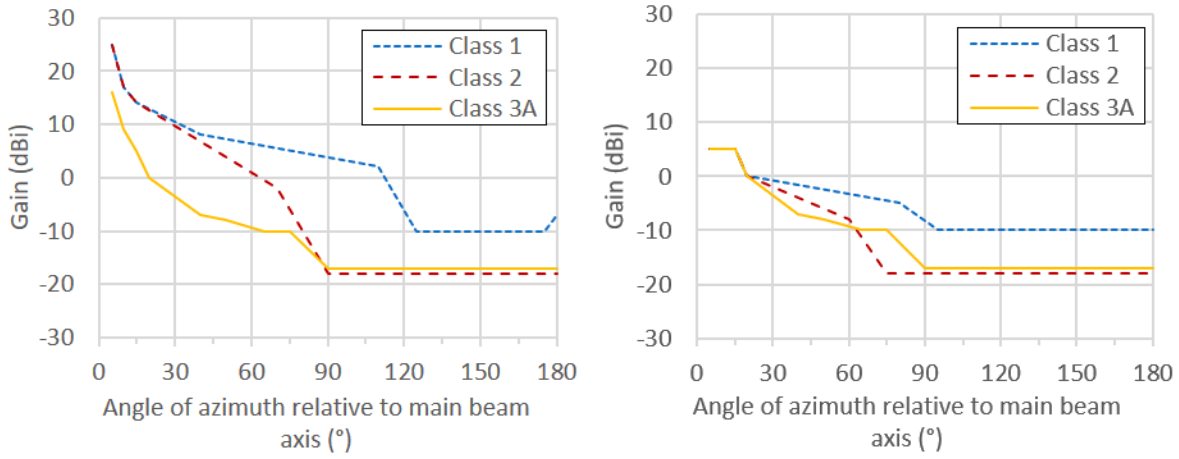

(a) (b)

Figure II.1 RPE specifications in co-polarization (a) and cross-polarization (b) from 47 to 66 GHz.

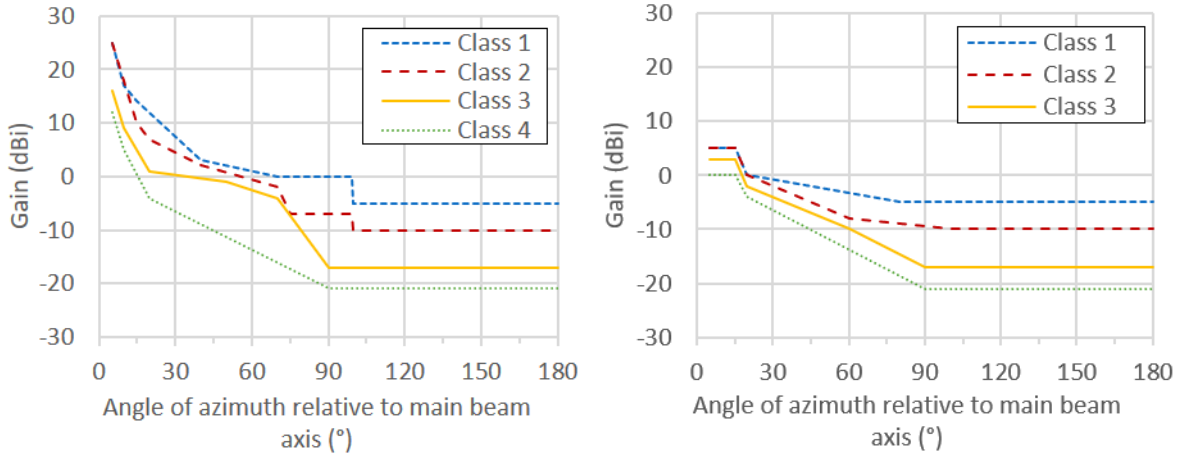

(a) (b)

Figure II.2 RPE specifications in co-polarization (a) and cross-polarization (b) from 71 to 86 GHz.

To have more insight into the required antenna-gain, we refer to the International Communication Union Recommendations (ITU-R). According to the Recommendation ITU-R F.699 [II.2], the boresight antenna-gain is related to the antenna diameter by the simple relationship:

$$20log\frac{D}{\lambda} \approx G_{max} - 7.7 \quad \text{(II.1)}$$

Where G_{max} is the main lobe antenna gain in dBi. As an example, considering an antenna of diameter D = 10 cm operating at 60 GHz, yields G_{max} = 33.7 dBi. Regarding the return loss, no limit is specified by norms, especially for outdoor radio units that don't need long feeder connections. Therefore, it depends on the unique specifications of the feeder's manufacturer.

On the other hand, more specifications can be found referring to MiWaves European collaborative project which aims to develop millimeter-wave wireless communication technologies for future 5G heterogeneous cellular mobile networks. MiWaves project fixed

some targets for this work derived from the system specifications and link budget analysis, they are listed in Table II.1. The antennas shall cover either the V band or the E band and provide a gain of 30 dBi or more. Still those requirements are not considered as a critical requirement at this stage of the development as the focus is on the demonstration of advanced and innovative antenna concepts.

Parameter	Value
Frequency	57-66 GHz (V-band) 71-76GHz 81-86 GHz (E-band)
Return loss	15 dB
Gain	30 dBi
3dB beamwidth	3°
Polarization	Linear
Surface	100×100 mm^2 max
Thickness	50 mm max
Electrical compliance	ETSI EN 302 217-4-2 Class 2

Table II.1 MiWaves specifications of antennas for 5G backhaul links.

II.1.2 State-of-the-art of V-band lens antennas

Aiming to achieve 30dBi gain antennas in V-band, we present below lens' antenna solutions. Lens antennas are considered as a simple-to-manufacture solution compared to planar arrays of radiators and are less bulky in size compared to reflector antennas. Many V-band lens antennas for backhaul applications are sold by specialist suppliers. Table II.2 references some of them with associated pictures in Figure II.3. For example, the air link series 60 GHz was proved to work for distances up to 800 m. Using a maximum transmission power of 8 dBm and a maximum EIRP of 44 dBm, it achieves a bit error rate lower than 10^{-10}, and a data rate ranging from 226 Mbps (BPSK modulation) to 1 Gbps (16QAM modulation) [II.3].

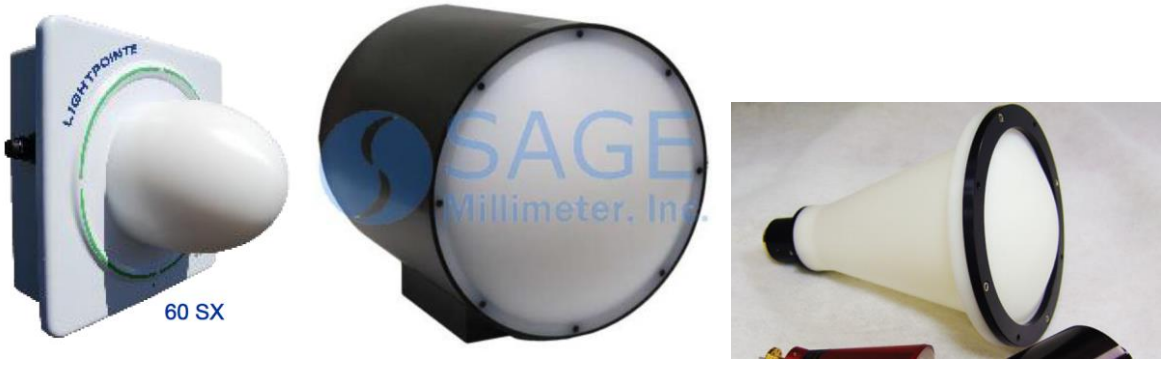

(a) (b) (c)

Figure II.3 (a) Light pointe wireless, Air link series 60 GHz: Integrated lens [II.3]. (b) SAGE, Millimeter, Inc. : V-Band Gaussian optics antenna [II.5]. (c) MI-WAVE : 258 Series, Horn lens antennas [II.4].

	Light pointe wireless, Air link series 60 GHz: [II.3]	SAGE, Millimeter, Inc. : V-Band Gaussian optics antenna [II.5])	MI-WAVE : 258 Series, Horn lens antennas [II.4]
Gain	36 dBi	36 dBi at 60 GHz	37 dBi at 60 GHz
Antenna diameter	12 cm (24λ)	15 cm (30λ)	15 cm (30λ)
Polarization	Linear	Linear	Linear
Frequency	59 to 63 GHz	58 to 68 GHz	57 to 66 GHz
-3dB beamwidth	2.5°	3°	2.3°
Unit price	NS	3250 $	1250 $

Table II.2 Some of the available Commercial lens antennas for backhaul applications.

Nevertheless, most of the commercial lens antennas are not cost-efficient mainly due to the horn feeding that require accurate micromachining and the expensive lens material used like Rexolite. Leveraging 3D printing technology, cheap 3D printed dielectric materials can be used for fast prototyping. This was demonstrated by the 3D printed lens design in V-band reported in [II.6], where authors harnessed the potential of 3D printing i.e. stereolithography, to fabricate a complex-shaped integrated lens antenna for optimized performances using ceramic material (Alumina). The lens featured corrugated surface (cf. Figure II.4 (a)) acting as a matching layer to overcome the high electrical permittivity of the material (relative electric permittivity $\varepsilon_r = 9$) causing internal wave-reflections at the air/dielectric interface. On the other hand, more simpler designs but still performing solutions were presented in [II.7] and [II.8] using ABS-M30 plastic and a simple elliptical design at 60 GHz and 120 GHz respectively, an example at 60 GHz is shown in Figure II.4 (b). ABS-M30 is more commonly used in 3D printing technics and is characterized by a lower electrical permittivity ($\varepsilon_r = 2.5$). Accordingly, we applied the same concept of ABS-M30 3D-printed elliptical lens to conceive a 30 dBi gain lens for backhaul applications. Moreover, in order to introduce a cheaper and easier-to-manufacture source, we investigate the possibility to feed the lens by a planar printed antenna using PCB technology and FR4 substrate. We also propose to complete our design by a MS-to-WG transition integrated into to the antenna PCB to connect it to available transceivers featuring a waveguide connection [II.9]. The complete proposed system is illustrated in Figure II.5.

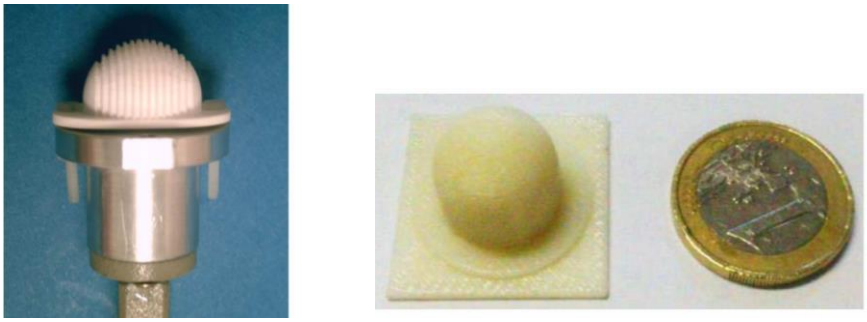

(a) (b)

Figure II.4 (a) 3D printed Corrugated lens made out of Alumina from [II.6] and (b) 3D printed elliptical lens made out of ABS-M30 operating at in V-band [II.7].

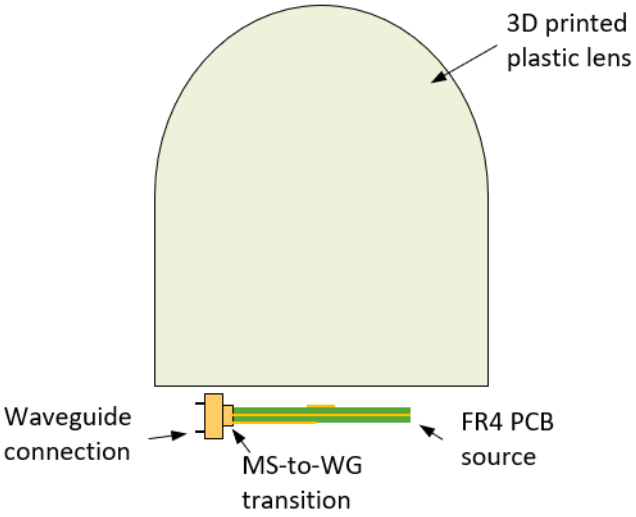

Figure II.5 Description of the complete lens, PCB source and waveguide connection system.

II.2 V-BAND PCB PATCH ANTENNAS

In this section, printed planar sources for the lens fabricated in standard FR4 PCB technology are presented. The aimed target is to design a planar antenna with a gaussian 10dB-half-beamwidth (10dB-HBW) near 50° (equivalent to 11 dBi directivity), to feed an extended elliptical lens (detailed in paragraph II.5) over V-band enabling to reach 30 dBi gain.

II.2.1 State-of-the-art of printed antennas in V-band

Printed antennas are more suitable for mass production, less bulky and have reduced cost compared to horn antennas traditionally used as a lens source. Two main integration schemes can be found for printed antennas: Antenna in Package (AiP) and Antenna on Chip (AoC). AoC solutions feature the antenna placed as close as possible to the chip of the RF radio, commonly in silicon technologies [II.10], [II.11]. However, those solutions suffer from low antenna efficiency (largely less than 10%) and poor gain due to the low resistivity of silicon as well as low fractional operating bandwidth. Therefore, complex fabrication steps are added to the process in order to enhance the printed antenna's efficiency (like machining an air cavity under the antenna) [II.11]. On the other hand, AiP systems are considered more suitable for the antenna application because they enable the use of other integration and substrate technologies more suitable for antennas radiation characteristics, resulting in achieving much higher efficiencies. Table II.3 concisely shows some of the planar antennas technologies that have been presented at 60 GHz resulting in efficiencies beyond 70%.

Still, PCB technology is the least costly solution between all the above mentioned. Nowadays PCB design rules and tolerances are sufficiently developed to meet with millimeter wave applications. Consequently, we chose to develop a planar antenna using standard PCB on glass-reinforced epoxy laminate material: FR4. FR4 advantages is its suitability for mass-production and low-cost, but its major drawback is the high dielectric loss (loss tangent around 0.01) that could limit the antenna-efficiency. Therefore, very few examples of 60 GHz antenna

based on FR4 PCB are reported in the literature. The most relevant examples in V-band are given in table II.4 and illustrated in Figure II.6.

Ref.	Gain	Technology	Bandwidth	Antenna-type
[II.12]	6-7 dBi	Integrated passive device (IPD™) flip chipped on High Temperature Co-fired Ceramic (HTCC) package with air cavity to increase efficiency	7 GHz, (12%)	Tapered slot antenna
[II.13]	5 to 7 dBi, Efficiency up to 93%	Low Temperature Co-fired Ceramic (LTCC) Ball Grid Array (BGA)	55.9 to 65.3 GHz (15%)	Yagi antenna
[II.14]	6 dBi	High Definition Integration (HDI) organic technology for System in Package (SiP) packaging	55 to 66 GHz (18%)	Slot coupled patch antenna

Table II.3 Printed 60 GHz antennas with different technologies and packaging.

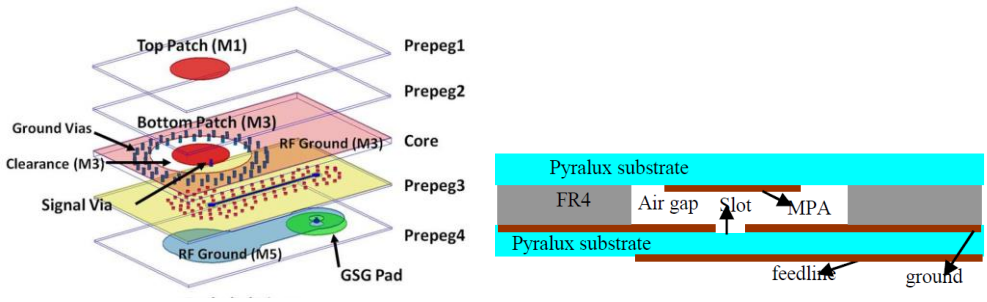

(a) (b)

Figure II.6 (a) Exploded view of a circular stacked patch antenna on FR4-PCB [15]. (b) Side view of membrane supported slot coupled single patch antenna [16].

Ref.	Antenna-type	10 dB Matching bandwidth	Broadside Gain	Efficiency
[II.15]	Circular stacked patch antenna	~14%	4.1 dBi	76%
[II.16]	Aperture coupled patch antenna	~10%	Max 7.6 dBi	80%

Table II.4 State-of-the-art 60 GHz antennas on FR4 PCB.

In [II.15], a via fence around the patches is used to limit the fringing fields due to surface waves propagation and stacked patches are used to increase the directivity and hence compensate the dielectric losses (cf. Figure II.6 (a)). In [II.16], an air gap is micromachined in the FR4 substrate to increase the efficiency of the antenna and limit the propagation of the surface waves (cf. Figure II.6 (b)). In addition, a superstrate dielectric layer is added above the antenna to leverage its gain, adding complexity and more material to the concept. Even though the efficiency achieved by the latter antennas is similar to those achieved by HTCC, LTCC or organic technologies, the directivity of [II.15] does not fill our requirements for illuminating the lens and [II.16] is too complex for mass production. In order to overcome those restraints, we propose a Slot Coupled Patch (SCP) antenna with a surrounding ring of vias forming a sort

of cavity. By only finely optimizing the dimensions of this cavity, beamwidth, efficiency and surface wave management can be improved.

II.2.2 60 GHz FR4 PCB single patch antenna

II.2.2.a Single patch design

Even though design rules of standard FR4 PCB aren't as aggressive as in HDI technologies, they are still sufficient for 60 GHz antennas design. The most important FR4 PCB design rules provided by the chosen supplier ASPOCOMP [II.17] are:

- Minimum conductor width: 60 µm.
- Minimum conductor space: 75 µm.
- Via diameter: 100 µm in prepreg/ 200 µm in core (cf. Figure II.7).

Two substrate's build ups were selected for the development of this antenna, depending on the MS-to-WG transition type that will be further integrated with the antenna (detailed in the next section). The substrate used for this PCB is Nelco® N4000-13 EP™ with a relative permittivity of ε_r = 2.7, and a dielectric loss tangent tanδ = 0.008. Figure II.7 illustrates the buildups' details. In both buildups, the thickness of all copper layers is 18 µm and solder masks (SM) cover both sides of the PCB.

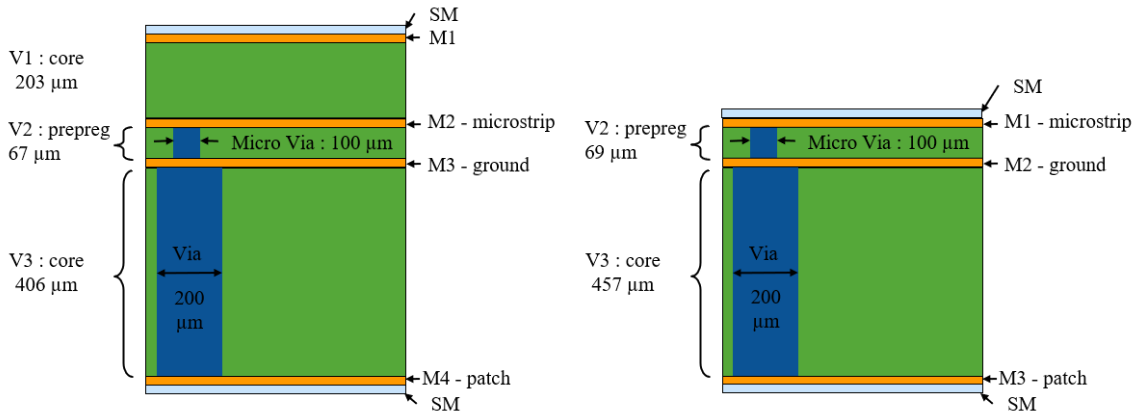

Figure II.7 FR4 PCB buildups: (a) three-layer buildup and (b) two-layer buildup.

The main parameters of the SCP antenna indicated in Figure II.8 were optimized to approach a directivity of 11 dBi and a return loss higher than 10 dB in the whole V band. The slot was chosen longer than the patch in order to shift down its own resonance before the patch's resonance and also increase the overall impedance bandwidth (~20%) [II.18]. A stub was added at the end of the microstrip line, surpassing the slot, to enhance the matching level. The core height is chosen thick enough also to enlarge the impedance matching bandwidth (0.17λ_G, guided wavelength).

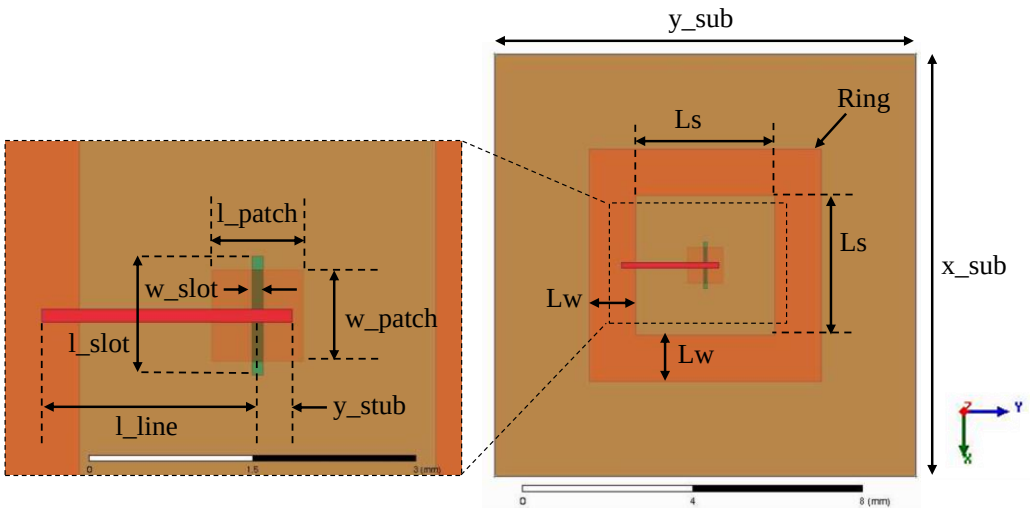

Figure II.8 Slot coupled-patch antenna design and dimensioning parameters.

Due to this important core thickness, surface waves are generated and significant power is dissipated into those surface waves. To harvest this lost power, we added a ring around the patch and optimized its dimensions to collect those surface waves and try radiating them in phase with the patch antenna. All the optimized parameters values are listed in Table II.5. The same design was implemented within both buildups from Figure II.7. Since the only difference between them was an added 200 µm core, only the width of the microstrip line had to be adjusted to make sure its characteristic impedance is equal to 50 ohms. Therefore, this width, w-line, is equal to 0.8 mm for the 3-layer buildup and 0.12 mm for the 2-layer buildup.

Parameter	y_sub	x_sub	l_patch	w_patch	l_slot	w_slot	l_line	l_stub	Ls	Lw
Values (mm)	10	10	0.85	0.85	1.1	0.1	4	0.32	3.3	1.1

Table II.5 Optimized values of the slot patch antenna parameters.

Simulation results show an impedance match of 10 dB on the whole V-band and even from 53 GHz to 69 GHz for both build-ups (about 28%), achieving a remarkable impedance bandwidth compared to previously mentioned printed planar antennas (cf. Figure II.9). Since the antennas behavior on both of the presented buildups are very similar, we'll only show the results with the two-layer buildup in the next parts. Simulated directivity versus frequency, depicted in Figure II.10 (a), varies from 7.7 dBi to 9.8 dBi from 57 to 66 GHz. Realized gain is about 1 dB lower than directivity including antenna dielectric and mismatch losses as well as the losses from the 4 mm microstrip feeding line. Resulting efficiency, presented in Figure II.10 (b), is above 80% over 20% of bandwidth, which is very close to the efficiency obtained in [II.14] and [II.15] but with less complicated and cheaper design. The 10 dB-HBW in E plane (along y axis) and H plane (along x axis) is ranging between 50° and 70° (cf. Figure II.11 a and b), depending on the operating frequency. Finally, side lobes are kept under -10 dB relatively to maximum broadside radiation and the surface waves are indeed well controlled with no apparent radiation in unwanted direction as shown in Figure II.12. Obtained performances approach our fixed goals (11 dBi directivity and 50° 10 dB-HBW) but don't meet with them precisely.

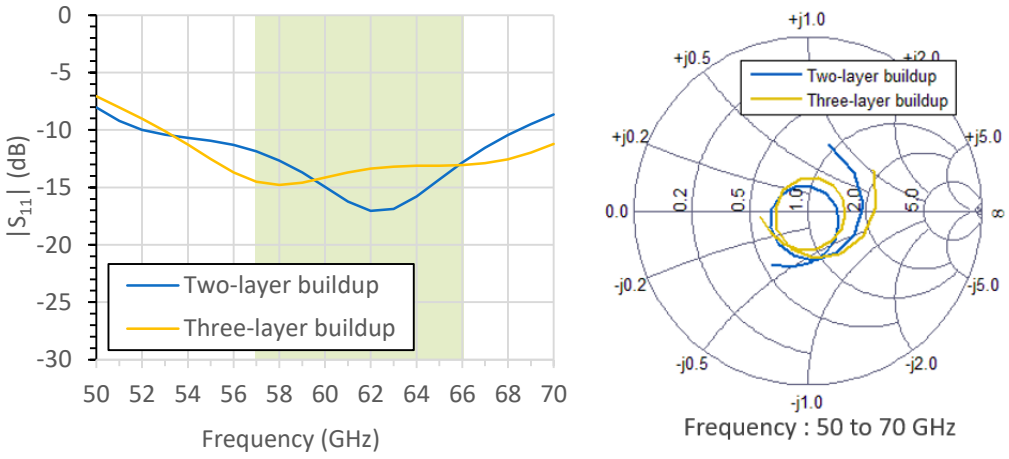

(a) (b)

Figure II.9 (a) Magnitude of the reflection coefficient $|S_{11}|$ and (b) input impedance versus frequency of the SCP antenna built on the two-layer and three-layer buildups.

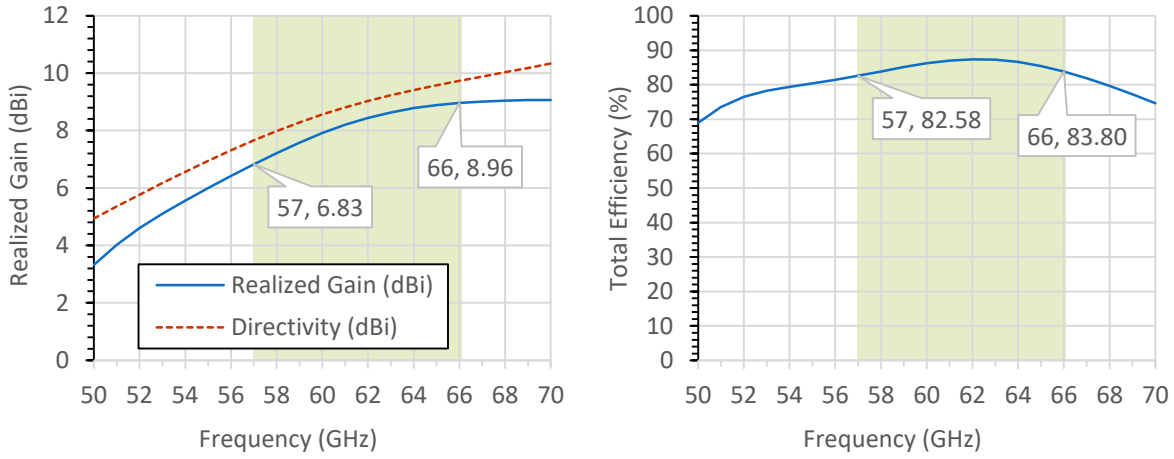

(a) (b)

Figure II.10 (a) Simulated broadside (φ = 0°, θ = 180°) realized gain, directivity and (b) total efficiency versus frequency of the SCP on the two-layer buildup.

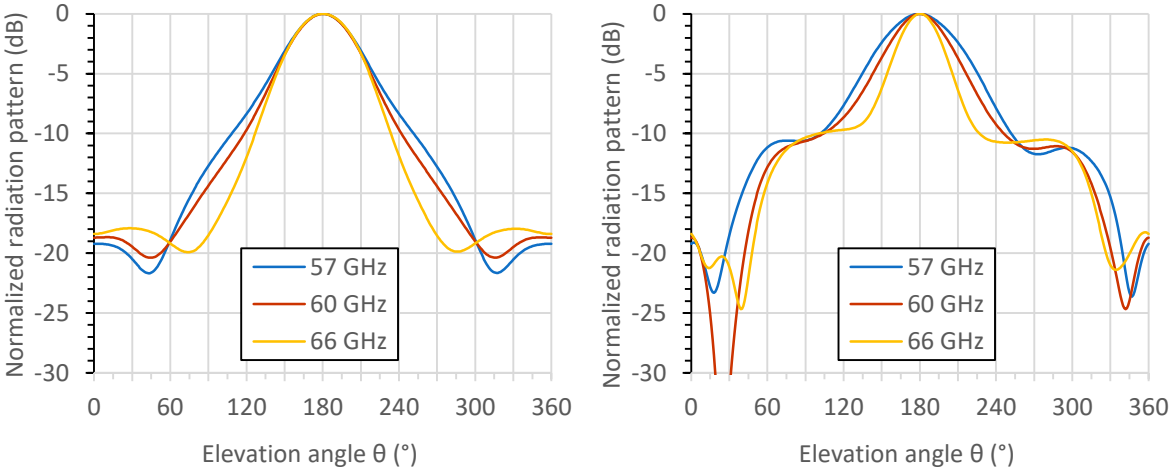

(a) (b)

Figure II.11 Normalized radiation patterns in (a) H plane (along x axis) and (b) E plane (along y axis) of the SCP using the two-layer buildup at different frequencies in V-band.

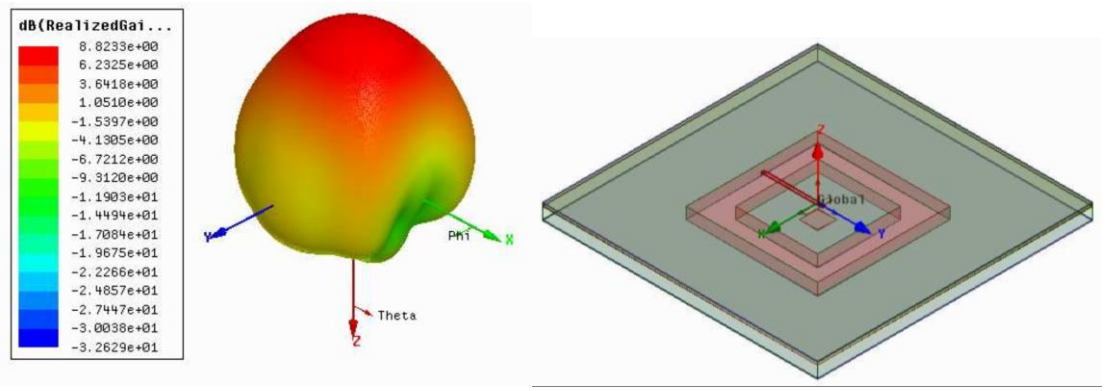

(a) (b)

Figure II.12 (a) Polar 3D plot of the gain of the SCP and (b) 3D view of the designed SCP.

II.2.2.b Surface-waves management

Generally, unwanted generated surface waves are blocked to avoid radiation in undesired directions. It is usually done by means of:

- Band gap structures: photonic band-gap [II.19], electromagnetic band-gap [II.20] or cavities [II.21] surrounding the main radiating element generating the surface waves.
- Disposing the radiating elements in an array-arrangement to suppress the generated surface waves by out-of-phase combination [II.22].
- Inserting an air cavity within the substrate to reduce the coupled power to surface waves [II.20].

Blocking the surface waves from propagating is an interesting solution as the antenna is not going to radiate in undesired directions. Still, a significant power from the feed is coupled to the generated surface waves leading to reduce the antenna gain. As an ambitious alternative, we propose here to rather efficiently use the generated surface waves to make them radiate in phase with the main antenna instead of blocking them and lose the power they convey.

The cut-off frequency of each surface waves' mode can be calculated according to [II.23] for the specific case of surface waves propagation within a grounded substrate structure. On order to predict the propagating surface waves modes for a certain substrate thickness, computations of the corresponding propagation constant were detailed in [II.23]. Using those calculations, we plotted in Figure II.13 the propagation constant to the wave number in air, β/k_0, of each surface waves' mode versus the thickness of the substrate to the wavelength in air, t/λ_0. Computations were conducted for a grounded dielectric substrate of ε_r = 3.7 corresponding to our substrate.

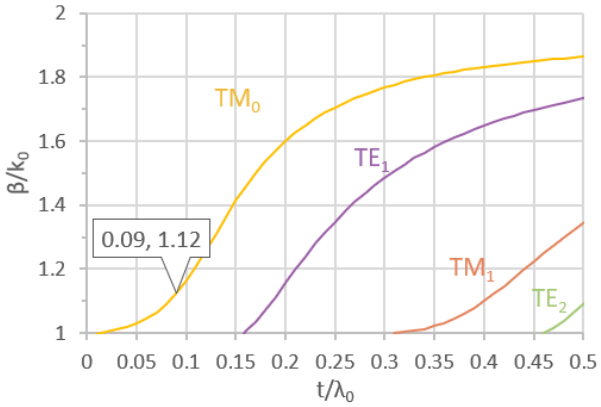

Figure II.13 Normalized surface wave propagation constants versus normalized thickness of a grounded dielectric slab with ε_r = 3.7 at 60 GHz.

As presented in Figure II.13, the first mode TM_0 has no cut-off frequency. Hence, the power loss in the surface waves cannot be avoided at any frequency but it can still be minimized by making a compromise on the choice of the thickness t. In other terms, minimizing the power coupled to surface waves can always be achieved by choosing a substrate with small thickness at the expense of a small operating bandwidth. In certain cases, like ours, where the needed bandwidth is 15% (V-band), the substrate thickness cannot be too small that's why a certain amount of TM_0 surface waves will be generated and an efficient management of them is obviously needed. The chosen core thickness corresponds to $t/\lambda_0 = 0.09$ at 60 GHz located after the cut-off of TM_0 mode and before that of TE_1 mode.

The concept of placing a ring surrounding the antenna is intended to stop the generated surface waves from diffracting at the edges of the antenna and interfering destructively with the main antenna radiation, reducing its broadside gain. In addition, by optimizing the inner dimension, Ls, along y axis and width, Lw, of the cavity we can manage to rather increase the directivity of the patch. Since the direction of the TM_0 mode is along y axis principally, we chose a square geometry. Figure II.14 (a) and (b), show the variation of the directivity versus Ls and Lw respectively. Notice how the directivity is reaching a maximum value for a given value of Ls and then drops significantly. The increase in directivity can be explained by currents induced on the ring surface by surface waves propagation and coupling constructively with the currents on the patch surface. The highest directivity point (Ls = 3.6 mm) corresponds to a perfect in-phase state between the currents on the ring and the currents on the patch. To illustrate this phenomenon, we plotted in Figure II.15 (a) the simulated surface current vector on the patch and the metallic ring's surfaces at 66 GHz at Ls = 3.6 mm. The drop of directivity occurring after the highest directivity point corresponds to out-of-phase currents between the patch and the ring, as illustrated by the surface current vector plot in Figure II.15 (b) for Ls = 4.2 mm. In fact, it was shown that Ls at which the directivity is maximum is equal to the wavelength of the propagating surface wave mode TM_0 [II.23]. Consequently, to avoid the out-of-phase state from occurring inside the bandwidth, we optimized the dimensions of the cavity at the end of the frequency bandwidth of interest (66 GHz). Concerning Lw (the size of the longitudinal surface's ring), the plot in Figure II.14 (b) show that the directivity is maximum

when Lw is close to the main patch' dimensions even if a flatter behavior is observed compared to the directivity when Ls varies. Hence, the two circled areas of the ring (cf. Figure II.15 (a)) act as secondary radiators highly contributing to the radiation of the whole structure with currents in-phase with the currents on the main patch surface. The final optimized structure can be assimilated to a 3×1 patch array, with each patch element radiating in-phase.

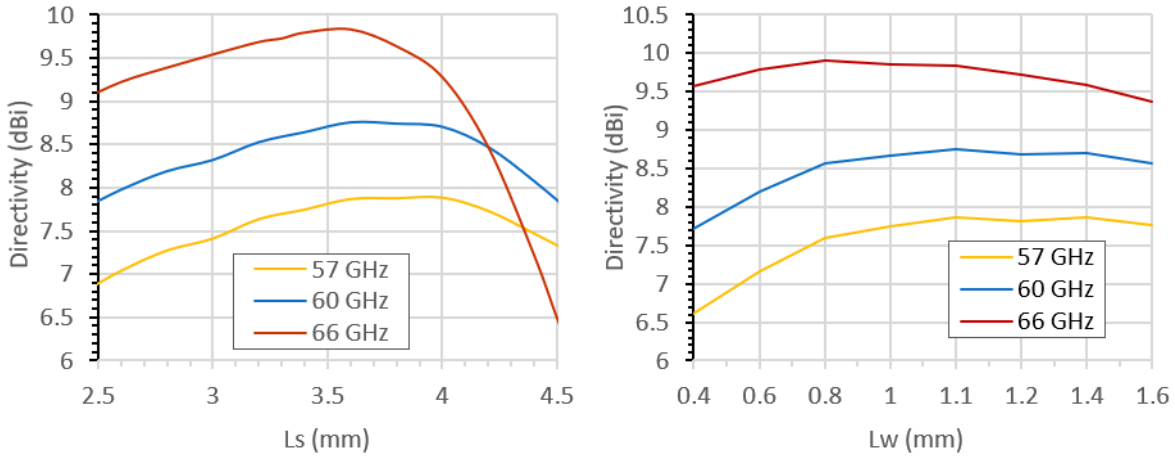

(a) (b)

Figure II.14 (a) Directivity of the SCP in the broadside direction (θ = 0, φ = 0) versus the ring dimensions, (a) Ls and (b) Lw.

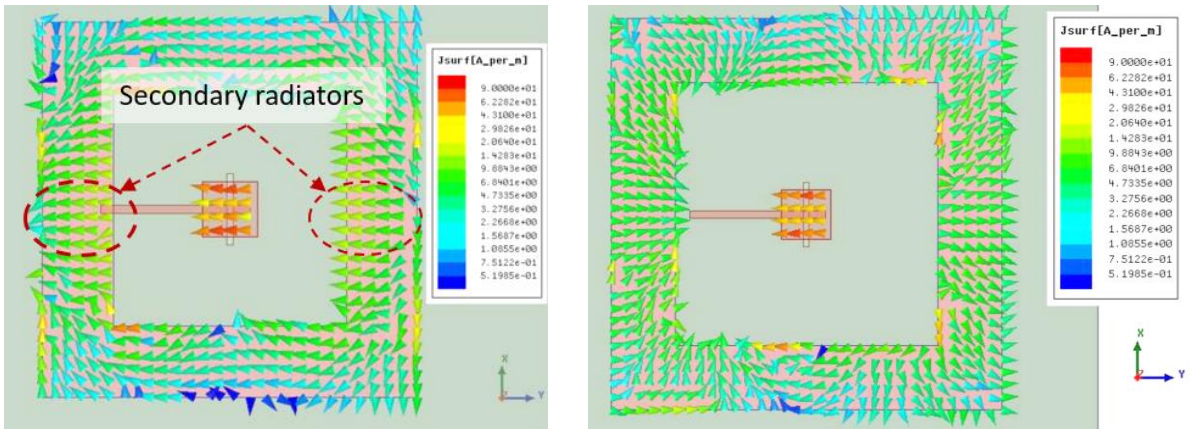

(a) (b)

Figure II.15 Simulated surface current vectors on the patch and the ring surface (radiation side), in log scale at 66 GHz for (a) Ls = 3.6 mm and (b) Ls = 4.2 mm.

II.2.2.c Fabrication and measurement of the single SCP FR4 PCB

All simulations presented until now have been achieved with a ring consisting of four compact metal walls. In practice, it isn't possible to implement such a structure using PCB technology (or even more expensive HDI BGA). Therefore, the metal walls have to be replaced by a row of vias under the metal ring printed on the same layer as the main patch, as presented in Figure II.16 and Figure II.17 (a). Fabricated PCB using Nelco substrate is shown in Figure II.17 (b) and (c). We measured this antenna using a Ground Signal Ground (GSG) coplanar probe with a 1.85 mm coaxial connector from Cascade Microtech [II.24] (cf. Figure II.18). The probe operates until a maximum frequency of 67 GHz. To feed the patch antenna with this

probe, GSG pads were added on the microstrip feeding line layer of the PCB (cf. Figure II.16 and II.17). The ground pads were connected to the main ground plane of the antenna through micro-vias in the prepreg layer (cf. Figure II.16).

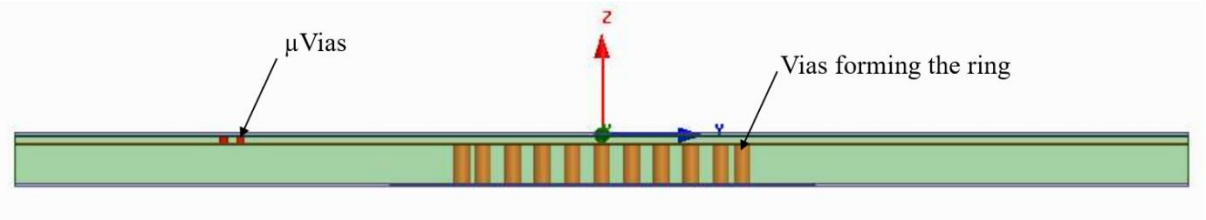

Figure II.16 Profile view of the simulation model of the SCP PCB.

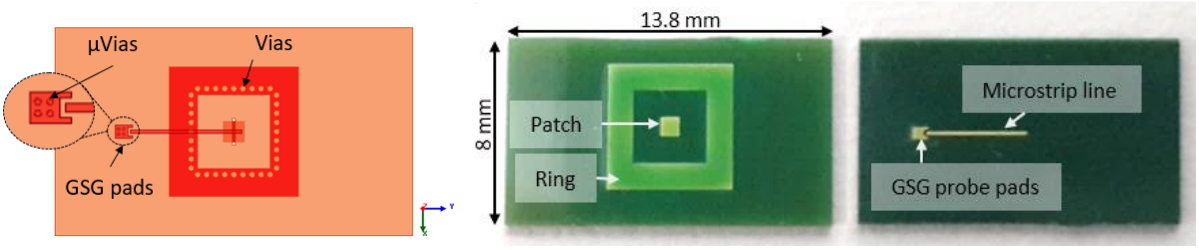

(a) (b) (c)

Figure II.17 (a) Top view of the whole structure with via ring and GSG pads (simulation model). (b) Top and (c) bottom view othe fabricated SCP antenna on FR4 PCB.

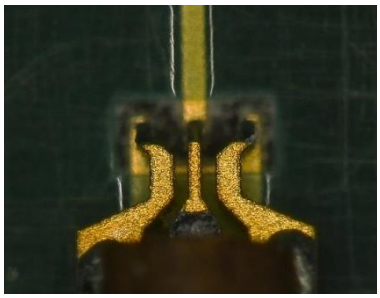

Figure II.18 Microscope photo of the GSG probe posed on the dedicated pads of the patch PCB.

The real dimensions of the fabricated structure were measured using X-ray scans. The obtained absolute errors respected the tolerances given by the manufacturer: +/- 50 µm. However, the most noticeable difference was the diameter of the fabricated vias, which was found to be equal to 100 µm instead of 200 µm. Retro-simulations were conducted taking into consideration the diameter of the fabricated vias to perform a fair comparison with measurements. Measurements were conducted using our in-house measurement system performing from 50 to 140 GHz [II.25], [II.26] (cf. Figure II.19). S_{11} measurements and simulations, shown in Figure II.20 (a). are in good agreement, with a slight frequency downshift of ~1 GHz. A satisfactory matching is obtained as return loss is higher than 10 dB from 55 to 67 GHz, corresponding to approximately 20% of relative bandwidth.

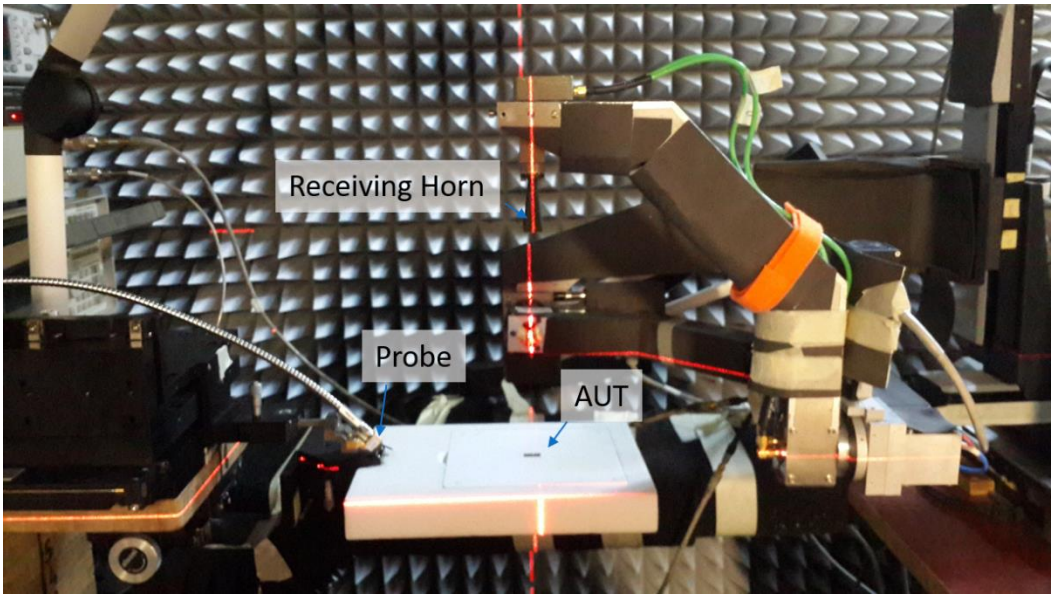

Figure II.19 50 to 140 GHz measurement system with the Antenna under Test (AuT).

The measured realized broadside gain, plotted in Figure II.20 (b) stays between 4 and 5 dBi from 57 to 64 GHz, however it drops significantly after 64 GHz reaching 0 dBi at 66 GHz. The early cut-off effect is mainly due to the fact that the fabricated vias are smaller than expected. As seen in the retro-simulations with vias diameter 100 µm versus 200 µm (cf. Figure II.20 (b)), the gain drop is well predicted and moved to lower frequencies when vias are made smaller due to the increased space between them. This broadside gain-drop correspond to the fact that the currents on the ring are no more in-phase with the currents on the main patch surface as illustrated in Figure II.21. Consequently, radiation occurs in other directions than broadside (originating from the ring) causing the broadside gain to decrease significantly.

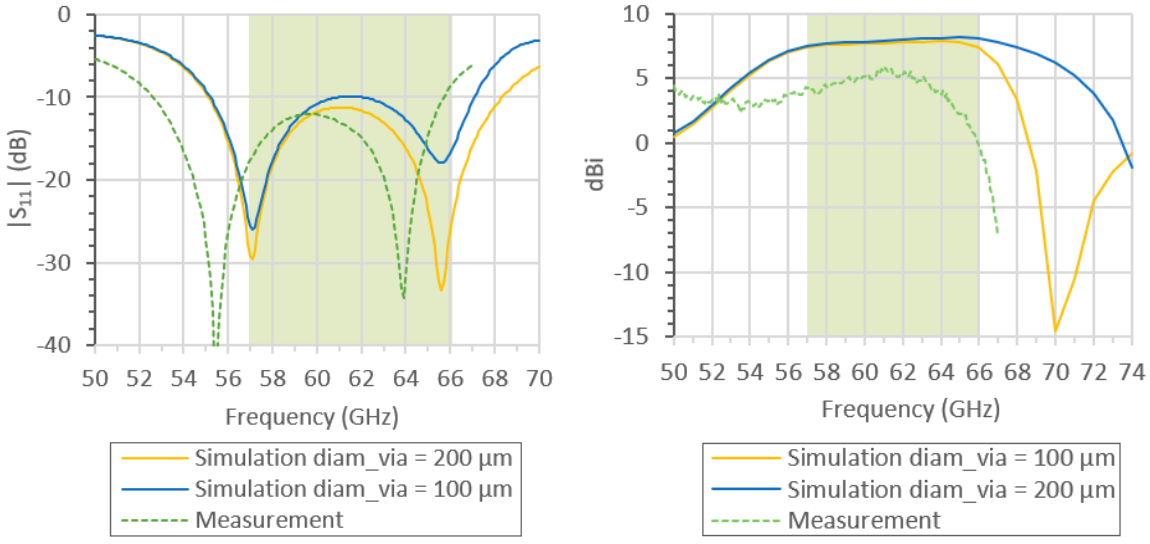

(a) (b)

Figure II.20 Measured and simulated (a)$|S_{11}|$ and (b) broadside realized gain (-z direction) of the FR4-PCB SCP with different vias' size.

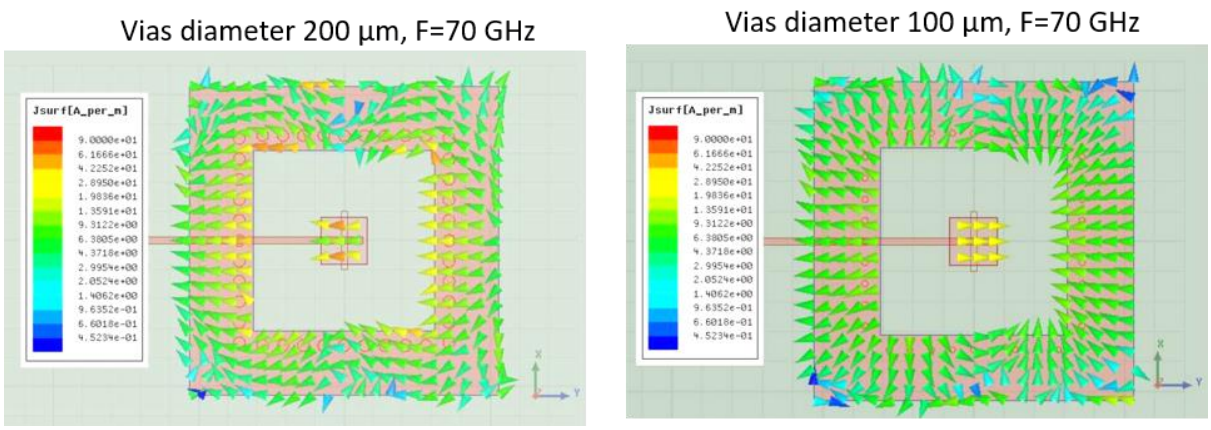

Figure II.21 Surface current vector at 70 GHz on the patch and ring surface of 100 µm and 200 µm vias diameter.

Still, some differences remain between the retro-simulation (diam_via = 100 µm) and measurements:

- The measured realized gain level is lower by 2 to 3 dB.
- The gain-drop is shifted towards lower frequencies by less than 2 GHz which is relatively small considering the measurement frequency (corresponds to 3.2 % of relative bandwidth).

Those differences can be explained by several reasons:

- The used electrical parameters (electrical permittivity and dielectric loss tangent) in simulation are taken from measurement at 10 GHz, hence we could be under-estimating the dielectric losses.
- Surface waves propagating in the core weren't completely coupled by the ring (especially that the vias are smaller than expected).
- The probe feeding was not precisely emulated in simulations.

Measured radiation patterns in H plane (cf. Figure II.22) are in good correlation except for side lobes appearing between 100° and 110°. Front to back radiation ratio is around 15 dB which is the main drawback of a slot coupled patch antenna (the back radiation is mainly due to the resonant slot), however being largely acceptable for our application. A moderate agreement is found between the simulated and measured E-plane especially at 60 GHz (cf. Figure II.22). The highlighted angular zone between 225° and 330° indicated in Figure II.22 in E-plane is not mechanically accessible, hence, no measurements are shown in this area. The measured radiation pattern is more directive in E-plane and side lobes appear between 90° and 120°. Indeed, it seems that there's still surface waves propagating beyond the ring, diffracting at the edges of the PCB leading to the appearance of those side lobes. A secondary important reason resides in the fact that the electrically large GSG feeding probe is placed in the longitudinal direction of the patch during this E-plane measurement (which is not the case in the H plane) and coupled currents to the body of the large probe are undoubtedly radiating causing constructive and destructive interferences in this E-plane. This is a well-known issue in probe-fed radiation measurement set-up at mm-wave frequencies.

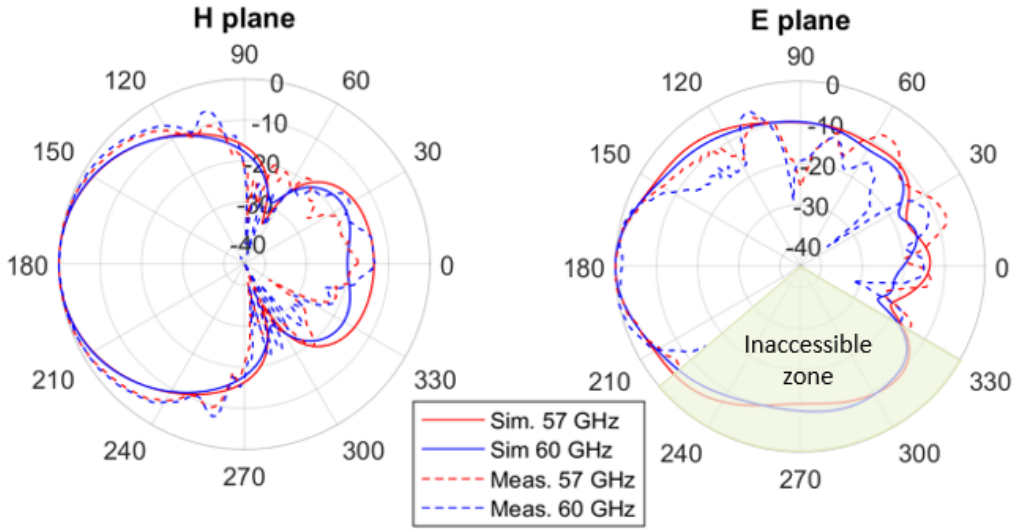

Figure II.22 Measured and simulated normalized radiation patterns of the patch antenna on FR4 PCB in E-plane and H-plane.

II.2.3 2×1 patch array on FR4 PCB

In order to further approach our goal of designing an 11 dBi directivity antenna (close to 50° 10 dB-HBW), we investigated the design of a 2×1 SCP array using the same FR4 PCB technology and a two-layer buildup (cf. Figure II.7). The array elements are aligned along H-plane (y-axis) and spaced by $0.5\lambda_0$ = 2.5 mm, λ_0 free space wavelength at 60 GHz, to limit as much as possible the rise of array's side lobes. Disposing the radiating elements along y-axis which corresponds to the direction of propagation of surface waves contributes to suppress the generated surface waves by out-of-phase combination. A microstrip line divider divides the power equally and in-phase between the patches elements and is matched using a quarter-wave impedance transformer. Two outer rings were added to the array instead of only one to reduce as much as possible the propagation of the surface waves (cf. Figure II.23).

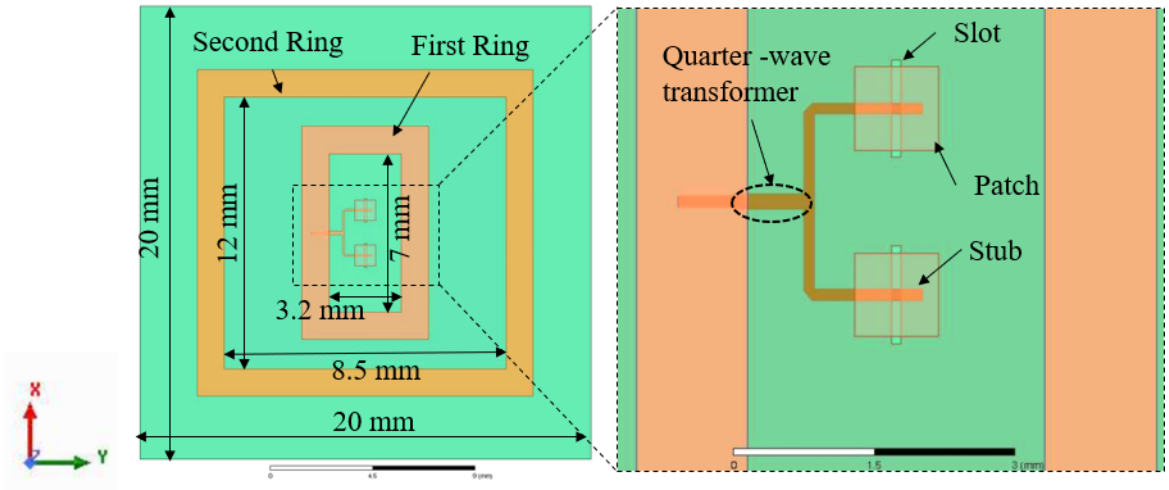

(a) (b)

Figure II.23 (a) Top view of the simulated model of the 2×1 patch array on FR4-PCB with double ring and (b) top zoomed view.

Following the same methodology of optimization used with the single patch surrounding ring developed in II.2.2, the dimensions of the first and second ring were optimized to obtain the highest directivity at 66 GHz. Optimized dimensions are indicated in Figure II.23. The simulated results demonstrated a return loss higher than 10 dB from 51 to 70 GHz (cf. Figure II.24 (a)). The simulated directivity lies between 10 and 12 dBi which is very close to the lens' illumination requirements (cf. Figure II.24 (b)) and the simulated realized gain is just 1 to 1.5 dB lower than the directivity, leading to an efficiency above 70% which slightly lower than the simulated efficiency of the single SCP (above 80%). The 10 dB HBW of the simulated radiation patterns in E and H planes (Figure II.25) lies between 40 and 50° which also satisfies the targeted specifications and indicates an efficient management of the surface waves from the double ring integration. Indeed, side lobes remain lower than 12 dB on the whole frequency band.

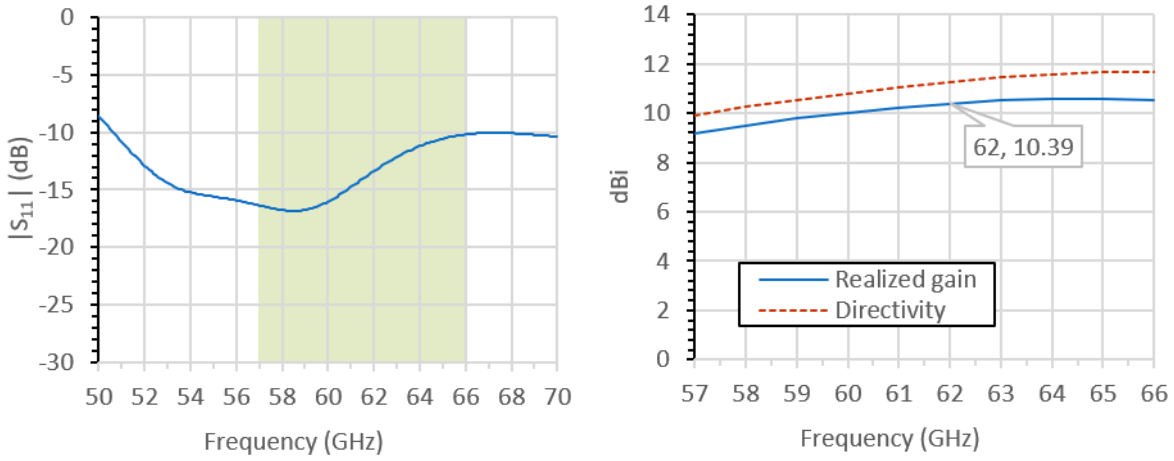

(a) (b)

Figure II.24 (a) Simulated $|S_{11}|$, (b) realized broadside gain and directivity of the 2×1 patch array on FR4-PCB from Figure II.23.

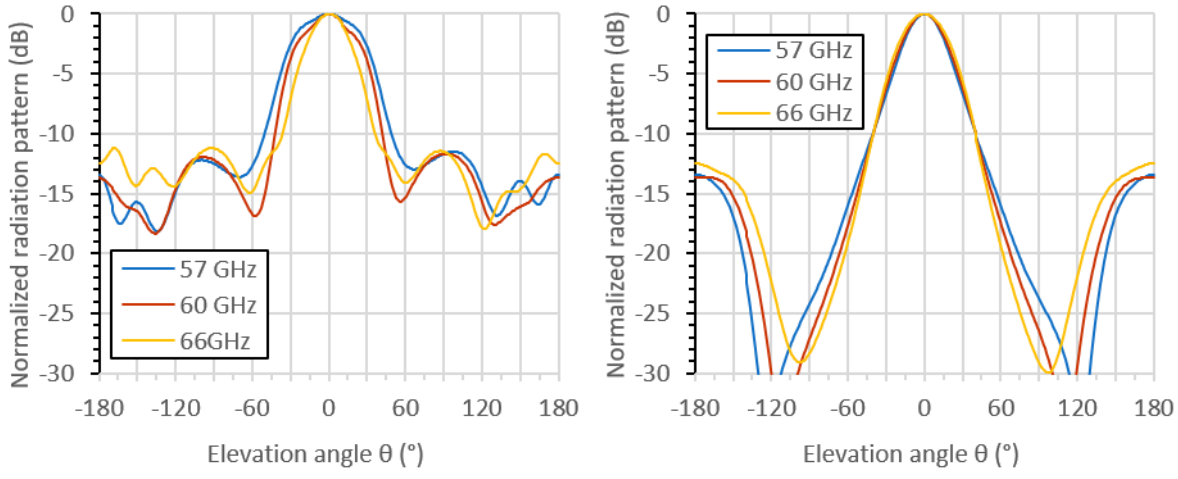

(a) (b)

Figure II.25 (a) Simulated normalized radiation pattern in E-plane (along y axis) and (b) H plane (along x-axis) of the 2×1 SCP array on PCB FR4.

Despite the fact that this antenna's simulated characteristics meet the fixed goals, more losses can be found in practice due the longer transmission lines needed to perform the power

division between the elements and giving that we might be under estimating the dielectric losses as was noticed from the single patch measurements. That's why we didn't proceed to the fabrication of this antenna for the first run, but it is strongly considered to be fabricated for the next fabrication run.

II.3 MS-TO-WG TRANSITION

The next step is to complete our antenna-design with a connection towards the transceiver to enable a full AiP solution. The most common solution is to use a coaxial cable as represented in Figure II.26 (a). Commercial connectors at 60 GHz are already available in the market like the SMPM precision connectors [II.27]. But according to our experience and after having conducted several measurements, such connectors exhibit high insertion losses (~ 3 dB) and are expensive when compared to FR4 board cost. Hence, we propose to use a built-in connection by means of a low-loss MS-to-WG transition (cf. Figure II.26 (b)).

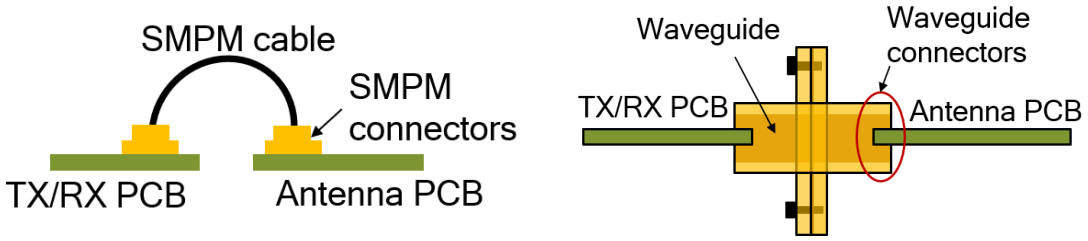

(a) (b)

Figure II.26 Connection between PCBs via (a) SMPM connection and (b) waveguide assembly.

II.3.1 Proximity coupling microstrip to waveguide transition

Our first proposed solution consists on designing a vertical MS-to-WG transition following the design of the planar proximity coupling transition reported in [II.28]. This transition, shown in Figure II.27 (a), can be composed of a single dielectric substrate positioned above the waveguide extremity. The conductor pattern with a notch (waveguide short) and the microstrip line are located on the upper plane of the dielectric substrate. A rectangular patch element and its surrounding ground are patterned on the lower plane of this dielectric substrate. Via holes are surrounding the aperture of the waveguide on the lower plane of the dielectric substrate to connect the surrounding ground and the waveguide short. Low insertion loss is achieved by transforming the quasi-TEM transmission mode into the TE_{10} fundamental waveguide mode with high efficiency utilizing the TM_{01} fundamental resonant mode of the patch, as illustrated in Figure II.27 (b). It was shown that this transition achieves a -10dB-impedance-bandwidth up to 20% (from 70 to 88 GHz) and an insertion loss lower than 1 dB [II.28].

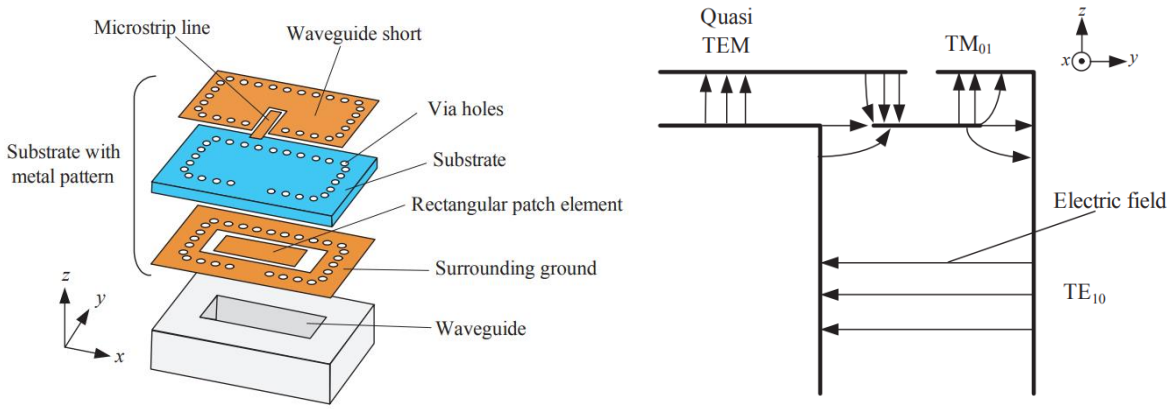

(a) (b)

Figure II.27 (a) Planar proximity coupling transition design proposed in [II.28]. (b) Transversal Electric field distribution in the yz-plane [II.28].

Hence, we optimized this design over V-band using an FR4 substrate. To integrate the antenna, we added a core and a prepreg build-up above the initial substrate in order to set the waveguide on one side and the antenna with associated radiation on the other side. This buildup corresponds to the three-layer buildup previously presented in Figure II.7 (a). The dimensions of the waveguide were chosen according to the dimensions of the standard WR15 waveguide, 3.759 mm × 1.88 mm, operating in single-mode between 49.9 to 75.8 GHz. The different metal layers of the optimized transition at V-band are illustrated in Figure II.28 and the position of the different metal layers is shown in Figure II.29 (a). Simulated insertion loss is below 2.4 dB, while the 10-dB impedance bandwidth is limited to 60 GHz to 66 GHz as demonstrated in Figure II.29 (b). The main difference between our design and the reference design is that the ground plane of the microstrip line is situated at M3 instead of M1. Hence this lowered the coupling between the waveguide and the line, consequently limiting the impedance bandwidth.

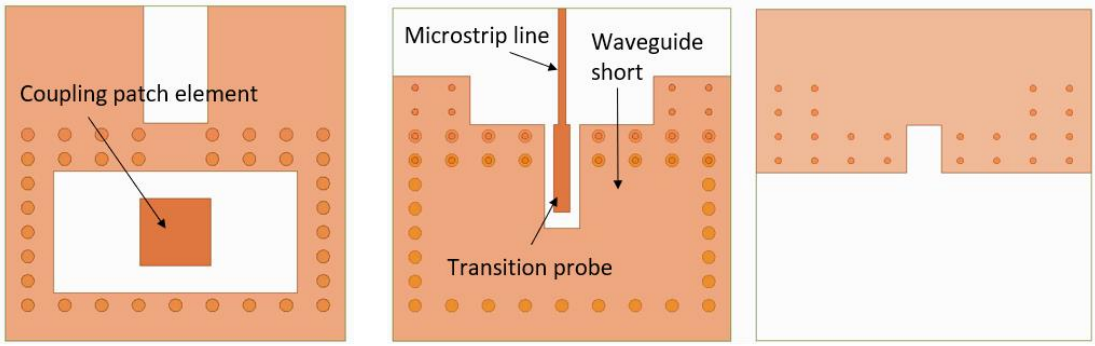

Figure II.28 Metallic layers of the proximity coupling vertical MS-to-WG transition optimized in V-band.

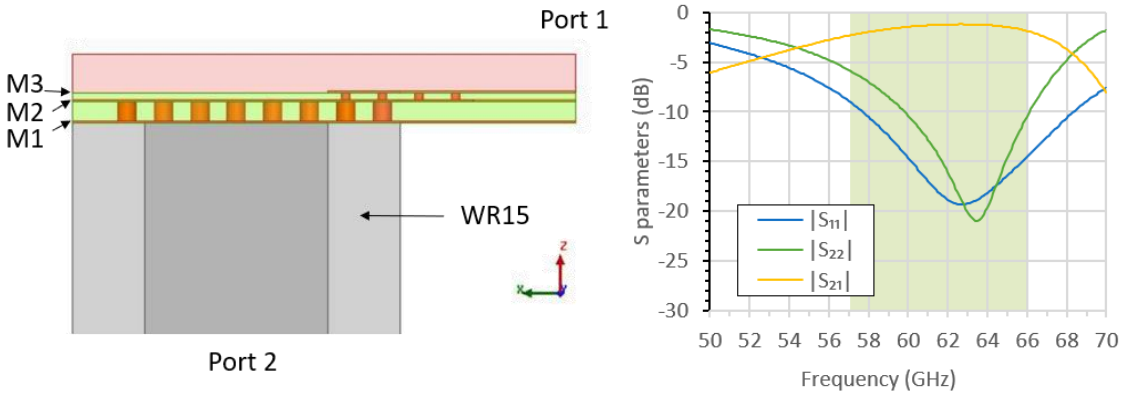

(a) (b)

Figure II.29 Profile view of the proximity coupling vertical transition (b) and corresponding simulated S-parameters in V-band.

Considering the simulation results it is unlikely to sustain a 10-dB impedance bandwidth over V-band using this MS-to-WG transition. Thus, we chose to adopt another kind of MS-to-WG transition, a horizontal fin-line antipodal transition [29] which is more promising in terms of impedance bandwidth and insertion loss.

II.3.2 Fin-line antipodal MS-to-WG transition

II.3.2.a Design and simulations

The reference design of the fin-line MS-to-WG horizontal transition is shown in Figure II.30 (a) and (b). The PCB with tapered antipodal fin-line is inserted in the standard WR12 waveguide structure in E-plane. The PCB has only one dielectric layer made out of Rogers (RO4003C). The metal via holes extend the waveguide walls inside the PCB structure along the length of the fin-line. This improves its reflection coefficient by eliminating the slot-mode excitation between two halves of the metal body.

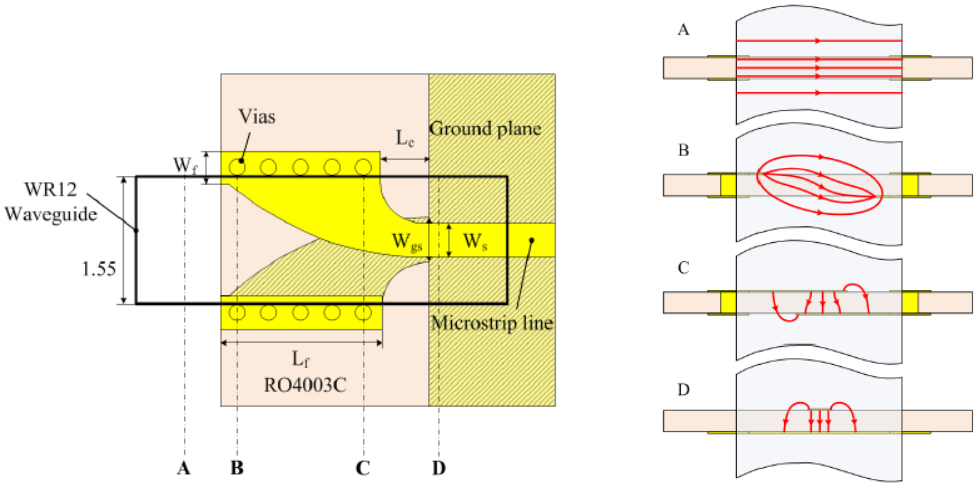

(a) (b)

Figure II.30 (a) Top view of the WG-to-MS fin-line antipodal transition (dimensions in mm) and (b) E-field transformation in different sections of the transition from [II.29].

The tapered antipodal fin-line smoothly transforms the incident TE_{10} (Figure II.30 (b), A cut) waveguide mode to a quasi-microstrip mode which is propagating in the area of overlapping antipodal fins of the transition (Figure II.30 (b), B and C cuts). E-field in the transition area concentrates and rotates by 90 degrees until the waveguide mode is transformed to the microstrip mode (Figure II.30 (b), D cut). Smooth transformation of all the field's mode allows the transition to operate on a wide frequency band. The fabricated Rogers (RO4003C) PCB back-to-back (BtB) fin-line transition with micromachined split-block waveguide is illustrated in Figure II.31 (a) and (b). Measurements of the fabricated back to back structure yielded a measured average loss close to 0.6 dB in E-band for a single transition (not including the loss in the microstrip line). Hence, this type of connection is much more performant in terms of losses compared to the SMPM coax connectors.

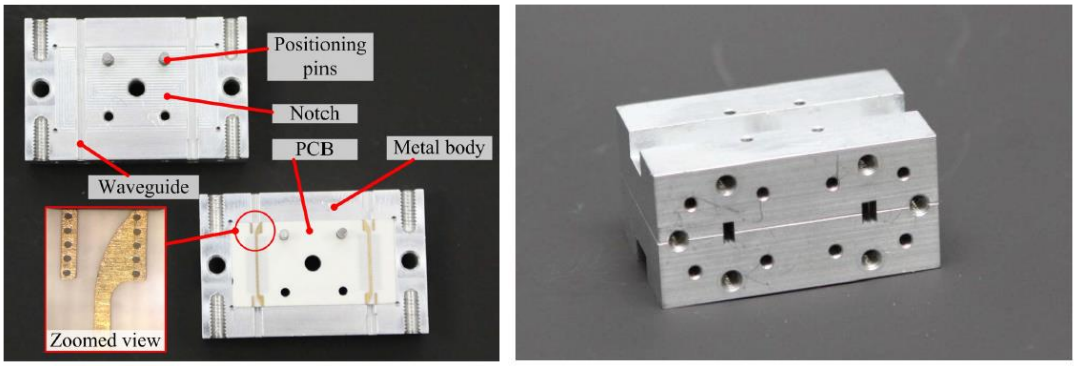

(a) (b)

Figure II.31 Picture of (a) the fabricated PCB and metal body of the back-to-back tapered antipodal fin-line WG-to-MS transition and (b) assembly in E-band [II.29].

This design was adapted and tuned for our two-layers FR4 PCB buildup (cf. Figure II.7 (b)). The parameters indicated in Figure II.30 were optimized to have the best matching and transmission performance in V-band while respecting the PCB design rules and are listed in table II.6.

Parameter	Lc	Lf	Ws	Wgs	Wf
Value (mm)	0.95	2	0.12	0.5	1

Table II.6 List of the optimized fin-line MS-to-WG transition parameters values optimized on V-band and using FR4 PCB substrate.

Figure II.32 shows the optimized design of the fin-line transition from microstrip to WR15 standard waveguide. The extremity of the waveguide facing the antenna was closed to limit any interference with its radiation. To avoid adding boundary limits than can modify the quasi TEM mode established along the microstrip line, a 0.3 mm × 0.3 mm squared hole was added around the microstrip line as shown in Figure II.32 (Face view). Simulated $|S_{11}|$ stays below -15 dB and simulated $|S_{21}|$ ranges between -0.6 and -1.2 dBi from 50 to 70 GHz (cf. Figure II.33), equivalent to 33% of relative bandwidth. A peak in the reflection loss was observed at port 2 (the waveguide port), which may be due to a standing created in the waveguide portion. Nonetheless, the obtained insertion loss level remains acceptable. It is also worth mentioning that the simulated insertion loss includes the loss of a 3 mm microstrip line.

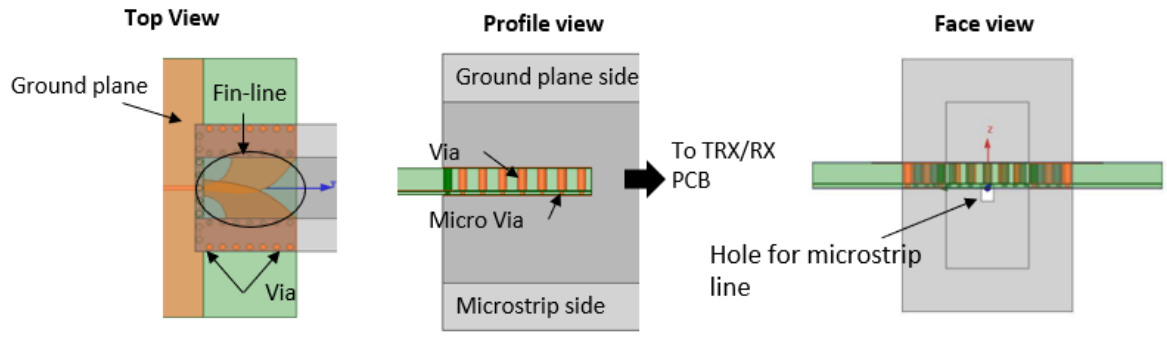

Figure II.32 Antipodal fin-line transition simulation model, top view, profile and face view.

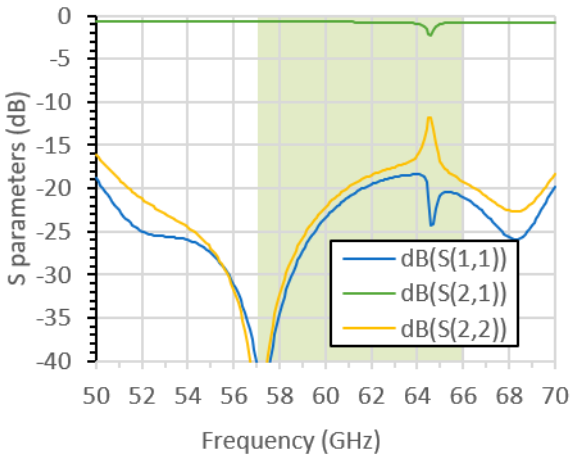

Figure II.33 Simulated S-parameters of the fin-line MS-to-WG transition, port 1 corresponds to the microstrip line port and port 2 corresponds the waveguide port.

Those low-loss and wide-band characteristics makes this transition a very suitable choice for being integrated with the antenna without considerably decreasing its efficiency or limiting its impedance bandwidth. Figure II.34 shows the simulated model of the single SCP antenna connected to the waveguide. The distance between the patch and the waveguide was optimized to limit any destructive radiation interference between the patch and the waveguide. Because the interference cannot be totally avoided, a dummy waveguide was added from the other side of the PCB to obtain a symmetrical structure and possibly a symmetrical radiation pattern in E-plane.

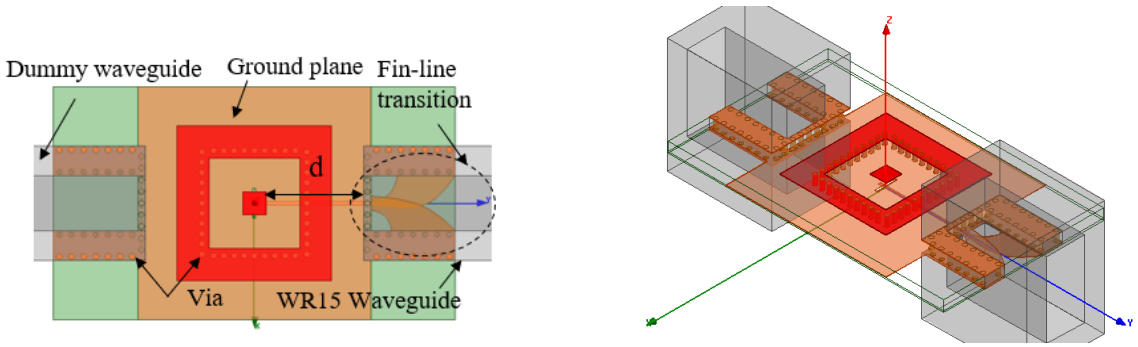

(a) (b)

Figure II.34 Fin-line transition integrated with the patch simulation model. (a) top view and (b) 3D view .

The simulated realized broadside gain (along z axis) of the antenna with transition is compared to that of the antenna alone in Figure II.35. The realized broadside gain wasn't significantly modified after adding the fin-line transition and stays between 8 and 9 dBi. In fact, the slight increase of gain seen at the beginning of the V-band can be reported to the fact that currents created on the surface of the waveguides in the vicinity of the patch are coupling with the radiation of the patch. Figure II.36 plotting the surface vector electric currents at 57 GHz illustrates this supposition.

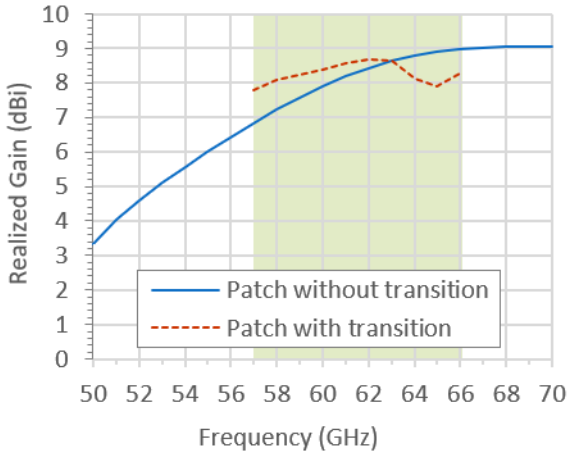

Figure II.35 Simulated realized broadside gain versus frequency of the fin-line transition integrated with the patch on the same FR4 PCB.

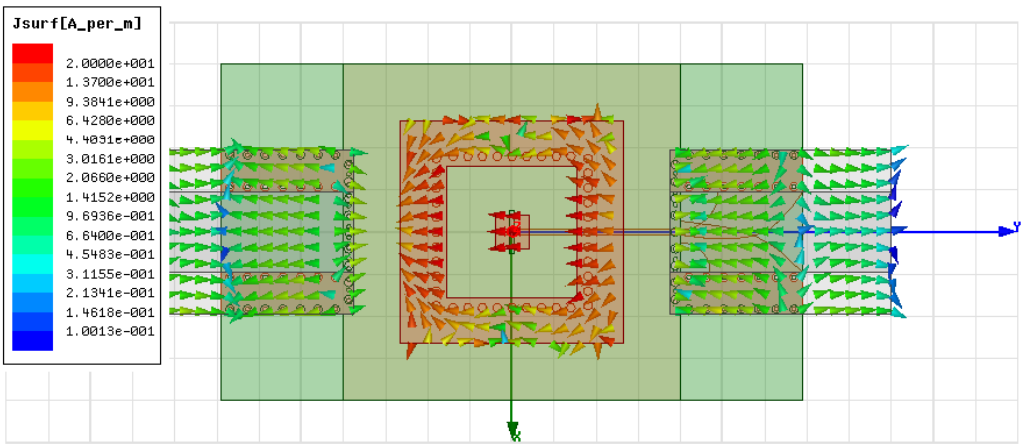

Figure II.36 Simulated vector surface currents at 57 GHz plotted on the patch, ring, and waveguide upper surface.

The radiation patterns in H and E-plane, plotted in Figure II.37 (a) and (b) respectively, show how the radiation patterns are still acceptable. The 10 dB-HBW stays between 45 and 60° in E-plane, and 45° and 75° in H-plane. Which is not so far from our goal. Moreover, we proved the usefulness and the good performance of this type of transition as the maximum simulated broadside gain loss of the antenna (after integration of the fin-line transition) is 1 dB.

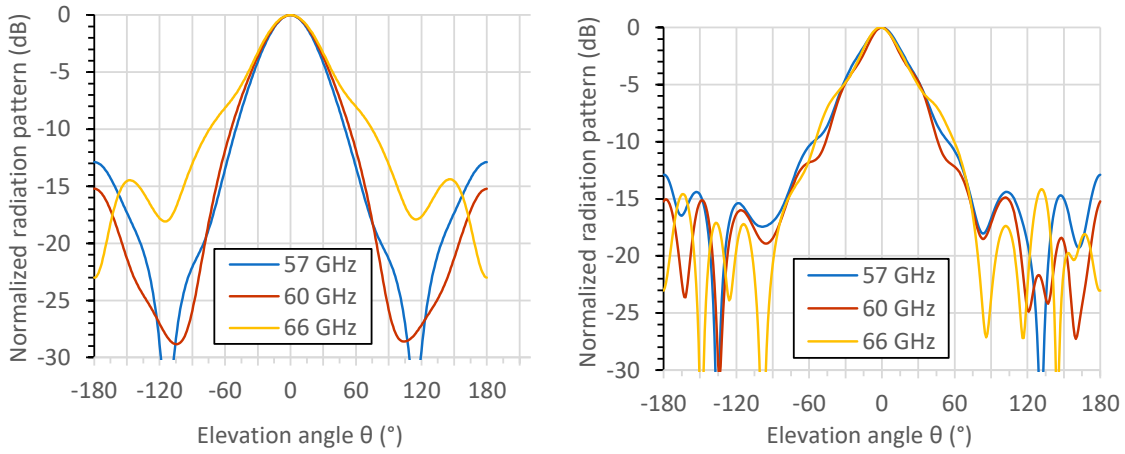

(a) (b)

Figure II.37 Simulated radiation patterns in (a) E and (b) H plane of the fin-line transition integrated with the patch on the same FR4 PCB.

II.3.2.b Fabrication of the SCP and MS-to-WG transition

For ease of assembly with the lens, we added waveguide H-bends to the patch and the waveguide structure. An H-bend distorts the magnetic field, by applying the bend around the thinner side of the waveguide (cf. Figure II.38). This shape of the waveguide's bend must have a radius greater than 2 wavelengths to prevent unwanted reflections and disturbance of the field [II.30]. The H-bends were designed following commercially available designs [II.31] and are illustrated in Figure II.39. Also, a connection between the flanges of the waveguide bends was added to ensure mechanical robustness.

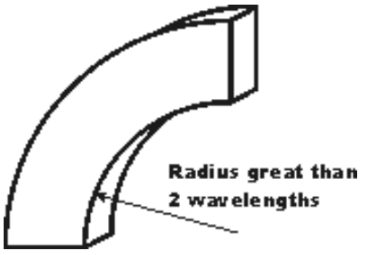

Figure II.38 Waveguide H-bend [II.30].

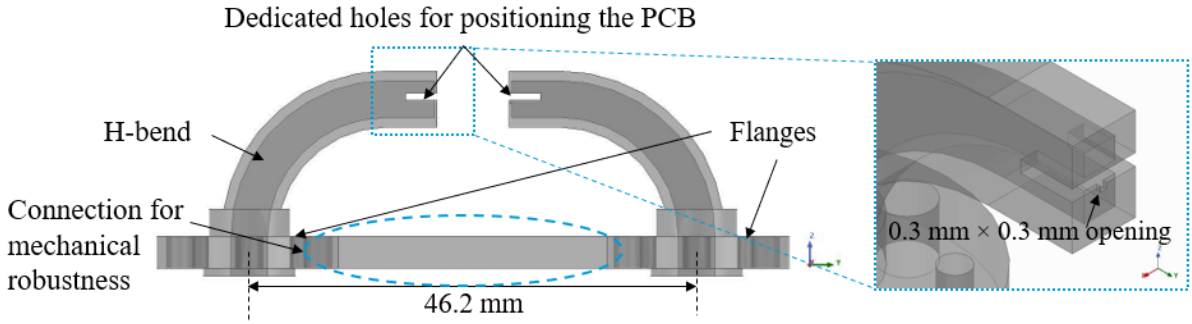

(a) (b)

Figure II.39 (a) Side view of the simulation model of the design of the waveguide H-bends and (b) detailed dimensions of the opening of the waveguide.

To fabricate the waveguide bends, we chose an additive manufacturing technique for easy, fast and cheap prototyping. The technique we chose is DMLS. Nevertheless, the main drawback of this method is the final surface roughness of the samples which might not be smooth without additional polishing (possible critical factor at mmW frequencies). As a matter of fact, the rough surface creates a longer path for the current to flow on it, thus increasing the ohmic losses of the conductor. This phenomenon is more pronounced at mmW frequencies due to the skin depth effect where most of the flow of the current occurs in extremely thin region beneath the surface of the conductor [II.32]. For example, by evaluating the skin depth δ at 60 GHz of aluminum using equation (II.10), we obtain 0.335 µm.

$$\delta = \sqrt{\frac{2\rho}{\omega\mu}} \qquad \text{(II.10)}$$

Where ρ is the resistivity of the conductor, ω is the angular frequency and µ the permeability of the material. On the other hand, the surface roughness expressed by Rq, a measure of the mean deviation of the height of the surface, can reach 35 µm [II.33] depending on the technology used, which is nearly hundred times the skin depth at 60 GHz. Hence, depending on the roughness obtained from the used technology, the attenuation loss in dB/m varies for each fabricated waveguide. Table II.7 summarizes some numerical results for waveguide prototypes fabricated by additive manufacturing technologies, pieces being either built out of a metallic material or coated by metal. Figures II.40 and II.41 illustrate the examples cited in Table II.7. For example the attenuation losses of the waveguide cited in [II.34] and [II.35] operating in W-band varies from 6.4 dB/m to 22 dB/m depending on the used technology. The DMLS gives the highest attenuation losses whereas printed pieces by digital light processing (DLP) and further post-metallized by electroless plating give the lower attenuation losses.

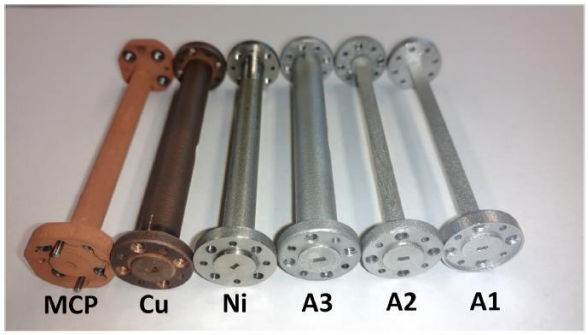

Figure II.40 Pictures of Straight WR10 waveguides implemented in a variety of materials. From left to right: metal (Cu) coated plastic (MCP), GRCop-84 (Cu), Inconnel 625 (Ni), and 3 AlSi10Mg with different DMLS laser settings [II.33].

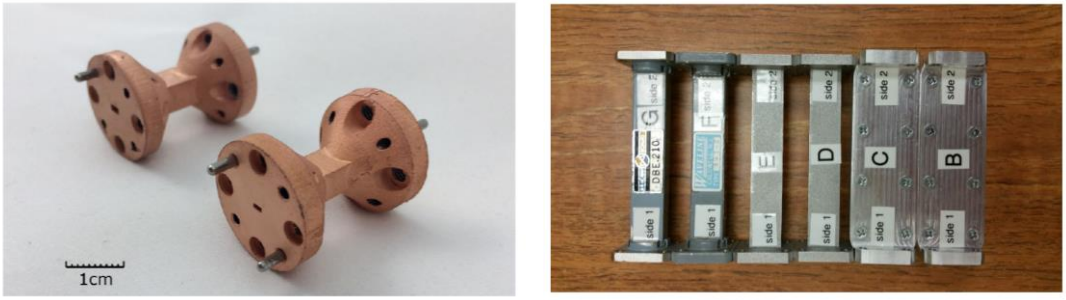

(a) (b)

Figure II.41 (a) Pictures of 3D printed D-band and W-band waveguides [II.34]. (b) Pictures of Waveguide test set consisting of two purchased, two fabricated by selective laser melting and two micromachined WR42 waveguide parts [II.35].

Ref	Printing and metallization technology	Frequency	Attenuation	Roughness Rq
[II.33]	DMLS AlSi10Mg	V-band (50 to 75 GHz)	11 dB/m	35 µm
		W-band (75 to 110 GHz)	10 to 22 dB/m	14 to 35 µm
[II.34]	DLP projector-based SLA + Electroless metallization process	W-band (75 to 110 GHz)	6.4 dB/m	NS
[II.35]	Selective Laser Melting (Aluminum)	K-band (18 to 27 GHz)	2.7 dB/m	5 to 11 µm

Table II.7 Performance of waveguide prototypes fabricated from different AM technologies and metallization techniques at different frequencies.

Our fabricated waveguides are depicted in Figure II.42 and II.43, using DMLS with AlSi10Mg powder:

- Back-to-Back (BtB) direct waveguide bends.
- BtB waveguide bends with slits dedicated to hold the PCB.

BtB bends were fabricated for calibration, to be able to assess the losses in the waveguide bends apart from the fin-line transition and the patch antenna. The flange contact faces were sanded to ensure good contact. Hand-machined screw threads and pinholes were used to improve the assembly quality. All the mechanical details and assembly of the designs presented in this thesis were realized with the help of Frederic Devillers under the collaboration with Orange Labs, Sophia Antipolis. In the same manner, to evaluate the losses of the fin-line transition independently from the antenna, we designed a BtB fin-line transition on a PCB of the same size of that of the antenna and transition to use with the same BtB waveguide bends with slits. BtB fin-line transition and single SCP with fin-line transition fabricated PCBs using Nelco® N4000-13 EP™ substrate are shown in Figure II.44 and II.45.

Figure II.42 Pictures of our fabricated samples for the back-to-back waveguide bends.

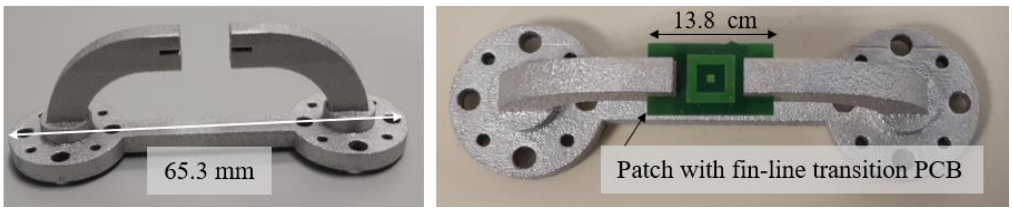

Figure II.43 Pictures of the fabricated samples of the back-to-back waveguide bends with welcome slit for the PCB.

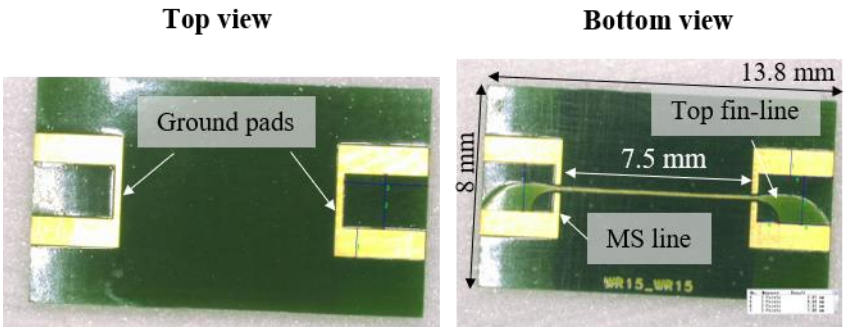

Figure II.44 Picture of (a) bottom view and (b) top view of the Fabricated BtB fin-line transition on FR4 PCB.

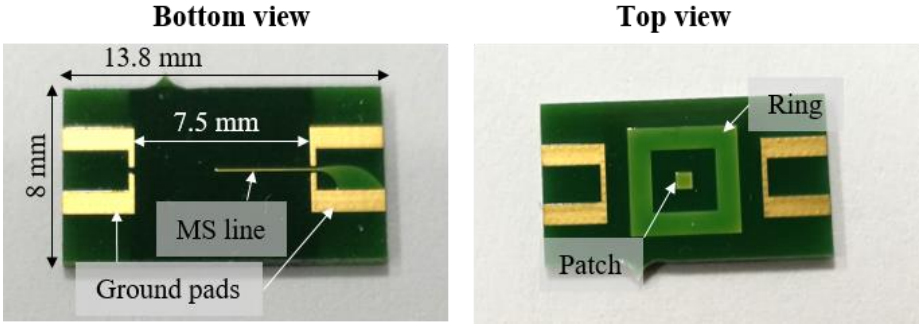

Figure II.45 Top and bottom view of the fabricated single patch with ring and fin-line transition.

II.3.2.c Measurements of the SCP fed by waveguide bends by means of the fin-line MS-to-WG transition

We conducted the measurements of the BtB waveguides bends and BtB fin-line transition after a two-port calibration using the WR15 calibration kit: HP V11644A. Overall, the measured insertion loss of the BtB waveguide bends from 50 to 67 GHz lies between 0.7 and 1.7 dB (cf. Figure II.46). Those measurements weren't compared with simulations, because simulation results indicated a very low insertion loss (under 0.1 dB). Hence, the measured losses are mainly due to reasons that were not taken into account in simulations like:

measurement precision, surface roughness, contact between flange, or the conductor ohmic losses.

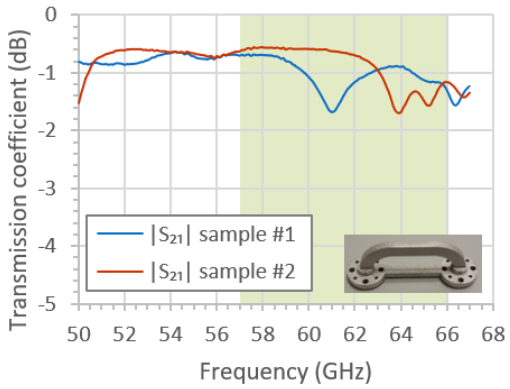

Figure II.46 Measured $|S_{21}|$ of two samples of printed BtB waveguide bends.

Measurements of the reflection and transmission coefficients of the BtB fin-line transition PCB inserted into the waveguide bends slits are plotted in Figure II.47 and II.48 respectively. Good measured matching level was obtained, $|S_{11}|$<-10 dB over all the bandwidth. Simulated and measured $|S_{11}|$ do not correlate because the simulation corresponds to a single transition with a straight waveguide of 2 mm length. Measured insertion loss of the whole structure stays between 5 and 7 dB in V-band. After subtracting the measured waveguide bends losses and dividing the obtained losses by two, a return loss between 2 and 2.8 dB is found for one transition without the waveguide bends and including the losses in the 3.75 mm microstrip line. Measured return loss is 1 to 2 dB higher than simulations. These results may also indicate an under-estimation of dielectric losses at the measurement frequencies.

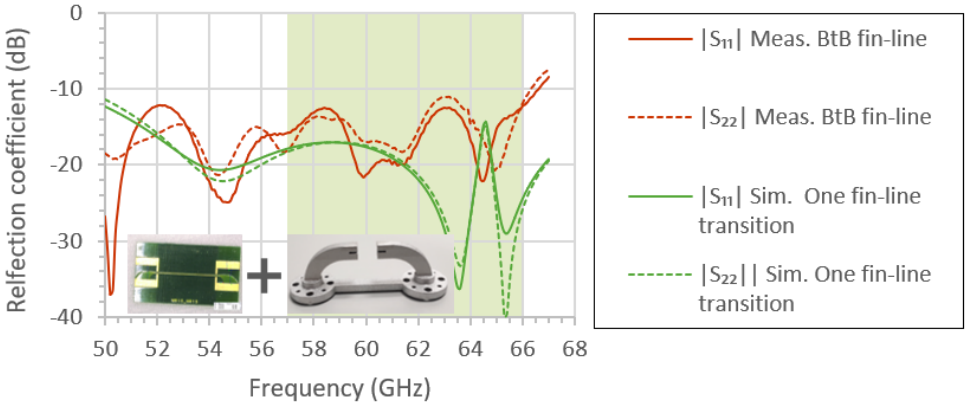

Figure II.47 Measured $|S_{11}|$ and $|S_{22}|$ of the BtB fin-line transition on FR4 PCB with two different printed waveguide bends samples.

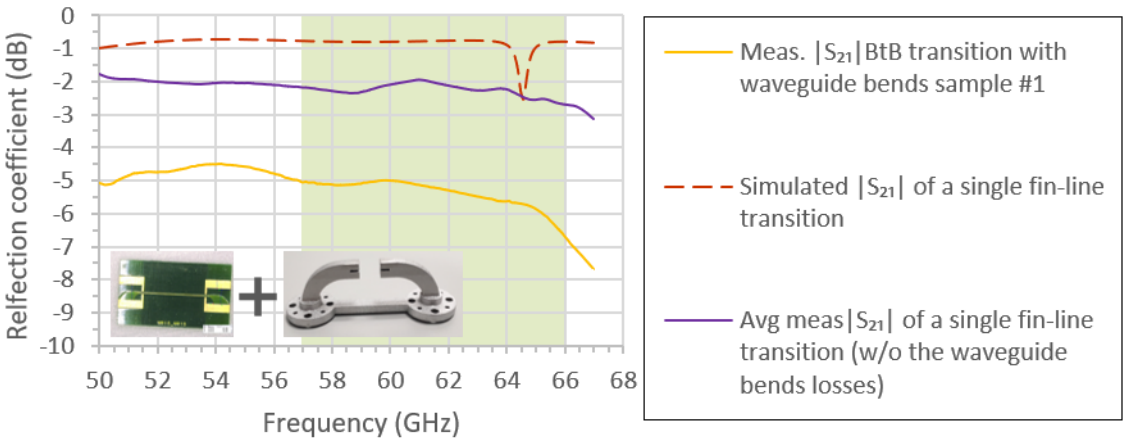

Figure II.48 Measured $|S_{21}|$ of the BtB fin-line transition on FR4 PCB with two printed waveguide bends samples.

After performing several measurements on different samples of the fin-line and the waveguide back-to-back structures, the average of all S_{21} magnitudes was calculated, then the maximum, minimum and average values over the frequency bandwidth were computed, results are listed in table II.8.

Frequency band: 50 to 67 GHz	**Max $\|S_{21}\|$**	**Min $\|S_{21}\|$**	**Avg $\|S_{21}\|$**
BtB waveguide bends	-0.6	-1.2	-0.7
BtB waveguide bends + BtB fin-line transition	-4.6	-5	-4.8
Single waveguide bend + single fin-line transition	-2.3	-2.5	-2.4
BtB fin-line without waveguide bends	-3.5	-4.3	-4
Single fin-line (including 3.75 mm MS line loss) without waveguide bend	-1.8	-2.1	-2

Table II.8 Averaged measurements of the $|S_{21}|$ of the printed BtB waveguide bends and BtB fin-line transition.

The average insertion loss of the single fin-line transition without the bends losses and including the loss in the 3.75 mm microstrip line is close to 2 dB. Simulation predict a 0.5 dB of loss in this line, hence finally the losses can be reduced to 1.5 dB approximately. The increased loss we obtain compared to the E-band fin-line transition presented earlier (presenting a 0.6 dB loss), can be explained by the roughness of the printed waveguides compared to micromachined ones and the higher losses of the Nelco® N4000-13 EP™ ($\tan\delta$=0.008 at 10 GHz) compared to Rogers RO4003C ($\tan\delta$=0.003 at 10 GHz). However, our results are still acceptable considering the ease of prototyping and the low-cost materials being used.

Next, we conducted the measurements of the single SCP with the designed MS-to-WG transition integrated on the same PCB and inserted in the waveguide bends dedicated slits. Measured broadside realized gain stays between 4 and 5 dBi from 54 to 61 GHz. However,

starting from 62 GHz the gain decreases and reaches 2 dBi at 66 GHz (cf. Figure II.49). Comparing the measured gain of the SCP with fin-line transition and the SCP fed by probe, the broadside realized gain remained almost the same at the beginning of the V-band and starts to drop after 62 GHz. From 50 to 62 GHz it seems that the integration of the MS-to-WG transition and waveguide bends didn't add any additional losses. At 64 GHz a maximum loss of 2 dB is observed. This observation can be explained by the fact that the edges of the waveguide is interfering constructively with the radiation of the patch increasing the whole directivity of the radiation, hence compensating the fin-line transition and waveguide bends losses as was illustrated in Figure II.36. The measured XPD level in broadside is stable at 20 dB from 50 to 56 GHz and increases to 25 dB at the end of V-band. Radiation patterns are traced in Figure II.50 in E and H plane at 60 GHz. We can still see high side lobes' level close to θ = 80°, especially in H plane. The measured -10 dB-HBW is close to 50° in E-plane and 60° in H-plane.

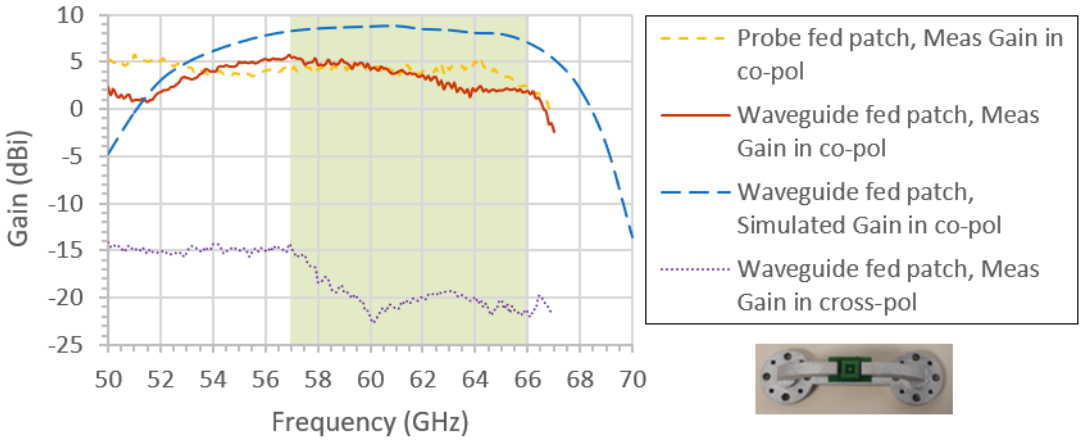

Figure II.49 Simulated and Measured broadside realized gain in co-pol and cross-pol of the of the SCP integrated with the fin-line transition PCB inserted in the waveguide bends slit.

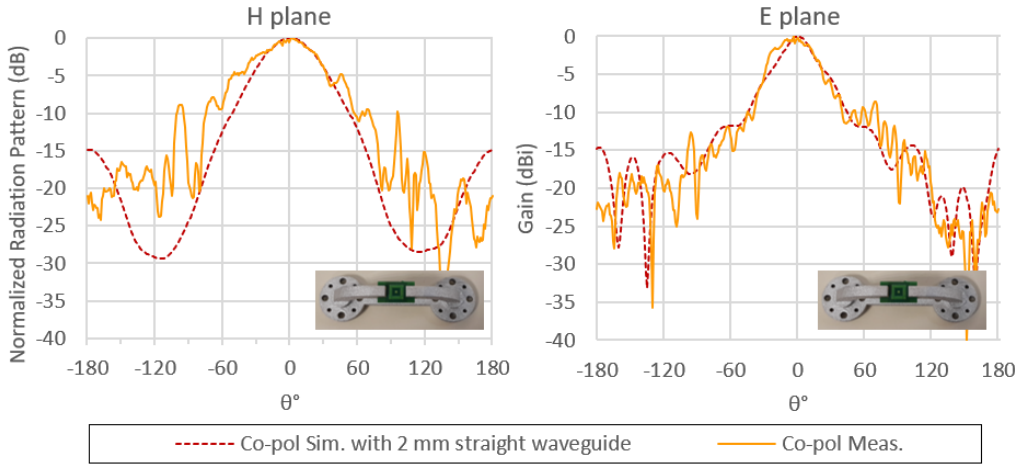

Figure II.50 Simulated and measured broadside realized gain in H and E planes versus the azimuth angle θ at 60 GHz of the SCP integrated with the fin-line transition PCB inserted in the waveguide bends slit.

Fair correlation is found between measured and simulated radiation patterns but many ripples can be noticed. Possible explanations of the distorted radiation patterns are:

- Excessive surface waves diffracted from the edges of the PCB and contributing to the whole radiation process.
- Currents that can be induced on the surface of the waveguide bends interfering with the patch radiation.

Despite the interference with the radiation of the antennas that was observed after integrating the fin-line transition, the measured performance remains acceptable and competitive with high-end commercial solutions like the SMPM connector.

II.4 EXTENDED ELLIPTICAL LENS

II.4.1 Extended Elliptical Lens Design

Fulfilling our goal to obtain a low-cost 30 dBi broadside realized gain antenna for backhaul applications, we use the aforementioned PCB antennas as a source of a single material elliptical lens [II.36]. Elliptical lenses are commonly used to collimate radiated beams. When the source is placed at the ellipse focal point, theoretically, all rays emerging from the lens surface are parallel to the lens axis, hence increasing the directivity of the source. Generally, low-loss plastics like high-density polyethylene is used for mmW lenses [II.37]. However, these materials are not commonly used in 3D printing and their use is limited for selective laser sintering methods. Thus, we chose a more common and cheaper material: ABS-M30 plastic. To print the lens, an in-house HP Designjet 3D printing machine was used with an ABS-M30 plastic filament having a diameter of 178 µm and employing the (FDM) 3D printing technique. The complex permittivity of the ABS-M30 at 60 GHz was estimated by using a open Fabry-Perot resonator as described in [II.38]. This method was implemented by the Instituto Universitário de Lisboa team (ISCTE-IUL, Pr. Jorge R. Costa) and the computed value was found to be $\varepsilon_r = 2.39 - j0.0164$, ($\tan\delta = 0.007$). Those parameters are important to finely optimize the lens shape.

For our application, we used an extended elliptical lens configuration consisting of a half of ellipsoid with radius a and b along the x and z axis, respectively (cf. Figure II.51 (a)). The half ellipsoid is extended by a cylindrical shape of height L and has a cylindrical symmetry around the z axis. The radius "a" of the lens is chosen depending on the desired directivity:

$$Dir[dB] = 20Log_{10}(\frac{2\pi a}{\lambda_0}) \quad \text{(II.11)}$$

Where λ_0 is the wavelength in free space at the operating frequency. Choosing 'a' leads to set b and then L by applying the following formulas, if ε_r has been chosen beforehand:

$$b = \frac{a}{\sqrt{1 - 1/Real(\varepsilon_r)}} \quad \text{(II.12)}$$

$$L = b/\sqrt{Real(\varepsilon_r)} \quad \text{(II.13)}$$

As we aim for a gain close to 30 dBi, we chose a = 5 cm corresponding to a directivity of 36 dBi at 60 GHz. Choosing a = 5 cm, implies that b = 6.5 cm and L = 4.1 cm. The dissipation loss in the dielectric can be computed using (II.13),

$$Loss[dB] = 27.3\sqrt{Real(\varepsilon_r)}(L+b)tan\delta/\lambda \quad \text{(II.14)}$$

Where (L+b) correspond to the height of the lens and tan δ the dissipation factor. For a = 5 cm, and the wavelength λ at 60 GHz a loss of 6.3 dB is computed. Which situates the gain of the lens at the limits of 30 dBi gain at 60 GHz.

To further increase the gain, one approach likely to be used consists on increasing the lens size, but this is not an efficient method as the dielectric losses will increase as well. A simpler way to increase the gain without increasing the size of the lens is to chop its interior resulting in a dome-type elliptical lens with air below it, as shown in Figure II.51 (b). In this way, the dissipation losses are reduced, compared to a plain lens, without reducing the directivity of the lens. The inner shape of the lens is chosen to be also an extended elliptical geometry. To ensure that no reflections will occur on the air-lens interface inside the lens and the outer plastic, the contour of the inside was optimized using the Genetic Algorithm routine in the ILASH tool [II.39]. ILASH is a software tool developed by the Instituto Universitário de Lisboa (ISCTE-IUL) for the design, analysis and optimization of circular symmetric integrated lens using Geometrical Optics/Physical optics (GO/PO) analysis. We were also able to benefit from the expertise of ISCTE-IUL team in lens design field to optimize the geometry of the lens. The optimized dimensions of the lens are depicted in Table II.9. Figure II.51 (c) shows the ray traces coming from an ideal source placed at the focal point of the lens to demonstrate how the lens collimates the source's rays. The dielectric losses of the dome elliptical lens are hence given by,

$$Loss[dB] = 27.3\sqrt{Real(\varepsilon_r)}((L+b)-(d+M))tan\delta/\lambda$$

Yielding 3.5 dB, this geometry enabled to reduce the dielectric loss by approximately 3 dB.

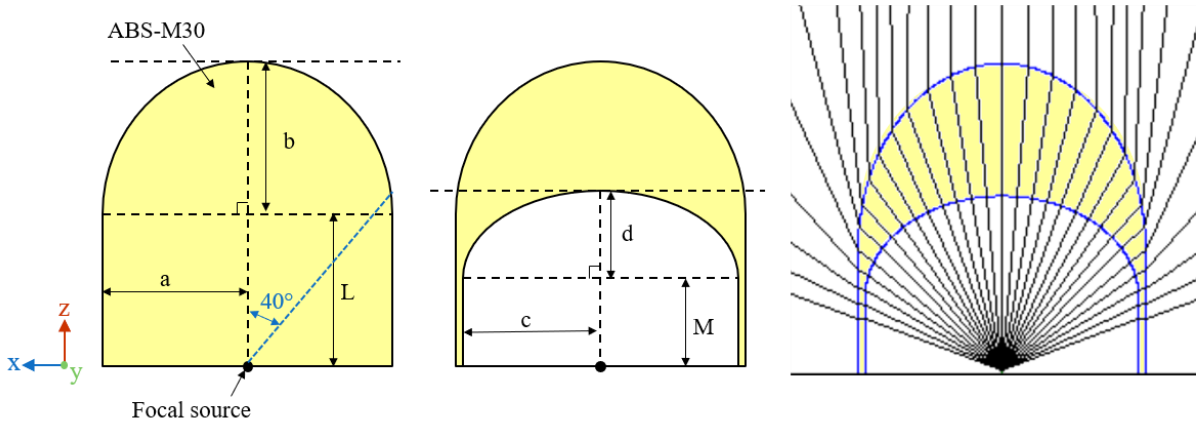

(a) (b) (c)

Figure II.51 Side view of the (a) plain extended elliptical lens design, (b) the chopped elliptical lens design and (c) ray traces analysis of the chopped elliptical lens calculated by ILASH.

Parameter	a	b	L	c	d	M
Value (mm)	50	64.72	41.09	48	32.5	26

Table II.9 Dimensions of the chopped elliptical ABS-M30 lens (optimized at 60 GHz).

It was demonstrated that the best coupling levels between the lens and the source are obtained with gaussian sources [II.36]. Hence, using ILASH tool we plot the evolution of the directivity of the presented lens versus the -10dB-HBW of an ideal gaussian source in Figure II.52 (a). The directivity of the gaussian source versus its -10dB-HBW is also plotted in Figure II.52 (b).

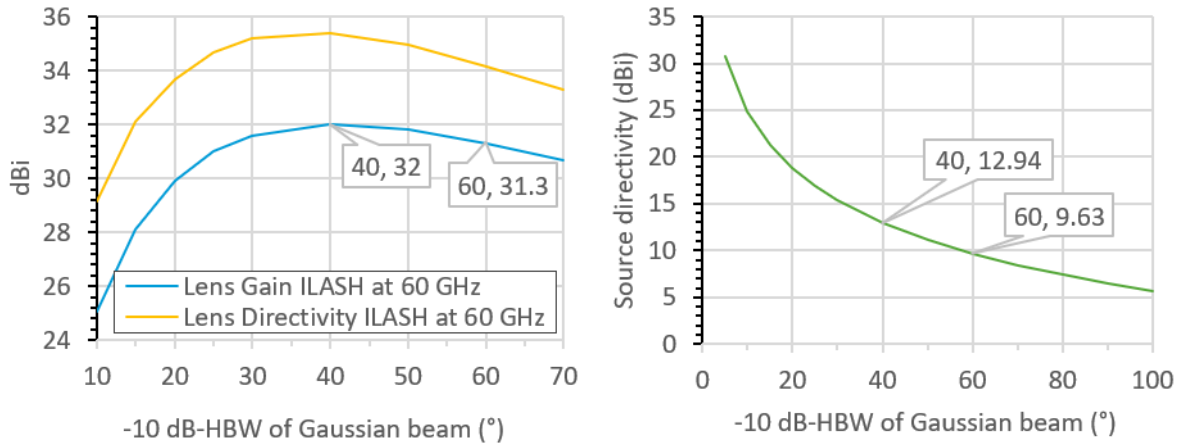

(a) (b)

Figure II.52 (a) Simulated broadside realized gain and directivity of the chopped elliptical lens versus the -10 dB HBW of a gaussian beam source simulated on ILASH and (b) corresponding directivity of the source.

The maximum directivity of the lens is obtained at a -10dB-HBW of 40°, corresponding to a source directivity of 13 dBi. A narrower beamwidth (equivalent to increasing the directivity) leads to an un-efficient use of the lens surface decreasing the directivity of the lens due to under-illumination. Seamlessly, a wider beamdwidth (equivalent to decreasing the directivity) will decrease the directivity of the lens because of the spill-over effect which can lead to increase the side-lobes level. Still, a beamwidth reaching 60 or 70° can also be acceptable since no significant drop in gain is observed. Following these results, we can fix the specifications of the source to a directivity between 10 and 13 dBi and a gaussian-like -10 dB-HBW between 40 and 60°.

II.4.2 Extended elliptical lens with the SCP source

II.4.2.a Simulations

Simulations of the designed elliptical dome-lens with two different sources, the single SCP antenna and the 2×1 SCP antenna on PCB presented in II.3 were performed using PO/GO ILASH analysis tool and the full electromagnetic simulation of CST (the latter was performed by ISCTE-IUL team). Figure II.53 shows the corresponding full electromagnetic simulation models. The simulated directivity and broadside realized gain obtained by ILASH and CST for

the single and 2×1 SCP sources are shown in Figure II.54. It should be noted that the gain obtained by ILASH don't include the losses in the sources. Hence the difference found between directivity and gain computed by ILASH correspond mainly to dielectric loss and illumination efficiency and was found around 2 to 4 dB for both the 2×1 and the SCP. The simulated broadside realized gain by CST of the lens fed by the single patch source is found to be close to 28 dBi along V-band, which is to 2 to 3 dB lower than that obtained by ILASH. Whereas that of the lens fed by the 2×1 source ranges between 28.5 and 30 dBi, which is closer to ILASH gain but still, a maximum difference of 3 dB was found between both gain simulations.

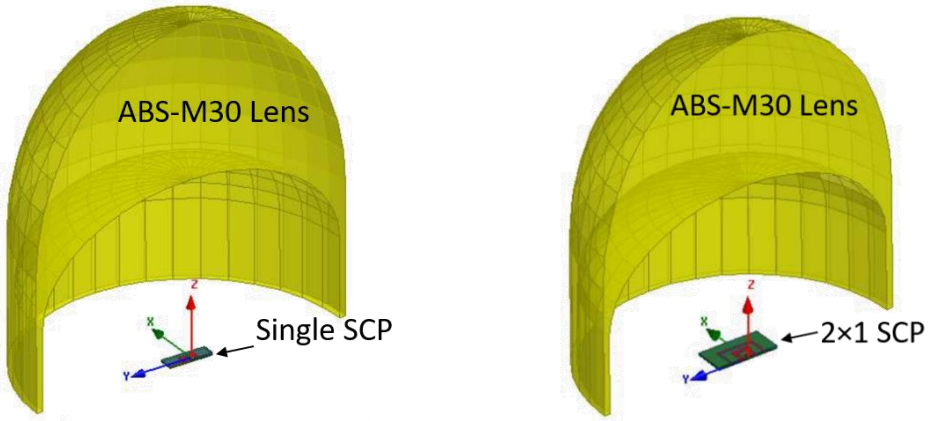

(a) (b)

Figure II.53 Simulation model of (a) the SCP single and (b) 2×1 source illuminating the dome elliptical lens (cut in ZY plane).

This difference between the gain simulated by ILASH and that of CST, is related to the internal loss of the source antennas like dielectric losses. Additionally, it is also related to the electromagnetic phenomenon that occur on the lens surface like the surface wave effect which cannot be taken into consideration by ILASH. Since no significant gain improvement was observed by using the 2×1 source (especially that the gain difference falls into the uncertainty range of the measurement system: +/-0.8 dB). We finally chose to only prototype the single patch source. The simulated normalized radiation patterns in E and H planes of the lens with the single SCP source performed by CST are illustrated in Figure II.55. Radiation patterns both in E and H-plane present side lobes below -10 dB and a -3 dB beamwidth of approximately 3°. ETSI 47-66 class 2 is respected in both planes at all frequencies however the ETSI 47-66 class 3A is not met especially in E-plane.

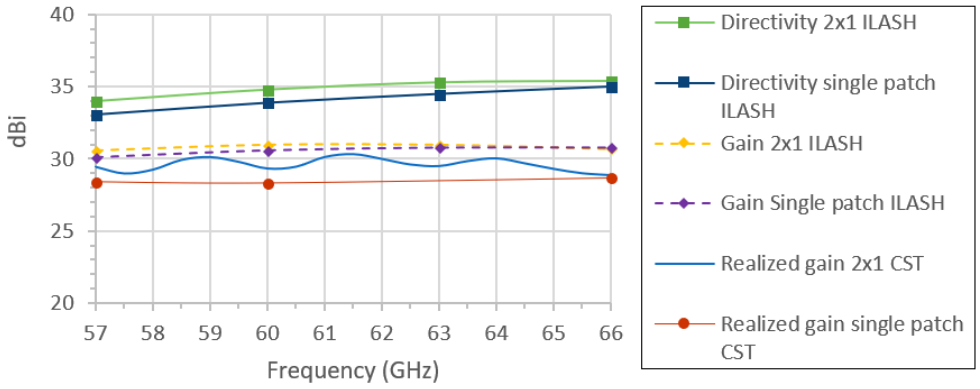

Figure II.54 Simulated directivity and realized gain in the broadside direction (along z) the lens with the single patch source and the 2x1 patch array source.

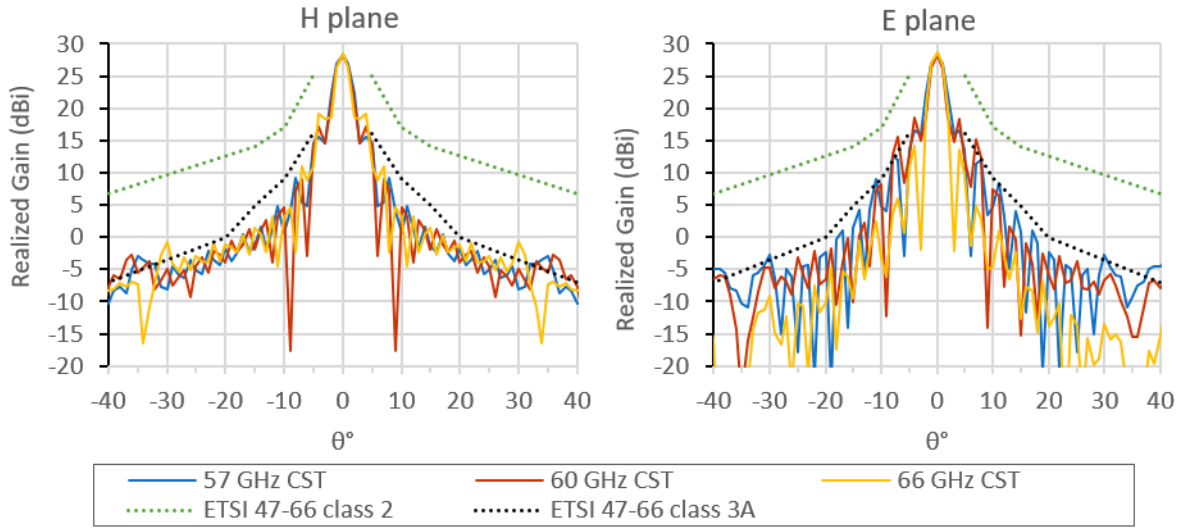

Figure II.55 (a) Simulated Gain in H-plane (along x) and (b) E-plane (along y) of the lens being illuminated by the single SCP source and comparison with ETSI 47-66 class 2 and 3A.

In order to measure the lens being illuminated by the patch, a dedicated plastic support with a foam holder for the source antenna was fabricated. The lens and support were 3D printed by the HP FDM printer using ABS-M30 filament, and the foam was machined, these parts are shown in Figure II.56. The plastic support and the lens are simply assembled by 4 screws.

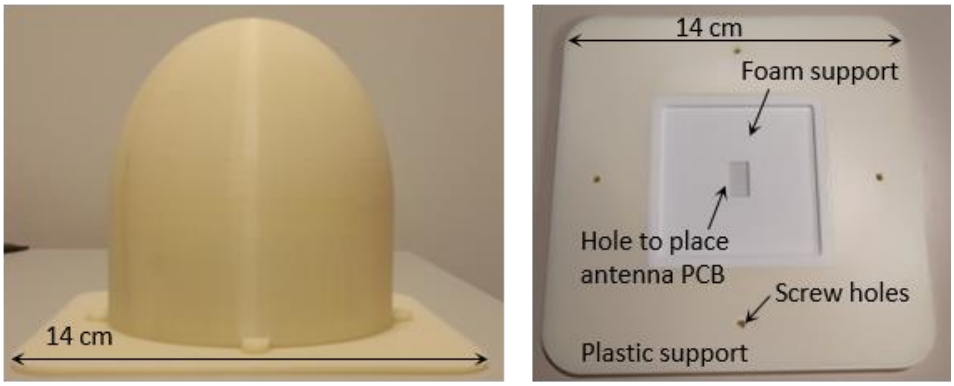

Figure II.56 Pictures of the chopped elliptical lens (left) and the plastic base with foam holder to place the PCB source antenna (right).

However, our measurement system is limited to phase-less measurements at a distance of maximum 80 cm between the AuT and the receiving probe-horn. Whereas the FF of this lens antenna is beyond the distance D_{FF},

$$D_{FF} = \frac{2d^2}{\lambda_0} = 4\ m \tag{II.2}$$

Where d is diameter of the lens equal to 10 cm and λ_0 the wavelength in free space at 60 GHz. Hence, the measurements of this lens cannot be achieved in FF region directly. On the other hand, the reactive NF limits are at a distance:

$$0.62\sqrt{\frac{D^3}{\lambda}} = 27.7\ cm \tag{II.3}$$

Therefore, one possible approach was to perform measurements in NF and then transform the measurements into FF by applying a phaseless NF-FF transformation. The implemented method is discussed in the next section.

II.4.2.b Near-field to far-field phaseless transformation

In this section we present the implementation of a NF-FF phase-less transformation based on the sources reconstruction method by members of Oviedo University [II.40]. This method was used and applied on NF measurements realized on the 60 -120 GHz bench measurement system in the context of a collaboration with members of Oviedo university.

The numerical application of this method relies on the minimization of a cost-function which relates the measured NF to a set of equivalent currents on a surface enclosing the antenna (cf. Figure II.57). Afterwards, the FF is calculated from the estimated equivalent currents. The main advantage of this method is that it can be applied to arbitrary surfaces. In order to estimate the phase of measured NF, it exploits the variation of the NF pattern with the distance, yielding the need of performing the field acquisition at least around 2 surfaces (R1 and R2).

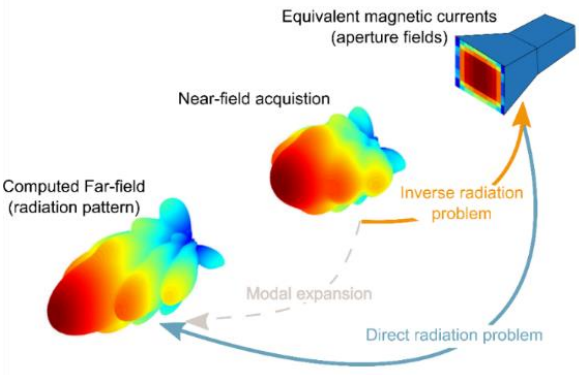

Figure II.57 Steps of the NF-FF transformation method based on the sources reconstruction method.

One of the crucial parameters for the accuracy of this method is the sampling step requirements in NF phase-less acquisitions, related to the radius of the minimum sphere enclosing the sources R_{min} (cf. Figure II.58 (a)). The angular steps along azimuth and elevation,

$\Delta\phi$ and $\Delta\theta$ respectively are expressed in function of R_{min} and the minimum wavelength of the measurement frequency bandwidth λ_{min} by the following equation:

$$\Delta\phi = \Delta\theta = \frac{\lambda_{min}}{4R_{min}} \quad \text{(II.4)}$$

In our case, considering R_{min} = 10 cm and λ_{min} evaluated to 4.5 mm at 66 GHz yields $\Delta\phi = \Delta\theta = 0.01125\ rad \cong 0.7°$, which was respected in our measurements. Another key element to consider is that for truncated NF acquisitions: FF is only valid inside an angular margin θ_{ff} (cf. Figure II.57 (b)):

$$\theta_{ff} = \theta_t - \sin^{-1}\left(\frac{R_{min}}{A}\right) \quad \text{(II.5)}$$

where A is the measurement distance and θ_t is the angular range of measurement. Hence, considering the lens dimensions and the angular range of measurements limited to -25 to 30° in E-plane and to -40 to 40° in H plane due to mechanical reasons, the angular margin of validity of our measurements would be approximately between -10 and 10°.

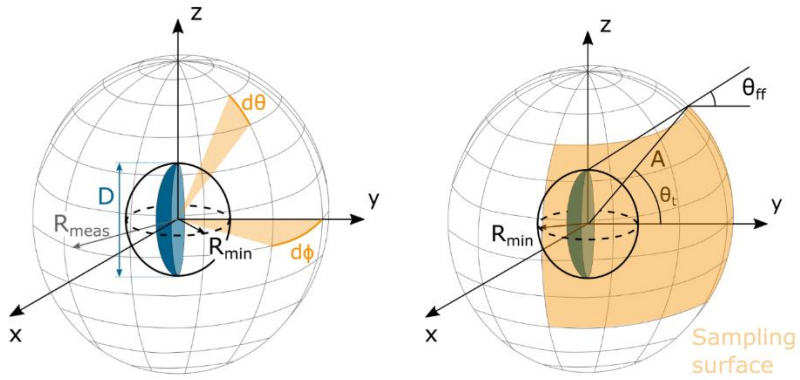

(a) (b)

Figure II.58 (a) Sampling requirement for the NF-FF phase-less transformation and (b) angular margin of valid FF estimated from the NF-FF phase-less transformation.

In the context of a post-doc mission in Polytech'lab, a Matlab program was especially developed by Dr. Ana Arboleya for applying this NF-FF transformation based on NF phase-less measurements. The Matlab code was developed along with a user-friendly graphical user interface (cf. Figure II.59). This program will be used for calculating the FF radiation patterns of the NF measurements in the next sections.

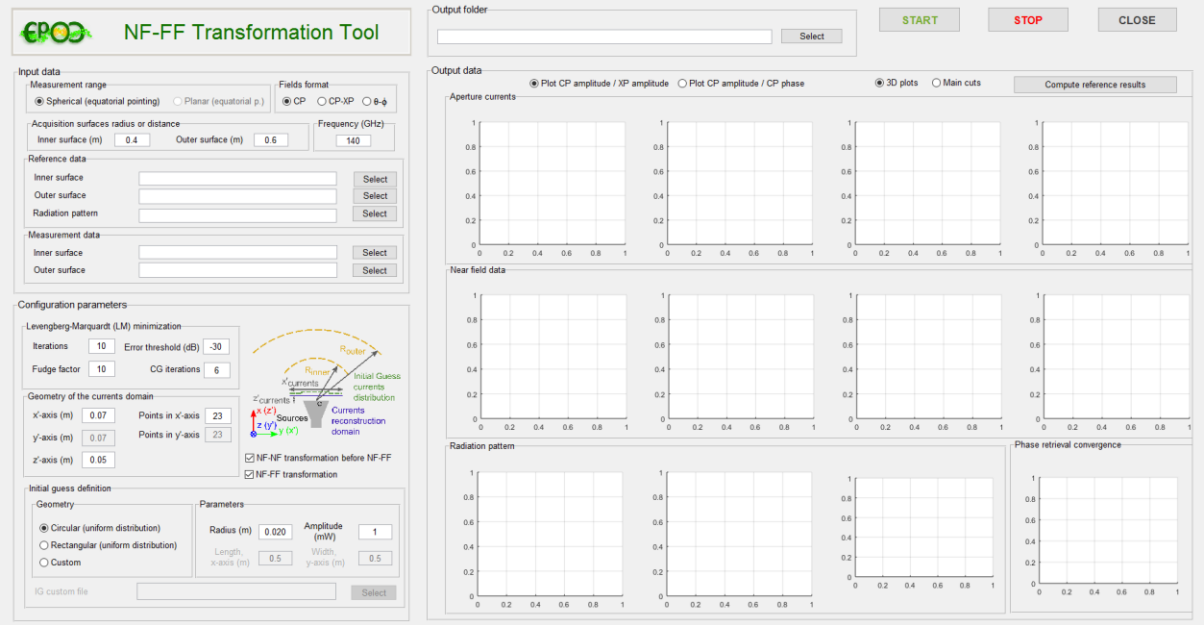

Figure II.59 GUI of the matlab code of the NF-FF phaseless transformation developed by Dr. Ana Arboleya.

II.4.2.c Measurements of the extended elliptical lens with the SCP source

We conducted the lens antenna measurements using the aforementioned measurement system, with the patch source being fed by a coplanar GSG probe with a 200 µm pitch (cf. Figure II.60). The conducted measurements were performed in NF at two different distances: 60 and 80 cm to be able to apply the NF-FF transformation method presented in II.4.2. A picture of the measurement bench configured at 60 cm distance is illustrated in Figure II.61. The simulated and measured $|S_{11}|$ of the PCB source with and without the lens are plotted in Figure II.62. After adding the lens, ripples and oscillations appear in $|S_{11}|$ mainly due to the reflections on the lens inner and outer surface. A frequency shift is noticed between the measured and the simulated $|S_{11}|$ of the source antenna with the lens: this may be due to the imprecision of the simulated patch source due to fabrication tolerances. Still, the matching level is acceptable with a return loss > 8 dB between 54 and beyond 66 GHz.

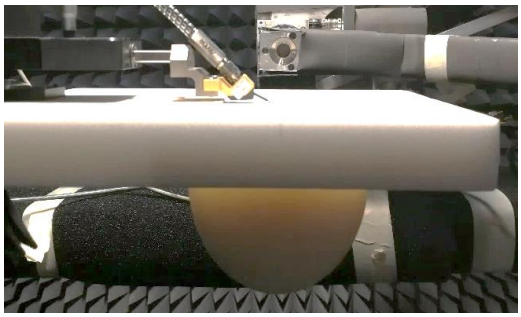

Figure II.60 Picture of the dome-type elliptical lens with the patch source fed by a coplanar GSG probe.

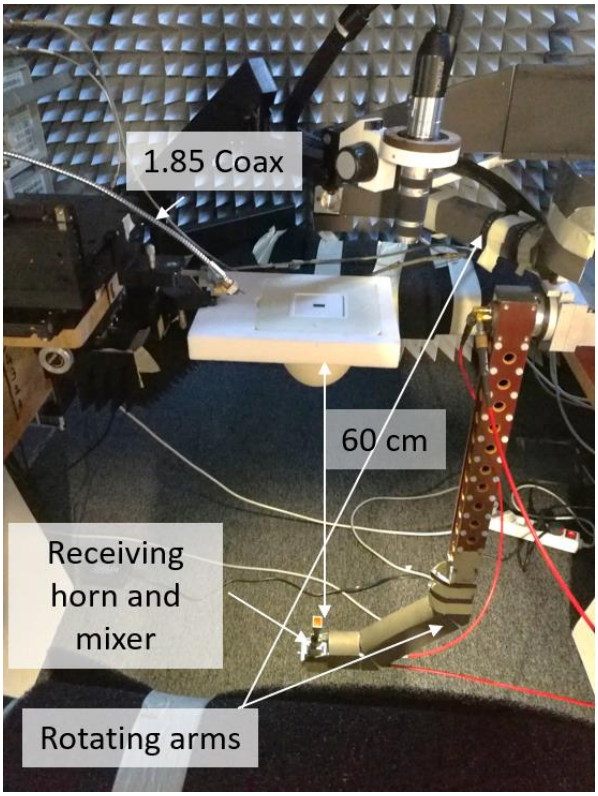

Figure II.61 Picture of the measurement bench configured at 60 cm distance.

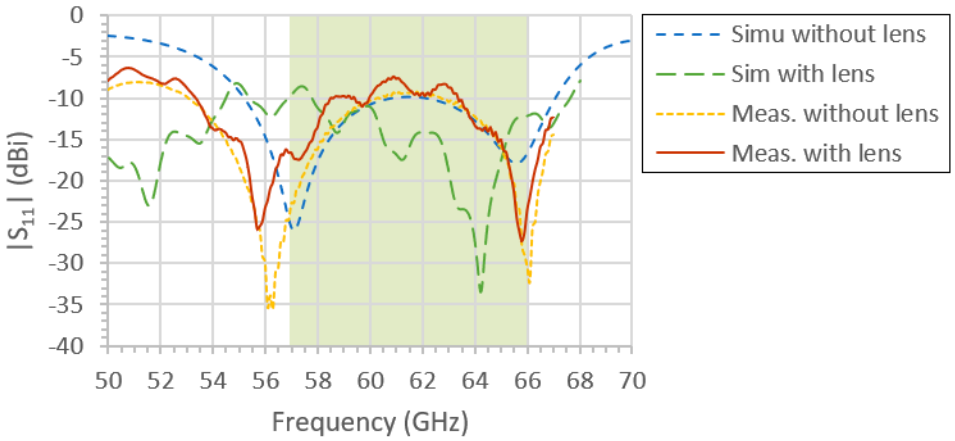

Figure II.62 Simulated and measured $|S_{11}|$ of the SCP source with and without the lens.

The measured realized broadside gain at 60 and 80 cm, plotted in Figure II.63, was found to be much more less than FF gain (28 dBi), ranging between 8 and 14 dBi. This was indeed a disappointing result, even in the NF region. The measured radiation patterns in E and H plane (cf. Figure II.64) were coherent with the measured gain, presenting a much wider beamwidth than the simulated FF one (20° at –3 dB) even if it's not completely fair to compare NF and FF data. Applying the NF-FF transform to those measurements didn't yield a more directive beamwidth.

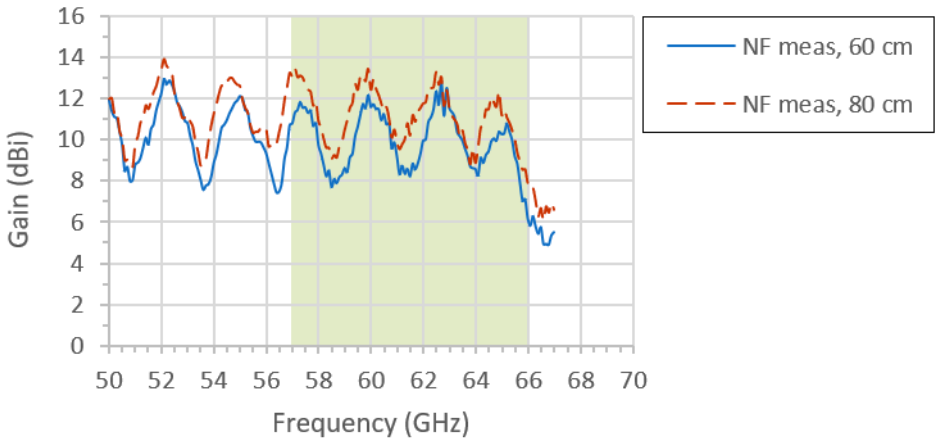

Figure II.63 Measured NF broadside realized gain and simulated FF broadisde realized gain of the lens fed by the patch source.

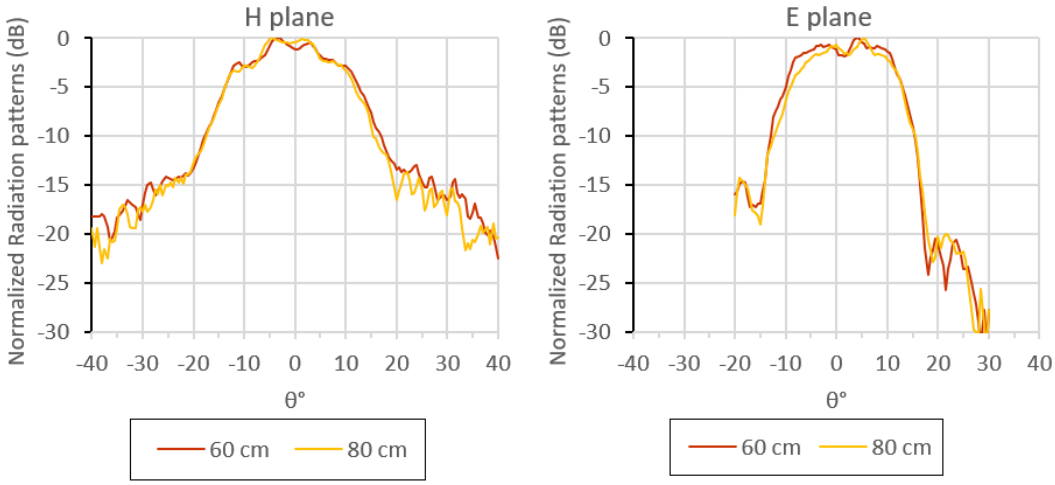

Figure II.64 Normalized measured gain radiation patterns in E (right) and H (left) planes at 60 and 80 cm at 60 GHz.

Another measurement with the SCP and MS-to-WG transition being used as a source of the lens, were also conducted to verify the latter presented results. Also, a dedicated base to hold the waveguide bends was fabricated and the lens was extended by a distance of 17.4 mm to align the phase center of the antenna with its focal center (cf. Figure II.65). It's also worth to mention that we managed to incorporate a special mechanism of "snap-fit clips" to the lens and base designs enabling a simple clips assembly. However, the same low broadside realized gain was recorded (cf. Figure II.66). This much lower-than-expected broadside realized gain can be explained by the following reasons:

- The measured source antenna radiation patterns are disturbed by excessive surface waves.
- The 10dB-HBW of the antenna is wider than 40°, which can not only decrease the illumination efficiency of the lens, but also induce new surface waves on the surface of the lens [II.41].
- The disturbed radiations can also lead to the assumption that the phase center of the source was shifted yielding that the source is no longer placed at the focal center of the lens.

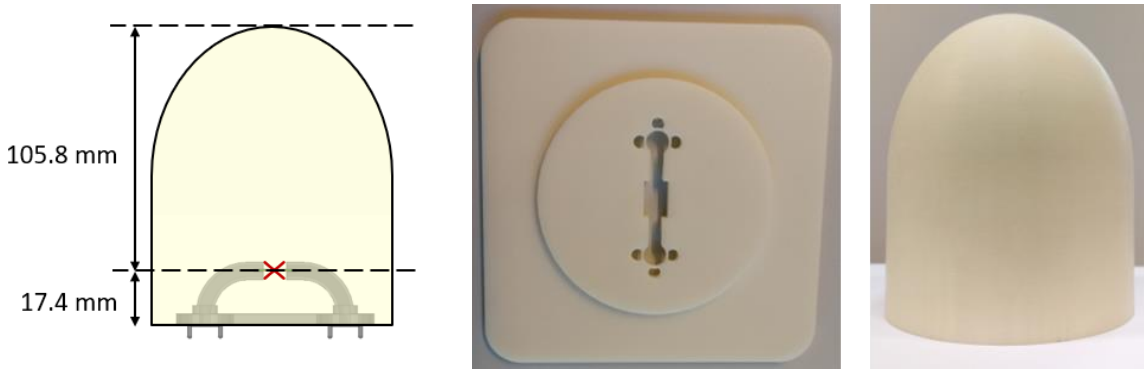

(a) (b) (c)

Figure II.65 (a) Extension of the elliptical lens's model. (b) 3D printed base to hold the patch PCB and MS-to-WG transition and (c) extended elliptical chopped lens.

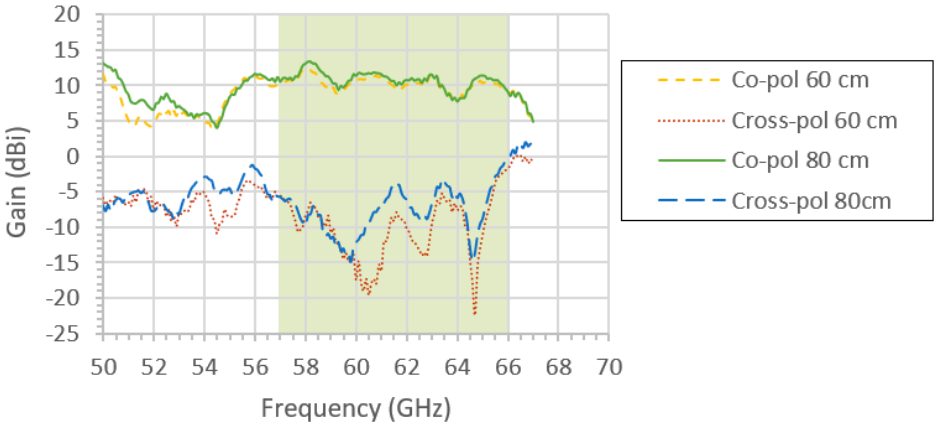

Figure II.66 Measured co-pol and cross-pol broadside realized gain at 60 and 80 cm of the elliptical lens being fed by the patch on PCB and MS-to-WG transition.

II.4.3 Extended elliptical lens fed by a corrugated horn source

In order to search for the explanation of the previous unexpected results, it was decided to feed the ABS lens with a different source. Therefore, further measurements were conducted to validate the design of the lens (geometry + ABS material). We present here the measurements of the elliptical lens being fed by a 60 GHz corrugated horn designed by Dr. Carlos Del Rios Bocio from the University of Navarra. Corrugated horns are characterized by low side lobes, compactness and polarization purity thanks to the corrugation mechanism. It was 3D printed by SLA and metallized afterwards by a special metallization process developed by Swissto12 (cf. Figure II.67 (a)) [II.42]. The measurements of this corrugated horn showed a broadside realized gain of 13 dBi along V-band and an almost perfect gaussian beam of 10dB-HBW equal to 40° (cf. Figure II.67 (b)), which are the ideal specifications to illuminate the lens.

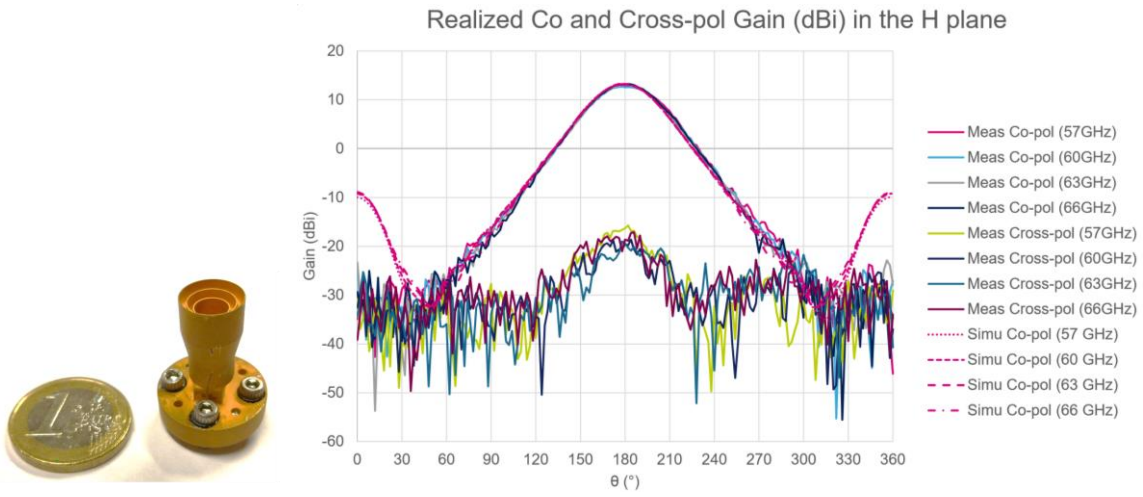

(a) (b)

Figure II.67 (a) Picture of the 3D printed corrugated horn and (b) measured radiation patterns at several frequencies in H-plane.

To hold the horn under the lens while aligning its phase center (located at approximately 2 mm from the surface of the horn towards the inside) with the focal point of the lens, a special base was designed to be used with the same lens measured previously with the probe-fed SCP. Figure II.68, show the corrugated horn being assembled to the designed plastic base and lens. Both base and lens were printed by the aforementioned FDM procedure using ABS-M30 plastic.

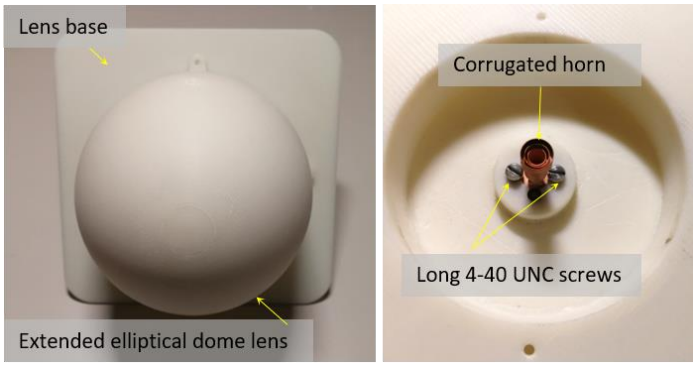

Figure II.68 Picture of the printed lens assembled to the base (left) and the corrugated horn fixed to the base (right).

As with previous measurements, we can't directly measure the FF of this antenna-system, so measurements were also performed at 60 and 80 cm. Measurements will be compared with full electromagnetic simulations conducted on HFSS of the simulation model illustrated in Figure II.69 (a). Figure II.69 (b) compares between measured $|S_{11}|$ of the horn alone and measured $|S_{11}|$ of the horn feeding the lens. After adding the lens, ripples appeared on the $|S_{11}|$ curve of the horn due to reflections on the lens inner boundaries, similarly to what was noticed with the patch source. The matching level is under 15 dB all over the bandwidth. Furthermore, the measured broadside NF realized gain ranges between 24 and 27 dBi from 57 to 66 GHz at 60 cm and between 27 and 29 dBi at 80 cm (cf. Figure II.70). The measured XPD level is higher than 15 dB from 57 to 66 GHz.

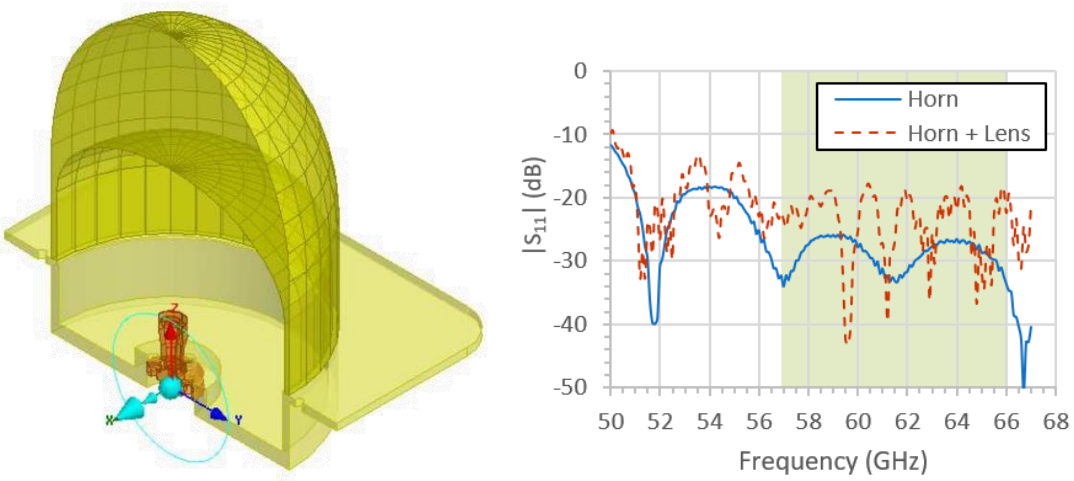

(a) (b)

Figure II.69 (a) Simulation model of the horn source and lens. (b) Measured $|S_{11}|$ versus frequency of the horn source alone and the horn illuminating the lens.

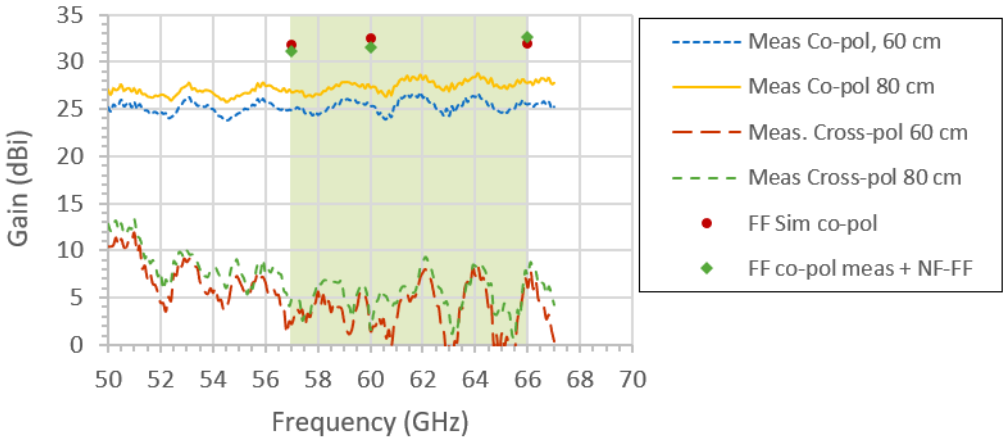

Figure II.70 Measured NF broadside (along z) realized gain in co-pol and cross-pol at 60 and 80 cm versus frequency, FF simulated broadside realized gain in co-pol, and estimated FF broadside realized gain after performing the NF-FF transformation.

NF radiation patterns are plotted in Figure II.71 at 60 GHz in E (along y) and H plane (along x). An increase of the directivity is noticed when the measuring distance is increased. Using the measured radiation patterns in E and H plane, the NF-FF phase-less transformation was applied, yielding the FF estimated broadside realized gain at 57, 60 and 66 GHz shown in Figure II.70 and the FF radiation patterns at 60 GHz plotted in Figure II.72. FF broadside realized gain obtained from applying the NF-FF transformations to NF measurements stays between 31 and 32 dBi which agrees well with simulations. The agreement between simulated and FF radiation patterns estimated by applying the NF-FF transformation is also fair as shown in Figure II.72, except that higher side-lobes were found in measurements. Presented radiation patterns are conform with ETSI RPE class 2 but surpass the class 3A RPE. We note again that the validity of the FF results is limited to the range $\theta \in$ (-10° to 10°). It's worth to mention that many of commercially available antennas only meet class 2 [II.43], hence it's not a limiting factor for the use of the antenna.

Those measurements demonstrate that the lens is radiating as expected and the electrical characteristics of the ABS-M30 plastic are very close to the permittivity we used for the design. Consequently, the fabricated single SCP sources on PCB are responsible for the bad results presented in the previous section. Indeed, it seems that the radiation pattern of those sources is not suitable for efficiently illuminating this kind of elliptical chopped lens. Bad fabrication accuracy resulting in an unprecise surface waves management was responsible for the measured distorted radiation patterns with respect to simulations. Hence, there is still some room for improvement of the PCB sources if a more controlled fabrication process is employed.

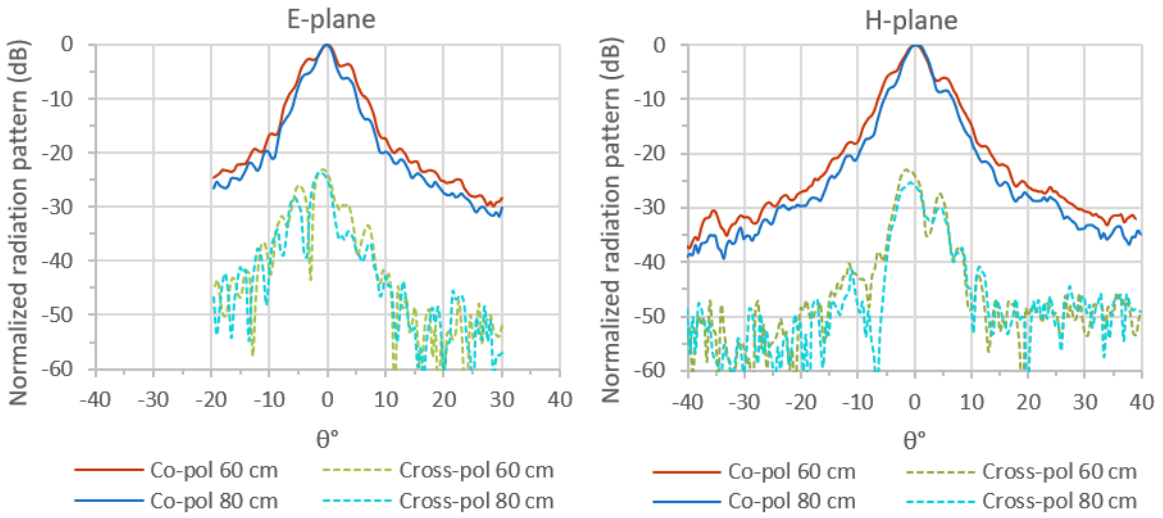

Figure II.71 Measureed NF normalized radiation patterns at 60 GHz in co-pol and cross-pol at 60 and 80 cm: E-plane (left), H-plane (right).

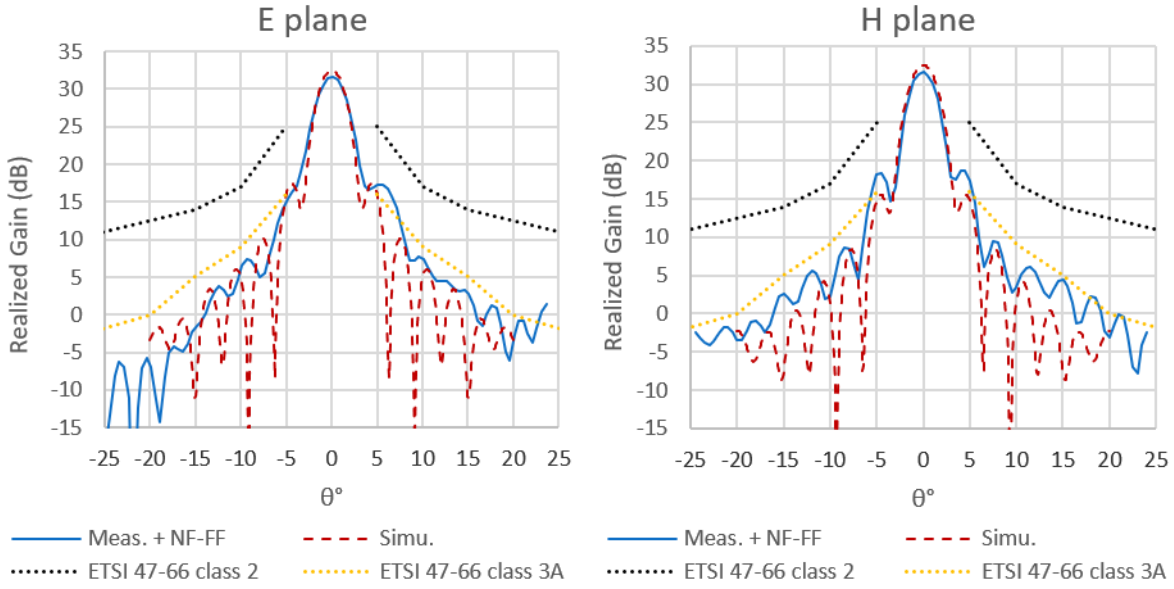

Figure II.72 Co-pol FF realized gain at 60 GHz versus the elevation angle, simulated and computed from NF measurements of the elliptical lens with corrugated horn source in E and H-planes and comparison with ETSI RPE.

It should be also noticed that we were not able to confirm those low gain results (SCP sources + lens) with several simulations which proves that we are clearly missing some important details in our simulation model of the lens fed by SCP sources. Finally, as

summarized in Table II.10, the 3D printed horn surely offers the most efficient solution with an acceptable price which normally should drop if mass production is to be considered. On the other hand, although the expected gain to be achieved by the SCP on FR4 PCB is lower, great reduction in price can be expected hoping to achieve simulated performances with the second run of fabrication.

Parameter	Lens fed by 3D printed horn	Lens fed by SCP on PCB
Gain (dBi)	33 dBi	28 dBi (simulation)
Efficiency	50%	30% (simulation)
Antenna Cost	~900$ (prototyping cost for one piece)	~20$ (prototyping cost for one piece)
Waveguide connection	Yes	No, needs MS-to-WG transition (prototyping cost: 250$ for one piece)
Total cost	~900$	~270$
Conclusion	High-end solution	Low-cost solution

Table II.10 Comparative summary between the two proposed sources.

II.5 FRESNEL LENS AND CORRUGATED HORN

For a more complete study of the possibilities offered by 3D printed lenses, we present in this section a transmit array based on the Fresnel lens concept designed by ISCTE-IUL team. Indeed, the chopped elliptical lens provided very interesting directivity and bandwidth performances but its weight, size and efficiency (50% considering the horn source and comparing measured gain to simulated directivity) are still considered as limiting factors. On the other hand, a transmit array is more compact and can provide higher radiation efficiency using the same kind of plastic material. Nonetheless, a minimum F/D ratio (ratio between focal distance and the aperture diameter) should be respected to obtain competitive directivity and bandwidth performances [II.44]. The proposed Fresnel lens is composed of several concentric rings with different height d, as shown in Figure II.73. A complete 360° phase shift cycle at 60 GHz, with reasonable transmission, can be obtained by varying the height "d" of the frequency selective surface rings. This enables a drastic decrease of the dielectric height, leading to achieve an efficiency higher than 80%, which is one of the key factors that make this solution interesting.

The aforementioned corrugated horn was used to feed this Fresnel lens. The fabricated 3D printed Fresnel lens using the same FDM printing technique used for the elliptical lens and the same ABS-M30 material is shown in Figure II.73 (b). The assembled structure with the corrugated 60 GHz horn is presented in Figure II.73 (c). The transversal dimensions of the Fresnel lens (10 cm ×10 cm) are very close the elliptical dome-lens dimensions, whereas the height of the total assembled Fresnel lens structure is 20% smaller. This lens was designed to meet the same backhaul links requirements: linear polarization and a gain surpassing 30 dBi.

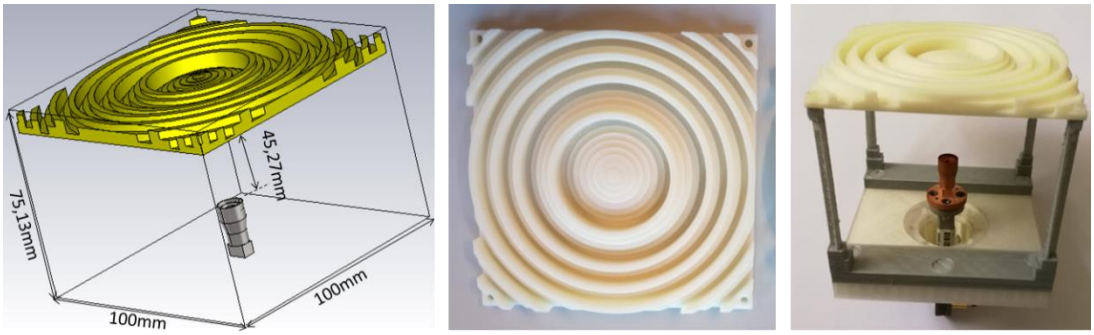

(a) (b) (c)

Figure II.73 (a) 3D view of the Fresnel lens simulation model at V-band. (b) Pictures of the fabricated fresnel lens using FDM with ABS-M30 (b) Top view and (c) assembled horn and fresnel lens.

We performed the measurements of this lens on our measurement system in NF at 40 and 60 cm and then applied the NF-FF transformation following the same method for the elliptical lens. Good matching level was obtained as measured return loss is above 15 dB all along V-band (cf. Figure II.74). The measured broadside realized gain in co-pol at 40 cm delivers 29 dBi gain at 50 GHz and drops to 22 dBi at 66 GHz (cf. Figure II.75). Higher gain is obtained at 60 cm (29 to 30 dBi from 50 to 58 GHz) but the same gain decrease at the end of V-band is observed.

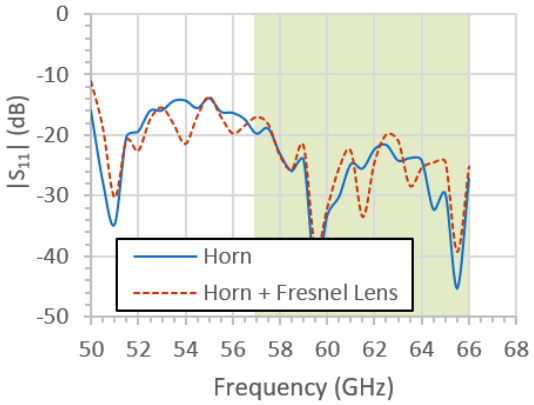

Figure II.74 Measured $|S_{11}|$ of the corrugated horn being used as a source to the Fresnel lens to the measured $|S_{11}|$ of the horn alone.

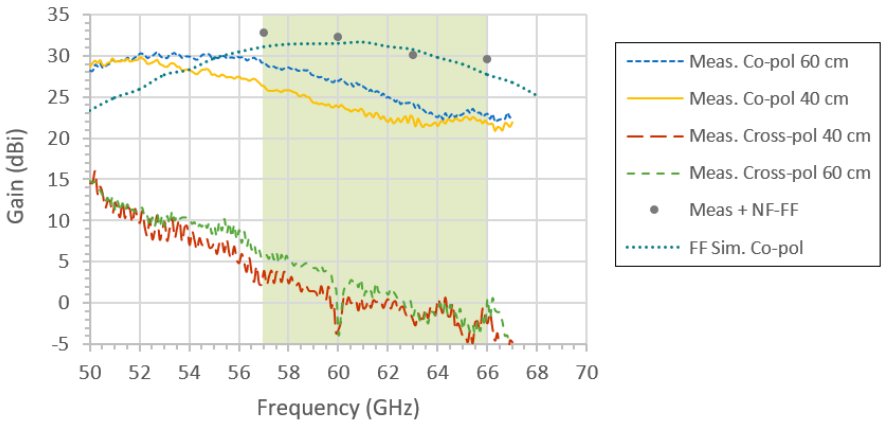

Figure II.75 Measured NF broadside realized gain at 40 and 60 cm of the fresnel lens fed by the corrugated horn source and FF gain estimated from applying the NF-FF transformation.

Good agreement between NF simulation (CST) and measurement in E-plane, and a slightly worse agreement is obtained in H plane (larger beamwidth than expected). An example of measured NF normalized radiation pattern at 60 GHz is shown in Figure II.76 to illustrate this observation. A fair agreement was also obtained between simulated FF normalized radiation patterns and that obtained from the NF-FF phase-less transformation applied on NF measurements, an example is illustrated at 60 GHz by Figure II.77. The radiation patterns meet very well the class 2 RPE but exceed the class 3A RPE.

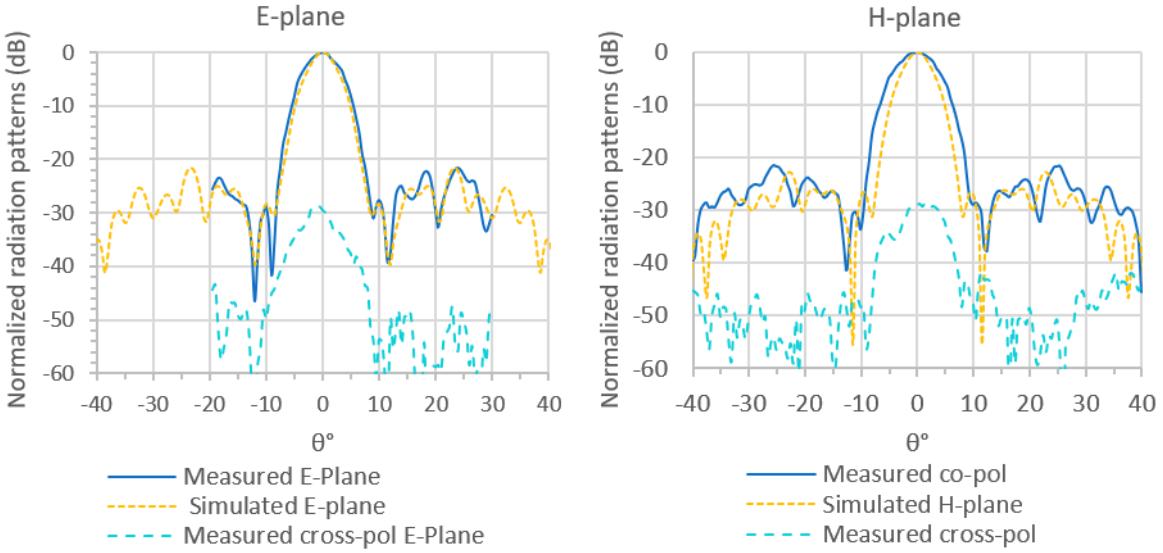

Figure II.76 Measured and simulated (CST) normalized NF radiation patterns at 60 GHz of the fresnel lens fed by the corrugated horn source. E-plane (left) H-plane (right).

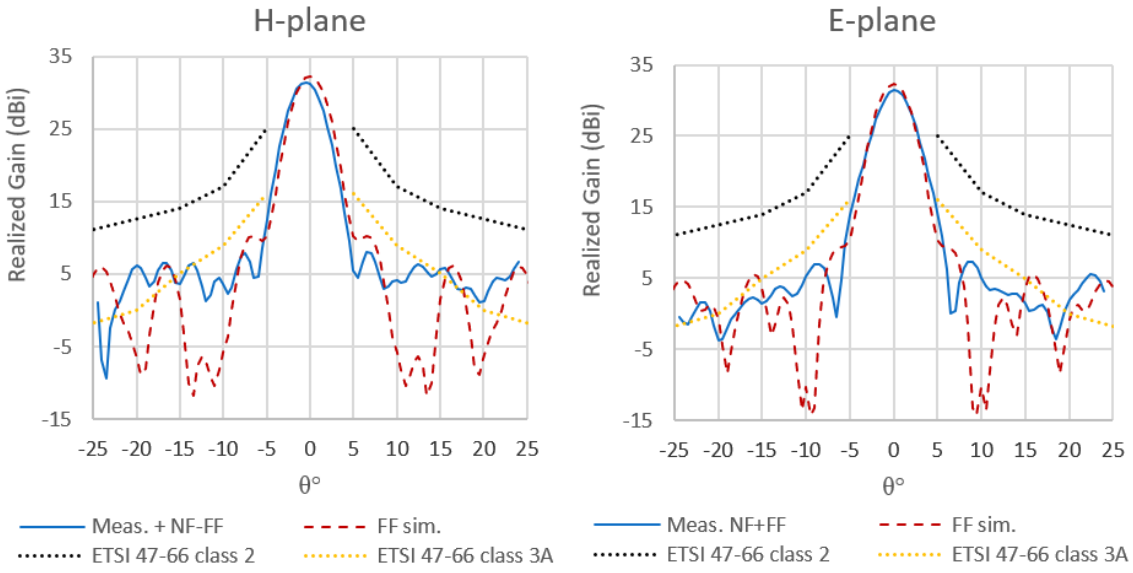

Figure II.77 Computed from measurements and simulated (CST) normalized FF radiation patterns at 60 GHz of the fresnel lens fed by the corrugated horn source. E-plane (left) H-plane (right).

The gain obtained from applying the NF-FF transformation to NF measurements is close to 32 dBi at 57 and 60 GHz and decreases to 29.5 dBi at 66 GHz which is in good agreement with simulations. However, it seems that we're slightly over-estimating the gain, this is related to the fact that our estimations come from a truncated measurement, hence the directivity of the

antenna cannot be computed accurately. Moreover, it turned out after increasing the accuracy of the simulations (by refining the meshing) that the distance between the lens and the horn should be increased by 2 mm to meet the 30 dBi gain criteria all over V-band and to align perfectly the horn phase center with the lens focal point. Therefore, another run of fabrication is actually undergoing and new measurements will be conducted soon.

Nonetheless, clear benefit of the Fresnel lens transmit array is shown in terms of bulkiness (82% of the height of the extended elliptical dome-lens) and weight of the system (32% of the total mass of the extended elliptical dome-lens). Even though the available bandwidth of the Fresnel lens is limited compared to elliptical lens, it appears as a very promising design and strong candidate for low-cost backhaul antenna-system.

II.6 CONCLUSION

In this chapter, we demonstrated the possibility of designing a simple-to-manufacture and low-cost V-band PCB antenna with fair broadside realized gain and wide bandwidth of respectively 5 dBi and 20%. Furthermore, we succeeded to add a waveguide interconnection to the PCB by means of a WG-to-MS transition using an antipodal fin-line transition with limited additional losses (lower than 2 dB). The waveguide H-bends connections were fabricated by DMLS AM technique enabling a cost-effective and easy-to-prototype design.

In order to achieve our goal of obtaining a 30 dBi gain antenna suitable for V-band backhaul applications, an extended elliptical chopped lens was optimized to collimate the rays originating from the patch's PCB source and therefore increase its gain. The elliptical lens was fabricated using FDM 3D printing technology with ABS-M30 plastic. However, opposingly to simulation results that predicted a minimum of 28 dBi broadside realized gain over V-band, the measured gain of this antenna-system was between 8 and 15 dBi. Those unexpected gain values were attributed to excessive surface waves refracted at the edges of the PCB and disturbing the radiation of the antenna due to the fact that the fabricated PCB didn't match the designed antenna's dimensions. The main consequences of those inaccuracies resulted in spurious radiations and distorted radiation patterns, far from being close to a Gaussian source. On the other hand, the same elliptical lens was measured with a 60 GHz corrugated horn source, yielding a broadside realized gain from 31 to 32.7 dBi over V-band estimated by applying the NF-FF transformation on NF measurements. These latter measurements demonstrated that the fabricated lens meets well the simulated designs and the ABS plastic electrical parameters are close to the one measured. This solution is very interesting due to its low-cost fabrication process which doesn't include any micromachining.

Finally, we presented a Fresnel Lens transmit array designed in collaboration with ISCTE-IUL. The lens was fabricated by FDM with an ABS-M30 filament and demonstrated a gain between 29.5 and 32.7 dBi, that was estimated by applying the NF-FF transformation of NF field measurements. Despite its limited bandwidth compared to elliptical lens, this antenna is a very promising solution due to its higher efficiency and lighter weight. Since a small misalignment between the phase center of the horn source and the focal point of the lens was realized, a new fabrication and new measurements are to be conducted soon.

II.7 PERSPECTIVES

In order to improve the radiation of the PCB patch antenna, we propose to add a second cavity around the main patch similarly to the 2×1 array design as shown in Figure II.78. This will be fabricated among the new batch of PCBs with a more controlled fabrication process.

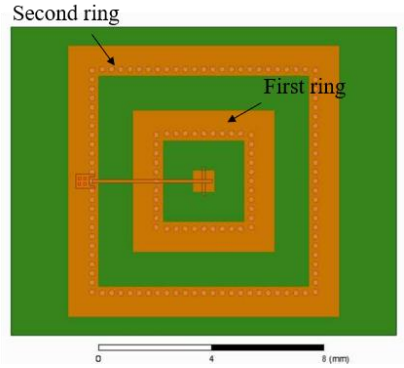

Figure II.78 Top view of the single SCP with double ring structure simulation model.

On the other hand, emerging high-performance plastic materials more suitable than ABS-M30 for harsh environments and adapted for 3D printing like PEEK (polyether ether ketone), opens up a new horizon for spatial applications. PEEK is a high-performance engineering plastic with outstanding resistance to harsh chemicals, and excellent mechanical strength and dimensional stability. The ESA has been conducting research on the use of PEEK to design cubesats and furthermore to a space-optimized PEEK printer to be used on 'zero-gravity' aircraft flights and eventually at the service of astronauts on the International Space Station [II.45]. In collaboration with ESA (Dr. Ugo Lafont) we have proven the performance of a 4 cm diameter extended elliptical dome-lens 3D printed using PEEK material. The lens operates at 120 GHz and is fed by a BGA 2×2 SCP array source [II.8]. The lens demonstrated a measured NF gain around 25 dBi from 110 to 140 GHz (cf. Figure II.79).

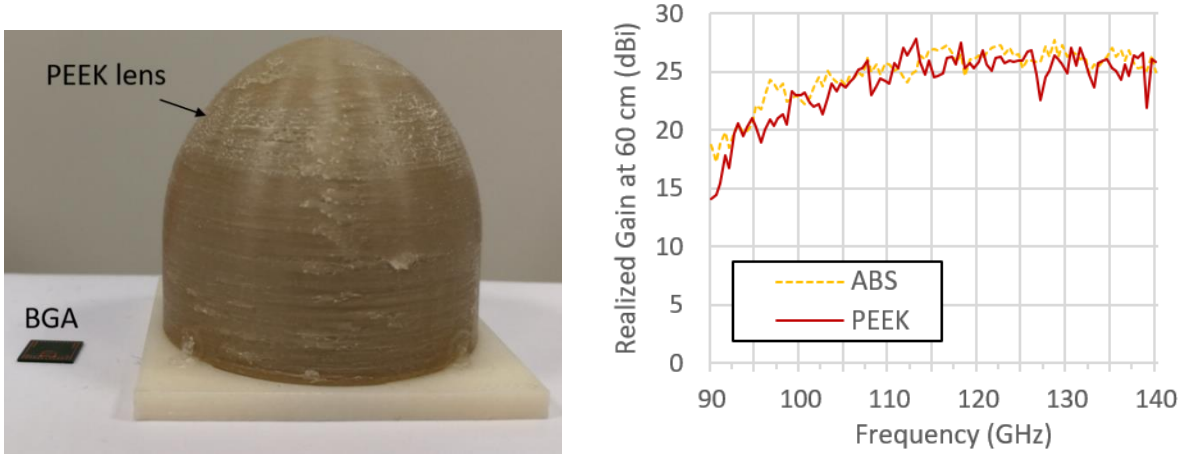

Figure II.79 (a) Picture of the extended elliptical dome lens and 120 GHz 2×2 SCP array BGA package (left). (b) Measured NF gain at 60 cm of the elliptical PEEK lens with the 2×2 BGA source and comparison with almost the same ABS lens.

The obtained measured gain was indeed very close to the one obtained with an ABS lens with almost the same geometry and diameter leading to the possibility of using designed lens

concepts in space applications. Moving forward to achieve the best compromise between performance and size, we study in the next chapter flat antenna arrays for fixed PtP backhaul links in V and E bands. Leveraging 3D printing technics, we present several wide band flat antenna arrays fed by low loss feeding networks.

II.8 REFERENCES

[II.1] "Fixed radio systems, characteristics and requirements for point to point equipment and antennas; Part4: Antennas." [Online]. Available: http://www.etsi.org/deliver/etsi_en/302200_302299/30221704/02.01.01_60/en_30221704v020101p.pdf. [Accessed: 12-Mar-2018].

[II.2] "Recommendation ITU-R F.699-8 : Reference radiation patterns for fixed wireless system antennas for use in coordinate studies and interference assessment in the frequency range 100 MHz to 86 GHz." [Online]. Available: https://www.itu.int/dms_pubrec/itu-r/rec/f/R-REC-F.699-8-201801-I!!PDF-E.pdf. [Accessed: 13-Mar-2018].

[II.3] "LIGHT POINTE WIRELESS, AirLink Series 60 GHz." [Online]. Available: http://nebula.wsimg.com/808dcbc4338e731541536415bf86230e?AccessKeyId=66B3AD0D27BFC4E361AB&disposition=0&alloworigin=1. [Accessed: 17-Mar-2018].

[II.4] K. Street, "SAGE millimeter, V-band Gaussian optics Antenna,".

[II.5] "258 Series, Horn Lens Antennas." [Online]. Available: http://miwv.com/drawings/258/MIWV_Series258.pdf. [Accessed: 18-Mar-2018].

[II.6] N. T. Nguyen, N. Delhote, M. Ettorre, D. Baillargeat, L. L. Coq, and R. Sauleau, "Design and Characterization of 60-GHz Integrated Lens Antennas Fabricated Through Ceramic Stereolithography," IEEE Trans. Antennas Propag., vol. 58, no. 8, pp. 2757–2762, Aug. 2010.

[II.7] A. Bisognin et al., "3D printed plastic 60 GHz lens: Enabling innovative millimeter wave antenna solution and system," in 2014 IEEE MTT-S International Microwave Symposium (IMS2014), 2014, pp. 1–4.

[II.8] A. Bisognin et al., "Ball Grid Array Module With Integrated Shaped Lens for 5G Backhaul/Fronthaul Communications in F-Band," IEEE Trans. Antennas Propag., vol. 65, no. 12, pp. 6380–6394, Dec. 2017.

[II.9] "60 GHz Transmitter/Receiver Waveguide Modules." [Online]. Available: https://www.pasternack.com/pages/Featured_Products/60-ghz-transmitter-receiver-waveguide-modules.html. [Accessed: 18-Aug-2018].

[II.10] Y. P. Zhang, M. Sun, and L. H. Guo, "On-chip antennas for 60-GHz radios in silicon technology," IEEE Trans. Electron Devices, vol. 52, no. 7, pp. 1664–1668, Jul. 2005.

[II.11] H.R. Chuang, S.W. Kuo, C.C. Lin and L.C. Kuo, "A 60 GHz Millimeter-wave CMOS RFIC-on-chip Dipole Antenna." [Online]. Available: http://www.microwavejournal.com/articles/4231-a-60-ghz-millimeter-wave-cmos-rfic-on-chip-dipole-antenna. [Accessed: 25-Mar-2018].

[II.12] Y. P. Zhang, M. Sun, K. M. Chua, L. L. Wai, D. Liu, and B. P. Gaucher, "Antenna-in-Package in LTCC for 60-GHz Radio," in 2007 International workshop on Antenna Technology: Small and Smart Antennas Metamaterials and Applications, 2007, pp. 279–282.

[II.13] J. Lantéri et al., "60 GHz antennas in HTCC and glass technology," in Proceedings of the Fourth European Conference on Antennas and Propagation, 2010, pp. 1–4.

[II.14] A. Bisognin et al., "Millimeter-wave antenna-in-package solutions for WiGig and backhaul applications," in 2015 International Workshop on Antenna Technology (iWAT), 2015, pp. 52–55.

[II.15] W. Hong, K.-H. Baek, and A. Goudelev, "Multilayer Antenna Package for IEEE 802.11ad Employing Ultralow-Cost FR4," IEEE Trans. Antennas Propag., vol. 60, no. 12, pp. 5932–5938, Dec. 2012.

[II.16] H. Vettikalladi, O. Lafond, M. Himdi, T. Sarrazin, and N. Rolland, "60 GHz membrane supported aperture coupled patch antenna based on FR4 and new thin Pyralux substrate," in 2012 42nd European Microwave Conference, 2012, pp. 209–212.
[II.17] "Aspocomp." [Online]. Available: https://www.aspocomp.com/. [Accessed: 28-Aug-2018].
[II.18] F. Croq and A. Papiernik, "Large bandwidth aperture-coupled microstrip antenna," Electron. Lett., vol. 26, no. 16, pp. 1293–1294, Aug. 1990.
[II.19] Y.-J. Park, A. Herschlein, and W. Wiesbeck, "A photonic bandgap (PBG) structure for guiding and suppressing surface waves in millimeter-wave antennas," IEEE Trans. Microwave Theory Tech., vol. 49, no. 10, pp. 1854–1859, Oct. 2001.
[II.20] W. E. McKinzie, D. M. Nair, B. A. Thrasher, M. A. Smith, E. D. Hughes, and J. M. Parisi, "60 GHz patch antenna in LTCC with an integrated EBG structure for antenna pattern improvements," in 2014 IEEE Antennas and Propagation Society International Symposium (APSURSI), 2014, pp. 1766–1767.
[II.21] J.-H. Lee, N. Kidera, S. Pinel, J. Laskar, and M. M. Tentzeris, "60 GHz high-gain aperture-coupled microstrip antennas using soft-surface and stacked cavity on LTCC multilayer technology," in 2006 IEEE Antennas and Propagation Society International Symposium, 2006, pp. 1621–1624.
[II.22] S. Beer, B. Göttel, H. Gulan, C. Rusch, and T. Zwick, "A 122 GHz four element patch array fed by electromagnetic coupling," in 2012 IEEE MTT-S International Microwave Workshop Series on Millimeter Wave Wireless Technology and Applications, 2012, pp. 1–4.
[II.23] A. Bisognin, "Évaluation de technologies organiques faibles pertes et d'impression plastique 3D afin de contribuer au développement de solutions antennaires innovantes dans la bande 60 GHz – 140GHz.," PhD thesis, Université Nice Sophia Antipolis, 2015.
[II.24] "Air Coplanar Microwave RF | Cascade Microtech, Inc." [Online]. Available: https://www.cascademicrotech.com/products/probes/rf-microwave/acp-probe. [Accessed: 27-Apr-2018].
[II.25] D. Titz, F. Ferrero, and C. Luxey, "Development of a Millimeter-Wave Measurement Setup and Dedicated Techniques to Characterize the Matching and Radiation Performance of Probe-Fed Antennas [Measurements Corner]," IEEE Antennas Propag. Mag., vol. 54, no. 4, pp. 188–203, Aug. 2012.
[II.26] A. Bisognin et al., "Probe-fed measurement system for F-band antennas," in The 8th European Conference on Antennas and Propagation (EuCAP 2014), 2014, pp. 722–726.
[II.27] "SMPM." [Online]. Available: https://www.radiall.com/products/rf-coaxial-connectors/hermetic-connectors/smpm.html. [Accessed: 23-Apr-2018].
[II.28] K. Seo, "Planar Microstrip-To-Waveguide Transition in Millimeter-Wave Band," in Advancement in Microstrip Antennas with Recent Applications, A. Kishk, Ed. InTech, 2013.
[II.29] A. Mozharovskiy, A. Artemenko, V. Ssorin, R. Maslennikov, and A. Sevastyanov, "Wideband tapered antipodal fin-line waveguide-to-microstrip transition for E-band applications," in Microwave Conference (EuMC), 2013 European, 2013, pp. 1187–1190.
[II.30] "Waveguide Bends and Twists :: Radio-Electronics.Com." [Online]. Available: http://www.radio-electronics.com/info/antennas/waveguide/waveguide-bends-e-h-twists.php. [Accessed: 30-Apr-2018].
[II.31] "WR-15 Instrumentation Grade Waveguide H-Bend with UG-385/U Flange Operating from 50 GHz to 75 GHz." [Online]. Available: https://www.pasternack.com/wr-15-

waveguide-h-bend-ug-385-flange-50-75-ghz-pe-w15b002-p.aspx. [Accessed: 30-Apr-2018].

[II.32] K. V. Hoel, S. Kristoffersen, J. Moen, K. G. Kjelgard, and T. S. Lande, "Broadband antenna design using different 3D printing technologies and metallization processes," 2016, pp. 1–5.

[II.33] S. Verploegh, M. Coffey, E. Grossman, and Z. Popovic, "Properties of 50–110-GHz Waveguide Components Fabricated by Metal Additive Manufacturing," IEEE Trans. Microw. Theory Tech., vol. 65, no. 12, pp. 5144–5153, Dec. 2017.

[II.34] J. Shen et al., "Rapid prototyping of low loss 3D printed waveguides for millimeter-wave applications," in Microwave Symposium (IMS), 2017 IEEE MTT-S International, 2017, pp. 41–44.

[II.35] M. Hollenbeck, K. Wamick, C. Cathey, J. Opra, and R. Smith, "Selective Laser Melting aluminum waveguide attenuation at K-band," in Microwave Symposium (IMS), 2017 IEEE MTT-S International, 2017, pp. 45–47.

[II.36] D. F. Filipovic, S. S. Gearhart, and G. M. Rebeiz, "Double-slot antennas on extended hemispherical and elliptical silicon dielectric lenses," IEEE Trans. Microw. Theory Tech., vol. 41, no. 10, pp. 1738–1749, Oct. 1993.

[II.37] H. Gulan, C. Rusch, S. Beer, T. Zwick, M. Kuri, and A. Tessmann, "Lens coupled broadband slot antenna for W-band imaging applications," in 2013 IEEE Antennas and Propagation Society International Symposium (APSURSI), 2013, pp. 424–425.

[II.38] C. A. Fernandes and J. R. Costa, "Permittivity measurement and anisotropy evaluation of dielectric materials at millimeter-wave ," XIX IMEKO World Congress, Fundamental and Applied Metrology, September 6−11, 2009, Lisbon, Portugal.

[II.39] E. Lima, J. R. Costa, M. G. Silveirinha, and C. A. Fernandes, "ILASH-Software tool for the design of integrated lens antennas," in 2008 IEEE Antennas and Propagation Society International Symposium, 2008, pp. 1–4.

[II.40] Y. Alvarez, F. Las-Heras, and M. R. Pino, "The Sources Reconstruction Method for Amplitude-Only Field Measurements," IEEE Trans. Antennas Propag., vol. 58, no. 8, pp. 2776–2781, Aug. 2010.

[II.41] E. B. Lima, J. R. Costa, J. R. Costa, and C. A. Fernandes, "Mechanical beam-steerable elliptical dome lens," EuCAP 2009, 2009.

[II.42] "Swissto12 - home." [Online]. Available: http://www.swissto12.ch/. [Accessed: 07-May-2018].

[II.43] "HUBER+SUHNER - SENCITY® Matrix." [Online]. Available: https://www.hubersuhner.com/en/solutions/wireless-infrastructure/products/mobile-backhaul/sencity-matrix. [Accessed: 18-Jun-2018].

[II.44] J. P. Teixeira et al., "Transmit array as a viable 3D printing option for backhaul applications at V-band," in 2017 IEEE International Symposium on Antennas and Propagation USNC/URSI National Radio Science Meeting, 2017, pp. 2641–2642.

[II.45] "3D printing CubeSat bodies for cheaper, faster missions," European Space Agency. [Online]. Available: https://www.esa.int/Our_Activities/Space_Engineering_Technology/3D_printing_CubeSat_bodies_for_cheaper_faster_missions. [Accessed: 04-Sep-2018].

III. V AND E-BAND PATCH ARRAY ANTENNAS FED BY DIELECTRIC FILLED WAVEGUIDE

In the previous chapter low-cost lens antennas were presented to answer the millimeter wave backhaul links requirements. Despite the simplicity of the lens antennas' structures, they remain bulky which limits their deployment for street level installations, where aesthetic concerns arise and community friendly designs are needed. For this reason, flat antenna arrays are becoming an interesting choice for backhaul links especially if they are able to deliver equivalent performance. However, the main challenge in developing this kind of antennas is to overcome the complexity of the feeding network to enable a cost-efficient solution. Generally, the cheapest and most suitable antenna array solutions for mass production are microstrip arrays which rely on the simplicity and the cost efficiency of printed circuits. Nevertheless, the losses encountered in the feeding network of those arrays limit significantly the achievable gain of the antenna array and reduce drastically its overall antenna efficiency.

On the other hand, the continuously evolving 3D printing technologies open the way for fast and easy prototyping of complicated mechanical structures with details reaching, nowadays, tens of microns without expensive manufacturing costs. Leveraging recent development of DAM technologies, we proposed in this chapter a flat patch antenna array fed by a dielectric waveguide. Filling the waveguide by a low-loss dielectric allows to reduce its transversal dimensions (considering the same frequency of operation than that of an air-filled waveguide) while maintaining a low insertion loss level. Reducing the waveguide dimensions not only allows further compactness of the feeding network but also puts less constraints on the spacing between the array elements. Hence the spacing between the array can be optimized to limit side lobes or avoid grating lobes appearance. This chapter begins by presenting state-of-the-art flat antenna arrays suitable for backhaul links in E and V-bands. In the next section, we present an optimized design of a unit-cell SCP fed by a dielectric waveguide. Then, we propose several configurations of waveguide feeding networks to enable the composition of arrays up to 32×32 elements based on the latter unit-cell. Finally, we discuss possible DAM prototyping methods.

III.1 STATE-OF-THE-ART FLAT ARRAY ANTENNAS

As shown previously, lens antennas have radiation characteristics suitable for backhaul application, but because they consist of a lens, a feeding source and several supporting rods, they are larger and heavier than flat-panel array antennas. Using a low-cost technology like

PCB, microstrip planar antennas suitable for mass production can be designed. Microstrip arrays are compact, light, easy-to-manufacture and can easily be integrated with other passive and active components of the wireless system. However, these antennas suffer from spurious radiation in the form of surface waves at high frequencies and high ohmic and dielectric losses especially in the microstrip line feeding network [III.1], [III.2]. This limits the achievable gain by large microstrip antenna arrays. Recently, Substrate Integrated Waveguides (SIW) were commonly used for the design of flat array antennas. SIW are realized with two rows of metallized via-holes in a metal-clad dielectric substrate, emulating a sort of waveguide, by standard PCB fabrication technique. The antenna based on the SIW scheme can easily be integrated with other circuits which leads to a cost-effective subsystem. Leveraging the benefits of SIW like low radiation losses, wide bandwidth and minimized spurious modes, antenna arrays with efficiencies between 40% and 70% were achieved [III.3], [III.4], [III.5]. Figure III.1 (a) shows an example of a 12-way SIW slot antenna array achieving an efficiency of 68% on a narrow impedance bandwidth of 6% [III.3]. Another example consisting of a 4×4 cavity-backed patch array fed by SIW [III.5] featured a 54% radiation efficiency at 60 GHz and a -10 dB impedance bandwidth over 22% (cf. Figure III.1 (b)). Although the feeding line losses in SIW are lower than in microstrip structures, they are still considered as a limiting factor when the SIW array dimensions become larger [III.6].

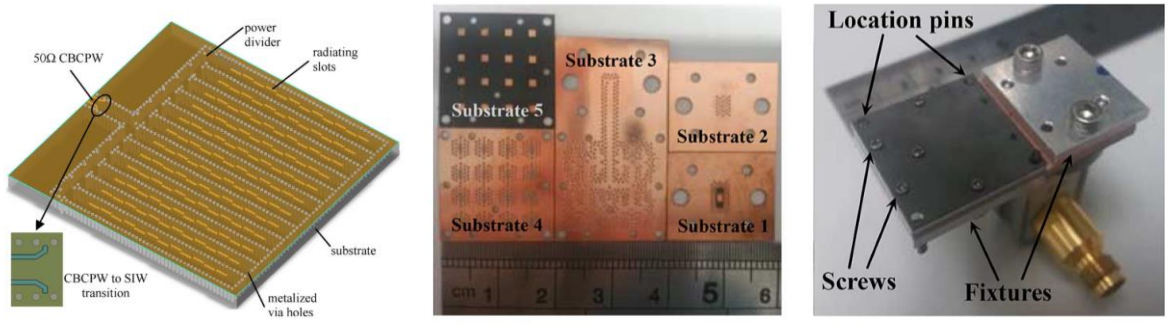

(a) (b)

Figure III.1 (a) 60 GHz SIW slot antenna array [III.3] and (b) 60 GHz patch array slot coupled to SIW [III.5] .

Waveguide slot antenna arrays are the most attractive candidates for high-gain and high efficiency planar antennas [III.7-9] because they suffer neither from dielectric nor radiation loss resulting from surface waves. However, waveguide slot arrays are very limited in impedance and gain bandwidth and require complicated and bulky corporate feed networks to improve these bandwidths. A corporate feed network typically uses waveguides and waveguide junctions to distribute the power to elements of the antenna array. Figure III.2 shows an example of a cavity-backed slot antenna array fed by a corporate waveguide network [III.9]. This antenna was manufactured by a process based on the diffusion bonding of many laminated thin copper plates. A gain exceeding 32 dBi was achieved by this design over only 8% of bandwidth, even with the use of a corporate waveguide feed.

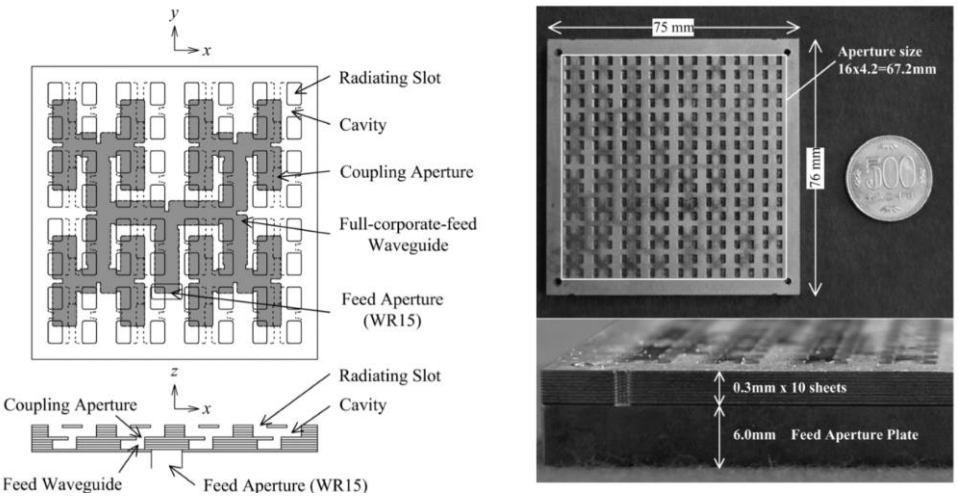

Figure III.2 60 GHz 16x16 elements slot waveguide array with corporate waveguide feeding network fabricated by diffusion bonding of laminated thin copper plates [III.9].

Another interesting high-efficiency approach is the gap waveguide technology introduced in [III.10]. The gap waveguides are formed by metal ridges or strips along which local waves can propagate. Parallel-plate modes are prohibited from propagating by providing one of the surfaces with a texture (metal pin surface, corrugations…) that emulates an artificial magnetic conductor or an electromagnetic bandgap surface on both sides of the ridges (or the strip). It was demonstrated that a cut-off bandwidth of up to 3:1 can be achieved by such waveguides [III.11]. These kinds of antennas have large potential for millimeter wave applications, however, their fabrication is still challenging. Based on this concept, a 16×16 element slot array fed by gap waveguides was proposed in [III.12] (cf. Figure III.3). The gap waveguide slot array was fabricated by milling and demonstrated a relatively high total efficiency above 70% over V-band and a 10dB-impedance bandwidth of 16%. Table III.1 compares the main performance of all the previously presented antennas.

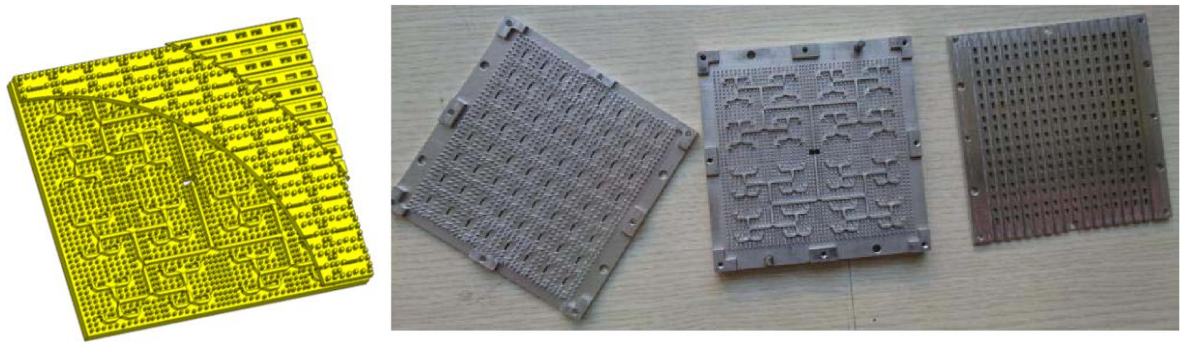

Figure III.3 16x16-element array antenna using gap waveguide technology simulation model (left) and fabricated prototype (right) [III.12].

On the other hand, commercial flat antenna arrays targeting backhaul links are already available. Table III.2 summarizes the performance of two commercial flat array antennas: the Sencity Matrix (by Huber & Suhner, cf. Figure III.4 (a)) [III.13] and the Gap Array Antenna [III.14] (by Gap waves, cf. Figure III.4 (b)). The first is a slot antenna array and the second is a gap waveguide array. Since, the bandwidth of the antennas (~20%) is not sufficient to cover

both E and V-band, a design for each band is proposed. Achieved gain ranges from 26 to 43 dBi depending on the different proposed sizes from each company.

Antenna type and technology	Gain (dBi)	Number of elements	Antenna size (w×d mm)	-10dB impedance BW	Efficiency
SIW Slot antenna arrays [III.3]	18-22	144	NS	59-62 GHz (5%)	NS
Cavity backed patches fed by SIW [III.5]	30.1	256	68×61	57.5-67 GHz (15.3%)	>50%
Slot array plate laminated [III.9]	32	256	67×67	59-64 GHz (8%)	>70%
Gap waveguide Slot array [III.12]	32.5	256	70×64	56-65.7 GHz (16%)	>70%

Table III.1 Previously reported 60 GHz planar antenna arrays.

Moreover, the SENCITY® matrix satisfies the ETSI class 2 RPE in 45° and 135° planes, hence it should be rotated during installation (cf. Figure III.4 (a)) whereas the Gap Antenna satisfies the ETSI class 3 RPE. The most noticeable characteristics of those antennas are there thin profile, close to 1 cm height. Both companies employ high-volume production methods like high precision injection molding for the manufacturing of these antennas. The antennas fabricated in plastic material are then covered with a metallic coating. Injection molding has its drawbacks, however, mainly because of the high expenses of making a mold. In fact, even though molds can be reused to make hundreds of thousands of parts, they can cost anywhere from a few thousand dollars to over $100,000. Moreover, this method is considered inflexible because of the need to make a new mold after each modification. On the other hand, DAM costs only include the price of material, manufacturing time, and labor. Moreover, there are many benefits inherent to this process, such as the ability to produce completely custom parts with virtually no upfront cost. With DAM, rather than needing a new mold for every new part, only a new digital file is needed. Additionally, DAM is capable of producing shapes that are impossible to produce with injection molding [III.15].

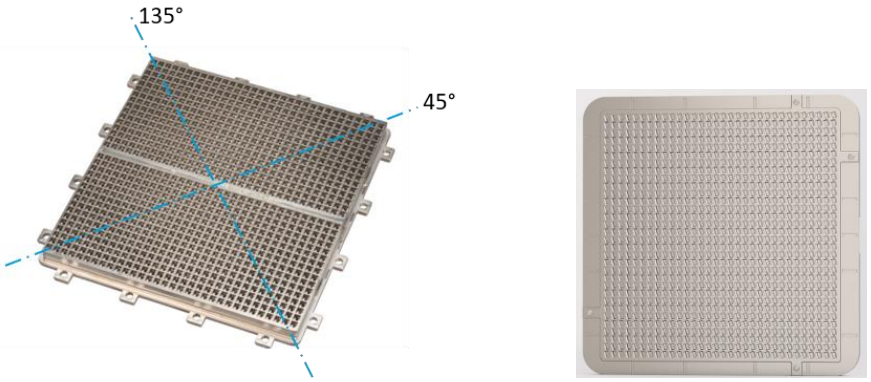

(a) (b)

Figure III.4 (a) V-band Sencity matrix (Huber & Suhner) [III.13] (b) and the E-band Gap Antenna (GAP waves) [III.14].

Antenna	Technology	Gain (mid-band)	Antenna size (w×d×h mm³)	Frequency	Weight (Kg)	ETSI class
GAP waves, Gap Antenna [III.14]	Gap waveguide	26 dBi	42.5 × 43.5 × 12.2	V-band	NS	NS
		32 dBi	93 × 93 × 15.8	V-band	NS	3
		38 dBi	118 × 118 × 8.2	E-band	NS	3
Huber & Suhner, SENCITY ® matrix [III.13]	Slot array	38 dBi	135 × 130 × 9.5	V-band	0.15	2
		38 dBi	102 × 106 × 8	E-band	0.08	2
		43 dBi	280 × 280 × 34	E-band	0.2	2

Table III.2 Commercial antennas' data extracted from the data sheets provided by the manufacturers.

Leveraging the potential of both DAM and printed circuits technologies, we decided to merge the advantages of both technologies to design a patch antenna array with low-loss waveguide feeding network. PCB technology was chosen to print the patch array substrate and DAM was chosen to be employed for the fabrication of the waveguide network. The antenna elements consist on a patch coupled to a dielectric-filled waveguide by means of an end-wall slot. The low-loss dielectric filling the waveguide allows to reduce the waveguide dimensions while ensuring a wide bandwidth impedance matching and a compact antenna design. In fact, a standard waveguide transversal dimensions are about $0.77\lambda_0 \times 0.39\lambda_0$ (free space wavelength at the central frequency of the operating band of the waveguide). This leads to increase the spacing between the elements beyond that value, consequently, higher side lobes are obtained or even grating lobes can appear [III.16]. This is why decreasing the waveguide dimensions is a critical factor.

Moreover, to meet ETSI requirements of 30 dBi minimum gain in V-band and 38 dBi gain in E-band, the single elements gain for a 32×32 array arrangement should be at least 0 dBi in V-band and at least 8 dBi in E-band. Following these guidelines, we conceived the unit-cell of the array as described in the next section.

III.2 UNIT-CELL: SCP ANTENNA FED BY DIELECTRIC-FILLED WAVEGUIDE

III.2.1 State-of-the-art: SCP antennas fed by waveguide

Only few examples and studies of patch antennas slot coupled to waveguide can be found in literature mainly due to mismatch issues. Traditional waveguide-to-microstrip transitions have been used either as wire-probe coupling, machined matching step sections or fin-line type transitions but those solutions aren't suitable in our application due to their bulkiness. Therefore, broad-wall and end-wall waveguide-to-microstrip transitions that rely on aperture coupling techniques are more suited for mmW antenna array applications. However, it was demonstrated that only a very low level of coupling can be obtained between the patch and the waveguide using broad-wall coupling slots (cf. Figure III.5 (a)) [III.17]. On the other hand, waveguide couplers using a slot in the end-wall of the guide (cf. figure III.5 (b)) are more

convenient configurations because they enable a modular connection of waveguide components to planar antennas. Moreover, they can be fabricated relatively inexpensively since specially machined waveguide parts or wire probes are not needed. Nonetheless, while spurious radiation is not an issue with this configuration (since the radiation from the slot should be co-polarized with the patch), it is generally not possible to match the input waveguide for any slot size [III.17]. To overcome this issue, several methods have been proposed to improve the impedance matching.

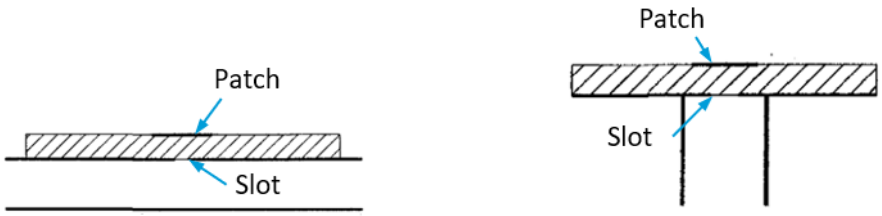

(a) (b)

Figure III.5 (a) Broad-wall waveguide slot (b) and end-wall waveguide slot coupled to patch antenna [III.17].

One solution consists in ending the waveguide by a horn-like taper [III.18] as illustrated in figure III.6 (a). Although good matching was achieved with this method, still, the impedance bandwidth remains limited (near 5% [III.18], [III.19]). Another more effective way to improve the impedance matching consists in loading the slot by a dielectric slab to achieve matching on a wide bandwidth as reported in [III.20] (cf. Figure III.6 (b)). This solution eliminates the need for a specially formed waveguide junction and simplifies assembly as well as testing. A design of a 3×3 array based on this matching method is presented in figure III.6 (b), achieving a measured 10 dB-impedance-bandwidth of 11% along with a simulated efficiency over 90%.

Inspired by this method, we opted for using a dielectric-filled waveguide to feed the patch antenna instead of using a dielectric slab. Moreover, to increase the impedance bandwidth, we decided to replace the coupling cavity by a dielectric-filled waveguide corporate network.

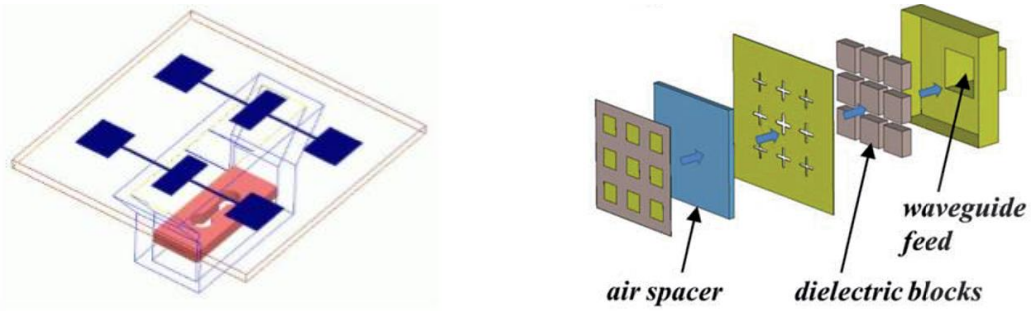

(a) (b)

Figure III.6 (a) 3D View of a 2×2 patch array antenna with end-wall slot coupling to a waveguide with horn-like taper [III.18]. (b) Exploded view of a 3×3 patch array coupled to a cavity by slots loaded by dielectric slabs [III.20].

III.2.2 Unit-Cell: Design and simulation

The proposed unit-cell consists of a patch coupled to a dielectric-filled waveguide through an iris-slot in the waveguide's end wall as presented in Figure III.7 (a). The dielectric we chose

to use is polyethylene (PE) a plastic characterized by low losses, estimated to approximately 4 dB/m [III.21] (ε_r = 2.3 and tanδ = 0.001). The concept of the antenna consists on coupling the guided TE_{10} waveguide mode to the patch's TM_{10} resonant mode through the slot as shown by the electric field distribution in figure III.7 (a) and (b).

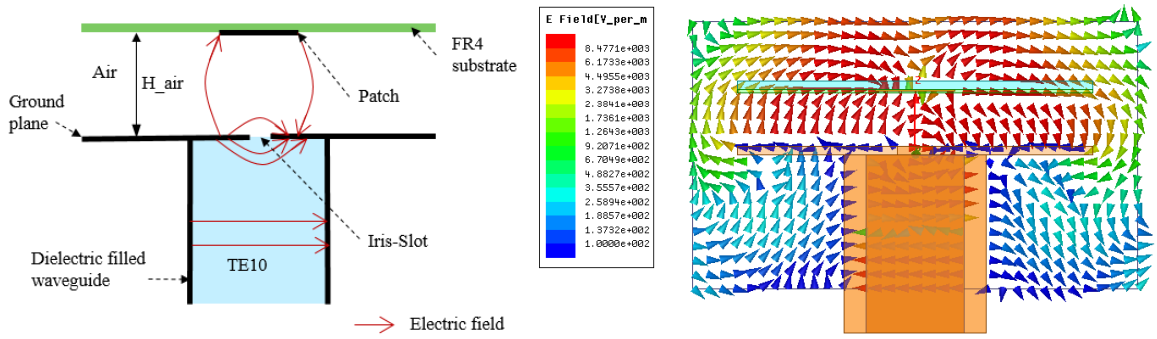

(a) (b)

Figure III.7 (a) Transversal schematic of the unit-cell antenna with electric field distribution and (b) associated simulated vector electric field using HFSS.

The patch is printed on a thin FR4 substrate and is held at a height H_air above the ground plane, the dielectric separating the patch from the slot is air. The low permittivity of the air does not allow surface wave propagation and hence allows to increase the thickness of the substrate leading to a wideband performance. To maintain the patch at the specified height plastic pillars or a foam substrate can be used. Giving the wide bandwidth capabilities of the proposed design, we opted for optimizing the structure to simultaneously cover V and E bands. Optimized parameters are indicated in Figure III.8 and corresponding values are listed in Table III.3.

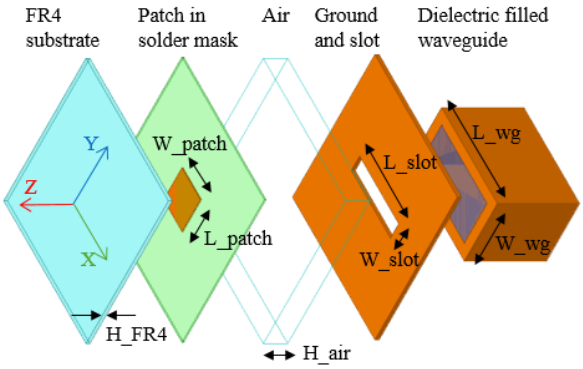

Figure III.8 Exploded view of the unit-cell simulation model.

L_patch = W _patch	L_slot	W_slot	H_air	H_FR4	L_wg	W_wd
0.9 mm	1.9 mm	0.4 mm	0.6 mm	0.1 mm	0.4 mm	1.1 mm

Table III.3 Value of the optimized parameters of the slot coupled patch to dielectric-filled waveguide single element.

The waveguide's length L_wg was chosen to asset the cut-off frequency of the TE_{10} mode below 57 GHz. The optimized value, equal to 2.2 mm, corresponds to a cut-off frequency of 45 GHz as given by (III.1) for rectangular waveguide TE modes.

$$f_{c_{mn}} = \frac{c_0}{2\pi\sqrt{\varepsilon_r}}\sqrt{\left(\frac{m\pi}{a}\right)^2 + \left(\frac{n\pi}{b}\right)^2} \quad hence, f_{c_{10}} = \frac{c_0}{2a\sqrt{\varepsilon_r}} \tag{III.1}$$

Compared to the standard WR12 waveguide used in E-band with dimensions of 3.1 mm × 1.55 mm, we managed to decrease the transversal dimensions of the waveguide to 2.2 mm × 1.1 mm (~30%).

On the other hand, the elementary antenna performance is mainly determined by two resonances: the patch resonance and the slot resonance. The slot is slightly longer than the patch in order to bring its resonance frequency before that of the patch. In this way, wide impedance and gain bandwidths are realized. The thickness of the FR4 substrate was chosen to be as thin as possible (~100 µm) to avoid power loss in surface wave modes. Finally, the height of the air separating the slot from the patch was optimized to enhance the coupling between the two resonances while maintaining good impedance matching in E and V-bands.

The antenna was simulated using HFSS software. The waveguide boundary limits where set by copper walls, as for all the waveguide designs in this chapter. A return loss higher than 10 dB was obtained covering both V and E bands (48% bandwidth) (cf. III. 9 (a)). The impedance locus, plotted in Figure III.9 (b), shows that a very good coupling is obtained between the different resonating structure forming a double loop, included in the VSWR = 2 circle from 56 to 90 GHz. This locus shows two tight loops near the center of the Smith chart. The locus is produced by the interaction between the individual resonances: a mutual resonance produced by the interaction of the waveguide and slot and a mutual resonance produced by the interaction of the slot with the patch. The mutual resonance between the waveguide and the patch is associated with the wider loop in the impedance locus and the mutual resonance of the slot and patch is associated to the narrower loop. These mutual resonances are also coupling to each other, resulting in the fact that one loop is completely inside the other.

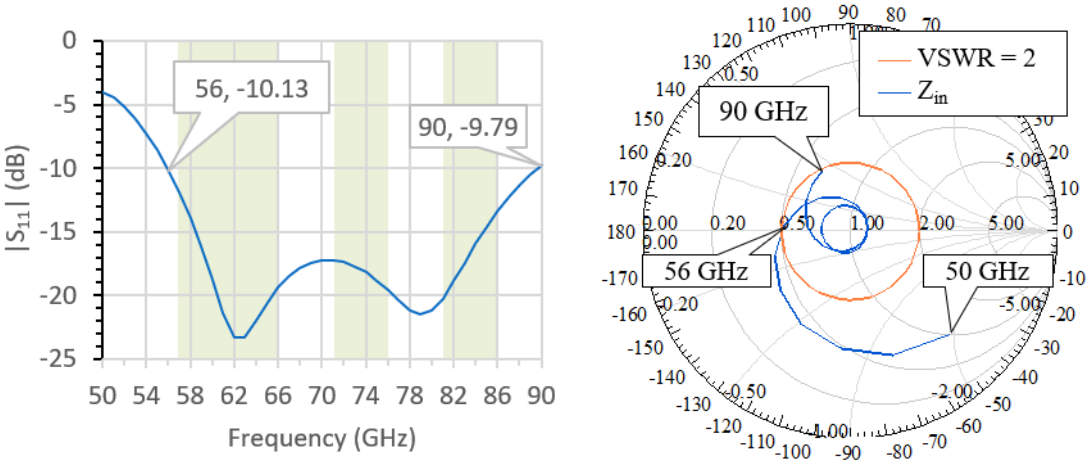

(a) (b)

Figure III.9 (a) Simulated $|S_{11}|$ (b) and input impedance versus frequency of the unit-cell.

Figure III.10 illustrates the broadside realized gain and the directivity obtained from the simulation of the unit-cell. The broadside realized gain is above 7.8 dBi from 57 to 90 GHz

(45% bandwidth), reaching 9.6 dBi at 82 GHz which is notably higher than the gain of a conventional slot coupled patch fed by a microstrip line [III.22]. This high-gain can be explained by the high efficiency (higher than 93%) of the proposed antenna which is achieved thanks to the low-loss dielectric-filled waveguide feed and the air substrate permittivity and height. In fact, the realized gain almost coincides with the directivity all over V and E bands.

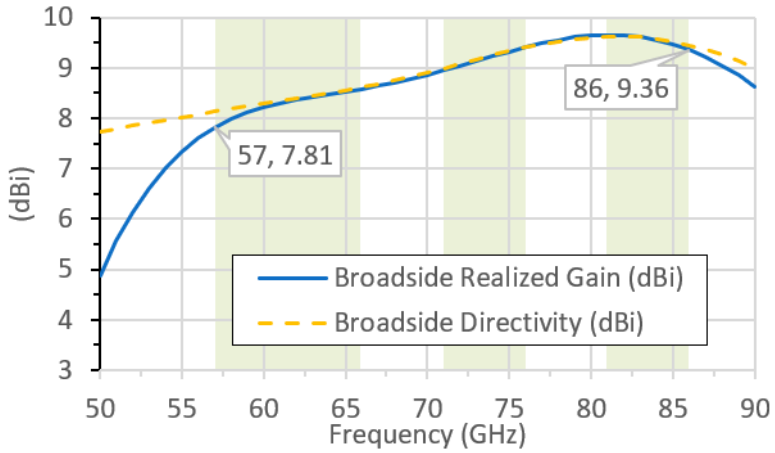

Figure III.10 Simulated broadside (along z) realized gain and directivity of the unit-cell.

Figure III.11 features the simulated normalized radiation patterns in E and H planes of the unit-cell. In H-plane, corresponding to an azimuth angle $\varphi = 0$, a very stable beamwidth of 140° at -10 dB is maintained from 57 to 86 GHz: almost no side lobes appear. In E-plane, corresponding to an azimuth angle $\varphi = 90°$, the -10 dB beamwidth decreases from 140° to 70° when frequency increases. Sidelobes appear at 71 GHz and reach a maximum level of -9 dB at 86 GHz (compared to maximum broadside radiation). All those simulations demonstrate an exceptional high efficiency and large bandwidth performance for this type of antennas.

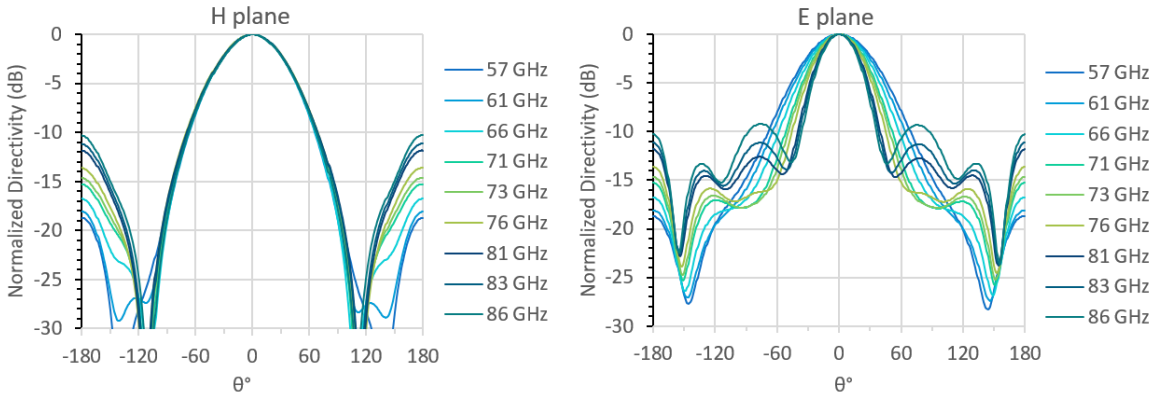

Figure III.11 Simulated normalized directivity versus elevation angle θ in E and H-planes of the unit-cell.

The next step was to design the feeding network to distribute the power between the elements of an array composed of this unit-cell to meet the gain requirements.

III.3 PATCH ANTENNA ARRAY FED BY A DIELECTRIC-FILLED WAVEGUIDE CORPORATE NETWORK

III.3.1 2×2 array elements spacing

To set the spacing between the radiating elements of the array, we first simulated a 2×2 array using a waveguide port at each waveguide's input. In order to choose the best spacing, two parameters were particularly studied:

- Side lobes level to be kept as low as possible to further respect ETSI RPE in a larger array.
- Mutual coupling between the elements to be kept as low as possible.

After optimizing the spacing between the array elements to limit the side lobes and mutual coupling, the chosen distances in H and E-plane are set to 3 mm and 3.2 mm respectively, as reported in Figure III.12 (close to $0.7\lambda_0$ at 71 GHz).

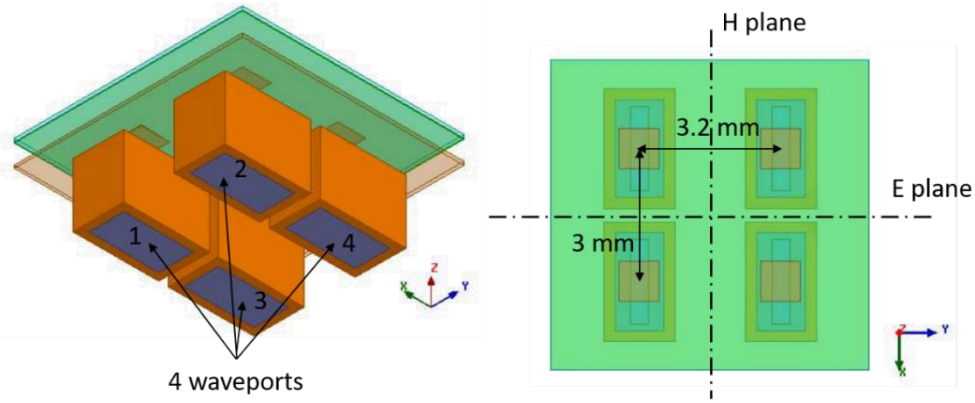

Figure III.12 3D view (left) and top view (right) of the simulation model of the 2×2 array.

Simulated S_{ij} coefficients, describing the port-to-port isolation between the array elements, are found to be below -15 dB all over V and E bands. More particularly magnitude of the Sij coefficients are higher for ports aligned along "y" than Sij coefficients corresponding to ports aligned along "x". This can be naturally explained because those ports in the "y" direction are closer. The port-to-port isolation level was found acceptable in our case because we're designing a fixed beam antenna. Furthermore, the matching level (S_{ii}) was not altered because of the presence of other adjacent radiating elements and stayed below -10 dB from 56 to 90 GHz as shown by $|S_{11}|$ in Figure III.13. All the other $|S_{ii}|$ superposed with S_{11} and hence are not shown for sake of clarity. Obtained simulated broadside realized gain varies between 12 dB to 15 dB in E and V bands. Radiation patterns, presented in Figure III.14, show a -10-dB HBW in E plane ranging between 19° and 36° and between 25° and 40° in H plane with a side lobe level always under -10 dB. Following these satisfactory results, the chosen inter-element distance will be used in the following array designs presented in this chapter.

To estimate the gain of higher complexity arrays obtained by the fixed spacing, we applied the array factor in HFSS to the unit-cell radiated fields. Results are illustrated in Figure III.15

for 16×16 elements and 32×32 elements arrays. The computed estimated gain of the 16×16 elements array lies between 32 and 33.6 dBi, hence it is yet insufficient to respect ETSI requirements. On the other hand, the estimated gain of the 32×32 array is above 39 dBi in E-band, consequently satisfying ETSI requirements. However, great attention in designing the feeding network is needed to limit the insertion-loss and return-loss to 1 dB and respect the 38 dBi gain requirement in E-band.

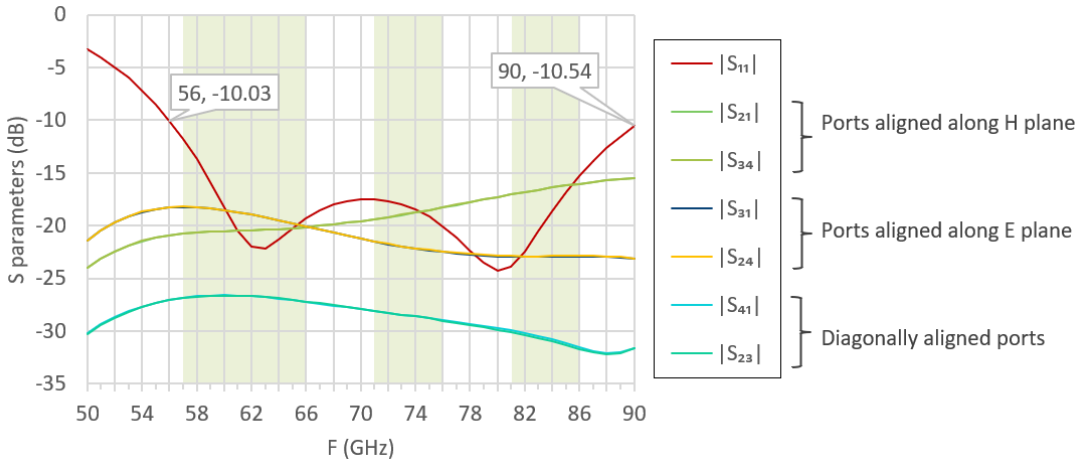

Figure III.13 Simulated reflection and port-to-port isolation coefficients versus frequency of the 2×2 array fed by four waveguide ports.

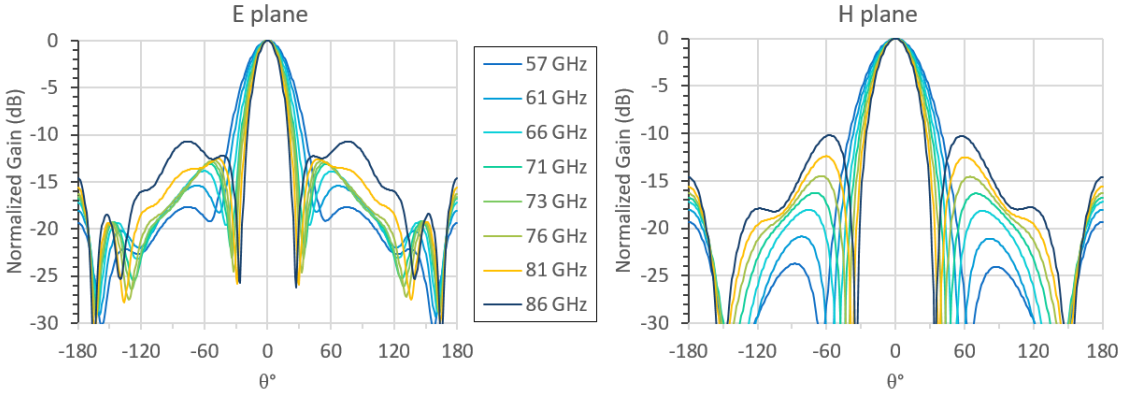

Figure III.14 Normalized radiation patterns in E and H plane of the 2×2 array for different E and V bands frequencies.

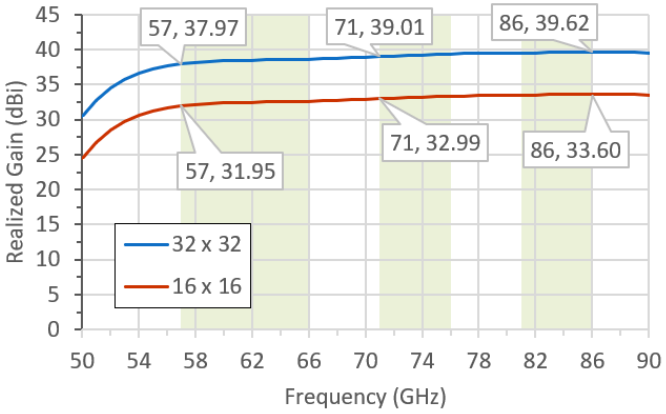

Figure III.15 Estimated broadside realized gain of a 32x32 and a 16x16 elements array antenna estimated by applying the array factor to the simulated unit-cell (from HFSS).

III.3.2 Corporate dielectric-filled waveguide feeding network

III.3.2.a The feeding network elements: T-junctions and twists

To avoid narrowing the achieved wide bandwidth (> 40%) covering both E and V bands by the unit-cell, we proceeded to design a corporate waveguide feeding network to feed our single radiating elements. The first step was to design T-junctions consisting on a simple three-port network that can be used for power division or power combining to feed the array elements by an equal signal (equal amplitude and phase). Figure III.16 and III.17 show the two main types of waveguide T-junctions: E-plane and H-plane T-junctions respectively. Both junctions divide the power equally between their two outputs. The E-field vectors at the outputs of the E-plane T-junction are orthogonal and 180° out of phase, whereas the E-field vectors at the outputs of the H-plane T-junction are collinear and in-phase. However, according to the S-parameter analysis of a 3-port-network like the T-junction, it is well known that it is impossible for a general lossless three-port junction of arbitrary symmetry to present matched impedances at all three arms [III.23].

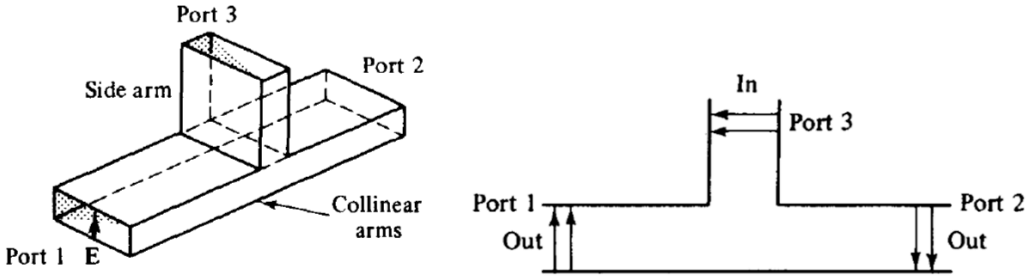

Figure III.16 3D view (left) and transversal view (right) of an E-plane T-junction power divider from [III.23].

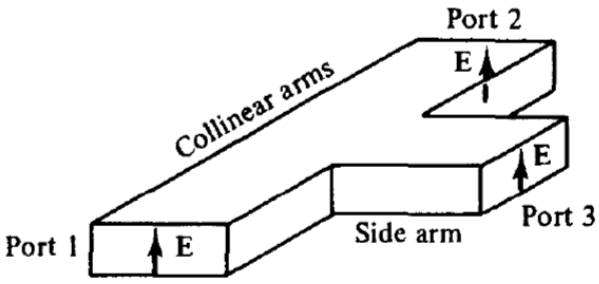

Figure III.17 3D view of the H-plane T-junction power divider from [III.23].

The lossless T-junction dividers can all be modeled as a junction of three transmission lines, as shown in Figure III.18. The fields within each of the waveguide regions are usually completely described by only a single propagating mode. In contrast the complete description of the fields within a discontinuity region generally requires, in addition to the dominant propagating mode, an infinity of non-propagating modes. The non-propagating nature of the higher-mode transmission lines restricts the complication in field description to the immediate vicinity of the discontinuity. Hence, the discontinuity fields can be effectively regarded as "lumped." Such discontinuities can be represented by means of lumped-constant equivalent circuits [III.23].

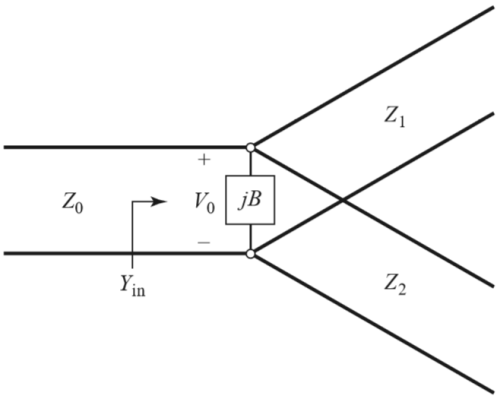

Figure III.18 Schematic of the transmission line model of a lossless T-junction divider.

In other words, there may be fringing fields and higher order modes associated with the discontinuity at such a junction, leading to stored energy that can be accounted for by a lumped susceptance, "B", leading to the equivalent circuit illustrated in Figure III.18. In order, for the divider, to be matched to the input transmission line of characteristic impedance Z_0, we must have,

$$Y_{in} = jB + \frac{1}{Z_1} + \frac{1}{Z_2} = \frac{1}{Z_0} \tag{III.2}$$

If all the transmission lines are assumed to be lossless (or at least of low-loss) like in the waveguide case, then, the characteristic impedances are real. If we also assume B = 0, then (III.2) reduces to

$$\frac{1}{Z_1} + \frac{1}{Z_2} = \frac{1}{Z_0} \tag{III.3}$$

In practice, if the susceptance B is not negligible, some type of discontinuity compensation or a reactive tuning element can usually be used to cancel this susceptance, at least over a narrow frequency range. The respective impedances of the output transmission line Z_1 and Z_2 can be selected to provide various power division ratios. Thus, for a 50 ohms input line, a 3 dB (equal split) power divider can be achieved by using two 100 ohms output lines. If necessary, quarter-wave transformers can be used to bring the output line impedances back to the desired value. If the output transmission lines are matched, then the input transmission line will be matched. There will be no port-to-port isolation between the two output ports, however and there will be a mismatch looking into the output ports [III.24].

One example of using reactive tuning elements is proposed in [III.25] (cf. Figure III.19). An H-plane T-junction is matched using an inductive post and two cylindrical capacitive posts. By tuning the posts dimensions, a measured return loss more than 20 dB was achieved over 6% of bandwidth. Depending on the inductive post position and dimensions, an equal power division can be applied by positioning it equidistantly from the output ports (2 and 3) or displacing it from the middle for an unequal power division.

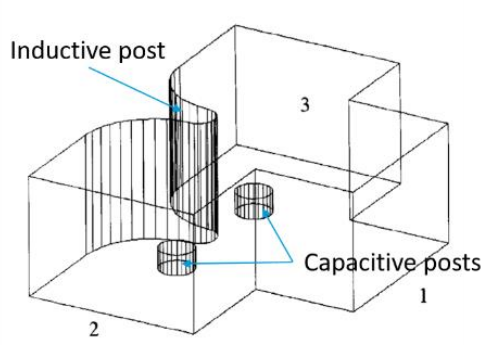

Figure III.19 3D view of a T-junction (H-plane) matched by an inductive post and two capacitive posts from [III.25].

Following the same concept, we designed dielectric-filled waveguide T-junctions to compose the feeding network of the patch array. Since, we're designing a 2D array, we'll need a divider in each transversal plane of this array (YZ and ZX planes indicated in Figure III.20 and III.21), hence both E and H T-junction were needed. Then the junctions are alternated, by making one connection in E-plane and the next one in H-plane leading to a final single input. Our main goal was to achieve a return loss of at least 15 dB over E and V-band for each divider to ensure a low return loss after composing the final structure.

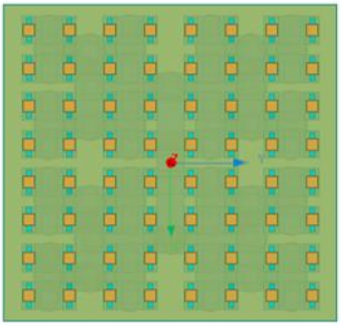

Figure III.20 Top view of an 8×8 array.

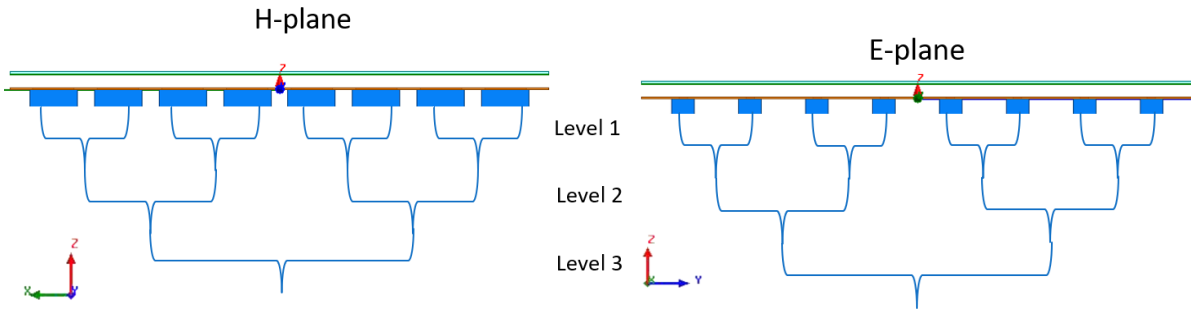

Figure III.21 Transversal view of the sketch of an 8×8 array feeding in E and H-plane.

The designed H-plane T-junction with dielectric filled waveguide featuring one inductive post and two capacitive posts is illustrated in Figure III.22. To feed the single patch elements placed along the ZY plane indicated in Figure III.22, we added chamfered bends to align the outputs along the x axis. Chamfered bends are less cumbersome than circular bends and hence are more convenient to be used with the waveguide divider. In fact, by using a 45° bend in the waveguide, the signal is reflected, and using a 45° surface the reflections occur in such a way

that the fields are left undisturbed [III.26]. Note that the metallic (copper) boundaries are not shown in the illustration for a clearer view. Using HFSS, the dimensions and locations of the posts along with the chamfer distance were optimized to obtain the best insertion and return loss at all ports. All the optimized parameters values, are listed in Table III.4.

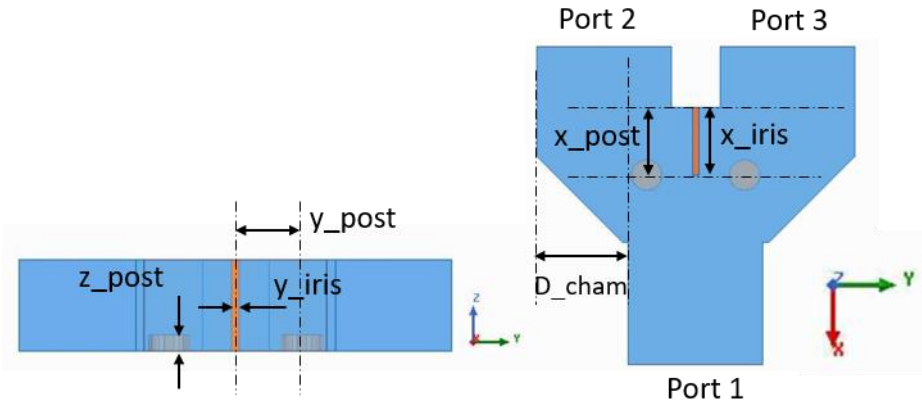

Figure III.22 Transversal view (left) and top view (right) of the designed dielectric-filled waveguide H-plane T-junction with inductive and capactive posts.

x_iris	y_iris	D_cham	x_post	y_post	z_post	r_post
1.1	0.2	1.4	1.1	0.5	0.2	0.25

Table III.4 Optimized parameter values (in mm) of the designed H-plane T-junction.

Simulated results featured a return loss at port 1 exceeding 15 dB, covering over 55% of bandwidth (47 to 87 GHz) (cf. figure III.23 (a)). Over this bandwidth the magnitudes of S_{21} and S_{31} (equal to the magnitudes of S_{12} and S_{13} respectively) were found to be under 0.1 dB and the maximum difference between them was found to be less than 0.01, hence, S_{31} was not shown. Additionally, the two output signals were found to be perfectly in-phase as shown in figure III.23 (b).

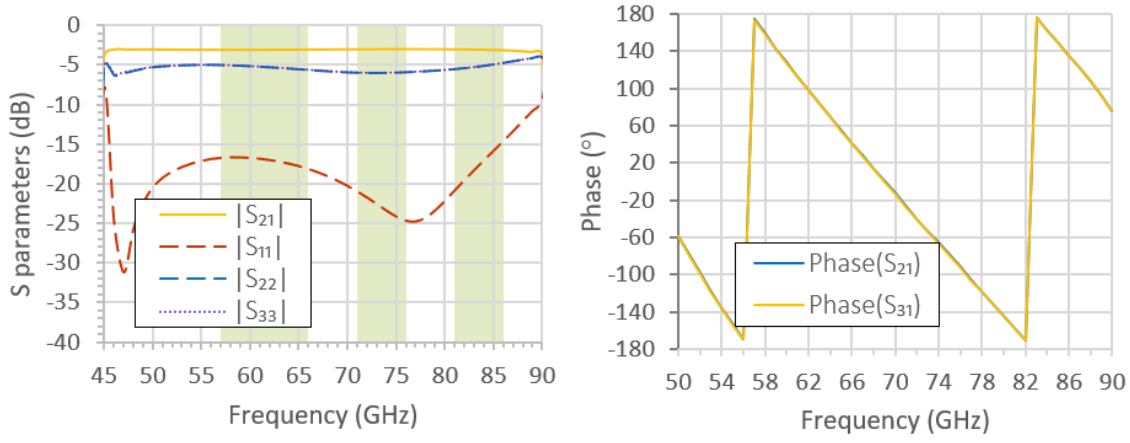

(a) (b)

Figure III.23 (a) Simulated S-parameters and (b) phase response at the outputs versus frequency of the optimized H-plane T-junction.

The divider's wide-bandwidth performance was achieved owing to the employed thin inductive post (200 µm width). However, this dimension approaches the limits of standard 3D

printing resolution, therefore, it might be a critical factor during fabrication. On the other hand, as predicted, a poor matching was found looking at the two-output port, nonetheless, it doesn't affect the insertion losses from port 1 to the ports 2 and 3 and vice versa.

Following the same principle applied for the H-plane T-junction, we designed a dielectric-filled E-plane T-junction. In this case, only an inductive post was sufficient to obtain good wideband matching. The designed divider is illustrated in Figure III.24 and optimized dimensions are listed in Table III.5.

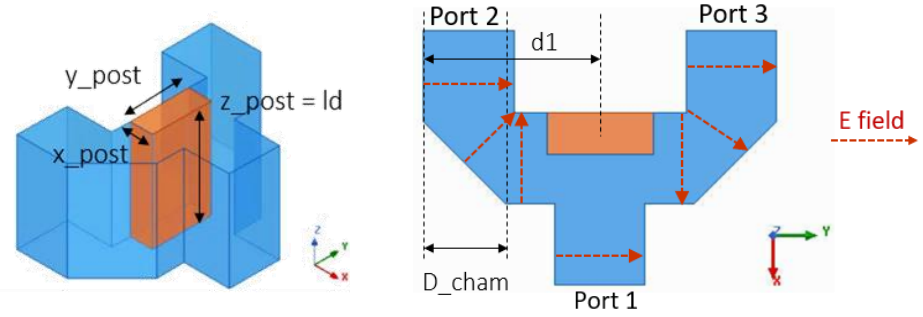

(a) (b)

Figure III.24 (a) 3D view and (b) Top view of the designed dielectric-filled waveguide E-plane T-junction and electric field vector distribution.

D_cham	x_post	y_post	z_post
1	0.5	1.3	2.2

Table III.5 Optimized parameter values (in mm) of the designed E-plane T-junction.

Oppositely to the H-plane junction, it was found from simulations that E-plane junction doesn't need a thin iris to be matched which makes it more suitable for manufacturing. Like the H-plane divider, chamfered bends were added to this junction. Those bends not only aim to connect the waveguide ends to the patch but also to align the phase of the output signals as indicated by the vector E-field in Figure III.24. Simulated results are as follow, from 57 to 86 GHz (cf. Figure III.25 (a) and (b)):

- $|S_{21}|$ and $|S_{31}| < -3.1$ dB
- $|S_{11}| < -19$ dB
- $|S_{33}|$ and $|S_{22}| < -6$ dB
- Phase(S_{21}) - Phase(S_{31}) = 0

The optimized T-junctions will be used to connect the waveguides feeding the array elements at the first level of the feeding network. However, after proceeding to the design of the junctions for the next levels (cf. Figure III.21), which demand larger distance between their outputs, we noticed that the matching bandwidth was decreasing with increasing distance between the outputs as demonstrated in figure III.26 (a) and (b). Notice how, by increasing d1 from 2.15 mm to 3.75 mm the -20 dB-impedance-bandwidth drastically decreases from 30 GHz to less than 10 GHz. We suppose that this effect is due to a capacitive effect which depends on the distance between the chamfered edge and the post, leading to shrink the loop on the impedance locus.

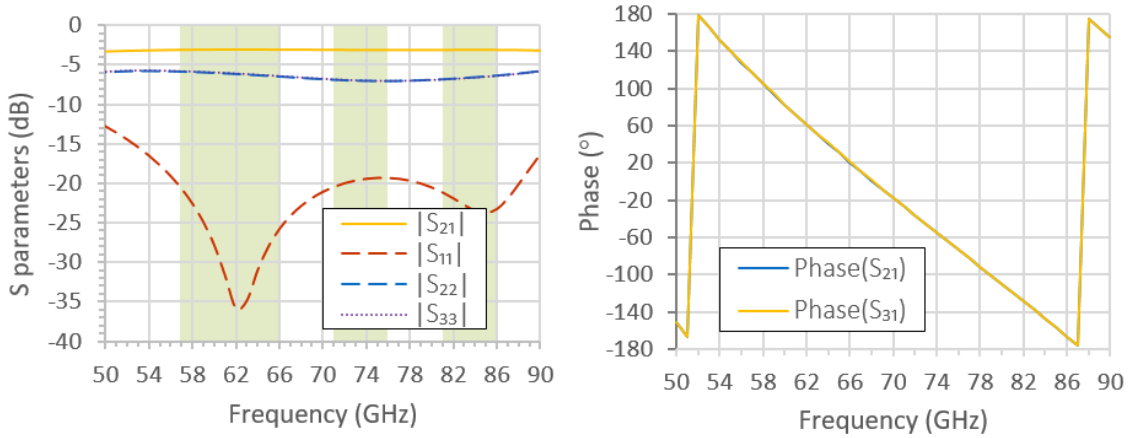

(a) (b)

Figure III.25 (a) Simulated S-parameters and (b) phase response at the outputs versus frequency of the optimized E-plane T-junction.

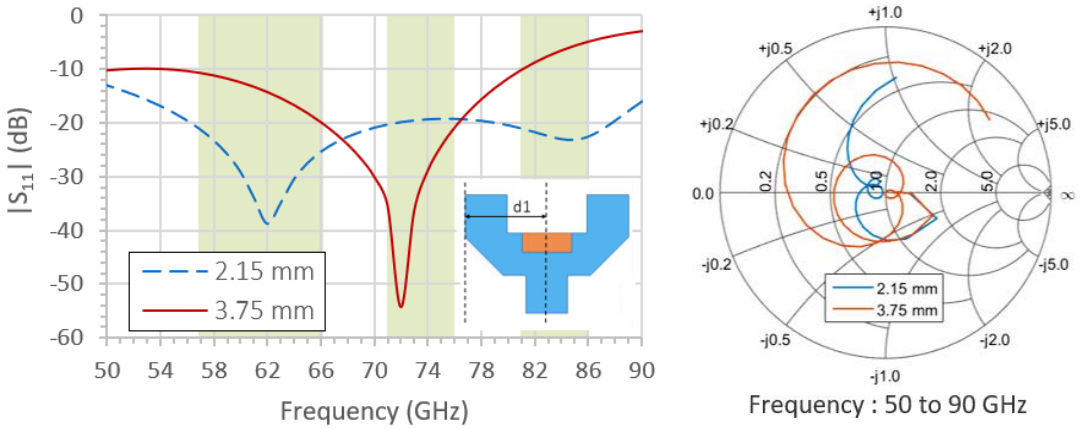

(a) (b)

Figure III.26 (a) Simulated $|S_{11}|$ and (b) input impedance of the E-plane T-junction versus frequency and distance d1.

To address this issue, we kept the distance d1 fixed to maintain the wide bandwidth performance and we added a 180° bended waveguide as demonstrated in figure III.27 (a). Owing to this configuration, we can change the distance between the outputs, d2, without changing the distance d1, hence the wide impedance bandwidth can be conserved. This is verified by the simulations shown in figure III.27 (b). Another purpose of adding a 180° bend is to be able to go downwards and upwards in the composition of the feeding network in the vertical direction, taking benefit of the existing space between the previous stage dividers. This operation is necessary to optimize and minimize the thickness of the feeding network. Following the same methodology, junctions with consecutive 90° bends can be added to orient the outputs along the "-x" direction depending on the direction along which we want to proceed deploying the feeding. The same concept can be applied to the H-plane junction.

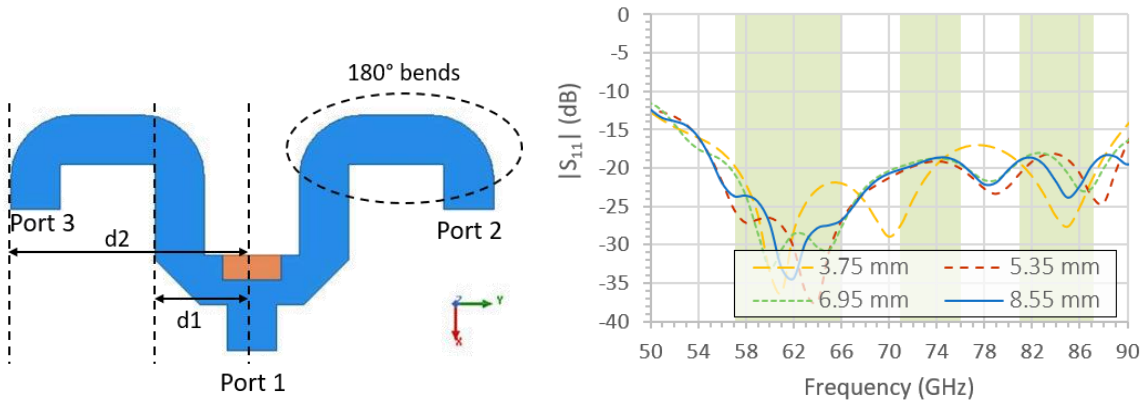

(a) (b)

Figure III.27 (a) Transversal view of the new design of the dielectric-filled waveguide E-plane T-junction with a 180° bend at each output and (b) Simulated $|S_{11}|$ versus frequency and distance d2.

Due to the fabrication limitations that can be faced because of the thin shape of the iris implemented in the H-plane T-junction design, we introduce here a third dielectric-filled waveguide component, namely a twist that can be used to replace the H-plane junction. A gradual twist in the waveguide is used to turn the polarization of the waveguide [III.26]. By employing the twist, we can use the previously designed E-plane junction to divide powers along both E and H-planes of the array as indicated in Figure III.28.

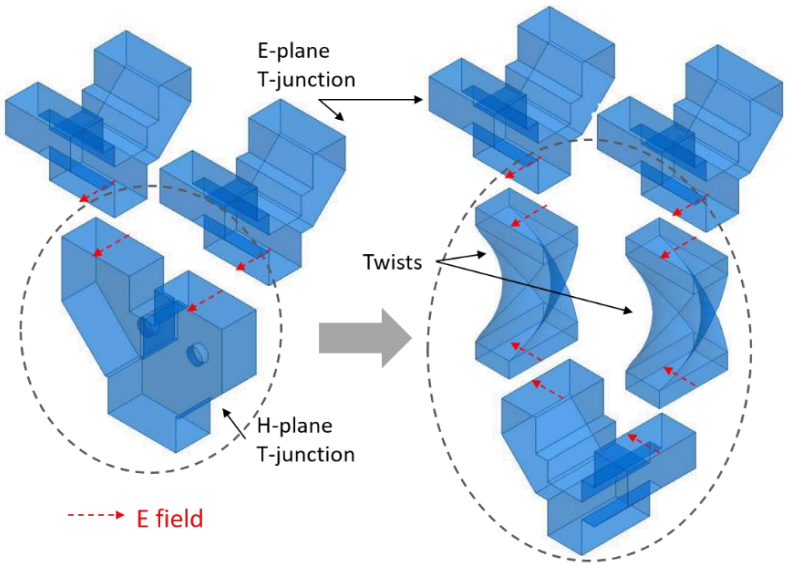

Figure III.28 H-plane and E-plane junctions solution Vs E-plane and twists solution.

Figure III.29 (a) and (b) show the design model of the twist and the simulated transmission coefficient versus frequency and the length of this twist, respectively. Starting from a 3-mm length, the twist has less than 0.1 dB of transmission loss in our bands of interest. Thus, we chose to set this length for the twists that will be used in all the following array feeding networks presented in this chapter.

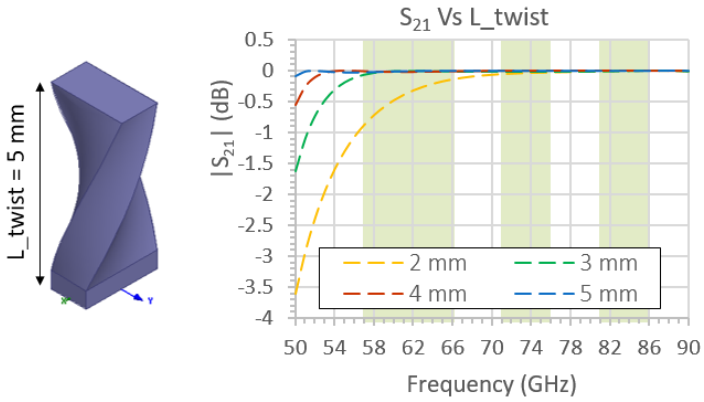

Figure III.29 (a) 3D view of a dielectric-filled waveguide twist and (b) corresponding simulated insertion loss $|S_{21}|$ versus frequency and the twist length.

III.3.2.b 2×2 to 32×32 Arrays

Our first 2×2 array feeding network consists in using two E-plane junctions at the first level to make the level 1 connections in E-plane (x-axis). Then a twist and another E-plane junction are employed to make the level 1 connection in H-plane (y-axis), as shown in Figure III.30. The simulated return loss of this structure is higher than 12 dB as illustrated in figure III.31 (a). The simulated broadside realized gain ranges between 12.5 and 15 dBi and total efficiency exceeds 90% all over the V and E bands (cf. figure III.31 (b)).

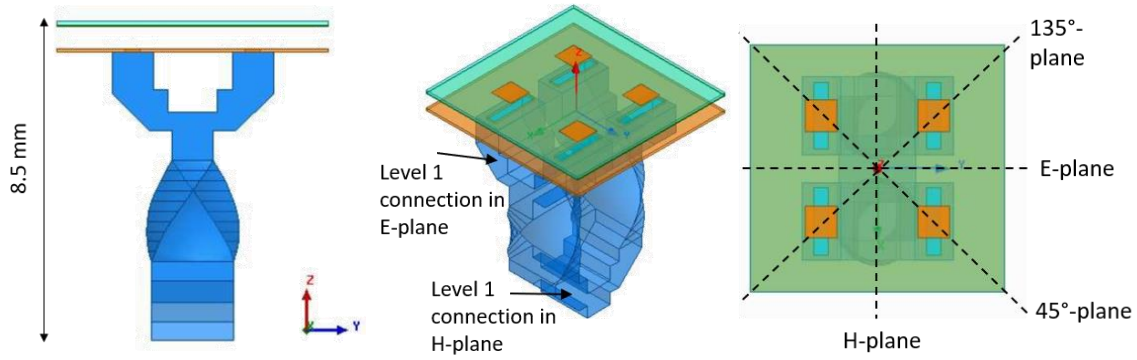

(a) (b) (c)

Figure III.30 (a) Transversal view, (b) 3D view and (c) top view of the 2×2 array design with feeding network composed by E-plane junctions and twist.

Normalized radiation patterns in E and H-planes are given in figure III.32 at several frequencies, however ETSI 47-66 class 2 RPE mask is only respected between -70° and 70° and ETSI 71-86 RPE mask is not respected at all in H-plane. Nevertheless, the radiation patterns in the 45° and 135° planes have lower side lobes and are more likely to respect ETSI RPE for higher array sizes. This implies that the antenna should be rotated by 45° during installation to respect ETSI standards (the same technic was used for the Sencity® Matrix antenna [III.13]).

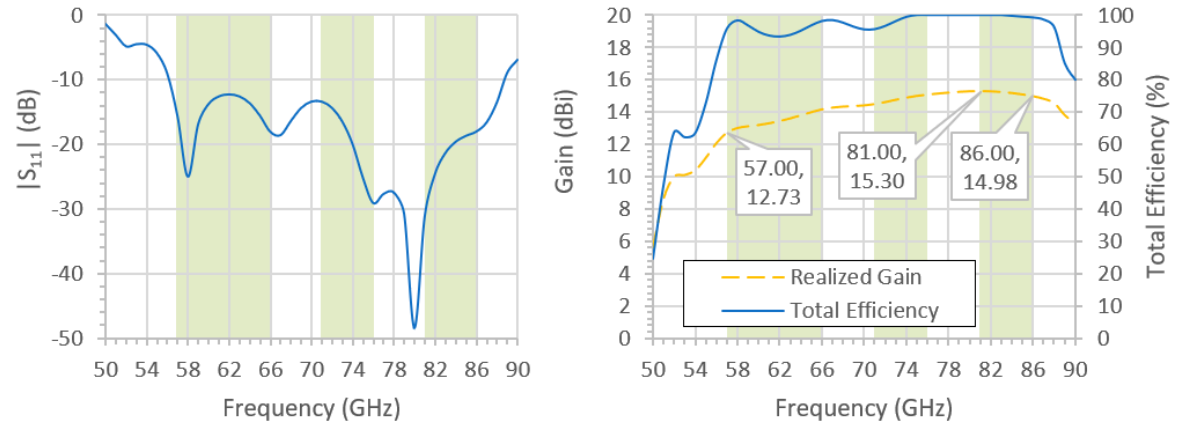

(a) (b)

Figure III.31 (a) Simulated $|S_{11}|$ and (b) broadside (along z) realized gain versus frequency of the 2×2 array from Figure III.30.

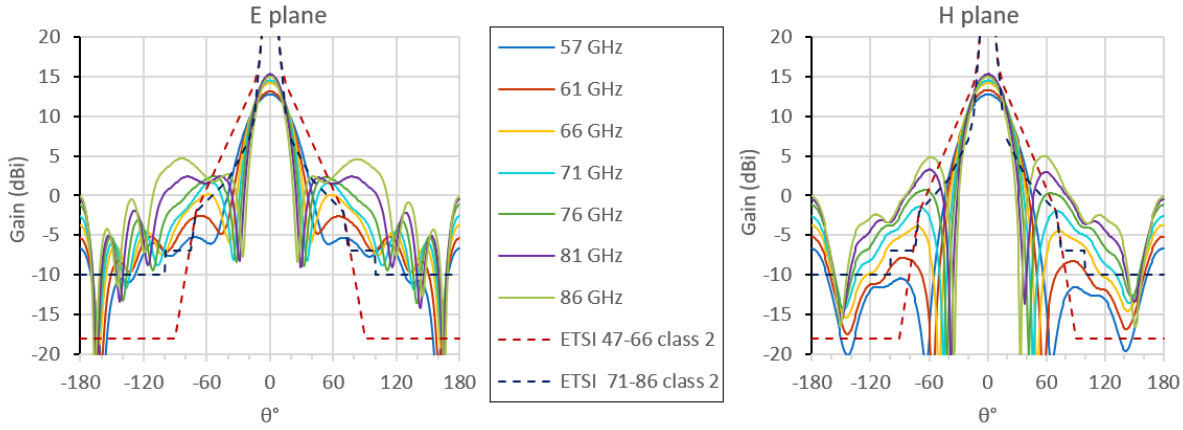

Figure III.32 Simulated gain versus elevation angle of the 2×2 array in E-plane (left) and H-plane (right) for various frequencies in E and V bands.

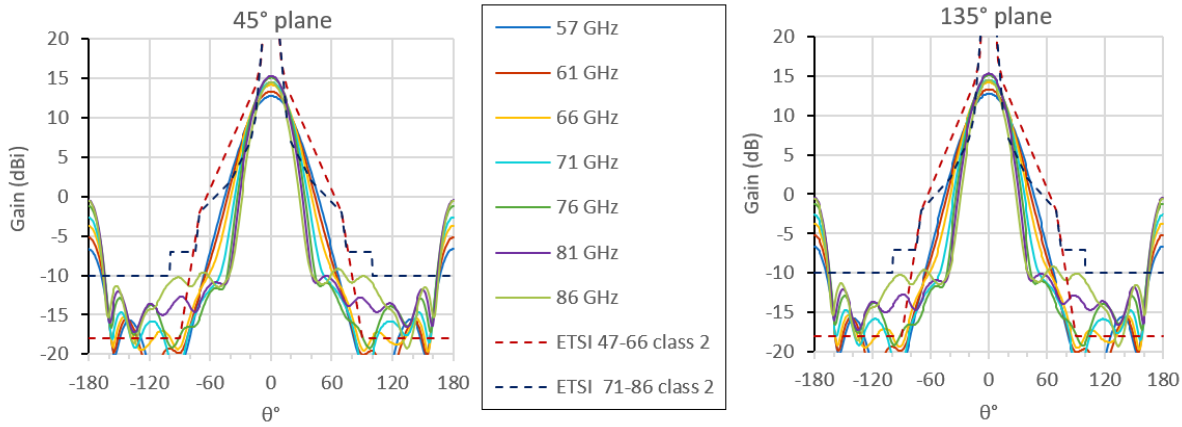

Figure III.33 Simulated gain versus elevation angle of the 2×2 array in 45° (left) and 135° plane (right) for various frequencies in E and V bands.

Following the same alternation between twist and E junctions, we proceeded to the design of an 8×8 elements array which was the biggest array we could simulate with a full electromagnetic simulation, given the memory resources we had available at this time. It's worth to mention that we couldn't use symmetry planes in simulations because of the twist

unsymmetrical disposition. Figure III.34 and III.35 shows the designed full 8×8 array. The feeding network is composed out of the 2×2 feed network we presented earlier connected to twists and E-plane junctions with 180° bends, employed to fill the gaps that exist between the former stages of the network.

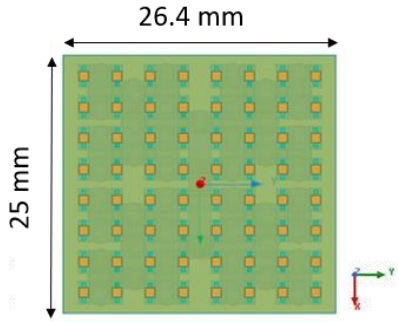

Figure III.34 Top view of the 8×8 elements patch array fed by dielectric-filled waveguide feeding network composed by E-plane dividers and twists.

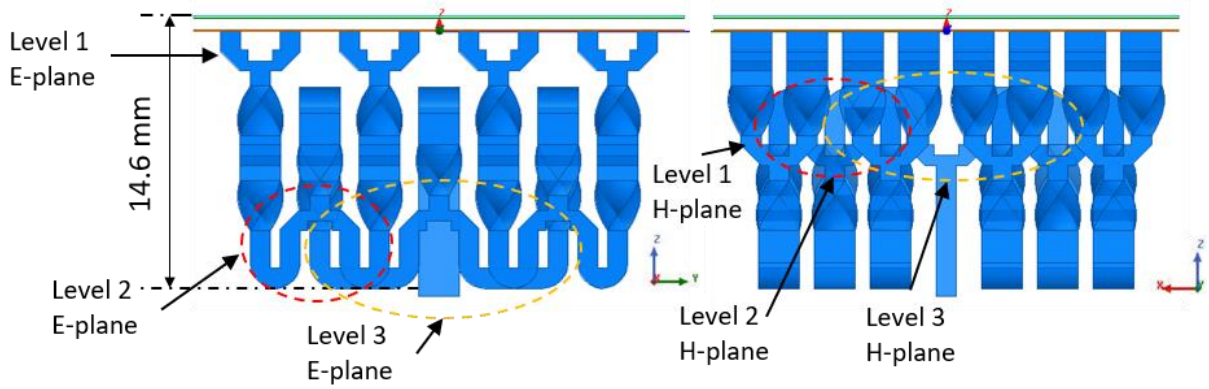

Figure III.35 Transversal views of the 8×8 elements patch array fed by dielectric-filled waveguide feeding network composed by E-plane dividers and twists.

Simulated return loss, featured in Figure III.36 (a), is higher than 10 dB from 58 to 86 GHz with slight overshoots however, close to 57 GHz, reaching 5 dB. On the other hand, the simulated broadside realized gain ranges between 21 dBi and 26 dBi with losses with respect to directivity between 3 to 1 dB (cf. figure III.36 (b)). Figure III.37 illustrates the radiation patterns in the 45° and 135° planes of the array, respecting the ETSI 47-66 and 71-86 class 2 between -170° and 170° at all frequencies.

Giving the limited memory resources we had available and to simulate at least the matching at the input of the larger arrays we used Keysight ADS software. By importing the simulated network parameters of each waveguide component from HFSS to ADS to create a library, we were able to simulate S_{11} at the input of the feeding structure. An example of a 4×4 array ADS simulation is illustrated in figure III.38. Each component's network parameters have been imported from HFSS into an S-parameter block in ADS and connected to reconstruct the feeding network. Figure III.39 compares the simulated $|S_{11}|$ of the 8×8 array using ADS and HFSS to check for ADS results reliability. An acceptable agreement was found between the two methods.

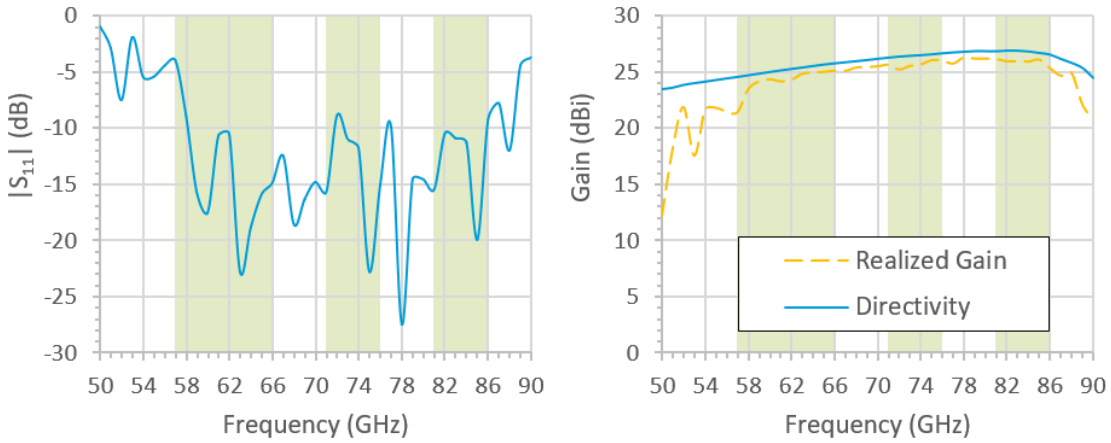

(a) (b)

Figure III.36 (a) Simulated $|S_{11}|$ and (b) simulated broadside (along z) realized gain of the 8×8 array from Figure III.34.

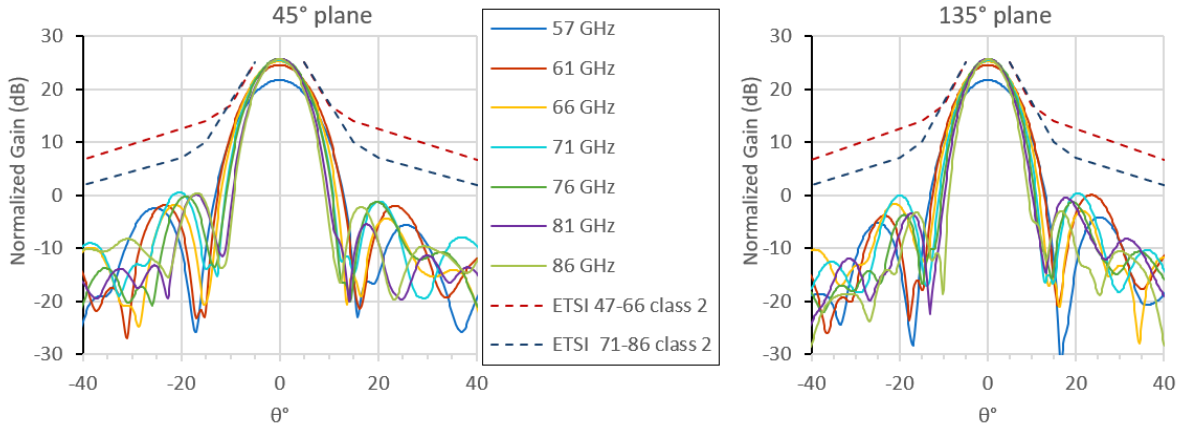

Figure III.37 Gain versus elevation angle in 45° (left) and 135° (right) planes of the 8×8 patch array from Figure III.34 and III.35 and compared with ETSI RPE.

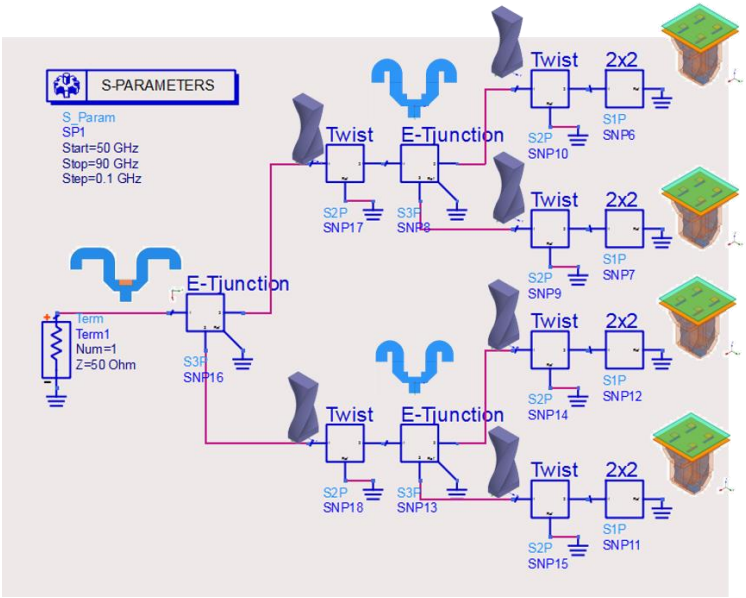

Figure III.38 ADS schematic simulation of the 4×4 dielectric-filled waveguide feeding network.

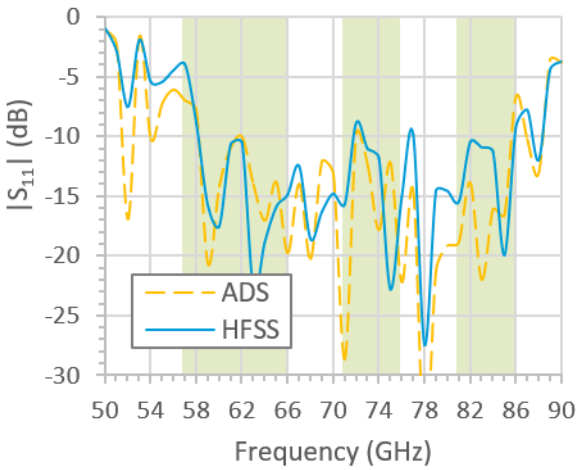

Figure III.39 Comparison between simulated $|S_{11}|$ of the 8×8 array obtained by ADS and HFSS simulations respectively.

As the 8×8 previous array demonstrated very interesting performance on a huge bandwidth, in the same manner, we designed the 32×32 elements array, depicted in figure III.40 and III.41. The size of the designed array is equal to 9.7 cm ×10.3 cm × 1.5 cm, which is very competitive compared to the commercial solutions mentioned in table III.2. For example, the dimensions of the 32 dBi gain array proposed by Gap Waves are 9.3 cm × 9.3 cm × 1.58 cm. Simulated matching using ADS, by means of the method described earlier is shown in Figure III.42. Resulting simulated return loss exceeded 10 dB from 59 GHz to 87 GHz and exceeded 7.5 dB over V and E-band.

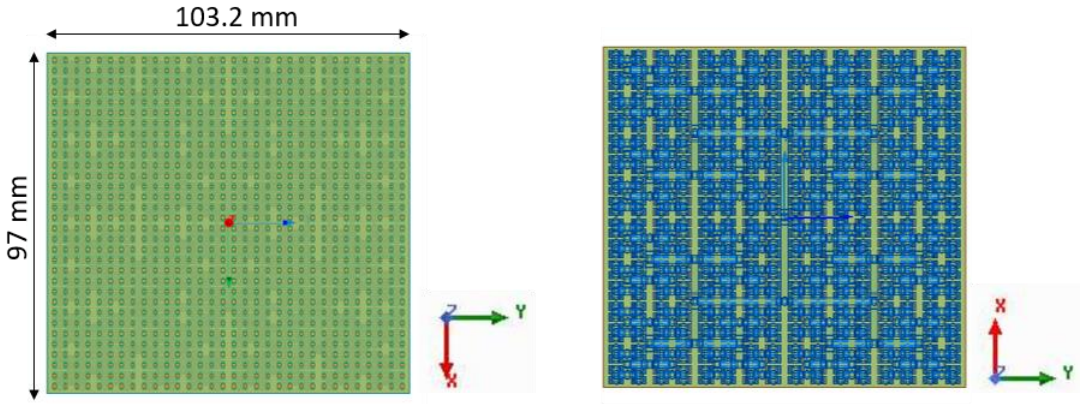

Figure III.40 32×32 patch array slot coupled to dielectric_filled waveguide coporate feeding network (Top and bottom views).

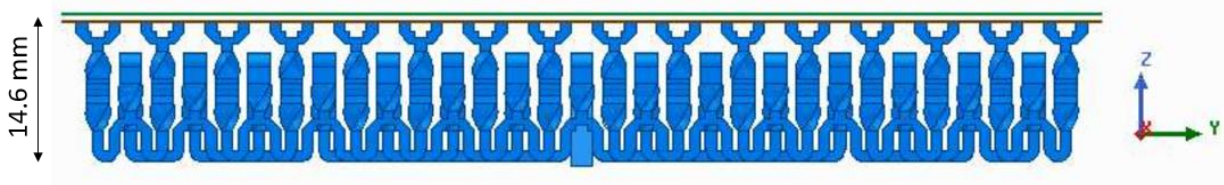

Figure 41 32×32 patch array slot coupled to dielectric-filled waveguide corporate feeding network (Transversal view).

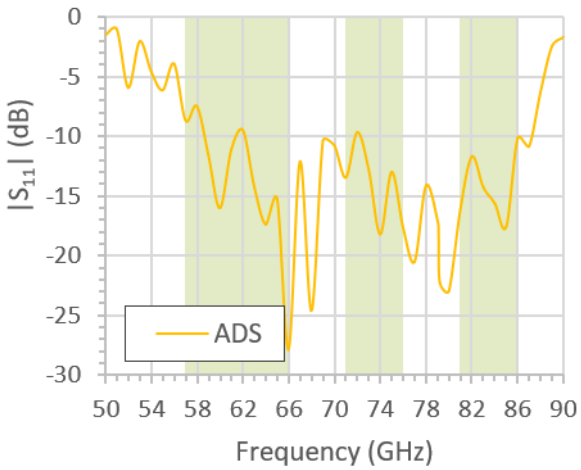

Figure 42 Simulated $|S_{11}|$ versus frequency of the 32×32 array using ADS.

Since we couldn't simulate the realized gain, RG, of the 32×32 array, we estimated it by applying the following calculation,

$$RG = G_{AF} - L_{mismatch} - L_d \quad \text{(III.4)}$$

Where $L_{mismatch}$ and L_d are the mismatch and dielectric losses respectively and G_{AF} is the gain calculated by the applying the array factor on the single element. The mismatch loss is giving by,

$$L_{mismatch} = 10\log(1 - |S_{11}|^2) \quad \text{(III.5)}$$

To estimate L_d, we simply considered the simulated losses between directivity and gain of the 8×8 array excluding the mismatch loss. This loss is mainly due to dielectric loss and simulations showed that its value is close to 0.7 dB over V and E-bands. By comparing the single feed length from the common input to one element of the 8×8 array (71 mm) to that of the 32×32 array (182 mm), we can esimate that L_d should be equal to 1.8 dB for the 32×32 array case. The expected realized gain calculated from (III.4) is plotted in Figure 43. The calculated realized gain of the 32×32 array was found above 35.5 dBi in V-band and ranged between 37 and 37.4 dBi over E-band. This method is certainly not precise but it permits to have an idea about the final gain.

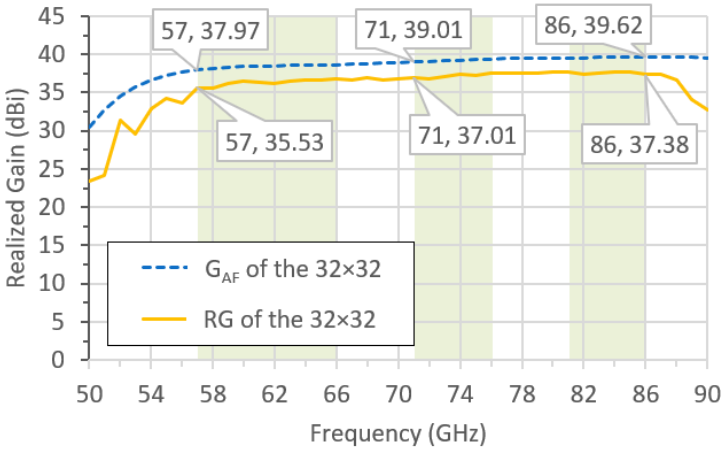

Figure III.43 Computed broadside realized gain of the 32×32 array by applying equation (III.4).

The patch arrays were fabricated using standard PCB technology and FR4 substrate Nelco® N4000-13 EP™. The buildup of the PCB simply consisted on a 100 µm core layer, a metallic layer comprising the patches and a solder mask, as shown in Figure 44 (III.a). Fabricated patch arrays are shown in Figure 44 (III.b). The substrate was dedicated to be held on a foam substrate of 600 µm thickness emulating air. The chosen foam was ROHACELL® [III.27] with measured electrical characteristics at 60 GHz very close to air; $\varepsilon_r = 1.08$ and $\tan\delta = 0.005$.

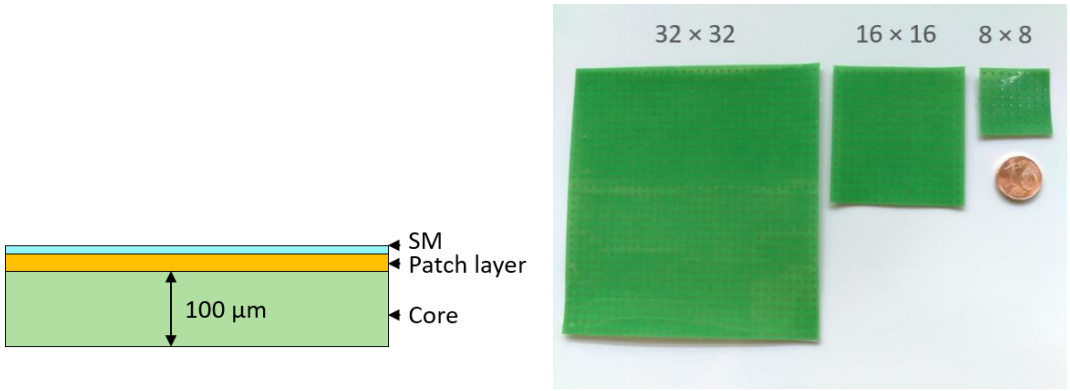

(a) (b)

Figure III.44 (a) One layer build up used to print the PCB patch arrays (b) Fabricated PCB patch arrays.

On the other hand, many fabrication processes have been considered for the prototyping of the proposed feeding network. The first method was to 3D-print the dielectric filling of the waveguide using SLS and high density PE (HDPE) powder [III.28-29]. However, the metallization of this plastic was found to be more complicated than expected because it cannot be metallized by electro- neither electroless plating methods. To metal-coat the dielectric waveguide, we finally decided to use an innovative sputter-coating process developed by JetMetal™ [III.30] to deposit a 1 µm-silver-layer. However, we received no positive answer about the possibility of fabricating our feeding network in HDPE. Another solution we studied for fabrication is injection molding [III.31]. The idea was to 3D-print an Aluminum mold by DMLS to simplify the fabrication process and then to inject the HDPE into the mold which would also serve as the metallic boundary of the structure. Unfortunately, we also did not receive any positive answer following our discussions with the corresponding manufacturing companies.

Hence, modifying the antenna feeding structure to simplify the fabrication steps seemed crucial. To encounter this difficulty, we decided to limit the use of the dielectric-filled waveguides to the first level of the divider (2×2) as illustrated in Figure III.45. Furthermore, by adding a transition from a dielectric-filled waveguide to a hollow metallic waveguide, we can continue to construct the feeding network using only hollow metallic waveguides. In fact, the use of the dielectric waveguide for the first level connections is inevitable since the spacing between the antennas (3 mm and 3.2 mm) doesn't permit to use a hollow waveguide. Nonetheless, the fabrication of prototypes of the presented antennas in this section is still under investigation.

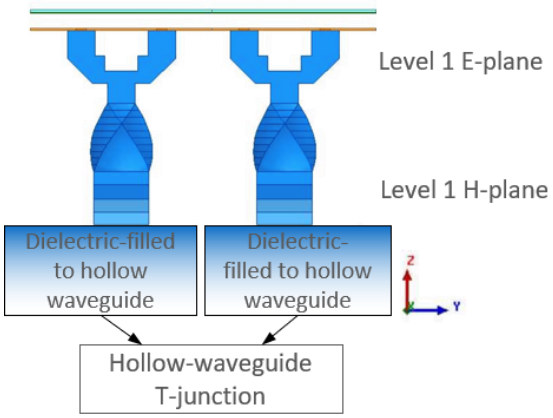

Figure III.45 Schematic of the proposed hybrid network of dielectric-filled and hollow metallic waveguides.

III.3.3 Corporate dielectric-filled and hollow waveguide feeding network

As explained in the previous paragraph, aiming to simplify the fabrication process, we studied the possibility of designing a hybrid dielectric-filled/hollow metallic waveguide feeding network. We limited the use of the dielectric filled waveguide to the first level of the network only (directly connected to the antenna elements) forming the 2×2 subset. In this context, we needed to investigate the designs of a transition from dielectric-filled to hollow waveguide.

III.3.3.a Dielectric-filled waveguide to hollow waveguide transition

To design such a transition, we studied two possibilities. The first solution consists in a slot coupling mechanism between the two waveguides via a transformer plate [III.32] as depicted in Figure III.46 (a). A wide slot in the transformer plate acts as a quarter-wavelength waveguide to transform the characteristic impedance. The slot plate is used as an intermediate plate to fill the gaps between different sizes of slots. This transition presented an insertion loss under 0.1 dB and a return loss above 20 dB over 20% of bandwidth (cf. figure III.46 (b)). Nonetheless, the achieved impedance bandwidth is limited relatively to our band of interest even though it is simple to fabricate.

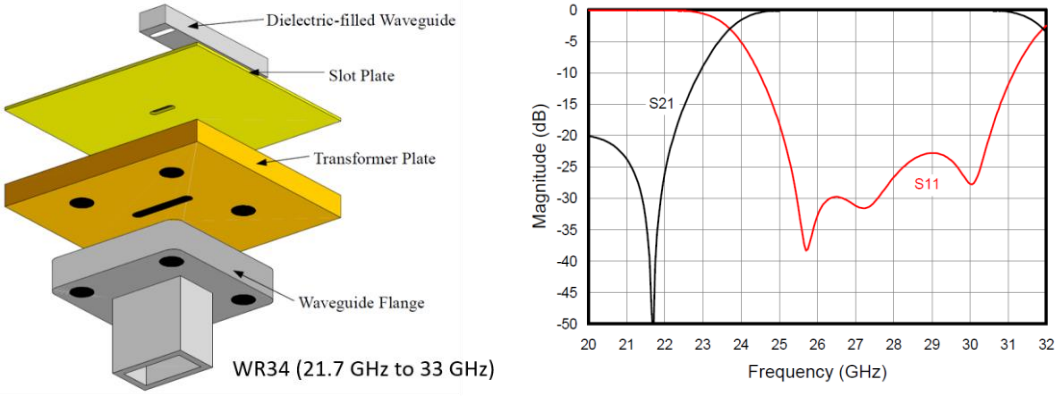

(a) (b)

Figure III.46 (a) Exploded view of the dielectric-filled to hollow waveguide transition using a transformer plate and (b) corresponding simulated S-parameters versus frequency [III.32].

Another solution featuring a wider response (-20dB-impedance-bandwidth about 40%) consists on using a tapered dielectric transition performing a smooth impedance transformation between the two types of waveguides [III.33]. The geometry of the transition is shown in Figure III.47. In this transition, the slab direction is parallel to the electric field (cf. Figure III.47 (b)), hence no variation of the fields along the air-dielectric interface occurs. Consequently, the electric field remains transverse to the direction of propagation and the appearance of additional superior propagation modes is avoided. The partially-filled waveguide will serve as a natural transition from hollow to dielectric-filled waveguide, thanks to the linearly tapered dielectric and waveguide metal walls.

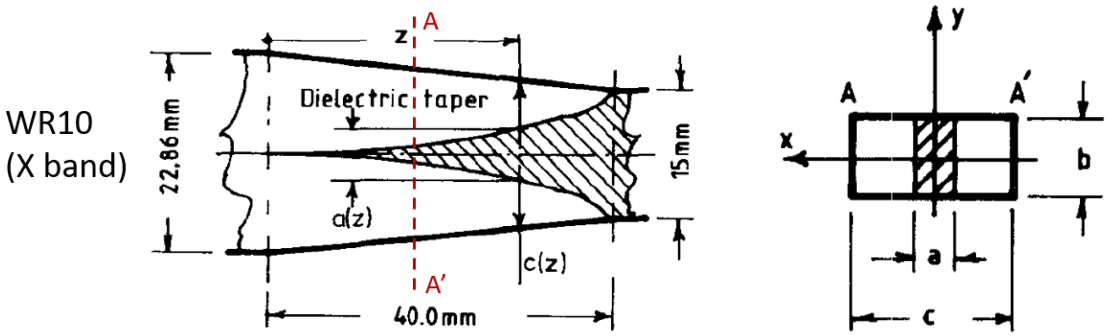

(a) (b)

Figure III.47 Top view of the tapered dielectric-filled to hollow waveguide by means of a tapered dielectric in X band from [III.33].

We proceeded to the implementation of this tapered transition as presented in Figure III.48, enabling the transition between a standard WR12 hollow waveguide and a dielectric-filled waveguide. The main optimization parameters are the width of the beginning of the dielectric slab (y_tran) and the length of the transition (d_tran), both indicated in Figure III.48. After optimizations, the chosen length of the transition was 5 mm and the starting width of the dielectric slab was set to 200 µm for ease of fabrication.

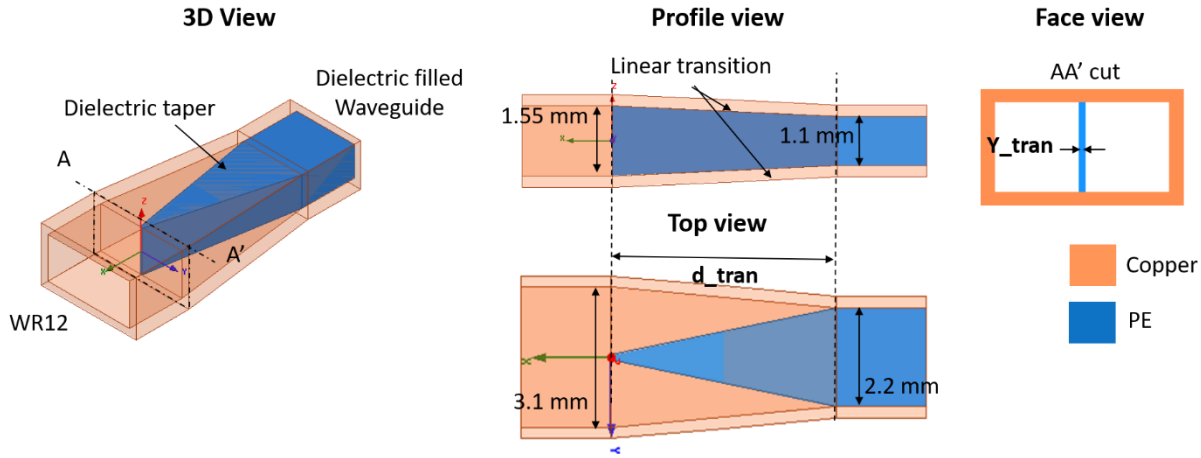

Figure III.48 Several views of the designed WR12 to dielectric-filled rectangular waveguide tapered transition.

Simulated S-parameters of this transition demonstrated a very low transmission loss (below 0.2 dB) on a very wide frequency bandwidth starting from 57 GHz to beyond 90 GHz and a return loss higher than 15 dB on the same frequency band (cf. Figure III.49). Considering those

excellent results, this transition was chosen to be used as a connection between the 2×2 dielectric-filled waveguide feeding networks (replicating the 2×2 structure presented in III.3.2.b) and a hollow metallic waveguide feeding network as was represented in Figure III.45.

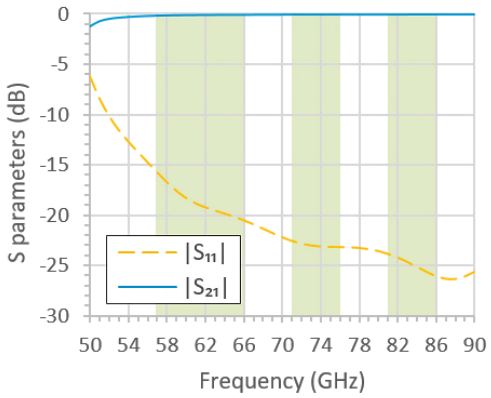

Figure III.49 Simulated transmission and reflection coefficients versus frequency of the tapered WR12 to dielectric-filled waveguide transition illustrated in Figure III.46.

III.3.3.b Feeding network designs and simulations

In the following designs, we chose to use the dielectric filled twist and E-plane junction presented in paragraph III.3.2.b for the 2×2 subset array. By means of the previously mentioned tapered transition, the 2×2 subset array was then connected to a WR12 hollow waveguide feeding network. To build the hollow metallic waveguide feeding parts, we only increased the dimensions of the E-plane and H-plane junctions presented in III.3.2.a to accommodate them to the WR12 waveguide and retuned the posts' dimensions. We used an H-plane T-junction instead of the twist in the hollow metallic waveguide feeding section to enable a split-block assembly which is further explained later on in this section. The designed 4×4 array with the hybrid feeding network is presented in Figure III.50 (the metallic boundary of the waveguides is hidden for more clarity).

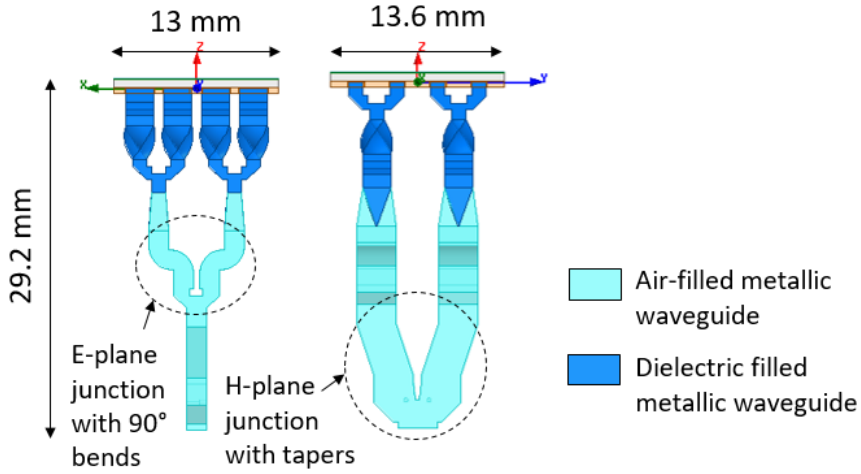

Figure III.50 Transversal view of the designed 4×4 array with hybrid feeding network.

Due to the integration of the transition, we were forced to continue the design of the feeding network in the vertical direction, increasing consequently the thickness of the array from ~1.5

cm to ~3 cm. The tapered transition was connected to an E-plane junction with two 90° consequent bends following the same concept presented in III.3.2.a. Then, an H-plane junction with tapers was used (cf. Figure III.50). Due to the fact that matching worsens with increasing distance between the outputs of the divider, the smallest possible distance between the outputs of the H-plane junction was fixed. Because there was not enough space for 90° bends, we added tapers to the outputs in order to adjust them at the corresponding spacing for connecting the previous stage of the networks (junctions). Finally, a good matching level was obtained, the obtained simulated $|S_{11}|$ of the whole 4×4 array with its feeding network stays below -10 dB from 56 to 87 GHz (cf. Figure III.51 (a)). Moreover, the simulated broadside realized gain increases from 16 to 21 dBi with a high efficiency, above 87%, over the V and E bands (cf. Figure III.51 (b)).

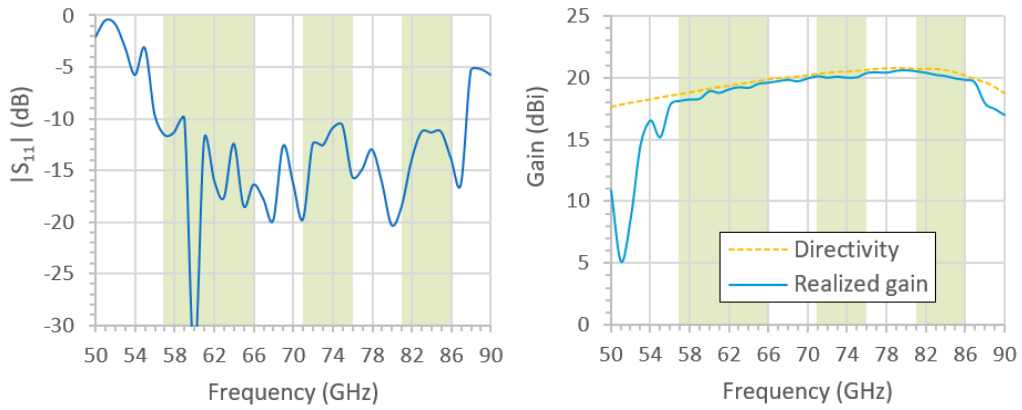

(a) (b)

Figure III.51 (a) Simulated $|S_{11}|$ and (b) broadside realized gain and directivity versus frequency of the 4×4 array with hybrid feeding network.

To construct the feeding of the 8×8 array, we can use the T-junctions with 180° bends to fill the space that exists between the previous stages of the feeding network, hence, we can avoid increasing its thickness. Figure III.52 shows the 8×8 array using E and H-planes T junctions with 180° bends to connect the 4×4 subsets together, the thickness of the array was kept around 3 cm.

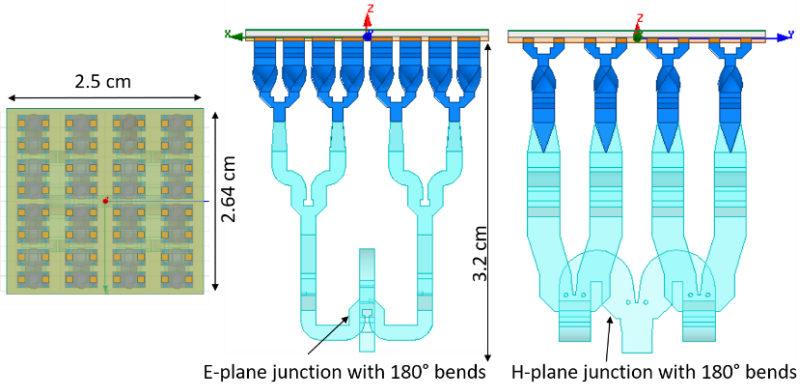

Figure III.52 Top view (left) and transversal views (right) of the optimized 8×8 array with hybrid WR12/dielectric-filled waveguide feeding network.

Nonetheless, the simulated $|S_{11}|$ (using both ADS and HFSS) of the 8×8 array begins to degrade at the beginning of the band as shown in Figure III.53 (a). Even after several optimizations of the parameters of the junctions, we were not able to improve the level of the $|S_{11}|$. Still, a return loss higher than 8 dB was simulated between 59 and 85 GHz and a minimum return loss of 6 dB was obtained over both V and E bands. Simulated broadside realized gain illustrated in Figure III.53 (b) stays between 23 and 26.5 dBi with a maximum loss of 1.5 dB with respect to the directivity, mainly due to mismatch. Since the feeding network doesn't affect at all the radiation patterns, we decided not to show them but you can refer to Figure III.37 that represents the radiation pattern of the 8×8 array case.

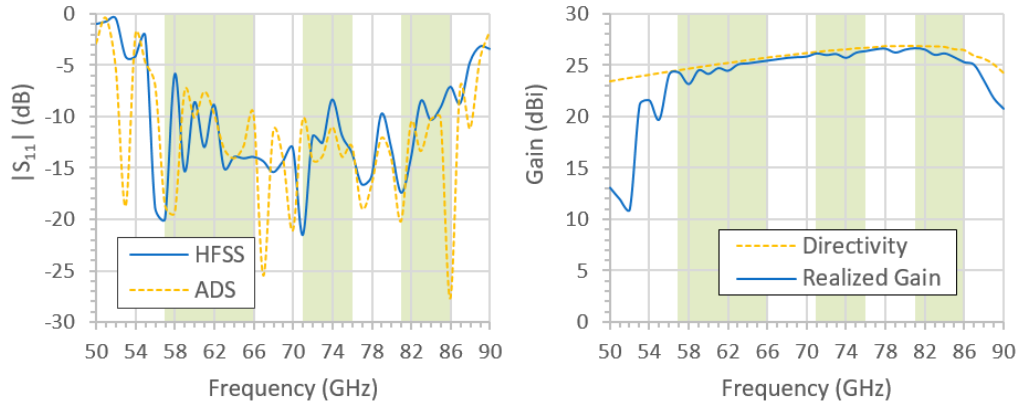

(a) (b)

Figure III.53 (a) Simulated $|S_{11}|$ and (b) realized gain and directivity versus frequency of the 8×8 array with hybrid feeding network.

In the same manner, the 32×32 array was designed and is illustrated in Figure III.54. Corresponding simulated $|S_{11}|$ using ADS is shown in Figure III.55. The return loss is higher than 7 dB over V and E-bands except for one peak reaching 5 dB at 61 GHz.

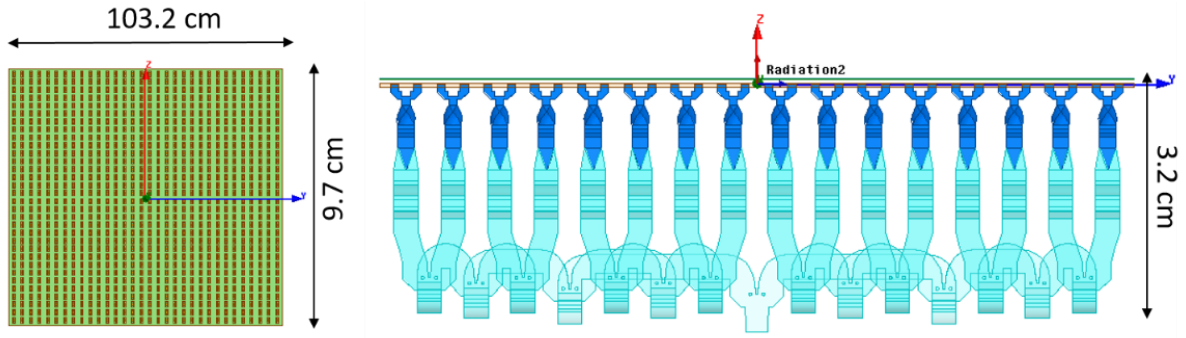

Figure III.54 Top view (left) and transversal view (right) of the optimized 32×32 array with hybrid WR12/dielectric-filled waveguide feeding network.

Usually, the matching of arrays with lossy feeding networks is naturally decreased when increasing the length of the feed. Oppositely, in the case of the waveguide feeding structure we proposed, $|S_{11}|$ does not decrease but rather increases with increasing complexity and length of the waveguide feeding network. In fact, the low-loss aspect of the waveguide leads to a low attenuation of the reflected waves. This leads to the appearance of standing waves at some discontinuities of the feeding network, consequently, return loss spikes are observed.

Nevertheless, results are very acceptable compared to commercial solutions, especially given the fact that the wide band performance is maintained.

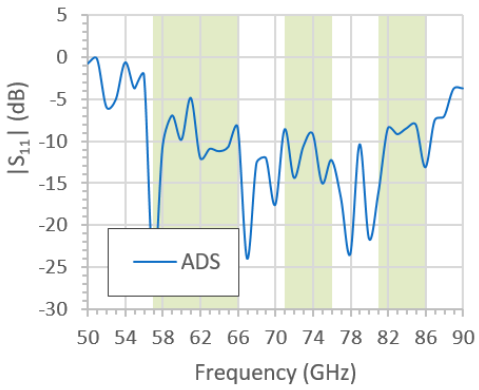

Figure III.55 Simulated $|S_{11}|$ of the 32×32 array with hybrid feeding network using ADS.

To estimate the realized gain, RG, of the designed 32×32 array, we applied equations 4 and 5 following the same method described earlier in III.3.2.b. The simulated losses between directivity and gain of the 8×8 array in this case of hybrid feeding network excluding the mismatch loss where found to be under 0.3 dB over V and E-bands. Since the losses in a hollow waveguide is about 1 dB/m we don't expect a significant increase in the loss, hence we chose L_d = 0.3 dB. The estimated realized gain the 32×32 array is plotted in Figure III.56 and was found above 36.4 dBi in V-band and ranged between 38 and 39 dBi over E-band. We note again, that this method is not precise but is employed only for estimation. Moreover, additionnal losses are most likely to be found in practice due to the surface roughness of the fabricated waveguides.

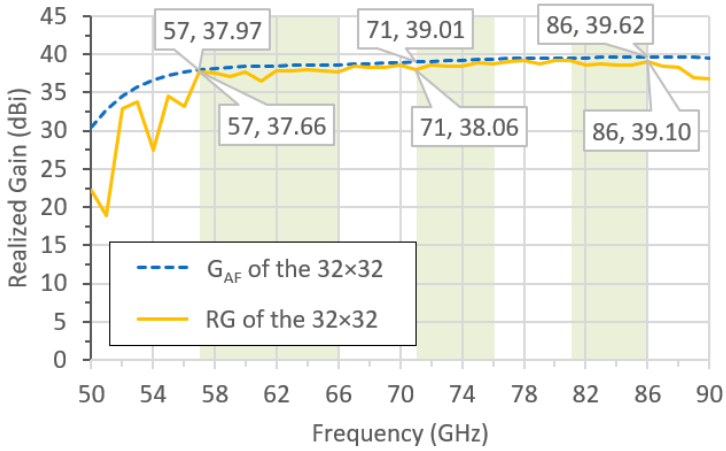

Figure III.56 Computed broadside realized gain of the 32×32 array by applying equation (III.4).

The fabrication method we considered consisted on adopting a split-block assembly for the WR12 waveguide feeding as shown in Figure III.57. The split-block assembly enables the ease of metallization and surface treatment of the waveguide's inner surface and is commonly used for high-frequency waveguide components. Since the alignment between the split-blocks is crucial in this design, pins were added to secure this alignment. For the dielectric-filled

waveguide parts, injection molding was considered. The mold can be printed by DMLS using Aluminum powder to keep a low-cost approach. However, this method was found to be complex because of the need of keeping the taper and the slots on the end-wall of the waveguides unmetallized (selective metallization) as shown in Figure III.58. Therefore, we needed to consider another type of fabrication. To do so it was necessary to rethink a completely new structure of the dielectric filled waveguide part.

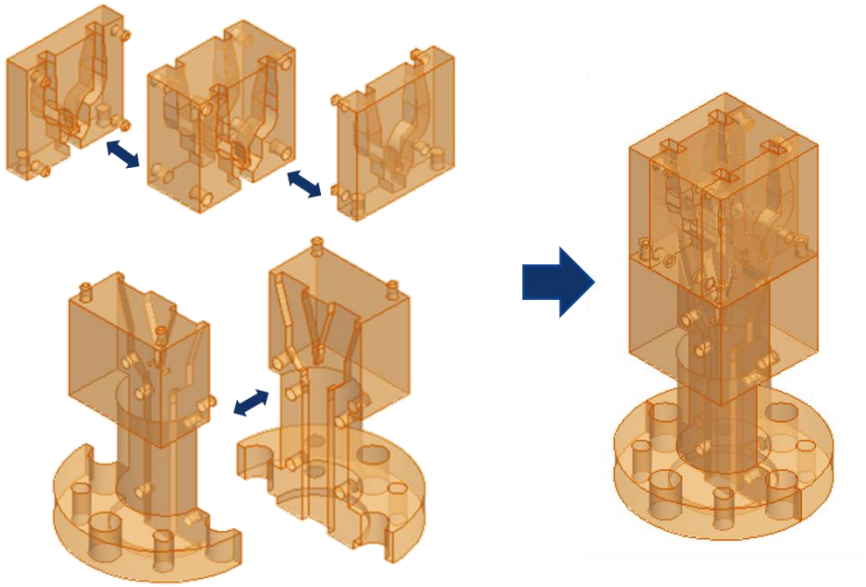

Figure III.57 3D view and exploded view of the assembly mechanism of the split block WR12 hollow metallic waveguide feeding network.

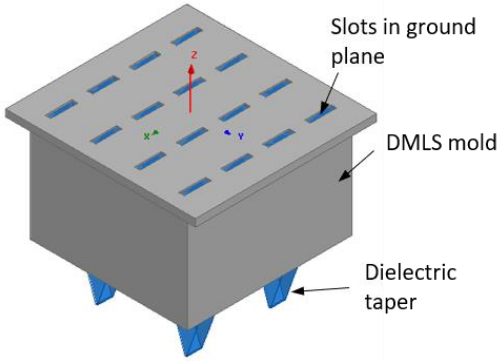

Figure III.58 3D view of the dielectric-filled waveguide feeding section if injection molding is considered for fabrication.

III.3.4 General comparison between the proposed structures

For an overall view of the designs presented, we gathered the principle characteristics of the 32×32 arrays in Table III.6. The 32×32 array with dielectric filled waveguide feeding clearly shows the advantage of a thinner profile of 1.5 cm of thickness. However, the metallization and fabrication of the HDPE feeding was a very complex procedure, hence we had to minimize the dielectric filled waveguide section. By using a mix of hollow and dielectric filled waveguide, even though the thickness was doubled, higher gain was obtained. Split block

assembly was considered for the hollow waveguide part and injection molding was considered for the dielectric filled waveguide part. Nonetheless, the injection molding was also complicated because we need to keep the taper of the transition and the slots without metallization.

	32×32 array with dielectric filled waveguide feeding network	**32×32 array with hybrid waveguide feeding network**
Design		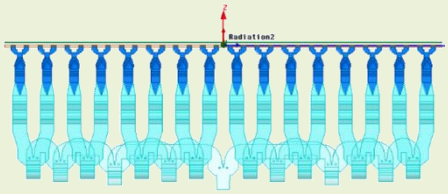
Thickness	1.46 cm	3.2 cm
$\|S_{11}\|$	< - 8 dB 59 GHz to 87 GHz < - 7 dB over V and E-band	< -7 dB over V and E-bands except for one peak reaching 5 dB at 61 GHz
Estimated Gain	35.5 to 36.6 dBi in V-band 37 to 37.6 dBi in E-band	36.4 to 37.7 dBi in V-band 38 to 39 dBi in E-band
Fabrication methods and Limitations	3D printing with HDPE and JetMetal® metallization Difficulties: complex dielectric structure.	Split-block assembly for the hollow waveguide + Injection molding of the dielectric parts. Difficulties: selective metallization and possibility of air gaps between the split blocks.

Table III.6 General comparison between the 32×32 proposed arrays.

Nonetheless, we succeeded to introduce several new concepts enabling the design of waveguide dividers with low insertion and return loss over a wide bandwidth (~40%). Even though todays fabrication methods don't meet with our design requirements, the continuous evolution of 3D printing may enable the fabrication of these designs in the future.

III.4 FOUR-WAY COMPACT DIVIDER

III.4.1 Design and simulation

Proceeding with the same goal of designing an easier-to-manufacture piece to further simplify the fabrication of the dielectric filled waveguide stage, we considered the design of a four-way divider instead of using two consecutive T-junction dividers. We cite here the most interesting solutions we found in the literature. A four-way divider was suggested in [III.9] for a 2×2 subarray of radiating slots based on a cavity structure (cf. Figure III.59 (a)). The cavity is partitioned into four spaces by two sets of walls extending in x the y and directions. A coupling aperture placed on the broadwall of a waveguide with an offset from its center axis excites the cavity. The elements of the 2×2 subarray are excited in phase and with equal amplitude, however the aperture coupling mechanisms limited the -15 dB-impedance matching level to 10%. Another example suggested in [III.35] employed stepped rectangular waveguides to provide a smooth impedance matching from standard rectangular waveguide to an oversized rectangular waveguide (cf. Figure III.59 (b)). On the top of the oversized rectangular waveguide, four microstrip patch antennas were placed to implement the equal power-dividing function. However, the simulated 15-dB return loss bandwidth was extremely limited (3%),

which may be due to the fact that the patch antennas were directly integrated on the surface of the waveguide. Also, a bigger number of steps may be required to obtain a wide band impedance transformation between the standard and the large waveguide.

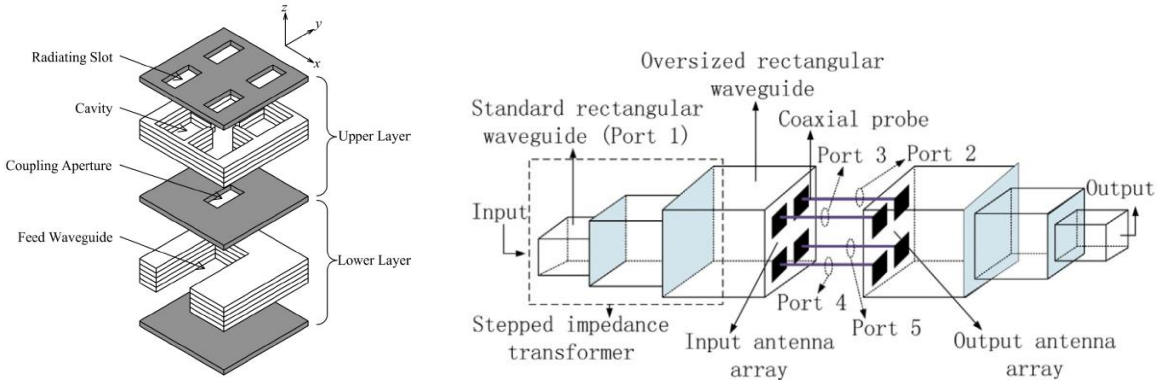

(a) (b)

Figure III.59 (a) Exploded view of the 2×2-element subarray with cavity and aperture coupling [III.9]. (b) Power divider/combiner using microstrip antenna and stepped waveguide [III.35].

None of the designs we found in the literature demonstrated a bandwidth sufficient for our case. Therefore, we managed to think and develop a novel concept of a four-way dielectric-filled waveguide divider based on unifying the H-plane and E-plane junctions in a compact one-stage divider. The design is depicted in Figure III.60 where the metallic boundary is hidden. The profile of the divider in ZX plane looks like the H-plane divider presented in III.3.2.a but without the cylindrical capacitive posts. The metallic wall that separates the output waveguides act like an inductive post in this case. Also, the chamfered edges act like the chamfered bends that were added previously to the junctions and allow a smooth impedance transformation. Following the same reasoning, the profile of the proposed divider in the ZY plane can be resembled to an E-plane T-junction.

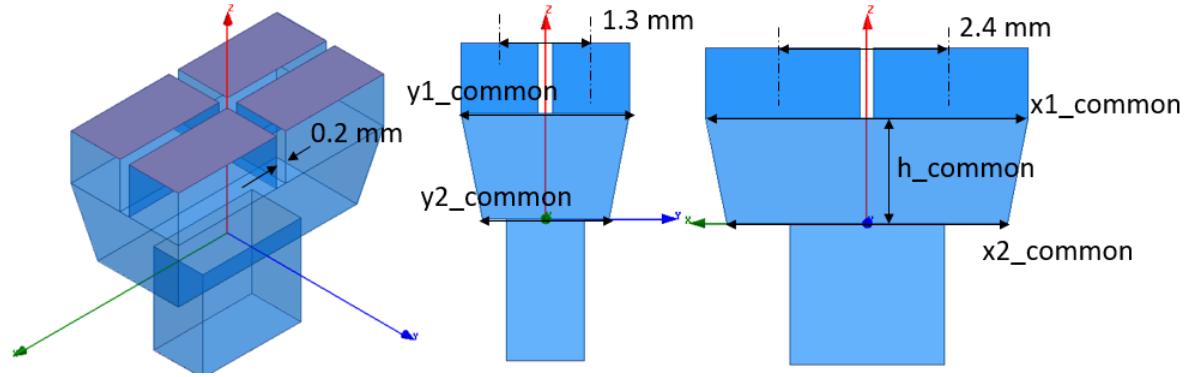

Figure III.60 Four-way dielectric-filled waveguide divider with optimization parameters (3D, front and transversal views).

The parameters indicated in Figure III.60 were optimized in HFSS to obtain the best impedance matching over V and E-bands and their values are listed in Table III.7. The height of the common part of the divider was a crucial parameter. The best performance was obtained with h_common $\cong \lambda_G/4$, where λ_G is the guide wavelength at 60 GHz and is given by,

$$\lambda_G = \frac{\lambda_d}{\sqrt{1 - (\frac{\lambda_d}{\lambda_c})}} \quad (1)$$

Where, λ_d is the wavelength in the dielectric and λ_c is the cutoff wavelength. This expression of guide wavelength is specific for waveguides' transverse modes. Hence the common part of the divider can be resembled to a quarter-wave impedance transformer.

Y1_common	Y2_common	X1_common	X2_common	H_common
4.6 mm	4 mm	2.4 mm	1.8 mm	1.5 mm

Table III.7 Values of the optimized parameters of the four-way divider from Figure III.60.

As explained III.3.2.a, since the best matching is obtained for the least distance between the outputs, the wall thickness separating the outputs was reduced to 200 µm to respect fabrication's requirements. Simulated S-parameters, represented in Figure III.61, illustrated a very wideband matching with a return loss higher than 15 dB from 53 to 86 GHz as well as a very low insertion loss (< 0.2 dB) on this wideband considering a theoretical output of -6 dB corresponding to a perfect power division.

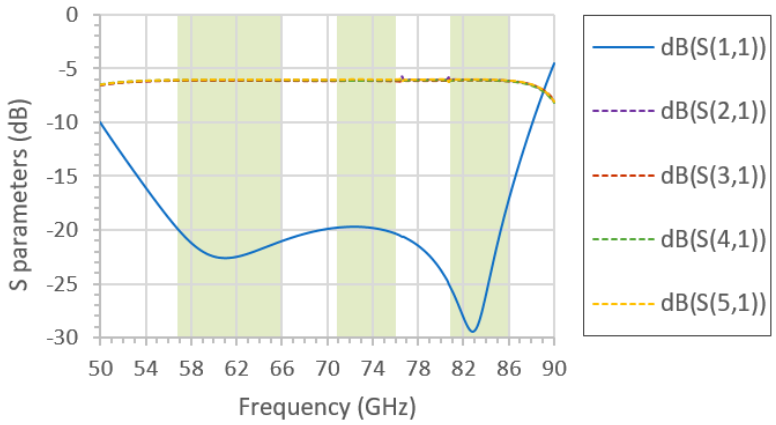

Figure III.61 Simulated S-parameters of the designed dielectric-filled one-to-four way waveguide divider.

Nevertheless, the distance between the outputs of the waveguide is smaller than the spacing between the elements of the array. Therefore, we needed to add tapers as represented in Figure III.62 to be able to connect the array elements to this new divider. Figure III.62 shows the implementation of the SCP antennas with the four-way divider and the transition from dielectric-filled waveguide to WR12 hollow waveguide. The simulated broadside realized gain of the whole structure is presented in Figure III.63 (a) with a comparison between ABS and PE filling, since ABS prototyping was found to be easier. Only 1 dB of difference in gain was found between the two dielectrics which is largely acceptable. The 10-dB impedance matching was satisfied all over the V and E bands similarly to the 2×2 array previously presented with twist and E-plane junction feeding, as illustrated by Figure III.63 (b). This innovative design enabled an easy mechanical assembly of the whole structure in the means of the proposed method shown in Figure III.64. The dielectric waveguide filling can be printed in one piece and the metallization in two pieces. A first metal piece containing the coupling slots and the

inner walls of the waveguide tapers, and a second metal piece consisting of the outer metallic walls of the divider, tapered transition and the standard UG-385/U flange.

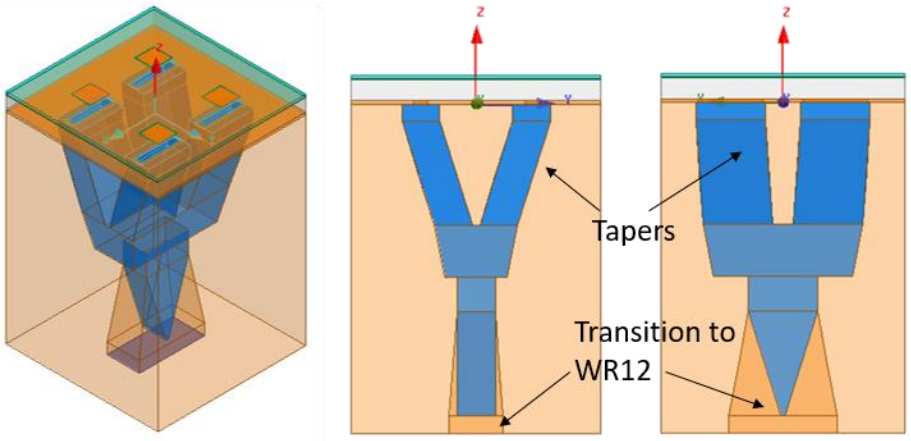

Figure III.62 2×2 array fed by the four-way waveguide divider and the dieletric-filled to hollow waveguide transition (3D, front and transversal views).

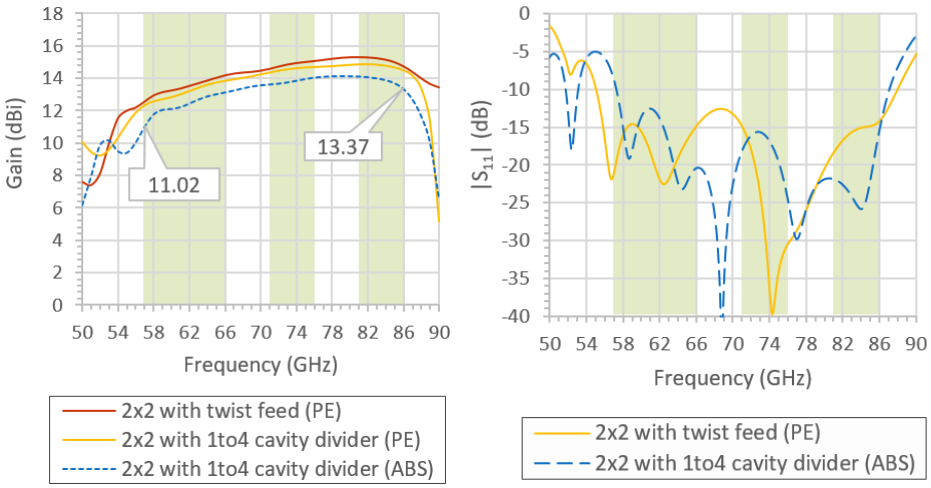

(a) (b)

Figure III.63 (a) Simulated broadside realized gain and (b) $|S_{11}|$ versus frequency of the 2×2 array from Figure III.62 with PE and ABS dielectrics.

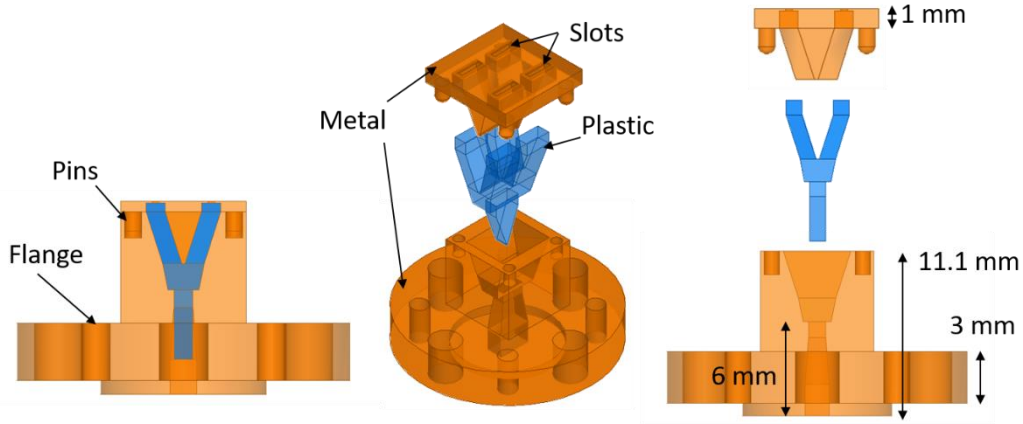

Figure III.64 Mechanical integration of the the 2×2 elements array with standard UG-385/U flange (compact transversal view, exploded 3D view and exploded transversal view).

In order to replicate this solution towards higher size and complexity arrays, the same hollow metallic waveguide feeding introduced in III.3.3.b can be used. The prototyping of this 2×2 array is discussed in the next section.

III.4.2 Prototyping tests using an in-house 3D printer

Using our in-house 3D printer (Form2 from FormLabs [III.36]) (cf. figure III.65), we were able to test the assembly presented in Figure III.64 prior sending it to be fabricated by a specialized company. The Form2 printer uses the SLA technology to deliver high-precision prints (up to 50 µm of details). Once the piece is designed, it's converted to a "STL" file and imported to the "Preform" software specific to the Form2 printer. The software enables to orient the piece on the build platform of the printer and automatically add supports to the piece. Supports are printed with the same material as the piece but with a geometry that allows to remove them easily. The parameters of the supports can be configured manually in the software like density, diameter and position. The global specifications of the printer are given in Figure III.66, among these, we highlight the thickness layer that can reach 25 µm.

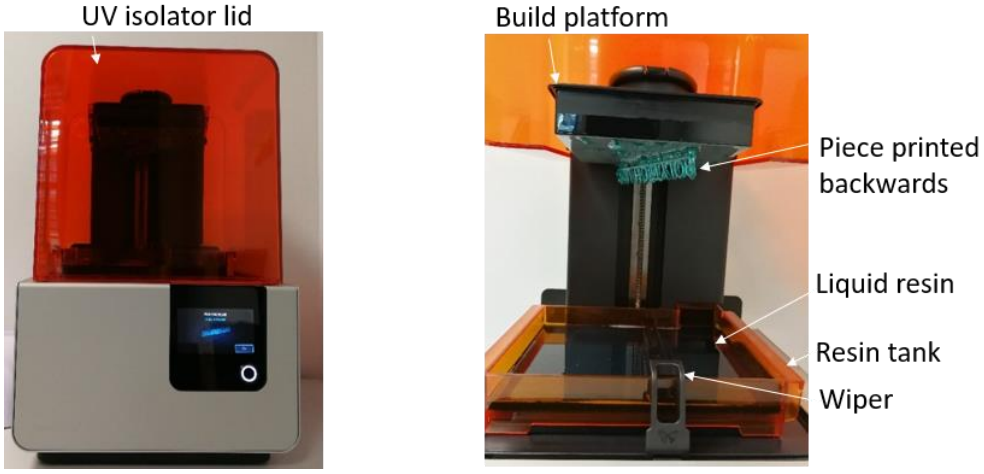

(a) (b)

Figure III.65 Pictures of the Form2 printer with (a) closed and (b) opened lid.

Figure III.66 Global specifications of the Form2.

Hence were able to study all the printing options and test various orientations to choose the ones that suit best our designs. Also support structures options like density and positions were optimized to ensure an easy disassembly as well as avoiding placing supports on critical surfaces (like flange surface). After several printing tests performed with this printer, an

accuracy of +/- 50 µm was proved, satisfying the needed tolerances of our latest design. The printing time depends on the size, density and layer thickness of the printing job. Printing three samples of the previously presented 2×2 array (cf. Figure III.64) took slightly less than 3 hours, considering a 25 µm layer precision. Many resins were tested in our lab: tough, clear and high temp. According to our application, we needed a material with a high tensile force and stiffness. The best solution (at the time we printed) was found to be the high temp resin known for its resistivity to deformation.

The printed pieces are then treated by two post-processing steps: washing by Isopropyl Alcohol (IPA) and curing by UV light. The printed pieces are washed with IPA using the Form Wash, featured in Figure III.67 (a), to remove all the uncured resin that cover the piece or the resin possibly trapped inside cavities in the printed piece. The Form Wash washes the pieces for a time specified by the user using a rotating turbine that agitates the alcohol. Once washing is complete, Form Wash automatically lifts the parts out of the IPA avoiding over-soaked warped prints. Then, the parts are left to air-dry. The final step consists in curing the piece by UV light using the Form Cure (cf. Figure III.67 (b) and (c)). This machine provides the necessary temperature and light for the printed piece to reach its final mechanical properties. Finally, supports can be cut and the surface of the piece is smoothed using glass paper to remove remaining supports marks.

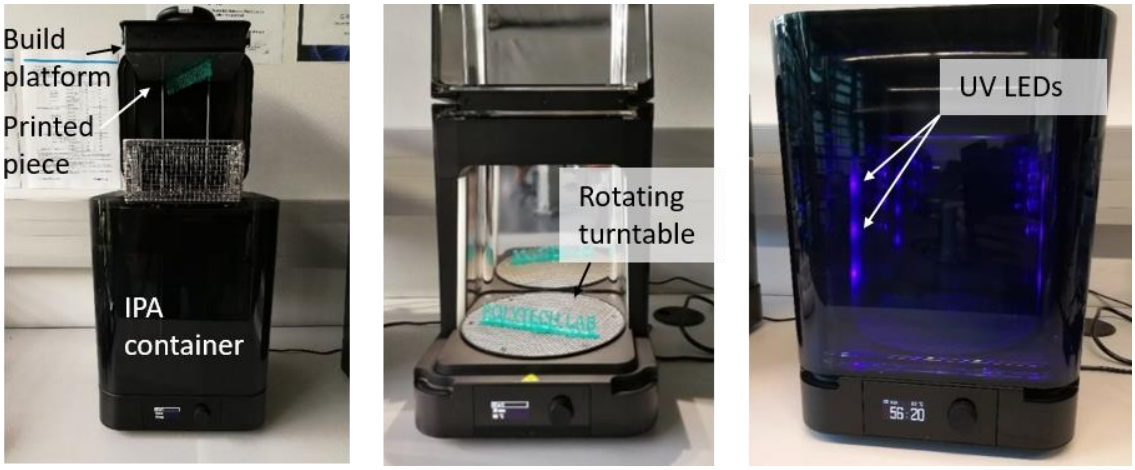

(a) (b) (c)

Figure III.67 (a) Form wash with parts lifted-out of the IPA container, (b) Form cure with open and (c) closed lid during curing.

Resins available at our lab were electrically characterized at 60 GHz at ISCTE-IUL using a Fabry-Perot resonator [III.37]. The estimated values from measurements performed on samples of High Temp resin were found to be: $\varepsilon_r = 2.8$ and $\tan\delta = 0.03$. The relative permittivity is fairly close to ABS ($\varepsilon_r = 2.48$ and $\tan\delta = 0.009$) but High temp resin is characterized by more losses. Replacing the ABS plastic with High temp in the simulations of the 2×2 array from Figure III.64, yielded 2 dB of additional losses between directivity and gain. Despite this drop of efficiency, we wanted to move further with the prototyping of the piece to have a first insight on the agreement between measurements and simulations. The pictures of the printed and post processed 2×2 array with one-to-four divider using High Temp resin are depicted in Figure

III.68. To metallize the parts destined to be used as the metallic boundary of the waveguide, we used an EMI 35 [III.38] aerosol metallic paint as a first try. The EMI 35 contains a special copper pigment within a resin base which creates an electrically conductive layer. Aerosol conductive paint is considered as a simple method of applying a high conductivity coating to non conductive plastics and was successfully used on ABS-M30 to metallize a 3D printed cassegrain reflector [III.39]. However this metallic coating didn't adhere successfully on our resins and cracks appeared with the slight pressure applied on the piece, as shown in Figure III.69. We also tested another type of metallization with silver pigments [III.40] that was sucessfully used to metallize 3D printed waveguides with a polymer resin in [III.41]. This type of metallic coating didn't show any cracks but was also unconvenient because it did not cover the surface of the parts uniformly (the corners of the parts were always left uncovered even after many tries). Even though other metallization solutions can be considered, the main challenges we faced is to take into account the tolerance of the fabrication method to prevent air gaps between the waveguide and the metallic boundary. This needed a deep study and good results are far to be achieved from the first try. The fabrication of this piece is still under study.

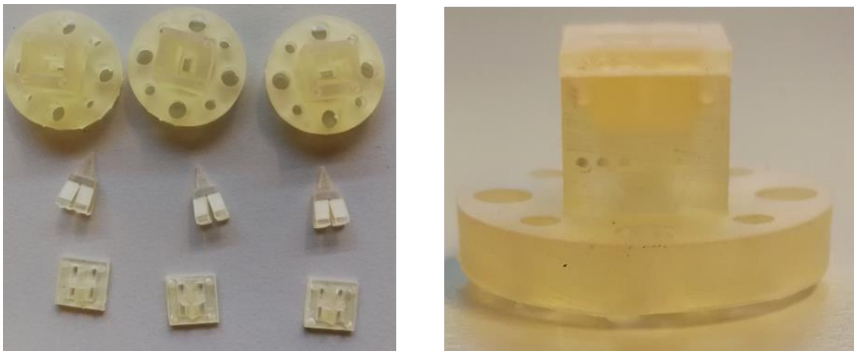

(a) (b)

Figure III.68 3D-printed 2×2 array of waveguide dielectric filling and boundaries (a) and assembled pieces (b).

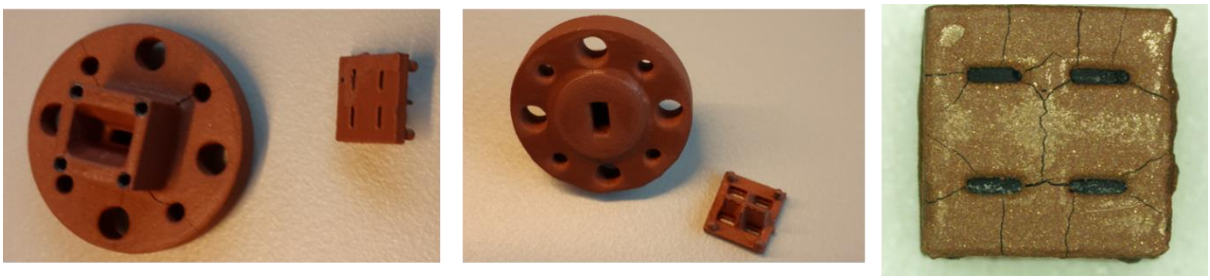

Figure III.69 3D printed 2×2 array with metallized boundaries using copper pigmented paint.

Even though manufacturing challenges were not resolved successfully, all the presented configurations of patch arrays demonstrated an efficiency higher than 50% over a very wide bandwidth (40%), which was not before achieved by a flat antenna array from the best of our knowledge. Giving all the manufacturing problems we faced with dielectric filled waveguide, an alternative solution was needed to realize our designs.

III.5 CONCLUSION AND PERSPECTIVES

For the purpose of designing a compact fixed-beam flat array with wide bandwidth to operate in the V and E bands, we presented a patch antenna array with corporate dielectric-filled waveguide network. The single element composing the array is a slot coupled patch fed by dielectric-filled waveguide demonstrating a very wide impedance bandwidth and efficiency exceeding 90% all over the E and V bands. To feed the array elements in phase with equal power, we proposed several configurations of corporate waveguide feeding network. All the configurations were composed by E or H-plane T-junctions and twists. The first configuration was composed exclusively of dielectric-filled waveguide. However, fabrication was too complicated to be accomplished. Thus, we introduced a hybrid feeding network including dielectric-filled and hollow waveguides. A tapered transition incorporating a tapered dielectric slab was designed to connect both parts of this feeding network. Still, the dielectric-filled waveguide feeding part was reported hard to fabricate by specialized company. To overcome this challenge, we finally presented a more innovative design of a compact one-stage four-way waveguide divider composed by merging E and H-plane T-junctions in a single structure. The final design of a 2×2 array fed by this divider demonstrated wideband matching performance and high efficiency while being simpler to prototype. Using an in-house 3D printer and post-processing machines, we were able to prove the feasibility of the mechanical assembly of this design, nonetheless gaps between the dielectric and waveguide were inevitable and we faced metallization problems. The overall performance of the presented arrays is compared with commercial antennas in Table III.8. The comparison shows that the simulated performances of our proposed array antenna are competitive in terms of broadside realized gain and size (width and depth), while bringing the added value of covering both E and V-band with one antenna array and feeding structure.

Antenna	**GAP waves, Gap Array Antenna [III.15]**		**Huber&Suhner, SENCITY ® matrix [III.14]**		**This work:**	
Technology	Gap waveguide		Slot array		Dielectric-filled waveguide network	Hybrid waveguide network
Frequency	V	E	V	E	V and E-band	V and E-band
Gain (dBi)	32 dBi	38 dBi	38 dBi	38 dBi	35.5 to 36.6 dBi in V-band 37 to 37.6 dBi in E-band	36.4 to 37.7 dBi in V-band 38 to 39 dBi in E-band
Antenna size (w×d×h mm)	93 × 93 × 15.8	118 × 118 × 8.2	135 × 130 × 9.5	102 × 106 × 8	103 × 97 x 14.5	103 × 97 x 32
$\|S_{11}\|$ and relative bandwidth	NS	NS	<-10 dB (14%)	<-7 dB (20%)	< - 8 dB (37%)	< -7 dB (40%, except for - 5 dB at 61 GHz)
ETSI class	3	3	2	2	2	2

Table III.8 Comparison between our proposed antenna arrays and commercially available arrays.

In the next chapter, we introduce an alternative for dielectric waveguide by exploiting the concept of ridged waveguides. In fact, by introducing ridges in a hollow metallic waveguide, the cut-off frequency is reduced, hence permitting to reduce the dimensions of the waveguide similarly to the dielectric-filled metallic waveguide. This allows to design antenna arrays fabricated in a single block avoiding air gaps and assembly problems.

III.6 REFERENCES

[III.1] A. Bondarik, D. S. Jun, J. M. Kim, and J. H. Yun, "Investigation of microstrip antenna array stacked structure realized on LTCC for 60 GHz band," Microwave and Optical Technoy. Letter, vol. 52, no. 3, pp. 648–652, March 2010.

[III.2] E. Levine, G. Malamud, S. Shtrikman, and D. Treves, "A study of microstrip array antennas with the feed network," IEEE Transactions on Antennas Propagation, vol. 37, no. 4, pp. 426–434, April 1989.

[III.3] X. P. Chen, K. Wu, L. Han, and F. He, "Low-Cost High Gain Planar Antenna Array for 60-GHz Band Applications," IEEE Transactions on Antennas and Propagations, vol. 58, no. 6, pp. 2126–2129, Jun. 2010.

[III.4] S. Cheng, H. Yousef, and H. Kratz, "79 GHz Slot Antennas Based on Substrate Integrated Waveguides (SIW) in a Flexible Printed Circuit Board," IEEE Transactions on Antennas and Propagation, vol. 57, no. 1, pp. 64–71, Jan. 2009.

[III.5] Y. Li and K.-M. Luk, "Low-Cost High-Gain and Broadband Substrate- Integrated-Waveguide-Fed Patch Antenna Array for 60-GHz Band," IEEE Transactions on Antennas and Propagation, vol. 62, no. 11, pp. 5531–5538, Nov. 2014.

[III.6] M. Bozzi, M. Pasian, L. Perregrini, and K. Wu, "On the losses in substrate-integrated waveguides and cavities," International Journal of Microwave and Wireless Technologies., vol. 1, no. 5, pp. 395–401, Oct. 2009.

[III.7] G. P. L. Sage, "3D Printed Waveguide Slot Array Antennas," IEEE Access, vol. 4, pp. 1258–1265, 2016.

[III.8] T. Tomura, M. Zhang, J. Hirokawa, and M. Ando, "Plate-laminated-waveguide corporate-feed 45-degree linearly-polarized aperture array antenna in the 60 GHz-band," in 2011 IEEE International Symposium on Antennas and Propagation (APS-URSI), 2011, pp. 3048–3051.

[III.9] Y. Miura, J. Hirokawa, M. Ando, Y. Shibuya, and G. Yoshida, "Double-Layer Full-Corporate-Feed Hollow-Waveguide Slot Array Antenna in the 60-GHz Band," IEEE Transactions on Antennas and Propagation, vol. 59, no. 8, pp. 2844–2851, Aug. 2011.

[III.10] P. S. Kildal, A. U. Zaman, E. Rajo-Iglesias, E. Alfonso, and A. Valero-Nogueira, "Design and experimental verification of ridge gap waveguide in bed of nails for parallel-plate mode suppression," IET Microwaves Antennas and Propagation, vol. 5, no. 3, pp. 262–270, Feb. 2011.

[III.11] E. Rajo-Iglesias and P.-S. Kildal, "Numerical studies of bandwidth of parallel-plate cut-off realised by a bed of nails, corrugations and mushroom-type electromagnetic bandgap for use in gap waveguides," IET Microwaves Antennas and Propagation., vol. 5, no. 3, p. 282, 2011.

[III.12] D. Zarifi, A. Farahbakhsh, A. U. Zaman, and P.-S. Kildal, "Design and Fabrication of a High-Gain 60-GHz Corrugated Slot Antenna Array With Ridge Gap Waveguide Distribution Layer," IEEE Transactions on Antennas and Propagation,vol. 64, no. 7, pp. 2905–2913, Jul. 2016.

[III.13] "HUBER+SUHNER - SENCITY® Matrix." [Online]. Available: https://www.hubersuhner.com/en/solutions/wireless-infrastructure/products/mobile-backhaul/sencity-matrix. [Accessed: 18-Jun-2018].

[III.14] P. Sjöqvist, "Fixed Beam," Gapwaves AB. [Online]. Available: https://gapwaves.com/fixed-beam/. [Accessed: 18-Jun-2018].

[III.15] A. Linneman, "High-Volume 3D Printing vs. Injection Molding - Shapeways Magazine." [Online]. Available : https://www.shapeways.com/blog/archives/35860-high-volume-3d-printing-vs-injection-molding.html. [Accessed: 18-Jun-2018].

[III.16] C. A. Balanis, Antenna theory: analysis and design, 3rd ed. Hoboken, NJ: John Wiley, 2005.
[III.17] D. M. Pozar, "Aperture coupled waveguide feeds for microstrip antennas and microstrip couplers," in Antennas and Propagation Society International Symposium, 1996. AP-S. Digest, 1996, vol. 1, pp. 700–703 vol.1.
[III.18] S. H. Choi and J. Y. Lee, "Microstrip patch array antenna fed by waveguide endwall coupler," in European Microwave Conference, 29 September - 1 October 2009, Rome, Italy, pp. 1468–1471.
[III.19] M. Jin, M. Qi, and W. Wang, "Waveguide-Fed Conformal Microstrip Patch Antenna Array," European Conference on Antennas and Propagation EuCAP, 2009.
[III.20] Robert Vilaltella, Jan Hesselbarth, and Hernen Barba, "High-efficiency dual-polarized patch antenna array with common waveguide feed," in Microwave conference (GeMiC), Aachen, Germany, 2014, pp. 1–3.
[III.21] H. I. Song, H. Jin, and H.-M. Bae, "Plastic straw: future of high-speed signaling," Science Reports, vol. 5, p. 16062, Nov. 2015.
[III.22] A. E. I. Lamminen, J. Saily, and A. R. Vimpari, "60-GHz Patch Antennas and Arrays on LTCC With Embedded-Cavity Substrates," IEEE Transactions on Antennas and Propagation, vol. 56, no. 9, pp. 2865–2874, Sep. 2008.
[III.23] N. Marcuvitz, Waveguide Handbook. IET, 1951.
[III.24] D. M. Pozar, Microwave Engineering. Wiley, 2004.
[III.25] T. Sehm, A. Lehto, and A. V. Räisänen, "Matching of a rectangular waveguide T junction with unequal power division," Microwave and Optical Technologies Letter, vol. 14, no. 3, pp. 141–143, Feb. 1997.
[III.26] "Waveguide Bends and Twists : Radio-Electronics.Com." [Online]. Available: http://www.radio-electronics.com/info/antennas/waveguide/waveguide-bends-e-h-twists.php. [Accessed: 30-Apr-2018].
[III.27] "Products & Services - ROHACELL® - High-performance structural foam cores." [Online]. Available: https://www.rohacell.com/product/rohacell/en/products-services/. [Accessed: 20-Sep-2018].
[III.28] "Diamond Plastics - Laser Sinter HDPE Powder." [Online]. Available: http://www.diamond-plastics.de/en/produkte/laser-hdpe-hx-17.html. [Accessed: 10-Jul-2018].
[III.29] R. ProResult and K. Rössler, "SLS Selektives Lasersintern," Kegelmann Technik.
[III.30] "https://www.jetmetal-tech.com/," Jet Metal ™. [Online]. Available: https://www.jetmetal-tech.com/. [Accessed: 10-Jul-2018].
[III.31] "Plateforme d'injection - IPC." [Online]. Available: /moyen/plateforme-dinjection. [Accessed: 10-Jul-2018].
[III.32] K. Sano and K. Ito, "A 26-GHz Band Dielectric Waveguide Diplexer with Flange Interfaces." Microwave Symposium Digest, 2005 IEEE MTT-S International, p106.
[III.33] J. A. G. Malherbe, J. H. Cloete, and I. E. Losch, "A Transition from Rectangular to Nonradiating Dielectric Waveguide (Short Paper)," IEEE Transactions Microwave Theory Technics, vol. 33, no. 6, pp. 539–543, Jun. 1985.
[III.34] S. Rahiminejad, E. Pucci, V. Vassilev, P.-S. Kildal, S. Haasl, and P. Enoksson, "Polymer Gap Adapter for Contactless, Robust, and Fast Measurements at 220–325 GHz," Journal of Microelectromechanical Systems, vol. 25, no. 1, pp. 160–169, Feb. 2016.
[III.35] K. Song, G. Li, Q. Duan, S. Hu, and Y. Fan, "Millimeter-wave waveguide-based out-of-phase power divider/combiner using microstrip antenna," AEU - International Journal of Electronics and Communications, vol. 68, no. 12, pp. 1234–1238, Dec. 2014.
[III.36] "Form 2 | Formlabs." [Online]. Available: https://formlabs.com/store/eu/form-2/. [Accessed: 10-Sep-2018].

[III.37] C. A. Fernandes and J. R. Costa, “Permittivity measurement and anisotropy evaluation of dielectric materials at millimeter-waves,” XIX IMEKO World Congress Fundamental and Applied Metrology September 6−11, 2009, Lisbon, Portugal p. 673-677.

[III.38] “EMI 35 200ML - KONTAKT CHEMIE - Coating, Conductive, EMI 35.” [Online]. Available: http://ie.farnell.com/kontakt-chemie/emi-35-200ml/coating-conductive-emi-35-200ml/dp/2142398. [Accessed: 11-Jul-2018].

[III.39] A. Bisognin, “Évaluation de technologies organiques faibles pertes et d’impression plastique 3D afin de contribuer au développement de solutions antennaires innovantes dans la bande 60 GHz – 140GHz.,” PhD thesis, Université Nice Sophia Antipolis, 2015.

[III.40] M. G. Chemicals, “843 - Super Shield™ Silver Coated Copper Conductive Coating - Acrylic Conductive Coatings (Original Series),” MG Chemicals. [Online]. Available: https://www.mgchemicals.com/products/emi-and-rfi-shielding/acrylic-conductive-coatings-original-series/super-shield-silver-copper-843. [Accessed: 11-Jul-2018].

[III.41] K. V. Hoel, S. Kristoffersen, J. Moen, G. Holm, and T. S. Lande, “Characterization of a 3D printed wideband waveguide and horn antenna structure embedded in a UAV wing,” 10th European Conference on Antennas and Propagation (EuCAP), 10-15 April 2016, Davos, Switzerland, pp. 1–4.

IV. V AND E-BAND OPEN DOUBLE RIDGE WAVEGUIDE ARRAY ANTENNAS

Although high efficiency and wide bandwidth performances were obtained by the designs of the SCP to dielectric-filled waveguide arrays, the fabrication of the prototypes was found to be expensive and complicated. Aiming for a simpler solution in terms of fabrication, we studied the possibility of using ridge waveguides both as feeding and radiating structures to construct a flat antenna array operating in both E and V bands. By adding proper ridges to a classical hollow metallic waveguide, the cutoff frequency of its dominant mode can be decreased. In the same time this approach does not affect the cutoff frequency of the next higher-order mode, consequently the bandwidth of the single mode operation is enlarged. We took advantage of this phenomenon to reduce the dimensions of a conventional waveguide while conserving the value of the cutoff frequency of its fundamental mode, leading to the same effect as filling the waveguide with a dielectric material. Because a dielectric filling was avoided with this technic, we were able to consider more fabrication technics to simplify the prototyping. We began this chapter by a brief presentation of the theoretical concept behind a ridge waveguide and its state-of-the-art applications. Based on this concept, we studied the conception of a 2×2 open ridge waveguide subset array with a four-way divider. Finally, a high precision micro-DMLS technic is evaluated for the fabrication of the 2×2 subset and measurement results are discussed.

IV.1 RIDGE WAVEGUIDE THEORY AND STATE-OF-THE-ART

The single or Double Ridge Waveguide (DRWG), shown in Figure IV.1 (a) and (b) respectively, consists of a rectangular waveguide loaded with conducting ridges on the top and/or bottom walls. This loading tends to lower the cutoff frequency of the dominant mode compared to a conventional waveguide with the same dimensions. In fact, the practical bandwidth of a conventional rectangular waveguide is slightly less than an octave (2:1 frequency range). This is because the TE_{20} mode begins to propagate at a frequency equal to twice the cut-off frequency of the TE_{10} mode. By contrast, ridge waveguides can achieve a bandwidth up to four-to-one between TE_{10} and TE_{20} modes cut-off frequencies along with better (more constant) impedance characteristics [IV.1]. This enhanced bandwidth can be understood by considering the center ridged section as a parallel-plate transmission line thereby lowering the cutoff frequency of the waveguide to below that of a conventional waveguide [IV.2]. On the other hand, the attenuation is several times that for conventional waveguides but is still much less than the one of a coaxial cable or a microstrip line. The ridge waveguide

concept enables to reduce the cross-section of the waveguide while maintaining the same fundamental mode cutoff frequency of a bigger size conventional waveguide. This enables to put less constraints on the inter-element spacing. Both single-ridge and double-ridge topologies achieve almost the same performances in bandwidth and attenuation but we limited our study to double ridge waveguide because we preferred to use a symmetrical geometry enabling a symmetrical radiation pattern of the single element.

To design the DRWG, the author of [IV.3] proposed charts relating the cutoff frequency, bandwidth and attenuation to the geometry of the waveguide. Those charts are illustrated in Figure IV.2 and IV.3 and correspond to the DRWG case. They were derived upon calculations based on the equivalent circuit of the ridge waveguide shown in Figure IV.1 (c) [IV.3]. The determining factors of the performance of the ridge waveguide are the width of the ridge, s, and the space between the ridge and the upper face of the waveguide, d, in case of the single ridge waveguide or the distance between two ridges in case of a double ridge waveguide (cf. Figure IV.1 (a) and (b)). Hence, the performance of the waveguide is expressed in function of the geometrical parameters s/a and d/b and the cutoff of the waveguide will be expressed by the extension factor λ_c/a, where λ_c is the cutoff wavelength. Moreover, all the presented charts correspond to an aspect ratio b/a equal to 0.5.

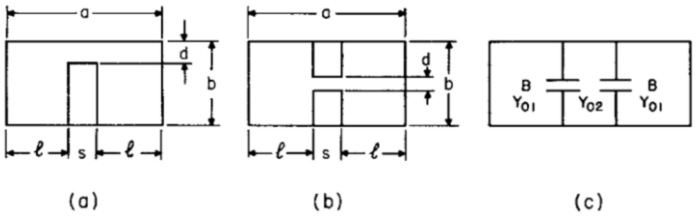

Figure IV.1 (a) Single and (b) double ridge waveguide cross-sections and their (c) equivalent circuit representation from [IV.3].

Figure IV.2 (a) plots the extension factor, λ_c/a, for the TE_{10} mode as a function of s/a and d/b for double ridged waveguide. The lowest cut-off frequency is obtained for s/a = 0.45 and its value decrease with a d/b decrease. Figure IV.2 (b) shows the theoretical bandwidth, $\lambda_{c1}/\lambda_{c2}$ (the ratio of the cut-off wavelength of the first mode over the cut-off wavelength of the next higher order mode), versus s/a and d/b. The widest theoretical bandwidth is obtained around s/a = 0.25 and it increases when the space between the ridges is narrower. By optimizing s and d, bandwidths exceeding 4:1 can be achieved. For more convenience, the losses of the double ridge waveguide are expressed in terms of normalized attenuation σ_n, the ratio of the ridge guide attenuation to the rectangular conventional guide attenuation of identical cut-off, both being considered at a frequency $f = \sqrt{3}f_c$, where f_c is the cutoff frequency and expressed in dB/m. Figure IV.3 plots the normalized attenuation versus s/a and theoretical bandwidth. The lowest losses can be found for s/a between 0.1 and 0.3 and are evaluated as approximately twice the losses of a conventional waveguide. On the other hand, the attenuation increases with increased bandwidth and reach up to 20 times the losses of a conventional waveguide. Hence, the dimensions of the ridges should be carefully optimized to obtain the best compromise between size, bandwidth and attenuation.

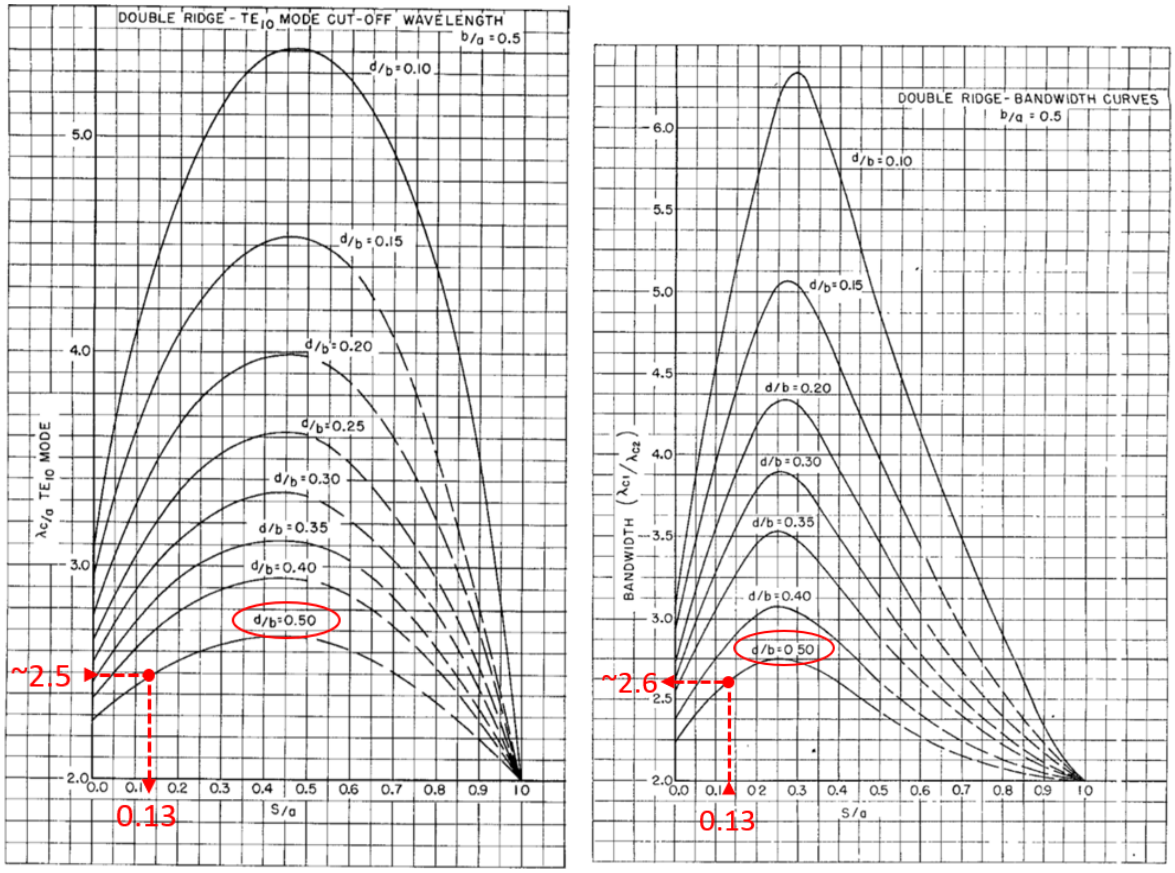

(a) (b)

Figure IV.2 (a) The extension factors, λ_c/a, for the TE_{10} mode plotted as a function of s/a and d/b (b) and the theoretical bandwidth as a function of s/a and d/b for the DRWG from [IV.3].

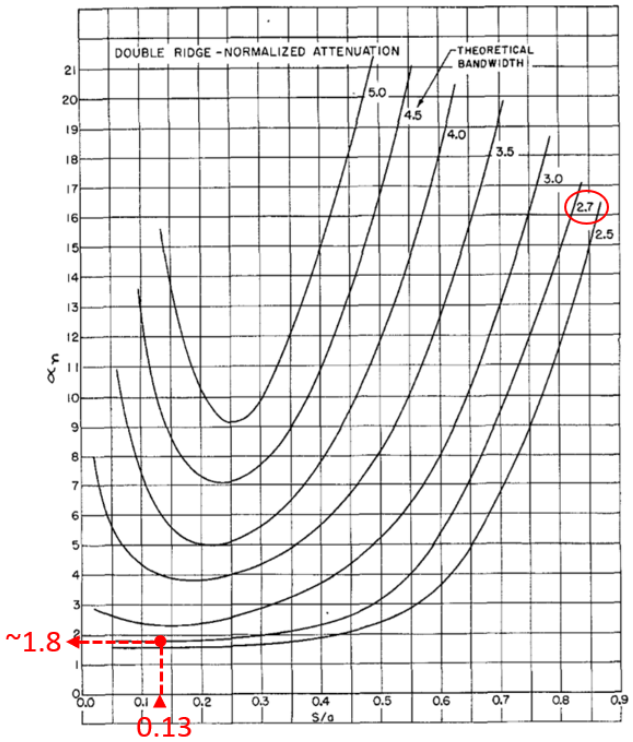

Figure IV.3 Normalized attenuation σ_n versus s/a and theoretical bandwidth from [IV.3].

In terms of applications, ridge waveguides are often used for wideband impedance matching purposes for example in waveguide to coaxial junctions [IV.4] or magic-T [IV.5]. The most known antenna application of the DRWG is the double ridge horn antenna characterized by it's extremely wide bandwidth (18:1 frequency range and exceeding 150% relative bandwidth), commonly used for wide range measurements [IV.6]. On the other hand, limited examples of antenna-arrays can be found based on ridge waveguide technology. One example that was developed in a detailed manner is the slotted ridge waveguide beam scanning array illustrated in Figure IV.4 ([IV.7], [IV.8]). The main advantage of using single ridge waveguide in this context was to reduce the waveguide dimensions from $0.7\lambda_0$ to $0.5\lambda_0$ leading to increase the beam scanning ability of the antenna from ± 25° to ± 90°. However, the slot radiation mechanism limits strongly the achievable impedance bandwidth as for the case of the two by eight slot array shown in Figure IV.5 (a) featuring a bandwidth below 7% for a VSWR < 2 (cf. Figure IV.5 (b)) [IV.7]. Other studies propose to divide the slotted waveguide into subarrays fed by power dividers (cf. Figure IV.6 (a)), widening the bandwidth to 17% ($|S_{11}|$ < -10 dB) (cf. Figure IV.6 (b)) [IV.9].

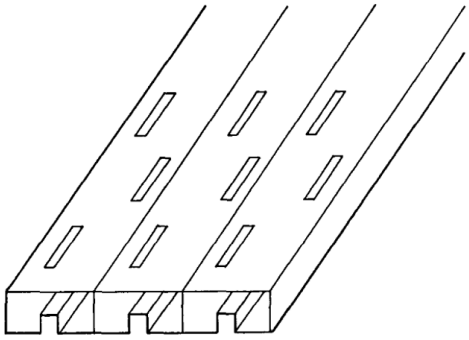

Figure IV.4 Slotted ridge waveguide beam scanning array [IV.7].

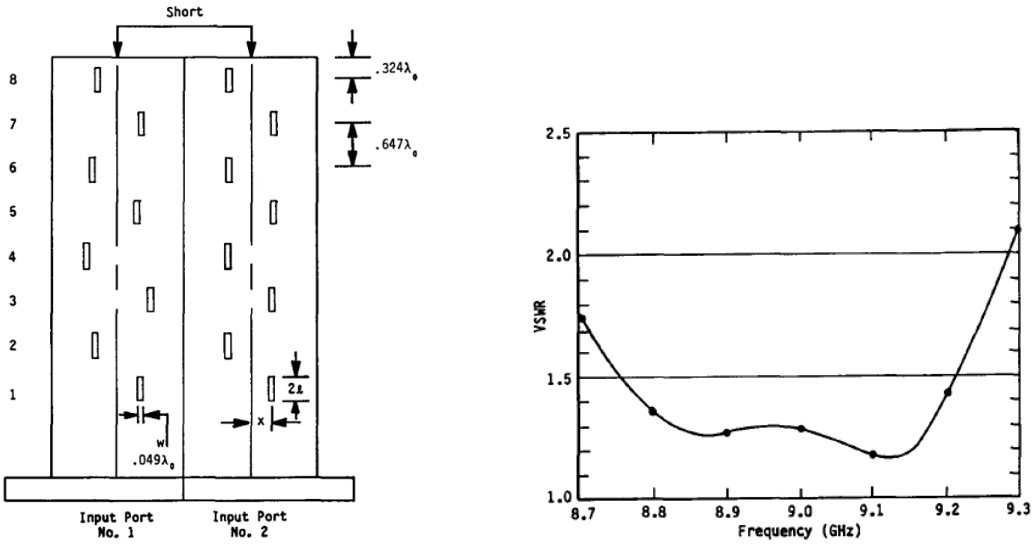

(a) (b)

Figure IV.5 (a) Layout of two-by-eight array of slotted single ridge waveguides and (b) corresponding VSWR versus frequency from [IV.7]

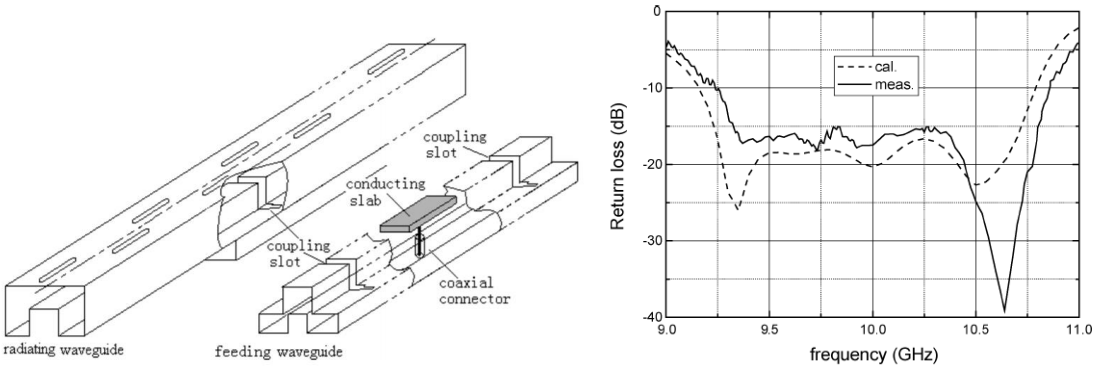

(a) (b)

Figure IV.6 (a) Waveguide slot array with a four-way power divider and coaxial connector and (b) corresponding return loss for a 16 element array from [IV.9].

Still, this is not enough to cover the bandwidth we aim for in this thesis. Therefore, taking benefit of the multiple advantages offered by the DRWG, we studied in the next section the implementation of an array composed of open DRWG radiating elements.

IV.2 UNIT-CELL AND 2×2 ARRAY OF OPEN DRWG

IV.2.1 E and V bands DRWG

The most important parameter to fix in a first step is the cutoff frequency of the DRWG. The useful bandwidth of a waveguide depends mainly upon how close to the lower cut-off frequency one is willing to work. In [IV.3] it was stated that, in practice, this usually ranges from 15 to 25% above the cutoff frequency of the fundamental mode [IV.3]. Since the beginning of our band of interest is near 57 GHz, the latter indication implies that the cutoff frequency of the DRWG should be close to 49.5 GHz or less. On the other hand, the main goal we target by using the DRWG concept is to be able to reduce its dimensions to at least $0.7\lambda_0$ (the free space wavelength of the waveguide at the center frequency 71.5 GHz, of both V and E bands). This parameter is essential to limit side lobes appearance, especially that we intend to use an open ridge waveguide as the radiating element of the array. Hence, the dimensions of our design were chosen to satisfy the following objectives:

- Largest transversal dimension of the waveguide, a (cf. Figure IV.1), should be less than $0.7\lambda_0$ (equal to 2.95 mm at 71.5 GHz).
- The cut-off frequency should be near 50 GHz.
- Respect the design rules for fabrication with 3D printing (minimum details of 200 µm to satisfy standard DMLS resolutions).
- Achieve the lowest attenuation possible which corresponds to the smallest s/a and the greatest d/b satisfying the above conditions.

We started the design of our DRWG by fixing the waveguide dimensions a and b to 2.4 and 1.2 mm, respecting the $0.7\lambda_0$ requirement and an aspect ratio a/b of 0.5. Then we chose the dimensions of the ridges to place the cutoff frequency around 50 GHz. To respect the design rules for fabrication and given the fixed a and b dimensions, the following conditions imply:

- s > 200 µm, hence s/a > 0.09.
- The height of the ridges should be greater than 200 µm, and the space between the ridges should be at least 200 µm, hence, 0.18 < d/b < 0.64.
- Cutoff frequency ≤ 49.5 GHz implies $\lambda_c/a \geq 2.5$.

Following those specifications and referring to the chart of Figure IV.2 (a), the s/a and the d/b values satisfying the above conditions are 0.13 and 0.5 respectively, leading to s= 300 µm and d = 600 µm. The position of those values is indicated in the charts of Figures IV.2 and IV.3 by red marks. Referring to the chart of Figure IV.2 (b) this leads to a theoretical bandwidth of 2.6 corresponding to pushing the cutoff frequency of the TE_{20} mode to 128.7 GHz. The chart of Figure IV.3 (b) indicates that the corresponding attenuation is about 1.8 times that of a conventional waveguide of the same dimensions. In practice the attenuation of a conventional waveguide depends on the method used for fabrication. For example, commercially available WR12 waveguides achieve an attenuation around 2 dB/m [IV.10, p. 12].

The DRWG with the latter fixed dimensions was simulated under HFSS to verify the expected performance. We also simulated a WR12 standard waveguide and a WR12 with double ridges to explicitly show the ridges effect. The simulation models and corresponding dimensions are illustrated in Figure IV.7. Table IV.1 shows the cutoff frequency of the TE_{10}, TE_{01} and TE_{20} modes directly obtained with simulations for each of the waveguides.

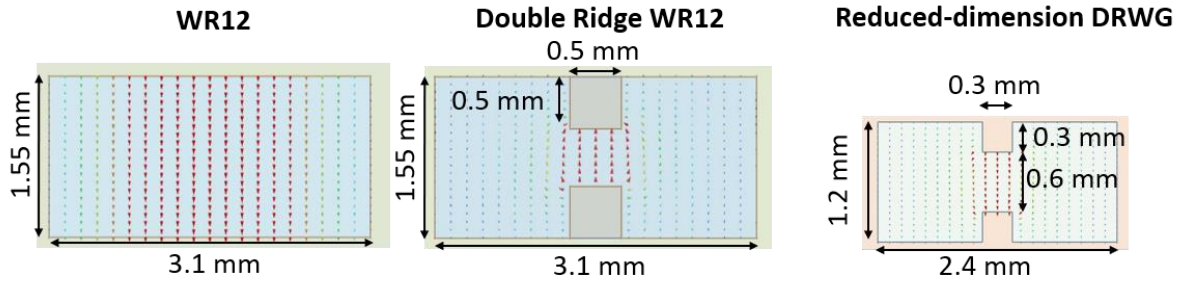

(a) (b) (c)

Figure IV.7 (a) Cross-section of a WR12, (b) double ridge WR12, (c) a reduced-dimension DRWG and vector E-field distribution of the fundamental mode for each case.

	WR12	Double Ridge WR12	2.4 x 1.2 DRWG waveguide (HFSS)	2.4 x 1.2 DRWG waveguide (design charts [IV.3])
F_{c10}	48 GHz	33 GHz	50.5 GHz	49.5 GHz
F_{c01}	97 GHz	98 GHz	128 GHz	128.7 GHz
F_{c20}	96 GHz	96 GHz	131 GHz	Not Specified (NS)

Table IV.1 Cut-off frequencies of the TE_{10}, TE_{01} and TE_{20} modes of a WR12, Double ridge WR12 and reduced-dimension DRWG.

It was found that 0.5 mm × 0.5 mm square ridges inserted in a standard WR12 waveguide could shift down the cutoff frequency of the fundamental mode to 33 GHz. Simultaneously, the cutoff frequency of the second mode f_{c01} remains the same after adding the ridges to the

WR12. Indeed, this mode is not significantly affected by the ridges since the ridges don't lie along the position where the electric field is maximum. By decreasing the dimensions of the waveguide and resizing the ridges, the cutoff frequency of the fundamental mode was increased back to 50 GHz. The parameters extracted from the design charts correspond well to simulated results. With this sizing, we managed to obtain a single mode bandwidth ranging from 50 GHz to 128 GHz.

Once the dimensions of the DRWG were fixed, we evaluated its radiation properties while being terminated by a simple open-end. The simulation of a 2 cm length open DRWG, illustrated in Figure IV.8 (a), resulted in a broadside realized gain ranging from 5.5 to 6.7 dBi between 57 to 86 GHz (cf. Figure IV.8 (b)). The simulated return loss was to found to be above 6 dB and the combined mismatch and attenuation losses were found to be equal to 1 dB between simulated gain and directivity. Hence, if the matching is enhanced, it would be interesting to use an open DRWG as a unit-cell for its simplicity and wideband characteristics.

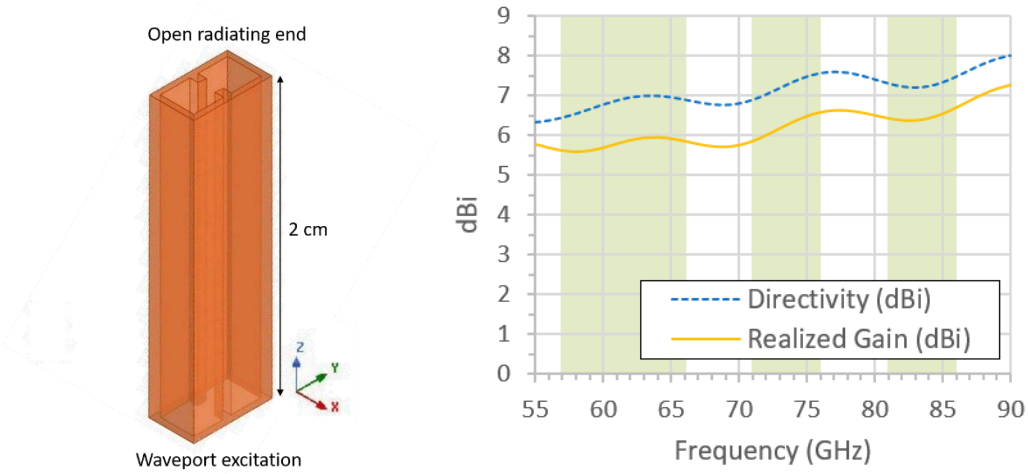

(a) (b)

Figure IV.8 (a) Open DRWG simulation model and (b) corresponding simulated broadside (along z direction) realized gain and directivity versus frequency.

IV.2.2 DRWG four-way compact divider

We started the study of the feasibility of the array composed of open DRWG unit-cells by replicating the four-way power divider presented in III.4.1 and replacing the dielectric filled waveguide by DRWGs. The design of the DRWG four-way divider is depicted in Figures IV.9 and IV.10 where ridges were added not only to the input and output waveguides but also to the common section of the divider.

The optimization of the parameters indicated in Figures IV.9 and IV.10, was first conducted while loading all the ports of the divider with waveports. The goal was to obtain the best matching in V and E-bands. As explained in III.4.1, the dimensions of the common part of the divider, y_com and x_com, were chosen to be equal twice the dimensions of the waveguide plus the minimum spacing between the 4 output of the waveguides which was set to be 200 µm. The height H_com was set to be equal to a quarter guided wavelength, $\lambda_G/4$ at 71 GHz

which is the center frequency between E and V bands. The guided wavelength, λ_G, is expressed in the same manner as for standard hollow metallic waveguide TE modes [IV.11],

$$\lambda_G = \frac{\lambda_0}{\sqrt{1 - (\frac{\lambda_0}{\lambda_c})}} \quad \text{(IV.1)}$$

Where λ_0 is the free space wavelength and λ_c is the cut-off wavelength. Using equation (IV.1), the guided wavelength is evaluated to 7.4 mm giving $\lambda_G/4$ equal to 1.9 mm which was then more finely optimized in HFSS to 1.8 mm. All the obtained optimized dimensions are listed in Table IV.2.

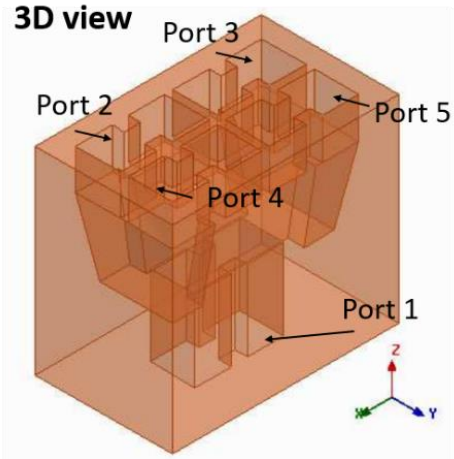

Figure IV.9 3D view of the simulation model of the designed four-way DRWG power divider.

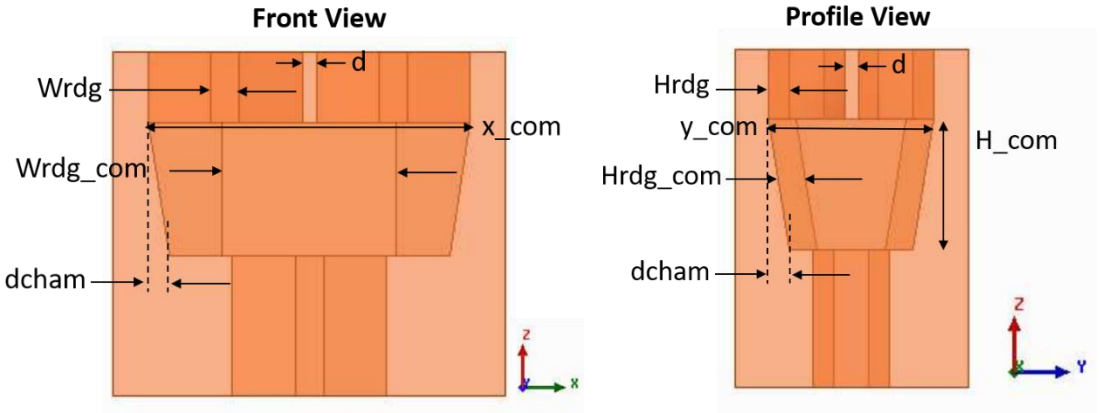

Figure IV.10 Front and profile view of the simulated model of the designed four-way DRWG power divider.

Wrdg	Hrdg	d	x_com	y_com	H_com	Wrdg_com	Hrdg_com	dcham
0.3	0.3	0.2	5	2.6	1.8	2.5	0.4	0.3

Table IV.2 Values (in mm) of the parameters of the optimized four-way DRWG divider.

Simulation results showed a return loss higher than 14 dB over E and V-bands (cf. Figure IV.11 (a)). Notice how the best matching was obtained at 74 GHz, the frequency at which λ_G = 4×H_com. The maximum amplitude deviation between simulated $|S_{21}|$, $|S_{31}|$, $|S_{41}|$ and

$|S_{51}|$ is under 0.05 dB (cf. Figure IV.11 (b)) and low losses were obtained as $|S_{21}|$ lies between -6.4 and -6.04 dB (relatively to the -6dB level corresponding to a perfect power distribution between the four ports). Moreover, all the outputs were found to be in-phase.

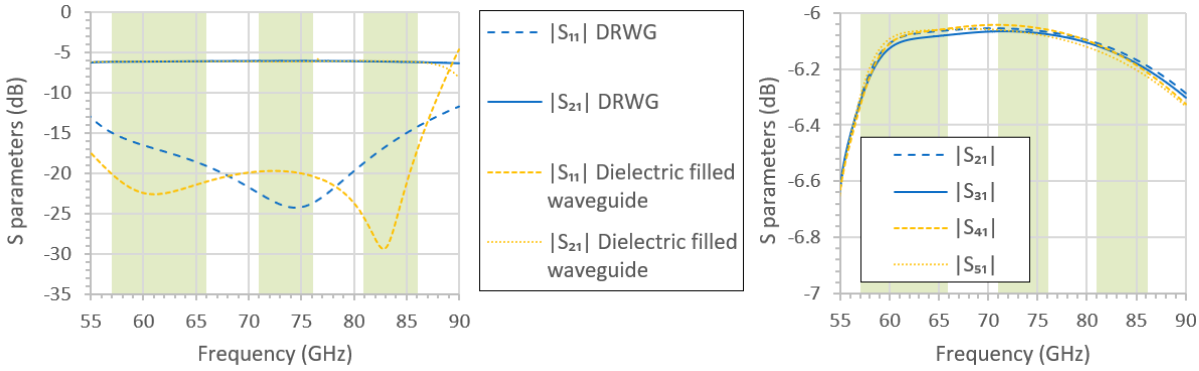

(a) (b)

Figure IV.11 (a) Simulated S-parameters versus frequency of the four-way DRWG divider compared to those of the dielectric-filled waveguide four-way divider. (b) Comparison of the simulated transmission coeffecients of the four-way DRWG divider.

The wide impedance bandwidth of the designed four-way divider, confirmed by simulations, paves the way for developing a corporate wide-band feeding network for an array of open DRWGs. In the next section, we present the study of the radiation properties of a 2×2 array with open DRWG radiating elements.

IV.2.3 Open 2x2 DRWG

The next step was to simulate the divider with open DRWGs (corresponding to ports 2, 3, 4 and 5 indicated in Figure IV.9). Figure IV.12 (a) and (b) illustrate the simulated $|S_{11}|$ and the input impedance locus of the open 2×2 DRWG. From the impedance locus it can be noticed that the capacitive reactance increases after opening the waveguide ends, even if the $|S_{11}|$ remains below -9 dB from 54 to 86 GHz which is acceptable. Nevertheless, to maintain a good impedance matching level for the larger size arrays a better level of matching is needed.

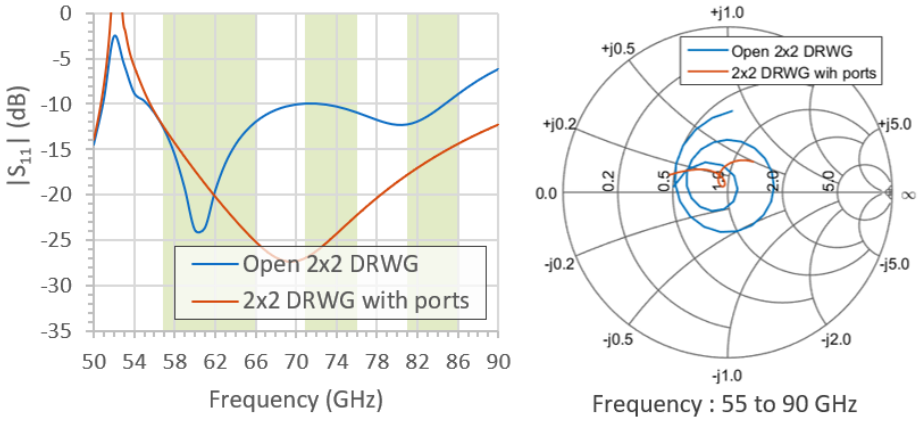

(a) (b)

Figure IV.12 (a) Simulated $|S_{11}|$ and (b) input impedance locus versus frequency of the 2×2 array of open DRWG compared with the four-way DRWG divider loaded with waveports.

One way to improve the matching is to follow the concept of horn antennas. The pyramidal shape used for horn antennas is basically employed to achieve an impedance match between the impedance of the input of the waveguide and the free space impedance. Hence, we simply slightly tapered the waveguide to improve the matching while keeping a low-profile aperture (less than $0.7\lambda_0$ equal to 2.95 mm at 71.5 GHz). As represented in Figure IV.13, the DRWG open-end dimensions were increased from 2.2 mm × 1.1 mm to 2.7 mm × 1.6 mm in an asymmetric fashion to keep the same spacing between the outputs of the four-way divider. The height of the radiating elements, h_horn, was fixed to 1.5 mm = $\lambda_G/4$, where λ_G is evaluated at 80 GHz to improve the impedance matching close to the end of the band.

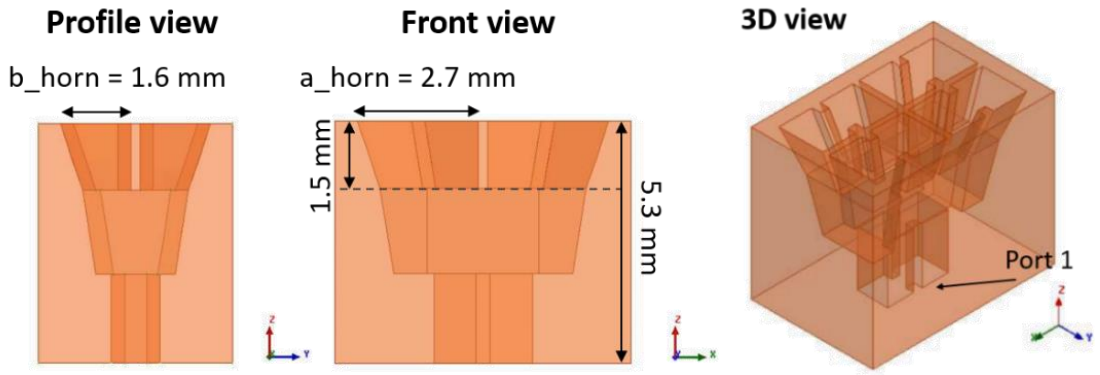

Figure IV.13 Various views of the simulated model of the 2×2 DRWG with asymmetric horn opening.

Figure IV.14 (a) and (b) show the corresponding simulated $|S_{11}|$ and the input impedance locus. By decreasing the capacitive load after tapering the waveguide outputs, the input impedance loops become smaller and closer to the center yielding a better matching. A wide -10dB impedance matching is found between 57 and 90 GHz (45% of relative bandwidth).

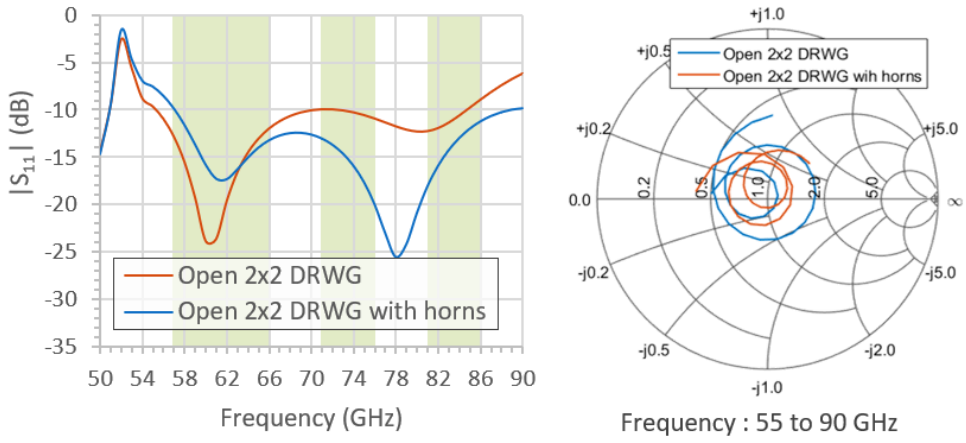

(a) (b)

Figure IV.14 (a) Simulated $|S_{11}|$ (b) and input impedance locus (b) of the 2×2 open DRWG with and without horn shaped open-ends.

The simulated realized broadside gain (along z direction), plotted in Figure IV.15, ranges between 10 and 13 dBi over the E and V-bands which is 3 dB lower than the gain obtained with the 2×2 SCP array fed by dielectric-filled waveguide. This is mainly due to the fact that the elements of the SCP array are more spaced in E-plane than the elements of the DRWG

array (3.2 mm versus 1.8 mm) and the fact that the patch increases the directivity of the slot. Nonetheless, the design is much simpler to manufacture than the SCP array fed by dielectric-filled waveguide and the lower gain can be compensated by increasing the number of elements in the E-plane in a larger-size array. In fact, we preferred not to increase the spacing between the elements to limit as much as possible the side lobes level. Additionally, the proposed array is not only practical but also highly efficient as the simulated efficiency is higher than 94 % from 57 GHz to 90 GHz. The simulated radiation patterns of the 2×2 array DRWG with horn opening in E and H-plane are depicted in Figure IV.16. Both side-lobes and back-radiation levels are below 15 dB for all frequencies.

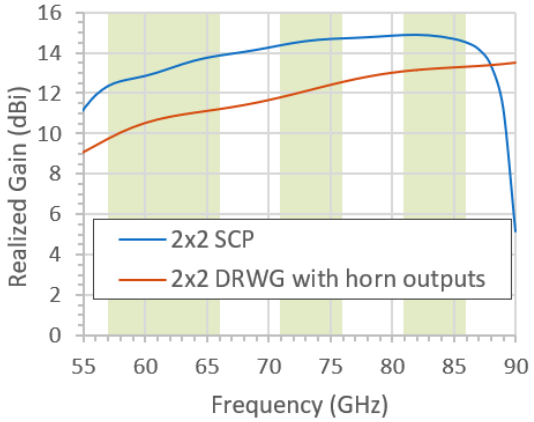

Figure IV.15 Comparison between the simulated broadside (along z direction) realized gain of the previous 2×2 SCP and the proposed 2×2 DRWG with horn outputs versus frequency.

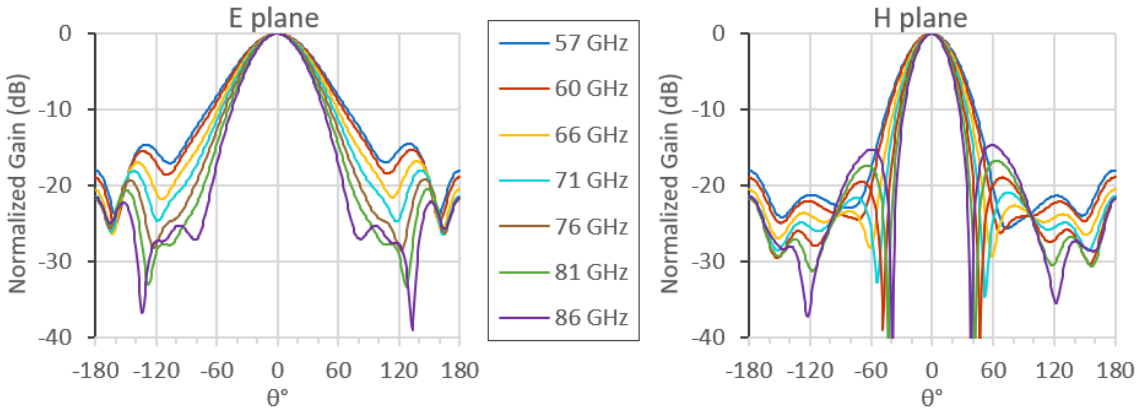

Figure IV.16 Normalized radiation patterns versus elevation angle in E and H plane of the 2×2 DRWG with horn outputs for different frequencies.

To verify that a larger size array would satisfy ETSI RPE, we applied the array factor computation from HFSS on the simulated 2×2 array in order to estimate the radiation patterns of a 32×32 array configuration. The spacing between the elements along x and y directions are 2.9 and 1.8 mm respectively. Results demonstrated that the class 2 RPE is not satisfied in E and H planes, an example at 71 GHz is shown in Figure IV.17. On the other hand, the RPE class 2 and 3 are respected in the 45° plane in a wide angular range as represented in Figure IV.18 implying that the antenna should be rotated by 45° during installation. Table IV.3 gives a general overview of the accordance with ESTI RPE and the corresponding angular range.

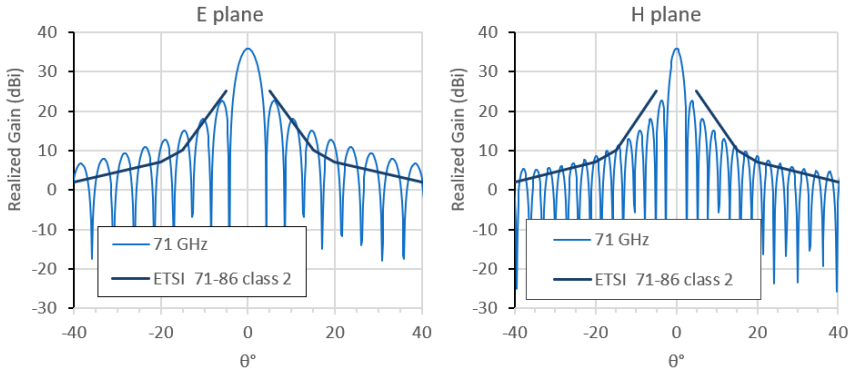

Figure IV.17 Realized gain versus elevation angle in E and H planes at 71 GHz of the 32×32 array after applying the array factor with ETSI 71-86 class 2 RPE mask.

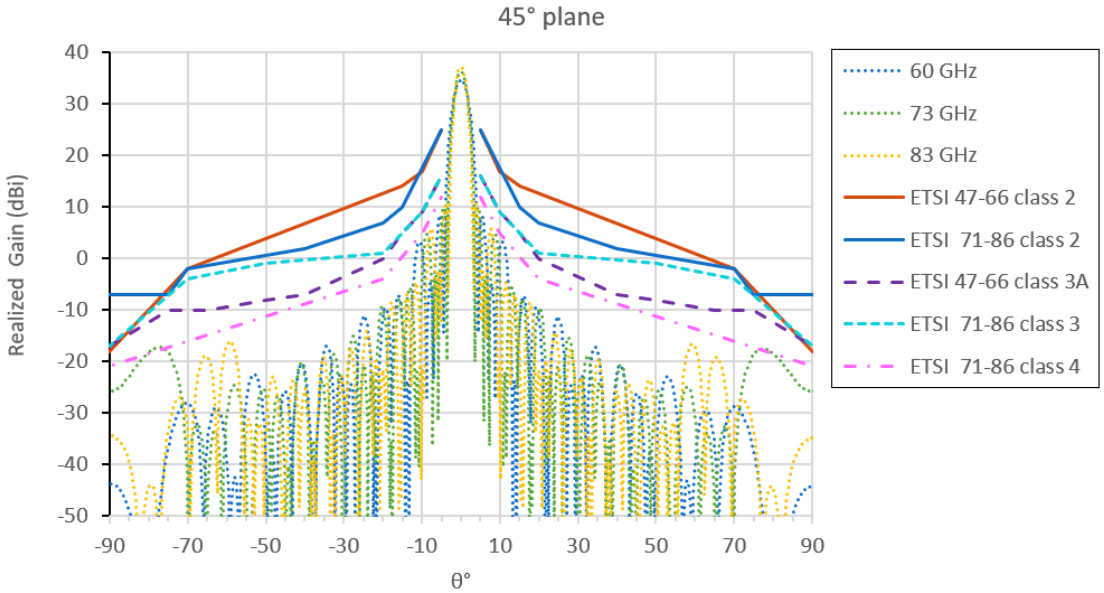

Figure IV.18 Realized gain versus elevation angle in the 45° plane of the 32×32 array after applying the array factor for various frequencies with ETSI RPE mask.

	47-66 class 2	47-66 class 3A	71-86 class 2	71-86 class 3	71-86 class 4
E-plane	Not respected	Not respected	Not respected	Not respected	Not respected
H-plane	**-45° to 45°**	Not respected	Not respected	Not respected	Not respected
45°plane	**-170° to 170°**	**-170° to 170°**	**-170° to 170°**	**-120° to 120°**	**-120° to 120°**

Table IV.3 The accordance of simulated radiation patterns of the 32×32 array (obtained by applying the array factor) with ESTI RPE mask and corresponding angular range.

Figure IV.19 illustrates the broadside realized gain resulting from applying the array factor to the 2×2 DRWG array for various number of elements. Estimated broadside realized gain exceeds 30 dBi starting from a 16×32 configuration (46.4 mm × 57.6 mm). Furthermore, the 32×64 (92.8 mm × 105.2 mm) array approaches best the gain obtained with a 32×32 SCP array fed by dielectric-filled waveguide with comparable dimensions (97 mm × 103.2 mm). Moreover, the gain obtained by the 32×64 ranging from 38 to 40 dBi verifies the ETSI gain requirements of at least 30 dBi in V-band and 38 dBi in E-band.

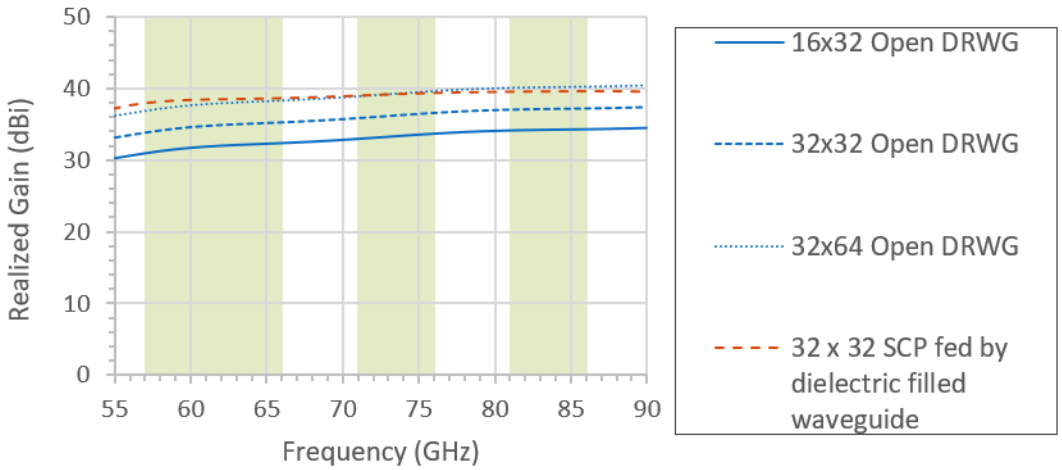

Figure IV.19 Broadside realized gain (along z) resulting from applying the array factor to the 2×2 DRWG horn array for various array sizes compared to the gain of a 32×32 SCP array fed by dielectric-filled waveguide (also obtained by applying the array factor to a the single element).

Hence, this ridge waveguide array configuration combines high efficiency and wideband performance. For the fabrication of the proposed antenna, metallic powder-bed based additive manufacturing technologies were investigated to enable a single-step manufacturing process. Prototypes and measurements results are discussed in the next paragraph.

IV.3 2×2 DRWG PROTOTYPE AND MEASUREMENTS

IV.3.1 Mechanical integration of the 2×2 DRWG with a DRWG to WR12 transition

In order to test and validate the proposed 2×2 DRWG array, we introduce in this paragraph a transition from a DRWG to a conventional hollow metallic waveguide. Relying on the same concept of tapered waveguide edges used in the design of the transition from dielectric filled waveguide to WR12, we designed the tapered DRWG/WR12 transition illustrated in Figure IV.20.

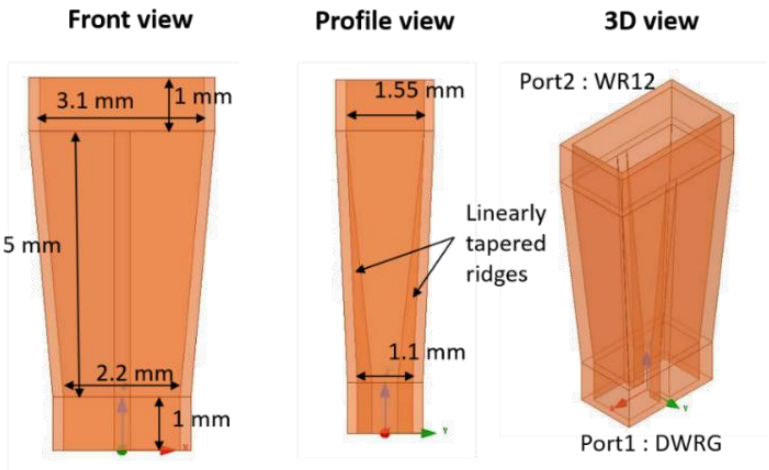

Figure IV.20 Various views of the simulation model of the proposed design of the DRWG to WR12 transition.

The profile view of the proposed structure shows that not only the outer dimensions of the waveguide were linearly transformed but also the height of the ridges, as was also employed in [IV.12]. In fact, the height of the ridges is linearly decreasing along the y axis until it reaches zero at the WR12 end (cf. Figure IV.20, profile view). As mentioned before, the taper role is to satisfy a smooth impedance transformation between the WR12 and the DRWG waveguides, hence the length of the transition was set to 5 mm after performing optimizations on HFSS. Simulated S-parameters of this transition are given in Figure IV.21 (a), demonstrating wideband and low-loss characteristics: the return loss is higher than 15 dB and the transmission loss is lower than 0.2 dB starting from 57 GHz to beyond 90 GHz. After adding this transition to the 2×2 DRWG array, no significant changes in the matching were observed owing to the low $|S_{11}|$ level of this transition (cf. Figure IV.21 (b)).

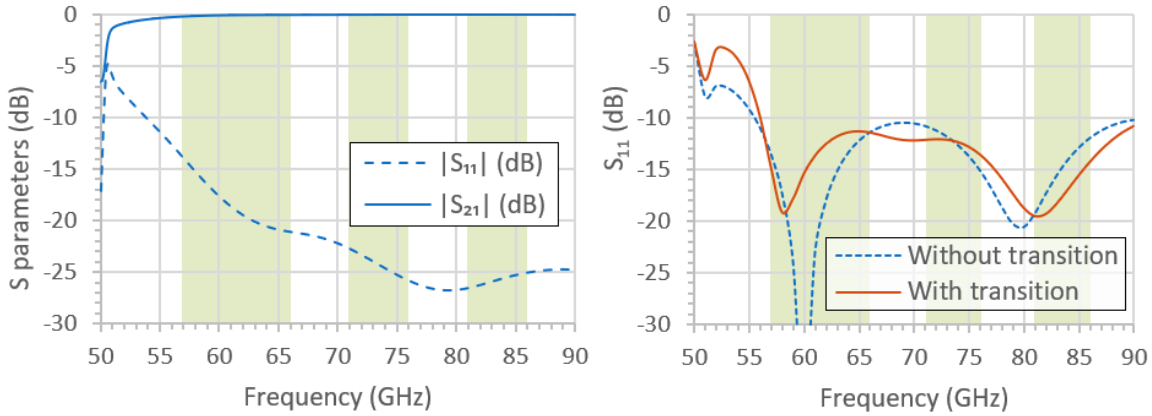

(a) (b)

Figure IV.21 (a) Simulated S-parameters versus frequency of the WR12/DRWG transition and (b) $|S_{11}|$ versus frequency of the 2×2 DRWG array with and without the latter transition.

The complete mechanical piece of the 2×2 DRWG array with an integrated flange and transition to standard WR12 waveguide is shown in Figure IV.22 and Figure IV.23. Thanks to DAM techniques, this antenna can be built in a single-block with all the elements being connected together, avoiding assemblies that could potentially introduce air gaps. The overall height of the prototype is 13.3 mm and transversal dimensions are 4.4 mm and 6.6 mm with a flange diameter of 19.1 mm. In the next section, we discussed the fabrication of the presented design.

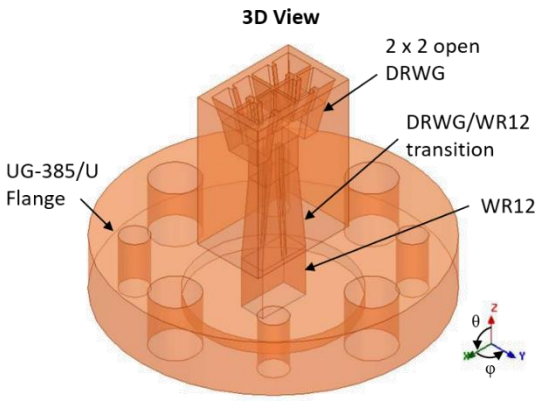

Figure IV.22 3D view of the 2×2 DRWG array with the WR12/DRWG transition and flange combined in one piece.

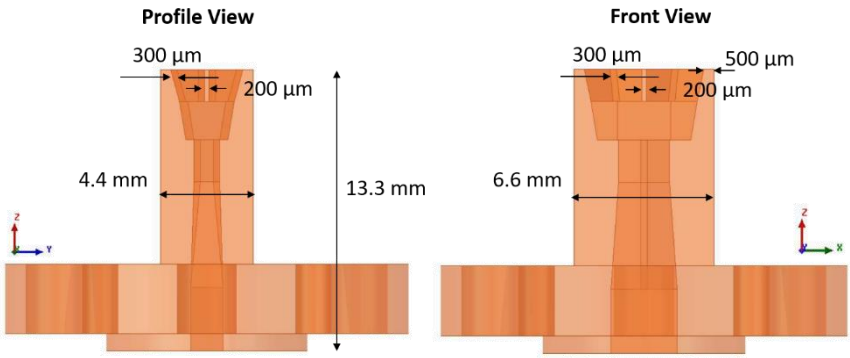

Figure IV.23 Profile and front views of the 2×2 DRWG array with WR12/DRWG transition and flange combined in one piece.

IV.3.2 Prototypes by DMLS micro-printing

In order to make a one-step fabrication process we chose to use DMLS manufacturing. To achieve the best precision and surface roughness, we chose an emerging technology called Micro Laser Sintering which combines the advantages of additive manufacturing and micro-machining. This technology is a standard powder-bed based Selective Laser Sintering (SLS) technology providing micro metal parts [IV.13]. The basis of this method is the combination of a very small laser beam spot size, special micro powder (particles sizes smaller than 5 µm) and very thin layers (1 to 5 µm). Micro metal parts of high dimensional accuracy, detail resolution (< 30 µm) and surface quality are manufactured this way, along with smooth surface finish of complete assemblies manufactured in one shot.

The material we chose is a chromium-nickel alloyed stainless steel (1.4404) [IV.14] with austenitic phase, which offers a good compromise between cost and efficiency. Austenitization means to heat the steel to a temperature at which it changes crystal structure from ferrite to austenite. Austenite is a non-magnetic allotrope of iron or a solid solution of iron, with an alloying element. It is characterized by high tensile strength and high corrosion resistance. Unfortunately, electrical characteristics like conductivity and permeability were not available from the manufacturer, hence we were not able to simulate accurately the used material (copper was used instead). Figure IV.24 shows some photographs of the manufactured pieces as they were extracted from the 3D printer with no surface finishing.

Figure IV.24 Photographs of the 2×2 DRWG 3D printed by micro laser sintering.

IV.3.3 Measurements of the 2×2 DRWG

Measurements were conducted with two different measurement setups. We preformed measurements in V-band with our in-house measurement bench. On the other hand, measurements in E-band where performed in collaboration with the Public University of Navarre (Prof. Carlos Del Rios Bocio). During V-band and E-band measurements, WR12/WR15 and WR12/WR10 transitions were used respectively to connect the WR12 flange of the antenna under test to the WR15 or WR10 waveguides connected to the PNA as shown in Figure IV.25. It's important to note that S_{11} and gain calibration in both measurements were applied at the reference plane indicated in Figure IV.25. Hence, both measured gain and return loss include the losses of the WR15/WR12 or the WR10/WR12 transition depending on the measurement system. It's also worth mentioning, that the sample that have been measured didn't undergo any post-processing steps after it was printed, which is the main breakthrough of this technology. $|S_{11}|$ measurements in E and V-band are plotted in Figure IV.26.

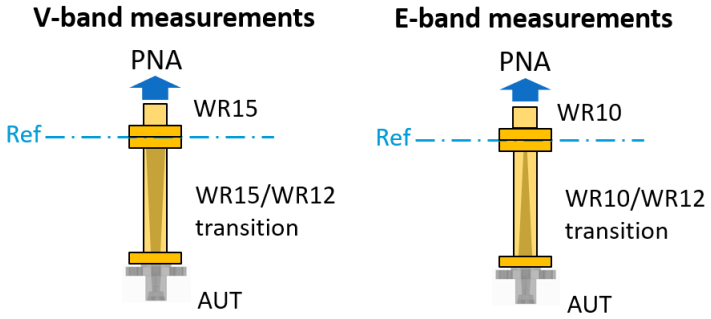

Figure IV.25 Reference plane of S_{11} and gain calibration in V and E-band measurements of the fabricated prototype.

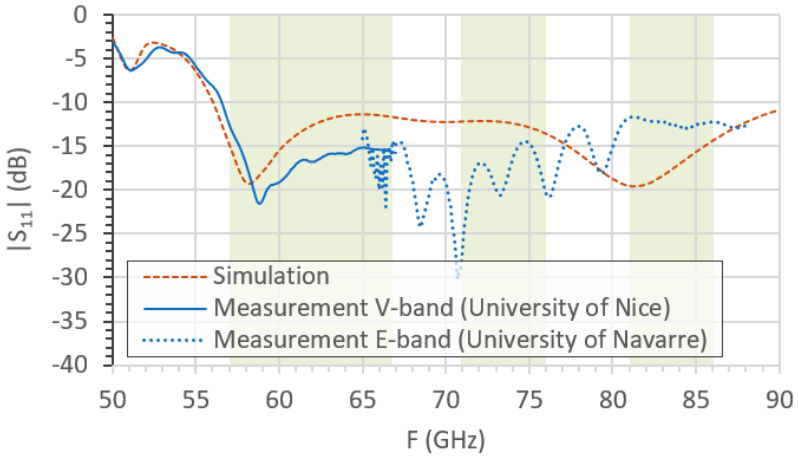

Figure IV.26 Measured and simualted $|S_{11}|$ versus frequency of the fabricated 2×2 DRWG.

Measured $|S_{11}|$ was found to be less than -11 dB from 57 to 86 GHz. Good agreement between simulated and measured $|S_{11}|$ was found in V-band except that measurements are slightly lower than simulations. This may indicate higher losses in the fabricated sample possibly due to surface roughness (due to granulated aspect of the surface of the printed piece), low conductivity or high permeability of the metallic alloy. We remind that copper waveguide

walls were used in the simulation model which does not correspond to the fabrication material. Worse agreement between measured and simulated $|S_{11}|$ was found in E-band which may be due to a standing wave created between the WR10/WR12 and the WR12/DRWG transitions. Ripples can also be seen in V-band measurements but with lower amplitudes. However, those results satisfy a 10-dB matching all over the bandwidth of interest.

Measured broadside realized gain in co- and cross-pol are illustrated in Figure IV.27. Measured co-pol gain lies between 9 and 9.7 dBi in V-band and between 12 and 14 dBi in E-band. Measured gain in V-band was found to be 1 dB lower than simulated gain which may be explained by the previously cited reasons. Additionally, it should be noted that our measurement system precision is about +/-0.8 dB. On the other hand, measured gain in E-band is not linear as was expected from simulations, furthermore it exceeds the simulated gain at 86 GHz. In fact, measurements performed in V-band are direct measurements of FF gain, whereas gain measurements in E-band are extracted from NF to FF transformation applied on planar scan measurements. This can explain why the measured gain in E-band is smoother and may imply that they potentially include additional errors. Nonetheless, the overall agreement between measured and simulated gain is very acceptable. Measured XPD level was found to be higher than 20 dB in V-band and higher than 30 dB in E-band, demonstrating a very good polarization purity. Measured cross-pol was not compared to simulations because simulations showed a very low level of cross-pol gain (under -300 dB) indicating that the measured value is mainly due to fabrication imperfections (round corners, round ridges, etc.).

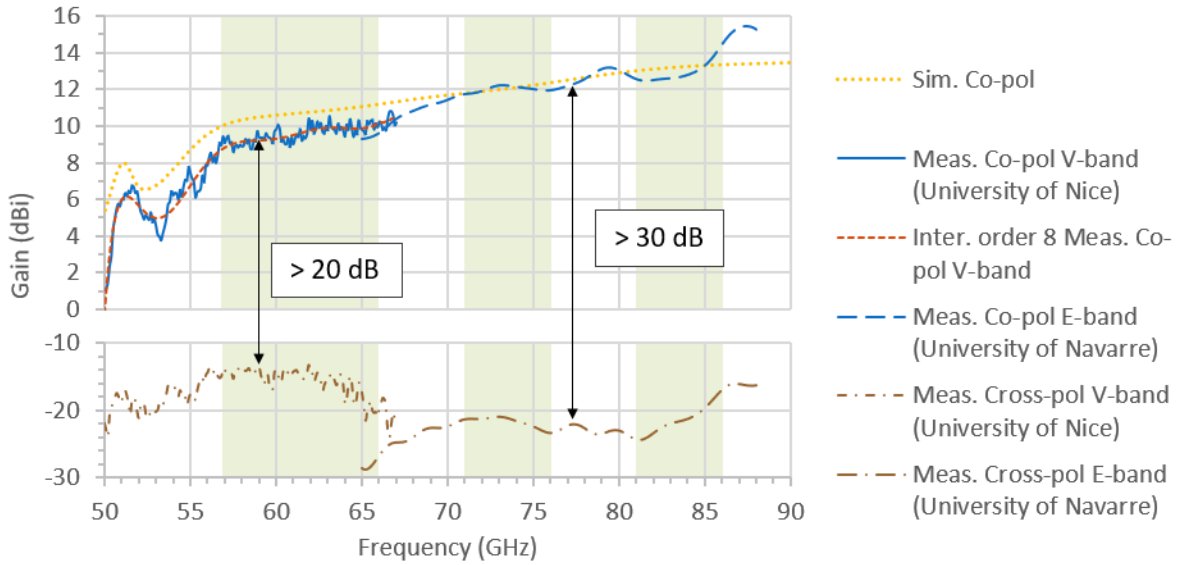

Figure IV.27 Measured and simulated broadside co- and cross-pol realized gain (along z direction) versus frequency compared to simulations of the 2×2 AuT.

Measured and simulated normalized co- and cross-pol gain versus the elevation angle θ in E and H planes at 60, 73 and 83 GHz are depicted in Figures IV.28, IV.30 and IV.31. Radiation patterns measurements in V-band were conducted from -180° to 180°, whereas radiation patterns in E-band are limited between -90 and 90°. At 60 GHz (cf. Figure IV.28), the correlation between measured and simulated radiation patterns is very acceptable between -60° and 60°. Beyond this range, simulation and measurement curves do not agree. Also, we can

notice a slight deformation of the E-plane radiation patterns in the main beam between -10° and 10°. Those differences can be explained by:

- The effect of the plastic support and screws that was used to hold the antenna in V-band measurements (cf. Figure IV.29).
- Interference from the receiving probe-horn situated at 20 cm from the AuT in V-band measurements.

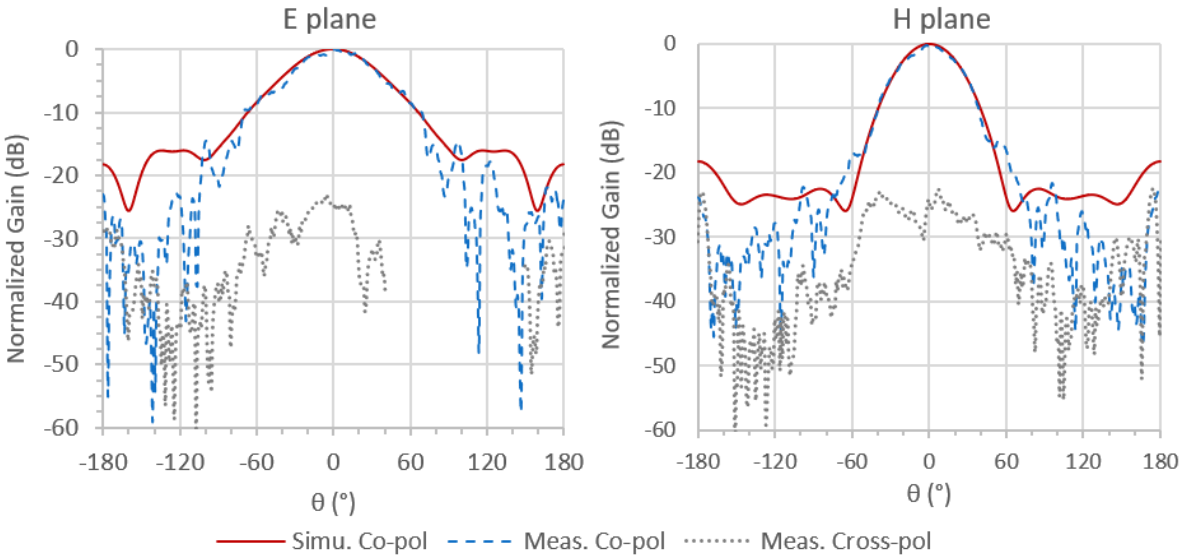

Figure IV.28 Measured and simulated normalized gain versus the elevation angle θ in E and H planes at 60 GHz of the AUT.

Figure IV.29 Plastic support used to hold the AuT in V-band measurements.

At 73 and 83 GHz (cf. Figure IV.30 and IV.31), also, good correlation was found between measured and simulated radiation patterns. In E-plane a cross-pol level of 20 dB was maintained on a wide angular range from -60° to 60°.

Moreover, we were also interested in inspecting the radiation patterns in the 45° plane since simulations demonstrated that the radiation patterns satisfy the ETSI RPE in the 45° and 135° planes and not in E and H planes. Since the antenna is symmetric with respect to X and Y axis, we only show here the radiation patterns in the 45° plane. Figure IV.32 depicts the simulated and measured normalized gain versus elevation angle in the 45° plane at 73 and 83 GHz, featuring a very good agreement between simulation and measurements in the -60° and 60° range. Beyond this range the correlation between the two curves is poor.

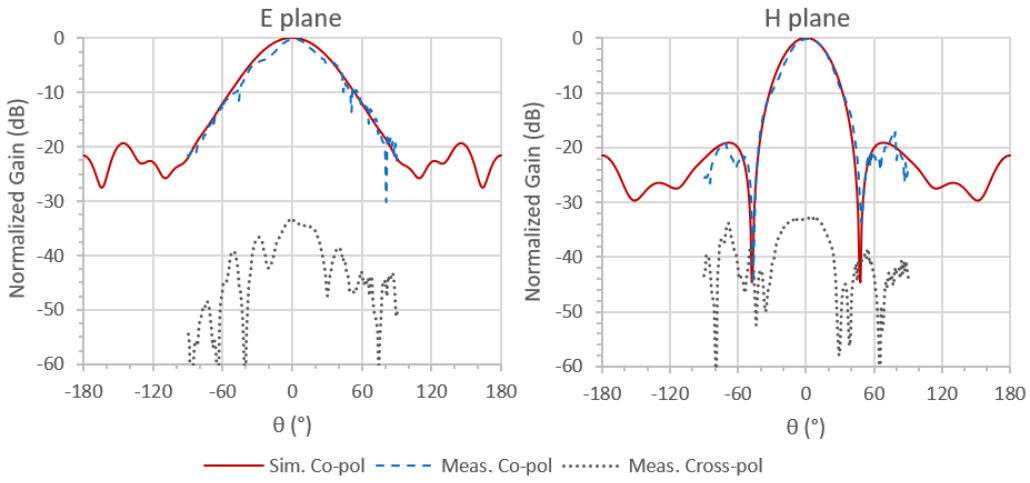

Figure IV.30 Measured and simulated normalized gain versus the elevation angle θ in E and H planes at 73 GHz of the AUT.

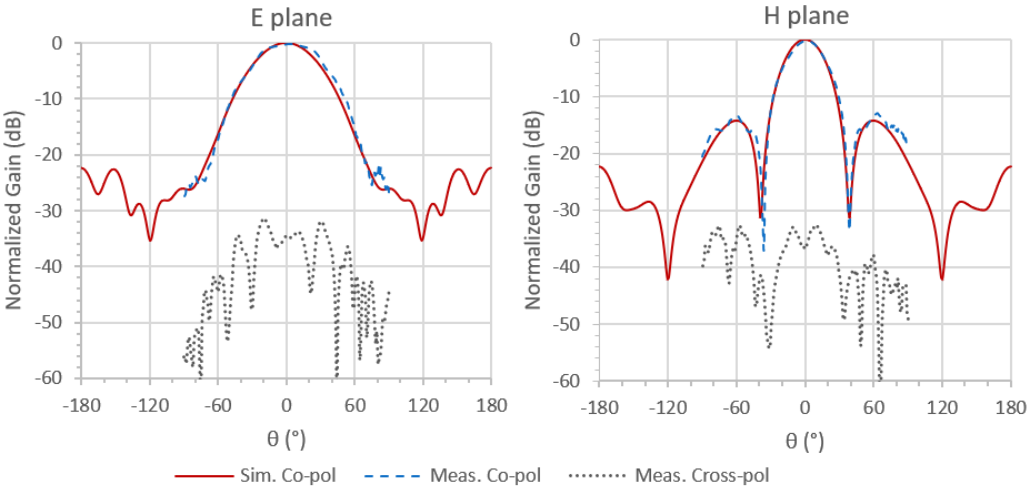

Figure IV.31 Measured and simulated normalized gain versus the elevation angle θ in E and H planes at 83 GHz of the AUT.

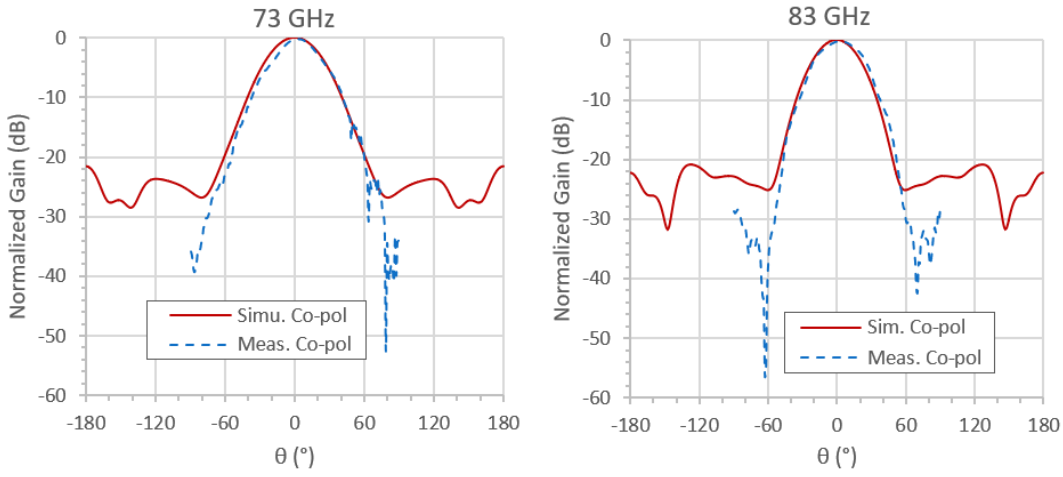

Figure IV.32 Measured and simulated normalized gain in the 45° plane versus θ at 73 and 83 GHz of the AUT.

In general, the observed differences between measurement and simulations beyond the range of -60° and 60° can be related to:

- the effect from the flange of the AUT that was not included in simulations.
- interference from the surrounding measurement system components.

Overall measurements results proved the validity of the novel proposed antenna as a state-of-the-art wideband array antenna. It also confirmed the additive manufacturing technics' high potential to reproduce fine details (down to 200 µm) meeting with millimeter wave applications requirements. The proposed 2×2 array demonstrated a very wideband matching and high efficiency (above 80% if the measured gain is compared to the simulated directivity). Further study consists on composing larger size arrays based on the presented subset array. In fact, the hybrid feeding configuration previously presented in III.3.3.b can be used to connect the 2×2 DRWG array instead of the 2×2 slot coupled patch arrays and dielectric-filled waveguide feeding (cf. Figure IV.33). The designed transition from DRWG to WR12 can be used to connect the DRWG subsets to the hollow metallic waveguide feeding network. The proposed concept can drastically simplify the prototyping process. A one-shot fabrication can be applied, resulting in a final piece of almost 3 mm thickness. Final configurations of large DRWG arrays with elements up to 32×64 are still under investigation.

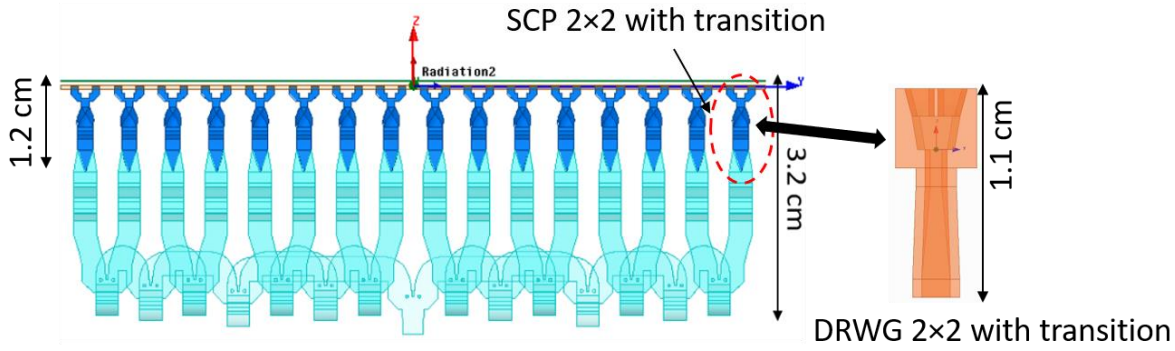

Figure IV.33 Illustration of a possible configuration of the larger size arrays composed out of the 2×2 DRWG subset.

IV.4 CONCLUSION AND PERSPECTIVES

Fabrication simplicity was brought to our design by using DRWG instead of dielectric-filled waveguide. Leveraging the wide bandwidth characteristic of the DRWG to reduce its dimensions, we were able to develop a high efficiency wide-band 2×2 array using asymmetric double ridge horns radiating elements. Prototyping was realized by micro laser sintering, a recently developed high accuracy DMLS technology based on micro-powder of ultra-small particles (which size can go down to 1 µm). Printed 2×2 DRWG array presented high resolution and needed no post-processing. Measurement results of the prototypes agreed well with simulations, demonstrating a -10dB-impedance-matching all over V and E bands and a measured broadside realized gain ranging between 9 and 14 dBi. Table IV.4 compares the proposed DRWG solution in a 32×64 array configuration, and the SCP array fed by dielectric filled waveguide proposed in chapter three and commercial solutions. The proposed antenna

array presents competitive transversal dimensions and achieve the widest bandwidth compared to the existing flat array antennas from the best of our knowledge. Nonetheless, this wide bandwidth was achieved at the expense of thickening the feeding network. From the mechanical point of view, the final product is expected to be heavier than existing commercial solutions but has the advantage of being more resistant and durable compared to the electroplating solutions of plastic adopted in [IV.15] and [IV.16]. The main advantage of our solution is its ease of fabrication as a one piece with no assembly nor post-processing needed, consequently economizing time, effort and cost. Most importantly it is the first solution to our knowledge to cover both V and E bands.

Antenna	Technology	Gain (dBi)	Antenna size (w×d×h mm)	Frequency	Weight (Kg)	ETSI class
GAP waves, Gap Array Antenna [IV.15]	Gap waveguide	26	42.5 × 43.5 × 12.2	V-band	NS	NS
		32	93 × 93 × 15.8	V-band	NS	3
		38	118 × 118 × 8.2	E-band	NS	3
Huber&Suhner, SENCITY® matrix [IV.16]	Slot array	38	135 × 130 × 9.5	V-band	0.15	2
		38	102 × 106 × 8	E-band	0.08	2
		43	280 × 280 × 34	E-band	0.2	2
This work:	SCP array with dielectric filled waveguide network	36 to 38 (32×32)	103 × 97 x 14.5	E and V-band	-	2
	Patch array with hybrid feeding network	34 to 38 (32×32)	103 × 97 x 32	E and V-band	-	2
	Open DRWG array	33 to 36 (32×32)	92.8 × 57.6 × ~30	E and V-band	-	2
		37 to 39 (32×64)	92.8 × 105.2 × 30	E and V-band	-	2

Table IV.4 Comparison between our proposed antenna arrays and commercial arrays.

IV.5 REFERENCES

[IV.1] D. M. Pozar, Microwave Engineering. Wiley, 2004.

[IV.2] "Dual Slant Linearly Polarized Antenna for Broadband High Power Applications." [Online]. Available: http://www.microwavejournal.com/articles/3652-dual-slant-linearly-polarized-antenna-for-broadband-high-power-applications. [Accessed: 24-Jul-2018].

[IV.3] S. Hopfer, "The Design of Ridged Waveguides," IEEE Transactions on Microwave Theory and Technics, vol. 3, no. 5, pp. 20–29, Oct. 1955.

[IV.4] S. B. Cohn, "Properties of Ridge Wave Guide," Proc. IRE, vol. 35, no. 8, pp. 783–788, Aug. 1947.

[IV.5] Y. He, D. Mo, Q. Wu, and Q. Chu, "A Ka-Band Waveguide Magic-T With Coplanar Arms Using Ridge-Waveguide Transition," IEEE Microwave Wireless Components Letters, vol. 27, no. 11, pp. 965–967, Nov. 2017.

[IV.6] V. Rodriguez, "Improvements to broadband dual ridge waveguide horn Antennas," in 2009 IEEE Antennas and Propagation Society International Symposium, 2009, pp. 1–4.

[IV.7] D. Y. Kim and R. S. Elliott, "A design procedure for slot arrays fed by single-ridge waveguide," IEEE Transactions on Antennas and Propagation, vol. 36, no. 11, pp. 1531–1536, Nov. 1988.

[IV.8] J. Tian and G. Sun, "Design of K-band single ridge waveguide slot antenna arrays," in 2017 2nd IEEE International Conference on Integrated Circuits and Microsystems (ICICM), 2017, pp. 291–294.

[IV.9] W. Wang, S.-S. Zhong, Y.-M. Zhang, and X.-L. Liang, "A broadband slotted ridge waveguide antenna array," IEEE Transaction on Antennas and Propagation, vol. 54, no. 8, pp. 2416–2420, Aug. 2006.

[IV.10] "WR-12 Instrumentation Grade Straight Waveguide Section 12 Inch Length with UG-387/U Flange Operating from 60 GHz to 90 GHz." [Online]. Available: https://www.pasternack.com/wr-12-straight-waveguide-section-ug-387-60-90-ghz-pe-w12s001-12-p.aspx. [Accessed: 12-Oct-2018].

[IV.11] N. Marcuvitz, Waveguide Handbook. IET, 1951.

[IV.12] M. W. Hyde and M. J. Havrilla, "Simple, Broadband Material Characterization Using Dual-Ridged Waveguide to Rectangular Waveguide Transitions," IEEE Transaction on Electromagnetic Compatibility, vol. 56, no. 1, pp. 239–242, Feb. 2014.

[IV.13] "Home - 3D MicroPrint GmbH." [Online]. Available: http://www.3dmicroprint.com/. [Accessed: 26-Jul-2018].

[IV.14] "Material - 3D MicroPrint GmbH." [Online]. Available: http://www.3dmicroprint.com/products/material/. [Accessed: 02-Aug-2018].

[IV.15] P. Sjöqvist, "Fixed Beam," Gapwaves AB. [Online]. Available: https://gapwaves.com/fixed-beam/. [Accessed: 02-Aug-2018].

[IV.16] "HUBER+SUHNER - SENCITY® Matrix." [Online]. Available: https://www.hubersuhner.com/en/solutions/wireless-infrastructure/products/mobile-backhaul/sencity-matrix. [Accessed: 18-Jun-2018].

V. Conclusion and perspectives

V.1 CONCLUSION

Several cost-efficient high gain antenna structures were proposed for backhaul links in E and V bands leveraging low-cost fabrication technologies like 3D printing and PCB. We managed to confirm the suitability of the PCB technology and FR4 substrates for the realization of a slot-coupled patch antenna achieving an efficiency above 50%, hence enabling 60 GHz antennas suitable for mass production. Figure V.1 illustrates that the designed antenna demonstrated a gain comparable with the gain achieved with other more expensive technologies in addition to a remarkable wide bandwidth while using a simpler and cheaper fabrication technology. Moreover, the design was completed with a microstrip-to-waveguide transition enabling a low-loss connection from the antenna to the RF PCB. By using DMLS to print the waveguide, an acceptable measured insertion loss of 2 dB was obtained. However, the imprecisions in the PCB fabrication process resulted in excessive surface waves generation which disturbed the patch radiation, consequently the source did not illuminate the designed lens efficiently. A second fabrication batch is considered with a better control process to reach our goals. Nonetheless, we managed to prove the functionality of the printed lens using FDM and ABS-M30 filament by demonstrating a gain exceeding 31 dBi over the whole V-band using a 3D printed corrugated horn source, enabling a cost-efficient competitive solution. For more insight on printed lens capabilities, a Fresnel transmit-array concept was 3D printed with FDM in ABS-M30. The Fresnel lens advantages are the reduction in the total height of the antenna system (60% of the lens height), weight reduction and most of all dielectric loss reduction leading to a higher efficiency. This is realized however at the expense of a narrower operating frequency bandwidth with respect to the elliptical lens. Conducted measurements of the Fresnel lens using our measurement bench demonstrated a gain ranging between 29.5 and 32 dBi over the V-band which is very close to ETSI gain requirements in V-band. Hence, we successfully proved the viability of 3D printing technology for high-gain lens antenna design.

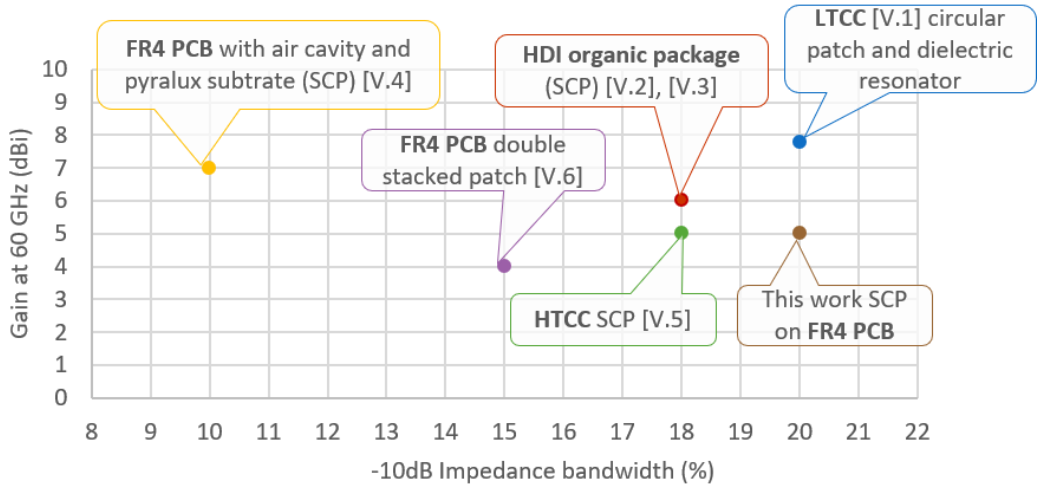

Figure V.1 Achieved gain and -10dB impedance bandwidth of our proposed SCP on FR4 PCB compared to other state-of-the-art integrated antenna technologies [V.1-6].

We completed our study by presenting a further compact flat antenna array design working in V and E bands. By means of a high-efficiency unit-cell composed of a SCP on PCB FR4 fed by a dielectric-filled waveguide, we proposed array designs going up to 32×32 elements covering both V and E bands with a single structure comprising the antenna and the feeding network. Innovative waveguide dividers were presented maintaining a matching level below -15 dB in the V and E bands. Based on those structures, we proposed two feeding network configurations: the first one fully composed by dielectric-filled waveguides and the second being composed by dielectric-filled and hollow metallic waveguides, which thickness are respectively 1.5 cm and 3 cm. Figure V.2 situates the proposed 32×32 slot-coupled patch array with hybrid network relatively to commercial antennas. It shows that the proposed antennas' upmost advantage is the impedance bandwidth covering both E and V-bands, which was realized however at the expense of increasing the total thickness of the antenna-system. Additionally, the estimated realized gain and occupied surface by the array are also competitive. Fabrication technologies like SLS using HDPE powder, injection molding with a DMLS mold and DMLS split-block were then studied for the fabrication of the prototypes. However, the latter methods were not found suitable for our designs. This encouraged us to think of an innovative four-way divider which enabled an easier prototyping and assembly. We successfully tested the fabrication of the proposed four-way divider by means of an in-house 3D printer. However, the possibility to metallize the printed pieces is still under investigation.

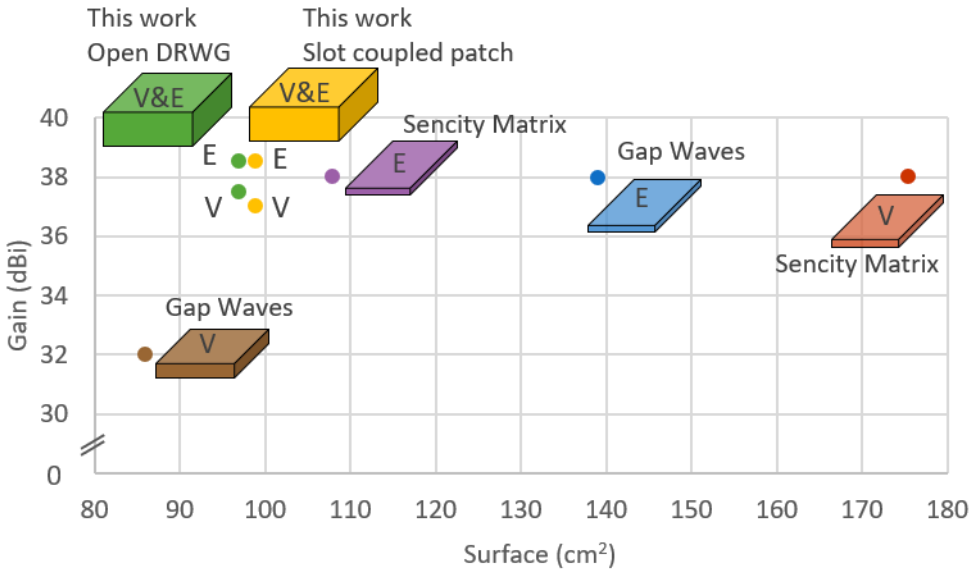

Figure V.2 Broadside realized gain versus occupied surface and thickness illustrated by the height of the parallelepiped of our proposed antenna arrays compared to commercial flat antenna arrays [V.7-8].

In the last chapter, we replaced the dielectric-filled waveguide by a DRWG. Using a unit-cell consisting of an open DRWG along with a compact four-way divider, we proposed a 2×2 subset array. The 2×2 subset was fabricated using micro-DMLS and demonstrated the expected wide impedance bandwidth (40%) with a minimum measured realized gain of 9 dBi without any post-treatment of the pieces. The 2×2 array subset can enable bigger size arrays with very competitive dimensions and realized gain (cf. Figure V.2) with a one-step, single-block fabrication. Even though micro-printing DMLS technique is relatively costly with respect to other printing

technologies, certainly other methods could be investigated as well like SLA with electroless metallization enabling lower weight characteristics and lower cost.

Finally, the proven concepts open-up the way for a myriad of applications especially with the continuous development of 3D printing technologies. The wide variety of materials can enable to use the presented designs within various contexts, like the upcoming satellite constellations network.

V.2 PERSPECTIVES

The proven utility of 3D printing arising technologies for the development of millimeter-wave high-gain antennas along with the availability of new highly-resistant 3D printing materials opens-up the way for spatial applications. In fact, satellite market is actually pushing towards the development of Low-Earth Orbit (LEO) Satellite Constellations in order to deliver worldwide low-cost high-speed Internet Connections. The main aim of the satellite constellation is to bring broadband access all around the globe along with other applications like in-flight entertainment and autonomous vehicle connectivity. The satellite constellation is based on deploying thousands of low-cost micro-satellites in LEO which encouraged many companies to race toward the development of low-cost satellites. Especially,

- OneWeb [V.9] is planning to launch 648 operational satellites, 175–200 kg in mass each, operating in 18 polar orbit planes at 1,200 km altitude.
- SpaceX [V.10] is planning to launch 4600 satellites orbiting at 1,400 km.

The structure of the constellation network and links to earth is featured in Figure V.3. Three main types of links can be distinguished, namely uplink from ground station to satellite, intersatellite links and downlink from satellite to ground.

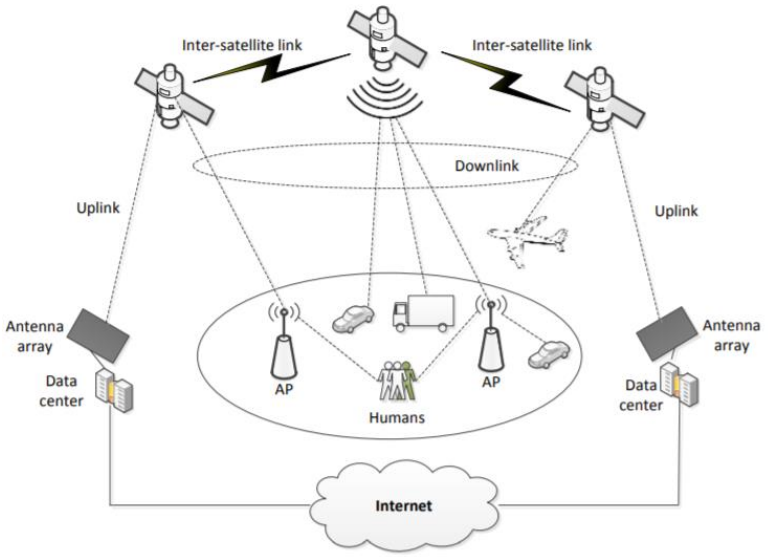

Figure V.3 Satellite broadband network system for LEO communications from [V.11].

In the downlink and uplink contexts, satellite and ground-user are always in relative movement, thus an antenna able to dynamically point is needed in order to track the satellite and establish the communication with it. This is why phased array antennas are being largely investigated for this application to enable electronic beam steering [V.12-13]. The satellites will operate mainly in Ku (12-18 GHz), K (18-26 GHz) and Ka (26– 40 GHz) frequency bands [V.14].

Swissto12 have already announced antenna arrays designs for the broadband satellite network using their own developed 3D printing technology with electronically steerable beams [V.15]. Following the same concept, the designed antennas presented in this PhD could be easily tuned to those applications using 3D printing materials suited to spatial environments. Examples of those materials are PEEK plastic [V.16] available for FDM or 17-4PH stainless steel alloy [V.17] offered by 3Dmicroprint for DMLS micro-3D-printing. The open double ridge waveguide or even the 2×2 array subset could be used for the realization of a single Receiver/Transmitter (RX/TX) phased array panel providing electronic scanning in elevation while azimuth scanning could be achieved mechanically (cf. Figure V.4).

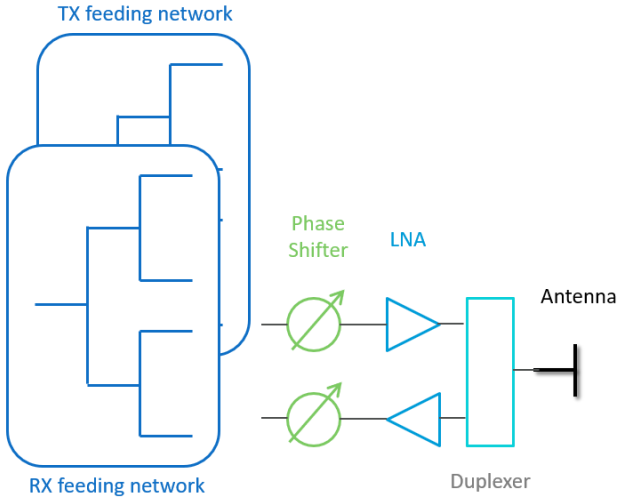

Figure V.4 Single RX/TX phased array panel building blocks.

V.3 REFERENCES

[V.1] D. S. Jun, D. Y. Kim, D. M. Kang, et J. W. Lim, "Design of patch antenna on LTCC substrate with broadband and high gain at millimetre wave band", Electronics Letters, vol. 49, nº 25, p. 1590-1591, déc. 2013.

[V.2] A. Bisognin, "Évaluation de technologies organiques faibles pertes et d'impression plastique 3D afin de contribuer au développement de solutions antennaires innovantes dans la bande 60 GHz – 140GHz", PhD thesis, Université Nice Sophia Antipolis, 2015.

[V.3] A. Bisognin et al., "Millimeter-wave antenna-in-package solutions for WiGig and backhaul applications", in 2015 International Workshop on Antenna Technology (iWAT), 2015, p. 52-55.

[V.4] H. Vettikalladi, O. Lafond, M. Himdi, T. Sarrazin, et N. Rolland, "60 GHz membrane supported aperture coupled patch antenna based on FR4 and new thin Pyralux substrate", in 2012 42nd European Microwave Conference, 2012, p. 209-212.

[V.5] D. Titz et al., "Industrial HTCC Antenna-Module SiP for 60-GHz Applications", IEEE Antennas and Wireless Propagation Letters, vol. 11, p. 576-579, 2012.

[V.6] W. Hong, K.-H. Baek, et A. Goudelev, "Multilayer Antenna Package for IEEE 802.11ad Employing Ultralow-Cost FR4", IEEE Transactions on Antennas and Propagation, vol. 60, nº 12, p. 5932-5938, déc. 2012.

[V.7] "HUBER+SUHNER - SENCITY® Matrix". [Online]. Available: https://www.hubersuhner.com/en/solutions/wireless-infrastructure/products/mobile-backhaul/sencity-matrix. [Consulted: 18-june-2018].

[V.8] P. Sjöqvist, "Fixed Beam", Gapwaves AB.

[V.9] "Virgin, Qualcomm Invest in OneWeb Satellite Internet Plan", SpaceNews.com, 15-janv-2015. [Online]. Available: http://spacenews.com/virgin-qualcomm-invest-in-global-satellite-internet-plan/. [Consulted: 16-march-2016].

[V.10] L. Grush, "SpaceX just launched two of its space internet satellites — the first of nearly 12,000", The Verge, 15-févr-2018. [Online]. Available: https://www.theverge.com/2018/2/15/17016208/spacex-falcon-9-launch-starlink-microsat-2a-2b-paz-watch-live. [Consulted: 28-sept-2018].

[V.11] F. Khan, "Mobile Internet from the Heavens", p. 7.

[V.12] S. A. Matos et al., "High Gain Dual-Band Beam-Steering Transmit Array for Satcom Terminals at Ka-Band", IEEE Transactions on Antennas and Propagation, vol. 65, nº 7, p. 3528-3539, juill. 2017.

[V.13] F. Tiezzi, S. Vaccaro, D. L. Del Río, D. Oro, C. D. Grano, et M. F. Rua, "Low-profile Ku-band array antenna for broadband mobile satellite communications", in Aerospace Conference, 2011 IEEE, 2011, p. 1–6.

[V.14] FCC, "FCC online table of frequency allocations". juill-2014.

[V.15] "Swissto12". [Online]. Available: http://www.swissto12.com/markets/#satellite-communications. [Consulted: 30-sept-2018].

[V.16] "PEEK Plastic | High Temp, Chemical Resistance | Curbell Plastics". [Online]. Available: https://www.curbellplastics.com/Research-Solutions/Materials/PEEK. [Consulted: 08-may-2018].

[V.17] "Material - 3D MicroPrint GmbH". [Online]. Available: http://www.3dmicroprint.com/products/material/. [Consulted: 02-August-2018].

List of Publications

International journal:

- Bisognin, N. Nachabe, C. Luxey, F. Gianesello, D. Gloria, J. R. Costa, C. A. Fernandes, Y. Alvarez, A. Arboleya, J. Laviada, F. Las-Heras, N. Dolatsha, B. Grave, M. Sawaby, A. Arbabian, "Ball grid array module with integrated shaped lens for 5G backhaul/fronthaul communications in F-band," IEEE Transactions on Antennas and Propagation, vol. 65, no. 12, pp. 6380–6394, Dec. 2017.

Invited talk:

- F. Gianesello, E. Lacombe, N. Nachabe, D. Titz, C. A. Fernandes, J. R. Costa, C. del Río Bocio, C. Luxey & D. Gloria, "Industrial packaging & antenna for consumer grade mm-wave products", IEEE MTT-S 2017, Honoluly, USA, 2017.

Conferences:

- N. Nachabe, C. Luxey, D. Titz, F. Gianesello, J. R. Costa, "High-efficiency & wideband aperture coupled patch antenna fed by a dielectric waveguide", 11th EuCAP, Paris, France, 19-24 March 2017.
- N. Nachabe, et al., "Système de communication sans fil point à point communiquant à 12.5 Gbps intégrant une antenne-lentille à 130 GHz", 20th JNM, Saint-Malo, France, 16-19 May 2017.
- N. Nachabe, C. Luxey, D. Titz, F. Gianesello, J. R. Costa, "Antenne patch large bande et à haute efficacité alimentée par un guide d'onde métallique chargé d'un diélectrique", 20th JNM, Saint-Malo, France, 16-19 May 2017.
- N. Nachabe, C. Luxey, D. Titz, J. R. Costa, S. Matos, F. Gianesello, C. A. Fernandes, "Low-cost 60 GHz 3D printed lens fed by a planar source with WR15 transition integrated on FR4 PCB," 2017 IEEE International Symposium on Antennas and Propagation USNC/URSI National Radio Science Meeting, pp. 2671–2672, San Diego, U.S.A., July 2017.
- J. P. Teixeira, S. A. Matos, J. R. Costa, N. Nachabe, C. Luxey, D. Titz, C. A. Fernandes, F. Gianesello, "Transmit array as a viable 3D printing option for backhaul applications at V-band," 2017 IEEE International Symposium on Antennas and Propagation USNC/URSI National Radio Science Meeting, pp. 2641–2642, San Diego, U.S.A., July 2017.
- N. Nachabe, C. Luxey, D. Titz, J. R. Costa, S. Matos, F. Gianesello, C. A. Fernandes, "Low-Cost Wide-Band V-band Patch Antenna on FR4 PCB," 2018 IEEE International Symposium on Antennas and Propagation USNC/URSI National Radio Science Meeting, Boston, U.S.A., July 2018.